Finite-Element Simulations of Glass-Forming Fluids using Mode-Coupling Theory

Inaugural-Dissertation

zur Erlangung des Doktorgrades

der Mathematisch-Naturwissenschaftlichen Fakultät

der Heinrich-Heine Universität Düsseldorf

vorgelegt von

Sebastian Steinhäuser

aus Moers

Neukirchen-Vluyn, Oktober 2023

aus dem Institut für Theoretische Physik II: Weiche Materie
der Heinrich-Heine-Universität Düsseldorf

Gedruckt mit der Genehmigung der
Mathematisch-Naturwissenschaftlichen Fakultät der
Heinrich-Heine-Universität Düsseldorf

Referent: Prof. Dr. Thomas Voigtmann
Korreferent: Prof. Dr. Jürgen Horbach

Tag der mündlichen Prüfung: 01.12.2023

Eidesstattliche Versicherung

Ich, Sebastian Steinhäuser, versichere an Eidesstatt, dass die vorliegende Dissertation von mir selbstständig und ohne unzulässige fremde Hilfe unter Beachtung der „Grundsätze zur Sicherung guter wissenschaftlicher Praxis an der Heinrich-Heine-Universität Düsseldorf" erstellt worden ist.

Neukirchen-Vluyn, 12.10.2023

S. Steinhäuser

Unterschrift

List of Publications

The following publication, based on this thesis, show results covered in chapter 4, regarding geometry-dependent residual stresses predicted by the MCT-ITT model. I performed the simulations and studied the results. The code basis was jointly created by Dr. Timm Treskatis and myself. Interpretation and discussion done by all authors of the publication.
Residual Stresses couple microscopic and macroscopic scales.
S. Steinhäuser, T. Treskatis, S. Turek, T. Voigtmann
under review for Physical Review Letters (Preprint: arXiv:2307.12764, 2023)

The following publications, based on this thesis, show results covered in chapters 5 and 4, regarding the numerical implementation of both the standard (local, chapter 4) and advected (chapter 5) MCT-ITT model and numerical results. I performed the simulations and studied the results. The code basis was jointly created by Dr. Timm Treskatis and myself. Interpretation and discussion done by all authors of the publication.
Finite element implementation of viscoelastoplastic flow using the advected MCT-ITT model.
S. Steinhäuser, T. Treskatis, S. Turek, T. Voigtmann
in process, 2023

Abstract

The non-Newtonian flow of glass-forming fluids displays multiple interesting phenomena that are different from those found in simple liquids. However, so far simulations of those glass-forming fluids do not use a constitutive equation that arises from a microscopic theory able to predict a glass transition. To determine the flow of any fluid in general one has to solve the non-linear Navier-Stokes equations, in our special case we can reduce these to the incompressible time-dependent Stokes equations since in the flow of glass-forming fluids advective inertial forces are negligible compared to viscous forces. In this work we present a combination of finite element method (FEM) fluid flow simulations with microscopic Mode-Coupling theory (MCT) as a source to provide constitutive equations. One challenge lies in the fact that MCT poses complicated integral equations that capture the entire flow-history of the glass-forming fluid. Another numerical difficulty lies in the fact that the fluid mechanical and the MCT equations are coupled via the Finger tensor, a rotation invariant measure for the deformation of a fluid element. To decouple the set of equations while remaining stable implicit algorithms an operator splitting technique was used.

Previously MCT has only been numerically solved in very simple setups, such as homogeneous channel flow. The combination of MCT to the highly flexible finite element method allows to simulate flow problems in various non-trivial geometries, such as the flow past obstacles or in an abrupt contraction, with desired local spatial resolution refinements. Furthermore by choosing adequate finite elements one can assure some import physical laws such as the conservation mass and momentum.

In general the dynamics of glass-forming fluids depends on slow collective structural relaxation processes that cause viscoelasticity. Viscoelastic fluids combine the response of an elastic solid at short observation time scales with that of a viscous liquid at long times. Our MCT model is able to produce all standard viscoelastic effect such as the appearance of a plug flow in channels or stress overshoots in start up flow curves. However, the biggest reward of tackling these more complicated integral constitutive equations is that one is able to recover flow-history dependent effects of the glass-forming fluids that empirical models cannot capture. One of these effects is the qualitatively correct formation of residual stresses after the removal of an external driving force, for example a pressure gradient. In our FEM-MCT simulations we were able to reproduce residual stresses that qualitatively show all features found in experiments while the standard empirical differential constitutive models cannot reproduce them at all.

Despite the huge success of the MCT-ITT model in predicting geometry-dependent residual shear stresses in glass-forming fluids the model does lack rheological correctness. From continuum mechanics it is known that the correct rate of change for a scalar quantity (such as the transient density correlation function ϕ) in the (laboraty fixed) Euler frame is given by the advected derivative $\frac{D}{Dt} \coloneqq \partial_t + [\vec{v} \cdot \vec{\nabla}]$. It turned out that in our advected MCT simulations, in which the velocities $|\vec{v}|$ are small, the advection term does not change the rheological effects of the MCT-ITT model. Most importantly we found the same residual shear stresses after a cessation of flow past a spherical obstacle as in the local MCT-ITT version. However, in simulations with bigger velocities $|\vec{v}|$ and therefore "bigger" $\vec{v} \cdot \vec{\nabla}$ and especially in two-component systems the advection will have a influence on the decay of the transient density correlation function ϕ and therefore on the stresses.

Kurzzusammenfassung

Die nicht-newtonsche Strömung von glasbildenden Flüssigkeiten weist zahlreiche interessante Phänomene auf, die sich von denen einfacher Flüssigkeiten unterscheiden. Bislang werden für Simulationen solcher glasbildenden Flüssigkeiten jedoch keine konstituierenden Gleichungen verwendet, die sich aus einer mikroskopischen Theorie ergeben, mit der sich ein Glasübergang vorhersagen lässt. Um die Strömung eines beliebigen Fluids zu bestimmen, muss man im Allgemeinen die nichtlinearen Navier-Stokes-Gleichungen lösen. In unserem speziellen Fall können wir diese auf die inkompressiblen zeitabhängigen Stokes-Gleichungen reduzieren, da die advektiven Trägheitskräfte im Vergleich zu den viskosen Kräften bei der Strömung von glasbildenden Flüssigkeiten vernachlässigbar sind. In dieser Arbeit stellen wir eine Kombination aus Finite-Elemente-Methode (FEM) Strömungssimulationen mit mikroskopischer Mode-Coupling-Theorie (MCT) als Ursprung der konstituierenden Gleichungen vor. Eine Herausforderung liegt darin, dass die MCT komplizierte Integralgleichungen aufstellt, die die gesamte Strömungsgeschichte der glasbildenden Flüssigkeit erfassen. Eine weitere numerische Schwierigkeit liegt darin, dass die strömungsmechanischen Gleichungen und die MCT-Gleichungen über den Finger-Tensor, ein rotationsinvariantes Maß für die Verformung eines Strömungselements, gekoppelt sind. Um den Gleichungssatz zu entkoppeln und gleichzeitig stabile implizite Algorithmen zu erhalten, wurde ein Operator-Splitting-Verfahren verwendet.
Bisher wurde die MCT nur in sehr einfachen Konstellationen, wie zum Beispiel in homogenen Strömungskanälen, numerisch gelöst. Die Kombination von MCT mit der hochflexiblen Finite-Elemente-Methode ermöglicht es uns, Strömungsprobleme in verschiedenen nicht-trivialen Geometrien zu simulieren, wie z.B. die Strömung um ein Hindernis oder in einer abrupten Verengung, mit gewünschten lokalen räumlichen Auflösungsfeinheiten. Außerdem kann man durch die Wahl geeigneter finiter Elemente einige wichtige physikalische Gesetze wie die Massen- und Impulserhaltung sicherstellen.
Im Allgemeinen hängt die Dynamik der glasbildender Flüssigkeiten von langsamen kollektiven strukturellen Relaxationsprozessen ab, die Viskoelastizität verursachen. Viskoelastische Flüssigkeiten kombinieren die Reaktion eines elastischen Festkörpers auf kurzen Beobachtungszeitskalen mit denen einer viskosen Flüssigkeit auf langen Zeitskalen. Unser MCT Modell ist in der Lage, alle viskoelastischen Standardeffekte zu reproduzieren, wie zum Beispiel. das Auftreten eines Pfropfenschrömung in Kanälen oder Spannungsüberschwinger in den Anlaufkurven. Der größte Vorteil dieser kompliziertteren integralen konstitutiven Gleichungen besteht jedoch darin, dass man in der Lage ist, von der Strömungsgeschichte abhängige Effekte der glasbildenden Flüssigkeiten zu untersuchen, die empirische Modelle nicht erfassen können. Einer dieser Effekte ist die qualitativ korrekte Vorhersage eingefrorener Spannungen nach dem Wegfall einer externen treibenden Kraft wie zum Beispiel eines Druckgradienten. In unseren FEM-MCT-Simulationen konnten wir eingefrorene Spannungen reproduzieren, die qualitativ alle in Experimenten gefundenen Merkmale aufweisen, während die standardmäßigen empirischen differenziellen konstituierenden Modelle sie überhaupt nicht reproduzieren können.
Trotz des großen Erfolgs des MCT-ITT-Modells bei der Vorhersage geometrieabhängiger Residualspannungen in glasbildenden Flüssigkeiten mangelt es dem Modell an rheologischer Korrektheit. Aus der Kontinuumsmechanik ist bekannt, dass die korrekte Änderungsrate für eine skalare Größe (wie z. B. die transiente Dichtekorrelationsfunktion ϕ) im (laborfixierten) Euler-Rahmen durch die advektierte Ableitung $\frac{D}{Dt} \coloneqq \partial_t + [\vec{v} \cdot \vec{\nabla}]$ gegeben ist.
Es zeigte sich, dass in unseren Simulationen der advektierten MCT, in denen die Geschwindigkeiten $|\vec{v}|$ klein sind, der Advektionsterm die rheologischen Effekte des MCT-ITT-Modells nicht verändert. Am wichtigsten ist, dass wir die gleichen residualen Schubspannungen nach einer Unterbrechung der Strömung an einem kugelförmigen Hindernis gefunden haben wie in der lokalen MCT-ITT-Version. In Simulationen mit größeren Geschwindigkeiten $|\vec{v}|$ und damit "größeren" $\vec{v} \cdot \vec{\nabla}$ und insbesondere in Zweikomponentensystemen wird die Advektion jedoch einen Einfluss auf den Zerfall der transienten Dichtekorrelationsfunktion ϕ und damit auf die Spannungen haben.

Acknowledgments

I am incredibly grateful for the opportunity to do my PhD (and M.Sc. previously) research under the excellent supervision of Prof. Dr. Thomas Voigtmann. He always showed a great positive attitude and always found some time for me, even in very busy times. In the last 4 and a half years (since summer semester 2019 to be precise) he shared an incredible amount of his extensive knowledge about theoretical physics with me. Thomas really inspired me and will always be a great role model for me.
The second biggest acknowledgments have to be made towards Dr. Timm Treskatis (TU Dortmund) for spending so much time with me on the implementation and perfection of the numerics. I am very glad that I could learn so much about finite elements and FEniCS implementation of such a skillful applied mathematician. I also really enjoyed some of our incredibly late (past midnight) discussions on simulation results and the physical interpretations behind them.
Further, I would like to acknowledge Prof. Dr. Jürgen Horbach for being available as a second reviewer and introducing me to computational physics in his brilliant lecture.
I also would like to thank my nice colleagues at DLR, especially my office mate Marcel Unger, my former office mate Dr. Julian Reichert and also of course Leon Granz, who also took care of our computers.
Finally I want to thank my whole family for supporting me for the last 27 years.

Contents

Chapter 0

Introduction and Outline

0.1 Introduction

Many fluids we encounter in everyday life are viscoelastic and shear-thinning. These terms refer to two "non-Newtonian" flow behaviors (since the description of the flow of ordinary fluids like water goes back to Newton[1]) that that provoke many interesting phenomena. They arise due to collective relaxation dynamics on the microscale and require sophisticated coarse-grained models to describe the continuum behavior.
This thesis is about one way to combine elaborate microscopic theory with macroscopic finite elements simulations to study viscoelastic (or viscoelastoplastic) flow of glass-forming fluids in non-trivial geometries.
To set the stage, recall that Newtonian fluid flow is described by the linear-response relation

$$\sigma = \eta\dot{\gamma},$$

where η is called the (dynamic) viscosity of the fluid. Thus in a Newtonian fluid the stress σ is proportional to the strain-rate $\dot{\gamma}$. This distinguishes them for solids where in linear response one finds that the stress is proportional to the strain (not the strain-rate):

$$\sigma \propto \gamma,$$

this relation is called Hooke's law.
Already in 1867 James Clark Maxwell[2] noticed that some materials show the properties of an elastic solid on short times, but behave like a viscous fluid on long time scales [40]. Silly putty is a toy that bounces from walls when thrown, but flows like a liquid when given enough time. Maxwell developed a simple model of viscoelasticity that is based on the mechanical analog of a serial connection of an elastic spring to a viscous damper / dashpot.

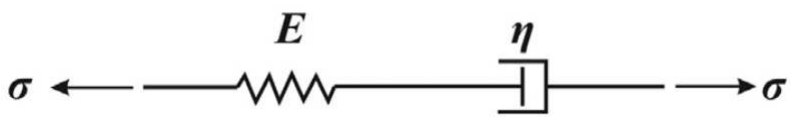

Figure 1: Schematic idea of the Maxwell element: a serial connection of an elastic spring to a viscous dashpot. Figure from [25].

[1] Sir Isaac Newton (25 December 1642 – 20 March 1727) was an English mathematician, physicist, astronomer, alchemist and theologian. He is widely recognized as one of the most influential persons in the scientific world.

[2] James Clerk Maxwell (13.06.1831 – 05.11.1879) was a Scottish mathematician and scientist mostly known for the classical theory of electromagnetic radiation.

The Maxwell model leads to a relation between stress σ and strain rate $\dot{\gamma}$ (a material law or constitutive equation (CE)) that is a differential equation:

$$\dot{\sigma} + \frac{1}{\lambda}\sigma = G_\infty \dot{\gamma}.$$

This heuristic model was – and still is – a huge success because it is able to combine the elasticity on short time scales with the viscosity on longer time scales, that we all know from honey for example. If one quickly turns the pot of honey to its side for a second or maybe two nothing will flow. The honey seems like a solid on this timescale of roughly one or two seconds. However if one leaves the pot of honey on its side for a couple of minutes the honey flow out of its pot like a liquid. The time necessary until the honey (or another Maxwell viscoelastic fluid) flows is the Maxwell time scale λ, the viscosity of the flow is then given by $\eta = G_\infty \lambda$.
The Maxwell model can nicely be modified to include other rheological effects such as shear-thinning and yield stress, which is the main characterization of plasticity in a material law. The effect of shear-thinning is especially known and appreciated among painters because it is desirable to apply paint (a colloidal suspension) very easily and evenly on a wall while painting but to have no further flow (creating varnish run / tear) afterwards when the paintbrush is no longer in contact with the paint. These characteristics are fulfilled if the dynamical viscosity is decreased while the painter shears the paint of thickness h between their brush with velocity v and the stationary wall (effective strain-rate: $\dot{\gamma} \approx v/h$), but again increased to a timescale such that the paint is basically not flowing and dries on the exact spots where it was painted on.
The second phenomenon mentioned before is the yield stress, which means that there is a minimum stress needed for a material to flow or deform. Viscous fluid like water have no (or a zero) yield stress, which means that only the tiniest amount of force is sufficient that for example they spread on a sheet of paper (neglecting surface effects). Materials like for example ink for a printer have a non-zero yield stress which is very helpful to achieve precise printing with sharp letters and edges since the ink drops will not spread out. However the combination of shear-thinning and yield stress is not always appreciated and can be very frustrating as we all know that from a bottle of ketchup (which is a standard example of a shear-thinning yield stress fluid). First no ketchup comes out of the bottle because the applied forces by gravity and carefully tapping the bottle are not sufficient to reach the yield stress and after the one big tap the yield point is crossed and due to the shear-thinning all of a sudden all the ketchup comes out really fast spreading all over our table.

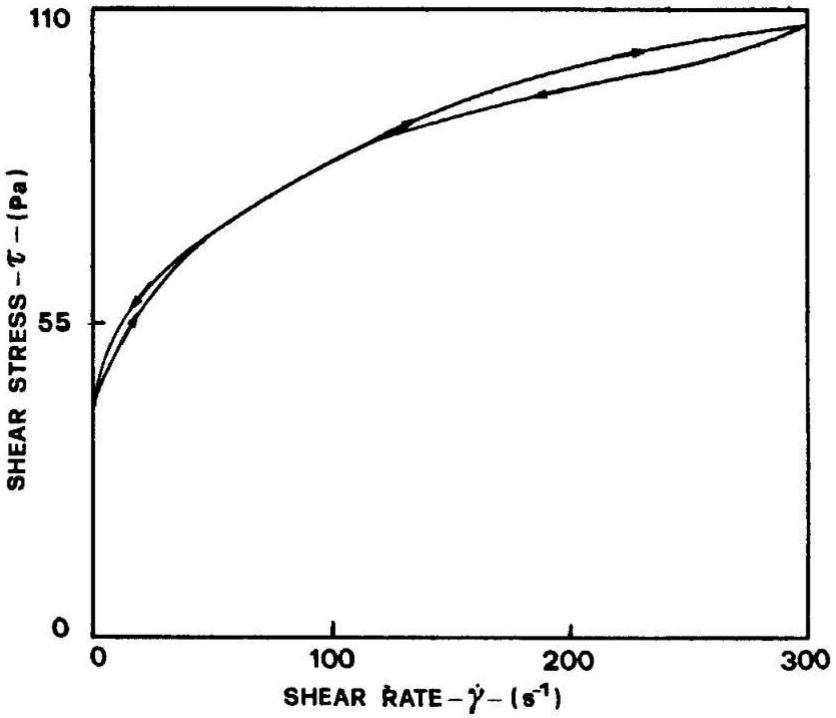

Figure 2: Typical measured flow curve of ketchup. One can see that ketchup is a very good example of a shear-thinning yield stress fluid, because at zero shear rate the stress (here denoted by τ) does not vanish, which is exactly the yield stress. Second one can see that the stress grows slower than linear with an increase of the shear rate, which does mean that the effective viscosity $\eta(\dot{\gamma}) = \tau(\dot{\gamma})/\dot{\gamma}$ decreases as the shear rate $\dot{\gamma}$ increases. Figure from [4]

.

This thesis aims to go even beyond those shear-thinning variants of these heuristically based Maxwell-like model (called generalized or nonlinear Maxwell or White-Metzner models) and uses an extension of the so called Mode-Coupling Theory (MCT). A very well established theory in describing (expectation values of) such colloidal suspensions or polymeric melts such as paint, ketchup or honey and many more. To deliver material laws / constitutive equations from first principles / statistical mechanics able to describe and simulate the flow of viscoelastoplastic material a formalism called integration through transients (ITT)[7] is used. This work specifically tackles the regime where the colloidal suspensions / polymeric melts are so dense that without shear the viscosity tends to diverge towards infinity. This regime where the viscosity of a colloidal system diverges is referred to as the glassy state and is roughly speaking somewhat in between a liquid and a solid (microscopically, for example liquid but macroscopically solid). The framework of MCT is highly successful in describing the glass transition that occurs when the packing-fraction of a colloidal (hard-sphere like) suspension reaches a certain threshold. The flow of glass-forming fluids displays multiple phenomena that are quite different from those found in ordinary (Newtonian) liquids, such as the appearance of plug flow in channels, or residual stresses after removal of the external driving force.

Crucially the MCT-ITT framework presents a constitutive equation in integral form, which can not be reduced to a (partial) differential equation as the common CEs, such as those of the Maxwell model (see above). The fact that one has to deal with integral equations will increase the computational cost – especially in terms of memory – drastically, but on the other hand one can argue that integral

constitutive equations are capable to provide a much richer set of phenomenology because not only the current state of the flow is taken into account but also the whole flow / deformation history of a fluid element.

To numerically simulate the flow of any fluid (not restricted to vicsoelastoplastic ones) there are numerous techniques, for example a simple finite differences scheme in both time and space or the Lattice Boltzmann[3] (LB) method, which is based on the main idea, to develop a highly simplified pseudo-particle simulation, which nonetheless reproduces the Navier-Stokes equation in the continuum limit. Both of these simulation techniques are not well established when dealing with complex flow geometries. To solve that issue one can use the more flexible, but mathematically more complex finite volume or finite element methods (FVM and FEM) where especially the FEM became increasingly popular in the last decades because of its flexible application to deformation (linear elasticity) but also fluid flow problems while making sure that basic physical laws such as mass and momentum conservation are fulfilled (at least cell-wise, sometimes with more sophisticated numerical algorithms even point-wise).

Main goal of this thesis is develop a FEM solver which uses the Mode-Coupling Theory to provide first-principles material laws for viscoelastoplastic fluids. To demonstrate the technique, various geometries such as the channel (with and without obstacles) and the 4 to 1 contraction / extension are used as exemplary cases to demonstrate how much richer constitutive equations of MCT explain qualitative flow phenomena observed in glass-forming (and more generally high viscoelastoplastic) fluids that can not (or not well enough) be captured by using standard empirical constitutive equations that are commonly used in conjunctiond with finite element simulations. One can state that this project combines the microscopical description of the fluid behavior provided by the material laws from the MCT extension with the mesoscopical fluid flow level described tb the Navier-Stokes equations.

0.2 Outline

The first chapter is a very brief introduction to the Mode-Coupling Theory of Brownian particles, but will also go into the numerical details of the schematic MCT equation. Further in this first chapter the linear / logarithmic schematic two-time MCT algorithm for computational fluid dynamics (CFD) is developed.

In chapter two a very short recall of conservation laws and an in depth discussion of both differential and integral constitutive equations is given. The chapter also provides a detailed recapitulation of the exentension of Mode-Coupling theory to non-linear rheology through the ITT framework. Furthermore some analytical calculations are done to gain basic understanding of the – in comparison to the MCT-ITT model – easier and widely used constitutive equation and see where they are lacking, for example in terms of capability to predict residual stresses.

Chapter three provides a introduction to the mathematical basics of the finite element method to numerically solve partial differential equations. It will also briefly focus on the implementation of finite elements and partial differential equations (in their weak formulation) using the FEniCS extension in the python3 programming language. It will not show any mathematical proofs, but will refer to excellent literature if more mathematical insight is desired by the reader.

[3] Ludwig Eduard Boltzmann (20 February 1844 – 5 September 1906) was an Austrian physicist and philosopher. His greatest achievements were the development of statistical mechanics, and the statistical explanation of the second law of thermodynamics.

Chapter four will present how exactly the combined FEM-MCT code basis is implemented. An in-depth derivation of the 'weak' equations and all discretizations are extensivly discussed, also the important mathematical details (like which order and elements are used) are discussed in compact form. Also the code will be applied to both the generalized (integral) Maxwell model and especially to the MCT constitutive model. The discussion will focus on start up and cessation of flow, stationary plug flow in the channel and an in depth discussion of residual stresses in different geometries.

In the fifth chapter an advectional extension of the schematic two-time MCT will be discussed and simulated. Like in the previous chapter all necessary equation will be derived in detailed steps. Simulation results will be compared with those of the standard (local) version of MCT-FEM.

Finally the sixth chapter will summarize the thesis and give an outlook towards further interesting research in the field of finite element simulations of glass-forming / viscoelastoplastic fluids.

Chapter 1

Mode-Coupling Theory

This chapter derives the basic equation of the so called mode-coupling theory of the glass transition (MCT). MCT is a microscopical theory which is able to describe the transition of a liquid into a so called glass or glassy state. The glassy state is commonly viewed as something in between a crystalline solid and a disordered liquid, because macroscopic properties such as a diverging viscosity and a bounded mean-squared displacement indicate a solid state, but microscopic properties such as the structure factor $S(\vec{q})$ are identical to those found in liquid state systems. In experiment a glass transition can be achieved by very rapidly cooling down or compressing a liquid below its melting point. Under certain conditions the liquid might not undergo crystallization but its viscosity η becomes so large that it basically stops flowing on any practical time scale [14, 2]. In this work the Brownian[1] dynamics version of MCT is used because the systems of interest are colloidal and polymeric suspensions in which a (Newtonian) background fluid acts as a thermostat.

1.1 Derivation of MCT for Brownian Particles

In the following we summarize the key concepts of MCT in quiescent systems for later reference. An overview of MCT extended to describe shear-thinning is given in section 1.4.

1.1.1 Brownian Motion and the Smoluchowski Operator

The overdamped limit of the stochastic equation of motion for one Brownian particle (labeled by index k) in a system of N Brownian particles reads [45]:

$$\mathrm{d}\vec{r}_k = \mu\vec{F}_k(\Gamma)\mathrm{d}t + \sqrt{2D}\cdot\mathrm{d}\vec{W}_k, \tag{1.1}$$

where $\vec{F}_k(\Gamma)$ is the direct interaction force resulting from system configuration Γ and $\mathrm{d}\vec{W}_k$ the Wiener process (white noise) acting on particle k. It is important to mention that the Brownian motion is driven by Wiener[2] processes $\mathrm{d}\vec{W}_k$ that are independent of each other. Furthermore D is known as the diffusion coefficient and μ the particle mobility, both will be set to unity in the following derivation. From the theory of stochastic differential equation for Markovian[3] processes (again [45, 58]) it is known that the set of equations 1.1 for each particle can be translated into a Fokker-Planck equation. In this particular case the equation is usually called the Smoluchowski [4] equation, determining the time evolution of the probability distribution function $\Psi(\Gamma, t)$ to find the system in configuration Γ at a

[1] Robert Brown (21 December 1773 – 10 June 1858) was a Scottish botanist.
[2] Norbert Wiener (November 26, 1894 – March 18, 1964) was an American mathematician.
[3] Andrey Andreyevich Markov (14 June 1856 – 20 July 1922) was a Russian mathematician.
[4] Marian Smoluchowski (28 May 1872 – 5 September 1917) was a Polish physicist.

given time t:

$$\partial_t \Psi(\Gamma, t) = \Omega(\Gamma)\Psi(\Gamma, t), \tag{1.2}$$

with the (forward) Smoluchowski operator (the Γ-dependence is dropped in the following to simplify the notation):

$$\Omega = \sum_{k=1}^{N} \vec{\nabla}_k \cdot (\vec{\nabla}_k - \vec{F}_k(\Gamma)). \tag{1.3}$$

The adjoint (or often called backward) Smoluchowski operator is given by:

$$\Omega^\dagger = \sum_{k=1}^{N} (\vec{\nabla}_k + \vec{F}_k(\Gamma)) \cdot \vec{\nabla}_k \tag{1.4}$$

and drives the time evolution of observables. This is similar to the switch from the Schrödinger[5] picture which describes the time evolution of the wavefunction (here instead of wavefunction the evolution of probability distribution function) to the Heisenberg[6] picture which describes the time evolution of operators (representing observables) in the theory of Quantum Mechanics.

1.1.2 MCT Equation for Brownian Particles

Transient Density Correlation Function

The observable of interest here is the particle density $\rho(\vec{r}, t)$, or to be precise its Fourier[7] transform $\hat{\rho}(\vec{q}, t)$ which are defined by:

$$\rho(\vec{r}, t) := \sum_{k=1}^{N} \delta(\vec{r} - \vec{r}_k(t)), \tag{1.5}$$

$$\hat{\rho}(\vec{q}, t) = \sum_{k=1}^{N} \mathrm{e}^{\mathrm{i}\vec{q}\cdot\vec{r}_k(t)} / \sqrt{N}. \tag{1.6}$$

The time-dependent transient density correlation function is defined as:

$$\Phi(\vec{q}, t) = \langle \hat{\rho}^*(\vec{q}) \mathrm{e}^{\Omega^\dagger t} \hat{\rho}(\vec{q}) \rangle, \tag{1.7}$$

with $\langle \dots \rangle$ the canonical / thermal average and the short notation $\hat{\rho}(\vec{q}) := \hat{\rho}(\vec{q}, 0)$. The time-dependent transient density correlation function is the time-dependent generalization of the static structure factor

$$S(\vec{q}) := \langle \hat{\rho}^*(\vec{q}) \hat{\rho}(\vec{q}) \rangle = \frac{1}{N} \sum_{i,j} \mathrm{e}^{\mathrm{i}\vec{q}\cdot[\vec{r}_j(0) - \vec{r}_i(0)]}. \tag{1.8}$$

The static structure factor $S(\vec{q})$ is known to be linked to the radial distribution $g(r)$. The radial distribution function measures how many particles are on average found within a distance of r and $r + dr$ away from a particle. $S(\vec{q})$ can be obtained from $g(r)$ via Fourier transformation [20]:

$$S(\vec{q}) = 1 + \frac{N}{V} \int_V \mathrm{e}^{-i\vec{q}\cdot\vec{r}} [g(r) - 1] \mathrm{d}\vec{r}.$$

[5] Erwin Rudolf Josef Alexander Schrödinger (12 August 1887 – 4 January 1961) was a Nobel Prize-winning Austrian and naturalized Irish physicist who developed fundamental results in quantum theory.

[6] Werner Karl Heisenberg (5 December 1901 – 1 February 1976) was a German theoretical physicist and one of the main pioneers of the theory of quantum mechanics.

[7] Jean-Baptiste Joseph Fourier (21 March 1768 – 16 May 1830) was a French mathematician and physicist born in Auxerre and best known for initiating the investigation of Fourier series.

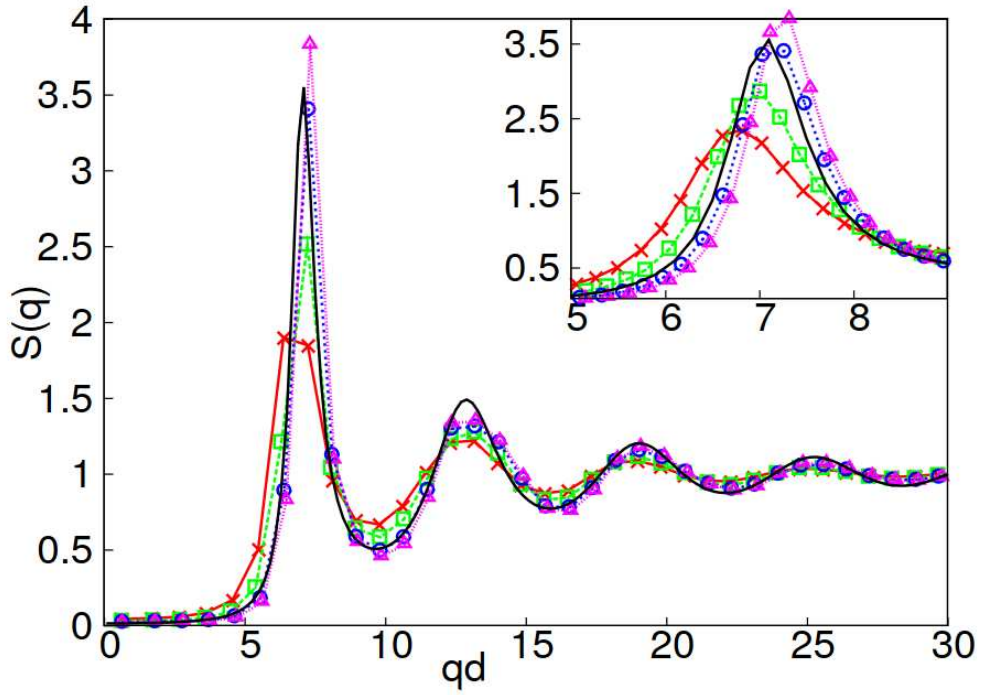

Figure 1.1: Static structure factor extracted from the simulations mimicking colloidal Brownian dynamics. The packing fractions φ = 0.45, 0.5, 0.55, and 0.57 are marked with crosses (red), squares (green), circles (blue) and triangles (magenta), respectively. Figure from [60].

One can see that for all of the packing fractions shown the static structure factor $S(q)$ looks like from an classical simple liquid. However in the transient density correlation $\Phi(q,t)$ one observes a two-staged decay. For the higher packing fractions (red crosses) the transient density correlation function of this colloidal system plateaus at first until it finally decays.

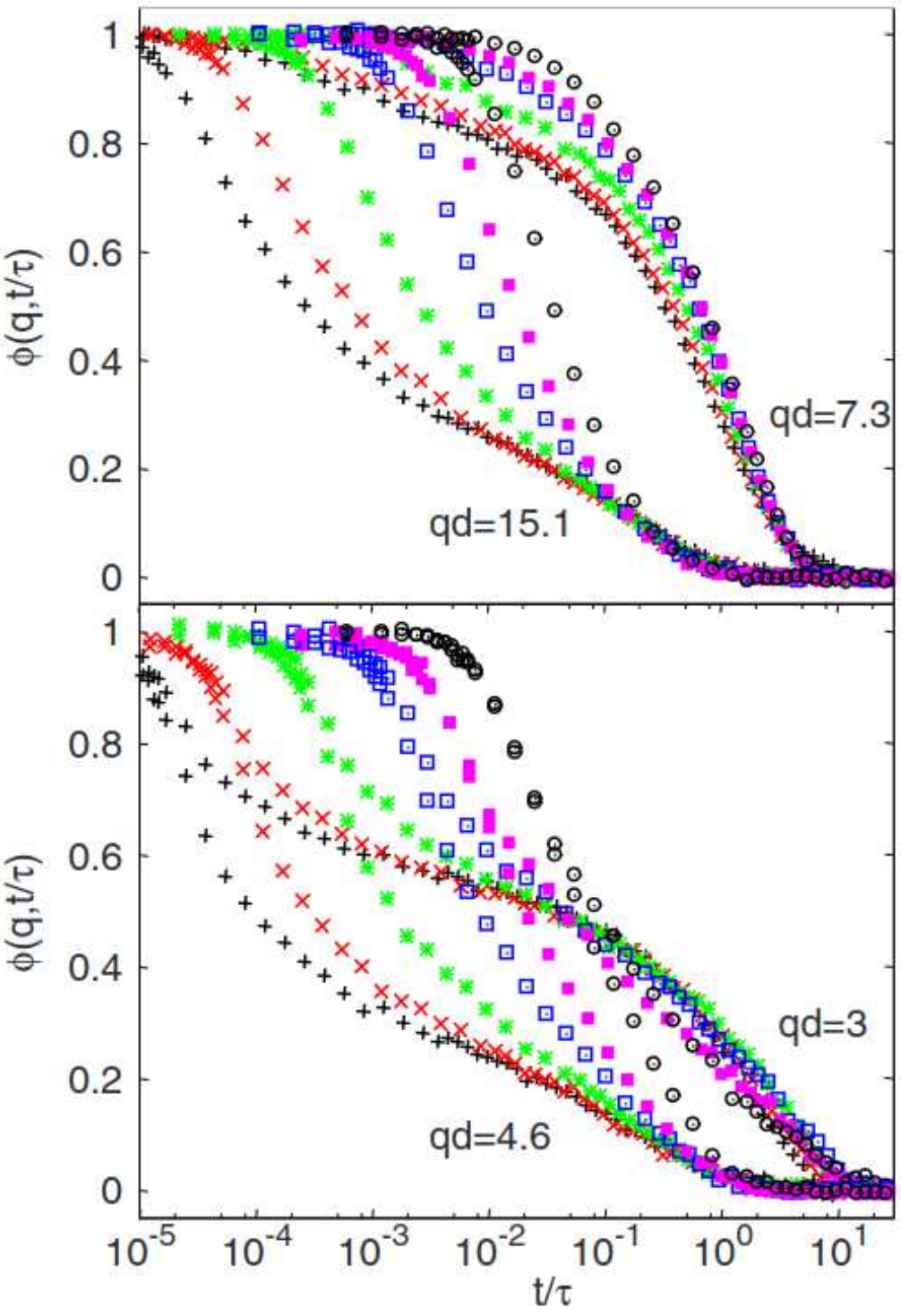

Figure 1.2: Dynamic correlation function extracted from the simulations mimicking colloidal Brownian dynamics. Packing fractions shown are $\varphi = 0.585$ (black plus symbols), $\varphi = 0.58$ (red crosses), $\varphi = 0.57$ (green stars), $\varphi = 0.55$ (blue open squares), $\varphi = 0.53$ (magenta filled squares) and $\varphi = 0.50$ (black circles). Note that t/τ is shown such that all correlation functions decay at $t/\tau \approx 1...10$. Figure from [60].

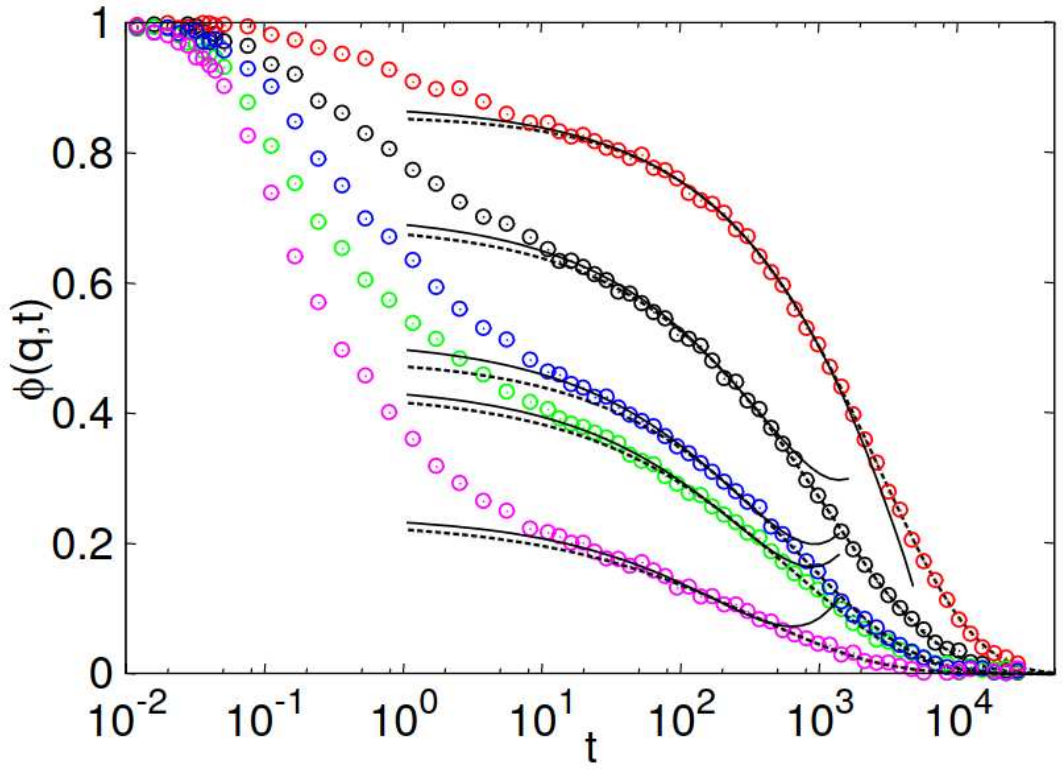

Figure 1.3: Fits of stretched-exponential functions (dashed black lines) to the dynamic density correlation functions obtained from simulations (circles) at $\varphi = 0.585$. The q-values are from top to bottom qd = 6.6 (red), 7.4 (black), 9.8 (blue), 12.8 (green) and 15.6 (magenta), with d being the particle diameter. The fit range was chosen as $t \in [10^2 : 10^5]$. Figure from [60].

Physical Interpretation: Caging Effect

The physical interpretation of this two-staged decay called the caging effect is best understood if one thinks about hard disks. The first stage one can refer to as the ballistic regime: the disk (or particle with another stiff interaction potential) moves freely until it collides with other particles. The plateau stage, also called β-relaxation, occurs since the disks is trapped (due to the high packing fraction) in a cage of other disks. This means that during caging (or β-relaxation) the mean-squared displacement of the disks is bounded by the area of its neighboring particles. Whether now a second decay from the plateau happens or not is decided (in terms of hard disks) by the packing fraction, if the packing fraction is above a certain threshold – and therefore the system in glassy state – the cages cannot be broken and there is no second decay (the second decay is called α-relaxation). If the system is close but below the glass transition the cages will break during β-relaxation (it will take longer the closer the system is to the glass transition point) and due to the escape of the cages the α-relaxation will occur [28].

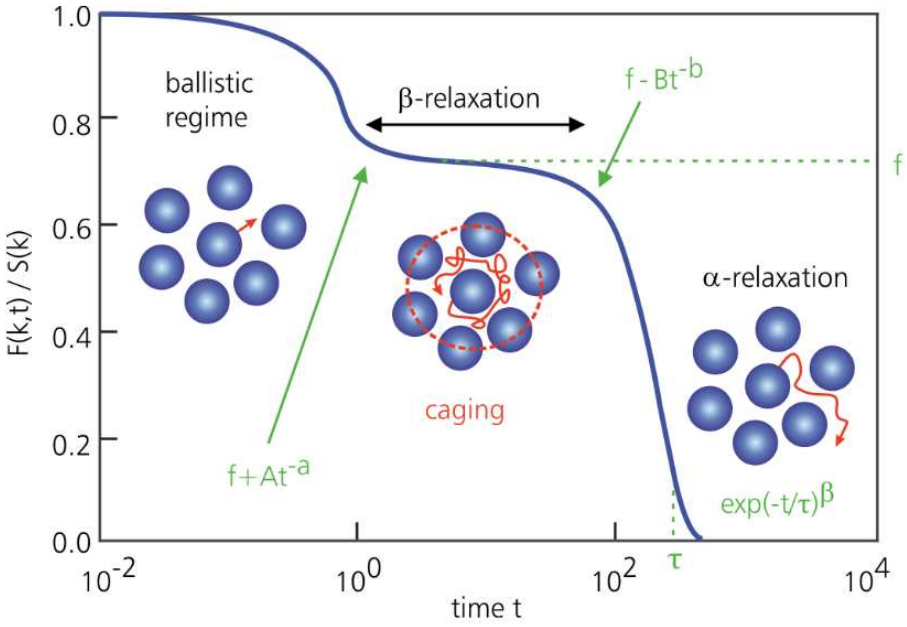

Figure 1.4: Typical MCT prediction for the transient density correlation function, here called $F(k,t)$, of a system close to its glass transition point as a function of time, for a wave number $k = k_0$ that corresponds to the first peak of the static structure factor. At very short times, particles undergo ballistic motion. At intermediate times, particles become transiently trapped in cages (β-relaxation) and the transient density correlation function correspondingly remains approximately constant. Only at sufficiently long times particles will break free and full relaxation takes place (α-relaxation) [28]. Figure from Ref. [28].

Mori-Zwanzig Projection Operator Formalism

To derive an equation of motion for $\Phi(\vec{q},t)$ one can now use the Mori[8]-Zwanzig[9] projection operator formalism. First introduce a projection operator

$$\mathcal{P} = \frac{|\hat{\rho}(\vec{q})\rangle\langle\hat{\rho}^*(\vec{q})|}{S(\vec{q})}, \tag{1.9}$$

to project onto density fluctuations. Also define the orthogonal projector $\mathcal{Q}$ by $\mathrm{Id} = \mathcal{P} + \mathcal{Q}$. Note that $\partial_t e^{\Omega^\dagger t} = \Omega^\dagger(\mathcal{P}+\mathcal{Q})e^{\Omega^\dagger t} = \Omega^\dagger\mathcal{P}e^{\Omega^\dagger t} + \Omega^\dagger\mathcal{Q}e^{\Omega^\dagger t}$ and use the Dyson decomposition

$$e^{\Omega^\dagger t} = e^{\Omega^\dagger\mathcal{Q}t} + \int_0^t e^{\Omega^\dagger\mathcal{Q}(t-t')}\Omega^\dagger\mathcal{P}e^{\Omega^\dagger t'}\mathrm{d}t', \tag{1.10}$$

in the second term to obtain an equation of motion for the density correlation function:

$$\partial_t\Phi(\vec{q},t) = -\omega(\vec{q})\Phi(\vec{q},t) + \int_0^t K(\vec{q},t-t')\Phi(\vec{q},t')\mathrm{d}t', \tag{1.11}$$

with

$$-\omega(\vec{q}) := S^{-1}(\vec{q})\langle\hat{\rho}^*(\vec{q})\Omega^\dagger\hat{\rho}(\vec{q})\rangle \propto -q^2 \tag{1.12}$$

[8]Hajime Mori (*1926) is a Japanese theoretical physicist working on nonequilibrium statistical mechanics and chaos theory.

[9]Robert Walter Zwanzig (9 April 1928 - 15 May 2014) was an American theoretical physicist and chemist who made important contributions to statistical mechanics

and the Mori-Zwanzig memory kernel defined by:

$$K(\vec{q},t) \coloneqq S^{-1}(\vec{q})\langle\hat{\rho}^*(\vec{q})\Omega^\dagger\mathcal{Q}\mathrm{e}^{\Omega^\dagger\mathcal{Q}t}\Omega^\dagger\hat{\rho}(\vec{q})\rangle. \tag{1.13}$$

Note that if $\mathcal{Q}$ and $\Omega^\dagger$ would commute, the Mori-Zwanzig memory kernel K would vanish and the equation of motion for $\Phi(\vec{q},t)$ would be a simple exponential decay, however since $\mathcal{Q}$ and $\Omega^\dagger$ do not commute further effort must be made.

Second Dyson Decomposition

Equation 1.11 is treated further in order to rewrite the memory kernel $K(\vec{q},t)$ into a so called MCT (friction) memory kernel. Therefore one first defines a further projection operator on the physical grounds, that one wants to obtain a memory kernel that is a correlation of fluctuating forces. Therefore define

$$\begin{aligned}\mathcal{P}' &\coloneqq -\hat{\rho}(\vec{q})\rangle\omega(\vec{q})^{-1}\langle\hat{\rho}^*(\vec{q})\Omega^\dagger, \\ \mathcal{Q}' &\coloneqq \mathrm{Id} - \mathcal{P}'\end{aligned} \tag{1.14}$$

to take out the one-particle reducible dynamics by a further Dyson decomposition

$$\mathrm{e}^{\Omega^\dagger\mathcal{Q}t} = \mathrm{e}^{\Omega^\dagger\mathcal{Q}'\mathcal{Q}t} + \int_0^t \mathrm{e}^{\Omega^\dagger\mathcal{Q}(t-t')}\Omega^\dagger\mathcal{P}'\mathcal{Q}\mathrm{e}^{\Omega^\dagger\mathcal{Q}'\mathcal{Q}t'}\mathrm{d}t'. \tag{1.15}$$

Inserting this Dyson decomposition into the Mori-Zwanzig memory kernel 1.13 one obtains

$$m(\vec{q},t) = \omega^{-1}(\vec{q})K(\vec{q},t) + \int_0^t \omega^{-1}(\vec{q})K(\vec{q},t-t')m(\vec{q},t')\mathrm{d}t', \tag{1.16}$$

with the defintion

$$m(\vec{q},t) \coloneqq S^{-1}(\vec{q})\omega^{-1}(\vec{q})\langle\hat{\rho}^*(\vec{q})\Omega^\dagger\mathcal{Q}\mathrm{e}^{\mathcal{Q}\Omega^\dagger\mathcal{Q}\mathcal{Q}'t}\mathcal{Q}\Omega^\dagger\hat{\rho}(\vec{q})\rangle. \tag{1.17}$$

The equations 1.11 and 1.16 can be combined to a single equation of motion for the density correlation function

$$\partial_t\Phi(\vec{q},t) + \omega(\vec{q})\Phi(\vec{q},t) + \int_0^t m(\vec{q},t-t')\partial_t\Phi(\vec{q},t')\mathrm{d}t' = 0, \tag{1.18}$$

which is called the MCT equation.

Mode-Coupling Approximations

The MCT approximation now consists of two intertwined steps: first the fluctuating forces $\mathcal{Q}\Omega^\dagger\hat{\rho}(\vec{q})\rangle$ that appear in $m(\vec{q},t)$ are replaced by their overlap with density pairs. Using the short-hand notation $\hat{\rho}_1 \coloneqq \hat{\rho}_1(\vec{q}_1)$ one introduces the pair-density projector

$$\mathcal{P}_2 = \sum_{1,2,1',2'} |\hat{\rho}_1^*\hat{\rho}_2^*\rangle\chi_{1,2,1',2'}\langle\hat{\rho}_{1'}\hat{\rho}_{2'}| \tag{1.19}$$

with a suitable normalization matrix χ. Second, the resulting dynamical four-point correlation functions that involve the reduced dynamics are replaced by the product of two-point correlation functions propagated by the full dynamics

$$\langle\hat{\rho}_1^*\hat{\rho}_2^*\mathrm{e}^{\mathcal{Q}\Omega^\dagger\mathcal{Q}\mathcal{Q}'t}\hat{\rho}_{1'}\hat{\rho}_{2'}\rangle \approx \langle\hat{\rho}_1^*\mathrm{e}^{\Omega^\dagger t}\hat{\rho}_{1'}\rangle\cdot\langle\hat{\rho}_2^*\mathrm{e}^{\Omega^\dagger t}\hat{\rho}_{2'}\rangle + \{1'\leftrightarrow 2'\} \tag{1.20}$$

together with a consistent approximation of χ [37].
Note that this is not just a simple mean-field approach of the style $\langle x\cdot y\rangle \approx \langle x\rangle\cdot\langle y\rangle$ because the four-point correlation functions propagated by the reduced dynamics are replaced by two-point correlation functions propagated by the full dynamics.

Excursion: Volterra Integral Theory

Alternative to the "standard" derivation using a second Dyson decomposition, as shown above, one can also use the existing mathematical theory of integral equations (see for example [54]) to derive the desired MCT equation.
Dividing the Mori-Zwanzig equation 1.11 by $-\omega(\vec{q})$ the resulting equivalent equation can be viewed as a Volterra integral equation of the second kind, with $-\omega^{-1}(\vec{q})\partial_t\Phi(\vec{q},t)$ as an in-homogeneity. The rich theory of these Volterra integral equation of the second kind (again [54]) leads (after rearranging all terms to the LHS) to the MCT equation:

$$\partial_t\Phi(\vec{q},t) + \omega(\vec{q})\Phi(\vec{q},t) + \int_0^t m(\vec{q},t-t')\partial_t\Phi(\vec{q},t')\mathrm{d}t' = 0,$$

with the MCT memory kernel $m(\vec{q},t)$ again given by

$$m(\vec{q},t) = \omega^{-1}(\vec{q})K(\vec{q},t) + \int_0^t \omega^{-1}(\vec{q})K(\vec{q},t-t')m(\vec{q},t')\mathrm{d}t'.$$

Derivation of the Dyson Decomposition

The Dyson decomposition (equation 1.10) can be found by differentiating and reinserting (to the LHS) the Ansatz

$$\mathrm{e}^{\Omega^\dagger t} = \mathrm{e}^{\Omega^\dagger \mathcal{Q} t} + \mathrm{e}^{\Omega^\dagger t}X(t)$$

to obtain (after canceling the $\mathrm{e}^{\Omega^\dagger t}\Omega^\dagger X(t)$ term on both sides and multiplying by $\mathrm{e}^{-\Omega^\dagger t}$) the following differential equation for $X(t)$:

$$\dot{X}(t) = \mathrm{e}^{-\Omega^\dagger t}\Omega^\dagger \mathcal{P}\mathrm{e}^{\Omega^\dagger t}.$$

After integrating this simple differential equation one recovers the Dyson decomposition 1.10 from above [47].

1.2 Schematic MCT

A schematic version of the mode-coupling theory equation (often called sMCT) is obtained by simply dropping the wavevector dependence:

$$\dot{\phi}(t) + \phi(t) + \int_0^t m(t-\tau)\dot{\phi}(\tau)\mathrm{d}\tau = 0 \tag{1.21}$$

and assuming the memory kernel $m(s)$ to be a polynomial (with non-negative coefficients) in the correlation function $\phi(s)$ itself. This can be motivated by the fact that the MCT dynamics close to the glass transition is governed by a bifurcation scenario with a single critical mode in q-space [24].

1.2.1 Bifurcation Equation

To find out about the long time limits of the correlation function $\phi(t\to\infty)$, which determine whether the system is in the glassy state $\phi(t\to\infty) > 0$ or not $\phi(t\to\infty) = 0$, one applies the Laplace[10]

[10] Pierre-Simon Laplace (23 March 1749 – 5 March 1827) was a French mathematician, physicist and astronomer. He worked, besides many other fields, on probability theory and partial differential equations.

transformation to the sMCT equation 1.21 which leads – regarding the properties of the Laplace transformation – to:

$$s\hat{\phi}(s) - \phi(0) + \hat{\phi}(s) + \hat{m}(s)(s\hat{\phi}(s) - \phi(0)) = 0.$$

Using initial condition, that $\phi(0) = 1$ one ends up with:

$$s\hat{\phi}(s) - 1 + \hat{\phi}(s) + \hat{m}(s)(s\hat{\phi}(s) - 1) = 0, \tag{1.22}$$

which is an algebraic equation relating the Laplace transformed memory function $\hat{m}(s)$ and the Laplace transformed correlation function $\hat{\phi}(s)$.
The final value theorem for the Laplace transformation (proof can be found in [56]) states that

$$\lim_{t\to\infty} g(t) = \lim_{s\to 0} s\hat{g}(s), \tag{1.23}$$

if g is bounded (and measurable) and the limit $\lim_{t\to\infty} g(t)$ exists. Both conditions are known [22] to be true for both m and ϕ. If one sets $\lim_{t\to\infty} \phi(t) =: f$, $\lim_{t\to\infty} m(t) =: m$ and multiplies our algebraic equation 1.22 by an additional factor of s before performing the limit $s \to 0$, one obtains the so called bifurcation equation:

$$f + m(f-1) = 0 \;\Rightarrow\; m = \frac{f}{1-f}. \tag{1.24}$$

The bifurcation equation is highly useful to study the long time limits and therefore the glass transition for a simple example memory kernel model, called the F12 model. Rigorous mathematics by W. Götze[11] proves that the biggest real solution of this bifurcation equation is the actual long term limit of the sMCT correlation function ϕ [22, 24].

1.2.2 F12 Model

The schematic F12 Model is an idea, first proposed by W. Götze [23], which dates back to the mid 80s of the last century. One assumes the (schematic) memory kernel to be a quadratic polynomial with non-negativ coefficients in ϕ itself:

$$m[\phi(t)] = v_1\phi(t) + v_2\phi^2(t), \tag{1.25}$$

where v_1 and v_2 are coupling coefficients / parameters set by the thermodynamic state of the system. The physical necessity that the memory kernel $m[\phi]$ has to vanish if $\phi = 0$ leads to the fact that there is no constant coefficient v_0 in this quadratic polynomial.

F1 Model

One could first look at the special case where the coefficient $v_2 = 0$. In this case the memory kernel is just a linear function in ϕ:

$$m(t) = v_1\phi(t),$$

this model of a memory function is called the F1 model.
In the long time limit $\phi(t \to \infty) = f$, this leads to to the bifurcation equation:

$$f(f + \frac{1-v_1}{v_1}) = 0. \tag{1.26}$$

[11] Wolfgang Götze (born 11 July 1937 – 20 October 2021) was a German theoretical physicist and father of the mode-coupling theory.

So if $0 < v_1 < 1$ then $f = 0$ is the biggest real solution of this quadratic equation. Otherwise if $v_1 > 1$ the biggest solution is $f = \frac{v_1 - 1}{v_1} = 1 - \frac{1}{v_1}$.

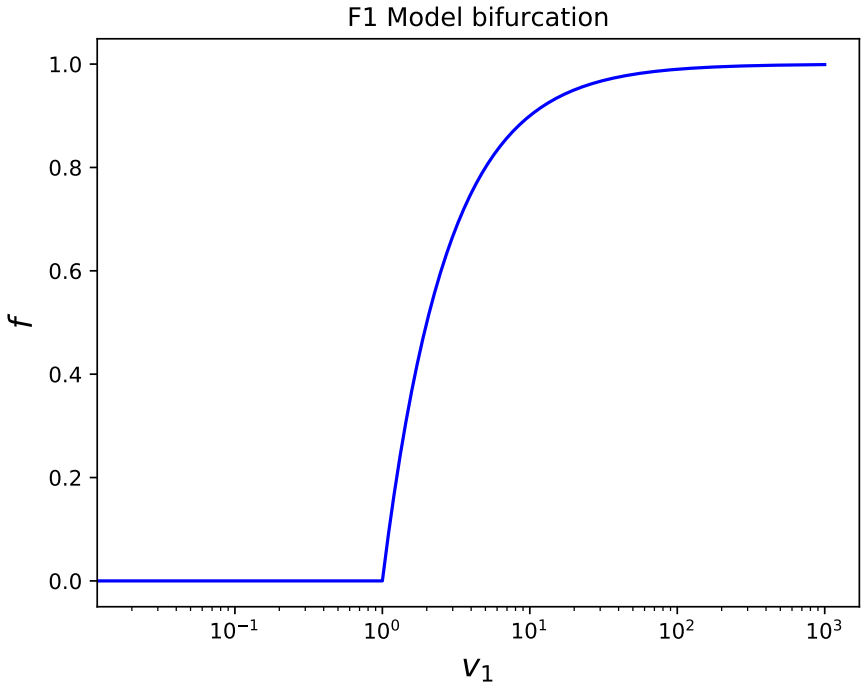

Figure 1.5: Bifurcation of the F1 model.

We can see that $f(v_1)$ is continuous, hence the F1 model does not predict any glass transition with a two-step decay of correlation functions.

F2 Model

Now assume that the coefficient v_1 vanishes, such that the memory function will be

$$m(t) = v_2 \phi^2(t).$$

This leads to the bifurcation equation:

$$f(f^2 - f + \frac{1}{v_2}) = 0. \tag{1.27}$$

This cubic equation has solutions $f = 0$ and $f = \frac{1}{2} \pm \sqrt{\frac{1}{4} - \frac{1}{v_2}}$, where $f = 0$ is the only real solution if $v_2 < 4$ and $f = \frac{1}{2} + \sqrt{\frac{1}{4} - \frac{1}{v_2}}$ is the biggest solution if $v_2 \geq 4$. This means that a jump in $f(v_2)$ occurs at $v_2 = 4$ indicating a dramatic change in the long time limit of the correlation function due to a minor change in the coupling parameter v_2. So this schematic model helps to understand why MCT is able to predict / describe the glass transition.

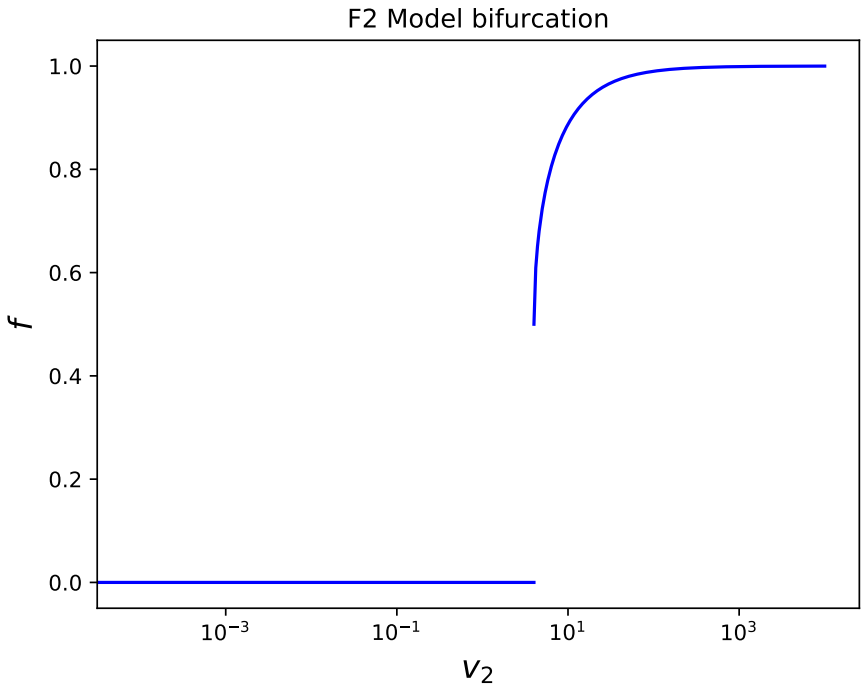

Figure 1.6: Bifurcation of the F2 model.

F12 Model

The superposition of the F1 and F2 schematic model leads to the full F12 model, where we have two positive parameters v_1 and v_2 (if one of these is zero it reduces to either the F1 or F2 model) and a memory function

$$m(t) = v_1\phi(t) + v_2\phi^2(t), \tag{1.28}$$

leading to the bifurcation equation:

$$f(f^2 + \frac{v_1 - v_2}{v_2}f + \frac{1 - v_1}{v_2}) = 0. \tag{1.29}$$

This cubic equation has solutions $f = 0$ and $f = \frac{v_2 - v_1}{2v_2} \pm \sqrt{\frac{(v_2 - v_1)^2}{4v_2^2} - \frac{1 - v_1}{v_2}}$. In the figure below the largest real solution of the bifurcation equation is plotted for $(v_1, v_2) \in [0, 5]^2$. Again for $v_2 > 1$ one can see jumps / discontinuities hinting that the F12 is able to mathematically mimic the glass transition behavior.

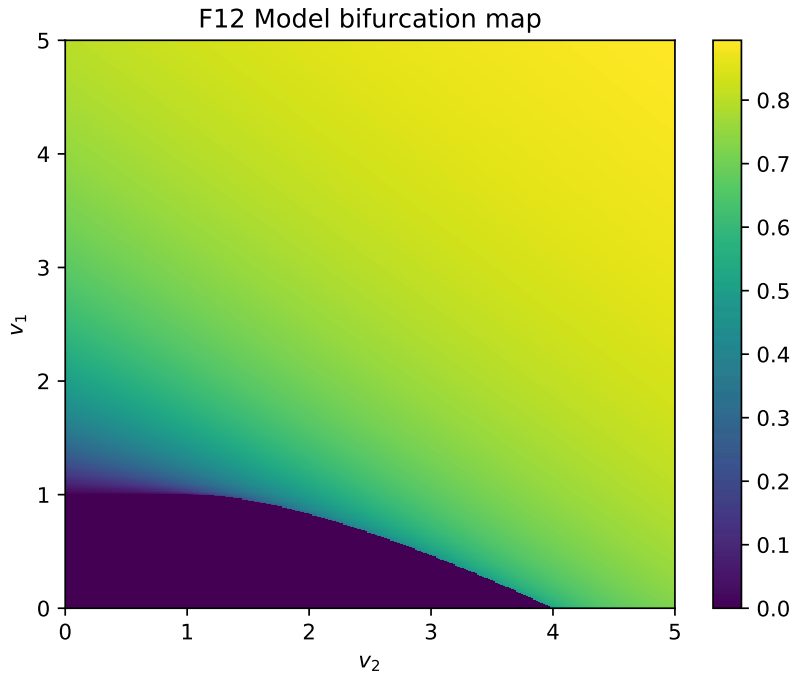

Figure 1.7: Bifurcation heat map of the F12 model.

1.3 Numerical Basics for sMCT

This section should give a brief introduction into the numerical basics of solving schematic MCT equations of the structure

$$\dot{\phi}(t) + \phi(t) + \int_0^t m(t-\tau)\dot{\phi}(\tau)\mathrm{d}\tau = 0$$

numerically. To have acceptable computational run times – with having to solve a lot of sMCT equations in the fluid dynamics simulations in mind – a fast decimation scheme is presented.

1.3.1 Discretization

A very important point in the discretization of this equation is that it has to respect the bifurcation equation. Otherwise one can not ensure that – at least – the correct long time limit, meaning whether the system is in the liquid ($f = 0$) or in the glassy ($f > 0$) regime, is found. For this reason the final discretized equation has to be an implicit equation – like the bifurcation equation itself – to recover the correct implicit connection between $\phi_i \equiv \phi(i \cdot dt)$ and $m_i \equiv m[\phi_i]$. First one should start on a linear time grid with grid size Δt, building on this, a quick and easy to implement code to solve these MCT-like equations, even for long times, will be derived.
The first thing is to use the implicit Euler[12] scheme to numerically approximate the derivative and some quadrature formula to approximate the convolution integral, here iterative undersums (left rectangular

[12]Leonhard Euler (15 April 1707 – 18 September 1783) was a Swiss mathematician, physicist, astronomer, geographer, logician and engineer who founded the studies of graph theory and topology and made pioneering and influential discoveries in many other branches of mathematics.

rule) are sufficient:

$$\dot{\phi}(t) + \phi(t) + \int_0^t m(t-t')\dot{\phi}(t')\mathrm{d}t' = 0 \rightarrow \frac{\phi_i - \phi_{i-1}}{\Delta t} + \phi_i + \Delta t \sum_{k=0}^{i-1} m_{i-k}\dot{\phi}_k = 0. \tag{1.30}$$

At this point another discretization of $\dot{\phi}$ inside the integral is necessary. Since ϕ is defined on $t \geq 0$ one might choose $\dot{\phi}_k = \frac{\phi_{k+1}-\phi_k}{h}$, to avoid the necessity of having to define ϕ_{-1}.
By restructuring the above equation one arrives at the implicit equation

$$\phi_i = -B \cdot m_i + C, \tag{1.31}$$

with the additional definitions of

$$\begin{aligned} A &:= 1/\Delta t + 1 + m_1, \\ B &:= (\phi_1 - 1)/A, \\ C &:= \left[(1/\Delta t + m_1)\phi_{i-1} - \sum_{k=1}^{i-2} m_{i-k}\left[\phi_{k+1} - \phi_k\right] \right] / A. \end{aligned}$$

However it is necessary to know ϕ_1 in order to get the algorithm started. One way would be to write out m_1 and solve this polynomial equation. The other option is to look at the short time limit of the MCT equation in which one just neglects the integral and observes an exponential decay $\phi(t) = \mathrm{e}^{-t}$ and therefore sets $\phi_1 = \mathrm{e}^{-\Delta t}$ or $\phi_1 = 1 - \Delta t$.
The resulting implicit equation 1.31 could be solved by iteration in the following way:

1. $\phi_i^{(0)} \leftarrow \phi_{i-1} \;\Rightarrow\; m_i^{(0)} = m[\phi_i^{(0)}]$
2. $\phi_i^{(n+1)} \leftarrow -B \cdot m_i^{(n)} + C$
3. continue steps 1. and 2. until $|\phi_i^{(n+1)} - \phi_i^{(n)}| < \varepsilon_1$ and $\dfrac{|\phi_i^{(n+1)} - \phi_i^{(n)}|}{|\phi_i^{(n+1)}|} < \varepsilon_2$ are reached.
4. $\phi_i^{(n+1)} \rightarrow \phi_i$,

with desired precisions ε_1 and ε_2. Mathematics by W. Götze proves that this iterative scheme converges towards the right solution[24].

1.3.2 Step Size Doubling and Decimation

Since the glass transition is observed on very long (logarithmic) time scales a linear time stepping would not lead to acceptable computational run times. Therefore it is common to use a decimation method (kind of a step size control) that uses exponentially larger steps the further the algorithm goes back in the history / memory integral. This is physically reasonable since one can imagine that the more recent correlations have bigger influence on the system than the ones far back in history. Therefore these more recent correlations must have the best resolution, while the influence of correlations far back in history is minor and one could trade some resolution in history for computational speed.
Here the discretized equation is solved on different blocks b (starting with the block $b = 0$) with a fixed amount of steps in each block, called the block size N_A. The total number of blocks is called N_B. After every block of N_A steps the step size is doubled from Δt to $2\Delta t$, which means that in block b the step size is $\Delta_b t = 2^b \Delta t$ (the initial block is denoted with $b = 0$). This doubling of step size from block to block is only allowed and does not ruin the numerical precision because $\phi(t)$ is known to only vary quickly on short time scale and vary slowly on larger time scales.

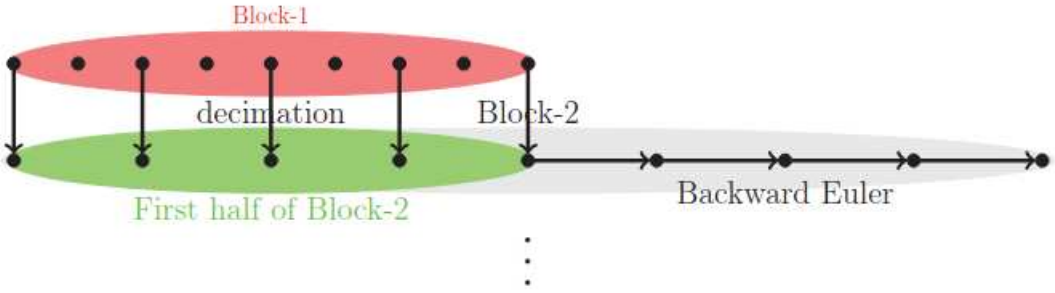

Figure 1.8: Schematic representation of block idea and the step size doubling. Figure from [36].

Only on the initial block $b = 0$ it is necessary to solve the whole block, then starting with block $b = 1$ one calculates the first half of the block $b = 1$ out of the values already given from the previous block $b = 0$. There are numerous ways to do so, the simplest way is to set $\phi_i^b \leftarrow \phi_{2i}^{b-1}$, alternatively one could calculate (weighted) averages with the neighboring points, for example $\phi_i^b \leftarrow (\phi_{2i}^{b-1} + \phi_{2i-1}^{b-1})/2$. With averaging like this one achieves that the integral (calculated by the trapazoidal-rule for example) over the first half of the block is still as exact as with the previous smaller step size.

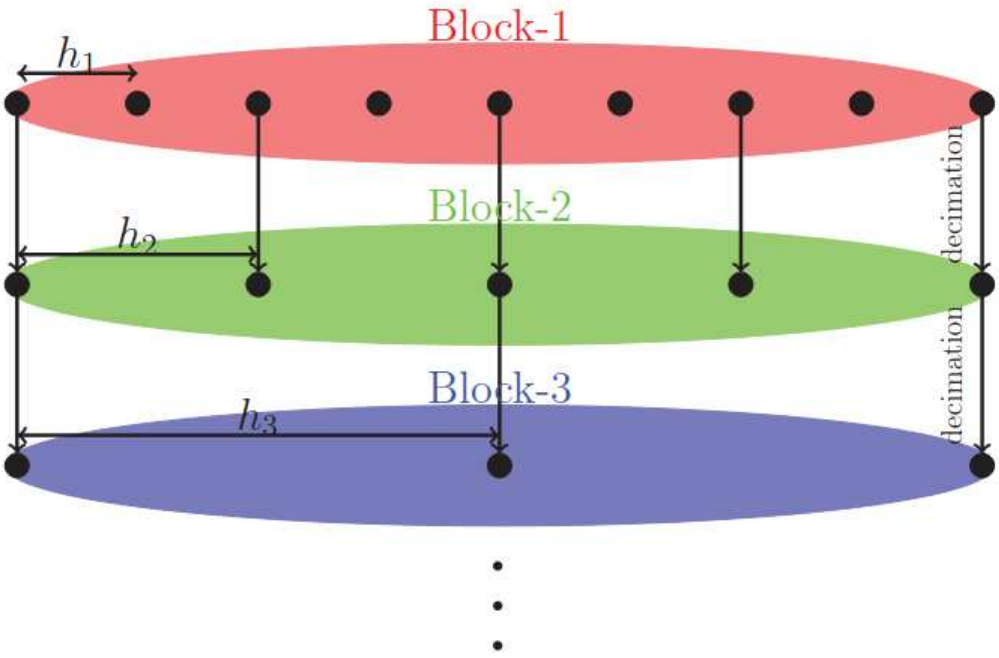

Figure 1.9: Schematic representation of the decimation procedure from [36].

1.3.3 Numerical Error from Doubling the Step Size

For the implicit Euler scheme the numerical error of the first derivative is known to be

$$E(f_i') = |\frac{f_i - f_{i-1}}{\Delta t} - f_i'| = |\Delta t \cdot f''(\xi)|,$$

with ξ being a time between the data points $i-1$ an i [52]. One can expect ϕ to vary slower than exponential, so for simplicity one can set $f(t) = e^{-t}$. An upper limit for $f''(\xi)$ on block b would be

$\frac{2}{(\Delta_b t \cdot N_A/2)^2} > \mathrm{e}^{-\Delta_b t \cdot N_A/2}$, therefore one calculates:

$$E(f_i') = \Delta_b t \cdot f''(\xi) \leq \Delta_b t \cdot \mathrm{e}^{-\Delta_b t \cdot N_A/2} < \frac{8}{\Delta_b t \cdot N_A},$$

which shows that despite doubling the step size $\Delta_b t$ the error does not increase from block to block. This even shows that the error goes to zero if $b \to \infty$, because the bifurcation equation is still respected and therefore the correct long term limit f obtained.

1.3.4 Bifurcation Equation

Recall that the long time limit ($t \to \infty$) of the system is determined by the bifurcation equation:

$$m = \frac{f}{1-f} \quad \Longleftrightarrow \quad f = \frac{m}{1+m},$$

with $\lim_{t\to\infty} \phi(t) =: f$, $\lim_{t\to\infty} m(t) =: m$. With these settings and $1/\Delta t \to 0$, because of the long time limit (or because b is big and therefore $\Delta_b t \to \infty$) the implicit equation 1.31 reduces to:

$$\begin{aligned} f &= -B \cdot m + C, \\ A &= 1 + m, \\ B &= (f-1)/A, \\ C &= mf/A. \end{aligned} \tag{1.32}$$

Here one needs to argue that for large enough step size Δt, the first point ϕ_1 is already in the long time limit, such that one could set $\phi_1 = f$ and $m_1 = m$. If one puts this all together the second version of the bifurcation equation above is recovered, which shows that this implicit algorithm is able to numerically predict the long time limits correct.

1.3.5 Numerical Solutions of the F12 Model

Finally one might briefly look at some solutions $\phi(t)$ of the F12 Model with different parameter sets (v_1, v_2). It is know from various sources ([8, 24] for example) that for $v1 = 2(\sqrt{2}-1)+\epsilon/(\sqrt{2}-1)$, $v2 = 2$ one expects a glass transition at $\epsilon = 0$. This means, that the density correlation function ϕ is expected to not decay to zero for $\epsilon \geq 0$ and to vanish for $\epsilon < 0$ in the long time limit. For the numerical calculation the algorithm is implemented exactly as described above with running times below 1 minute on a standard modern laptop or PC. The numerical parameters are $dt = 0.01$ using 40 blocks with a block size of 1000 steps in each block. For decimation scheme the simple version $\phi_i^b \leftarrow \phi_{2i}^{b-1}$ was used.
One can observe that the expected behavior of the correlators is recovered (dacay to zero for $\epsilon < 0$) and that the analytically calculated long time limits f from the bifurcation equation are also recovered within the numerical errors.

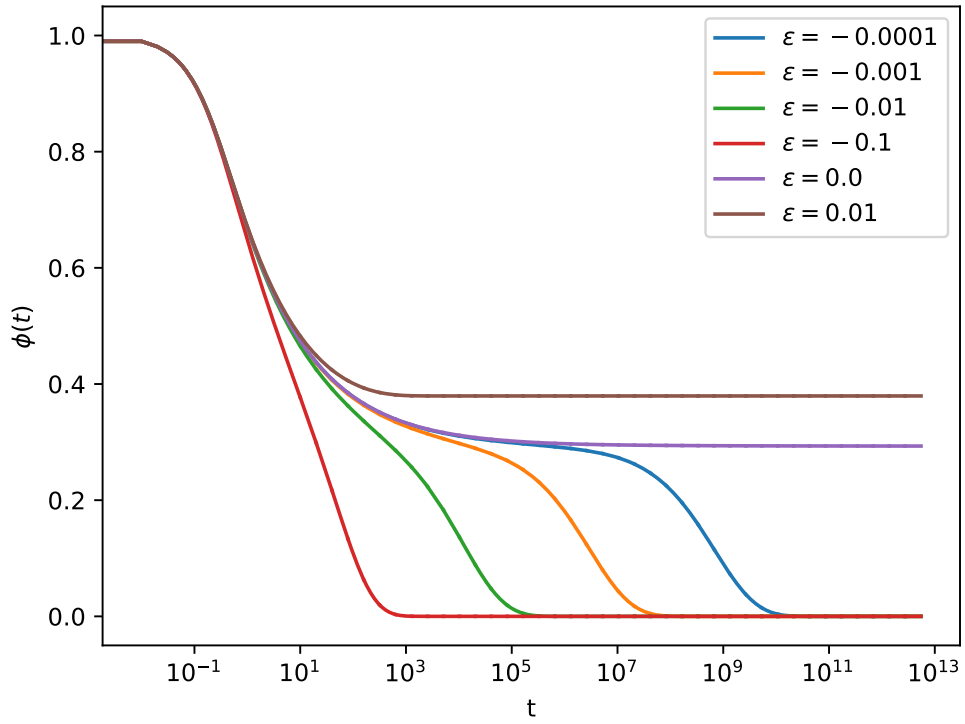

Figure 1.10: Numerical solution of the schematic MCT equation in the F12 Model with different parameters ϵ, below, above and exactly at the analytically calculated glass transition point $\epsilon = 0$.

1.4 Two-Time MCT

In later extensions of MCT to non-stationary driven systems (for example in case of a startup flow, cessation of flow or in oscillatory shear) the correlation function ϕ no longer depends only on one time – which has actually been a time difference – but on two times t, t' (final time t and reference time t' with $t \geq t'$)[6, 5]. On the other hand the memory kernel now depends not only on two but even on three times $t \geq t'' \geq t'$ with t'' an intermediate integration time. The memory kernel also functionally depends on the deformation history, which is encoded in the tensor $\underline{\underline{B}}(t, t')$. $\underline{\underline{B}}(t, t')$ (called the Finger tensor) is a measure of the deformation history of a fluid element and will be discussed in detail later on in this thesis.
The schematic MCT equation under time-dependent shear generally reads:

$$\partial_t \phi(t, t') + \phi(t, t') + \int_{t'}^{t} m(t, t'' t', [\underline{\underline{B}}]) \partial_{t''} \phi(t'', t') \mathrm{d}t'' = 0. \tag{1.33}$$

However one often reduces the memory kernel to the known F12 model with some prefactors taking in account the shear [8].

1.4.1 Two-Time MCT for Time Dependent Shear

Since the F12 Model is very well known to capture quantitatively many aspects of the glass transition the target of the following Ansatz is to reuse the F12 model but to also introduce some shear-thinning effects. To do so one makes the assumption

$$m(t, t'', t', [\underline{\underline{B}}]) = h_{tt'}[\underline{\underline{B}}] h_{tt''}[\underline{\underline{B}}] m_{F12}[\phi(t, t'')], \tag{1.34}$$

with $m_{F12}[\phi(t,t'')] = v_1\phi(t,t'') + v_2\phi^2(t,t'')$ the standard F12 model – for simplicity in the following denoted by $m(t,t'')$ – and further one chooses the h-operator to be:

$$h_{tt'}[\underline{\underline{B}}] = \frac{\gamma_c^2}{\gamma_c^2 + \mathrm{tr}(\underline{\underline{B}}(t,t') - \underline{\underline{\mathrm{Id}}})}. \tag{1.35}$$

This means that the operator $h_{tt'}$ evaluates the Finger tensor at times (t,t') and performs the calculations above. In general one could also introduce another factor $h_{t''t'}[\underline{\underline{B}}]$, but – in analogy to [8] – this factor is neglected throughout this thesis.
For the case of quasi one dimensional simple shear these h-factors (because of the trace of the deformation measuring tensor $\underline{\underline{B}}$) reduce to

$$h_{tt'}[\gamma] = \frac{1}{1 + (\gamma(t,t')/\gamma_c)^2}, \quad \gamma(t,t') = \int_{t'}^{t} \dot{\gamma}(s)\mathrm{d}s, \tag{1.36}$$

with $\dot{\gamma}(s)$ the scalar strain-rate and γ_c the critical yield parameter. This critical yield parameter determines how strong the shear is taken into account (most of the time one sets $\gamma_c = 0.1$). The limit $\gamma_c \to \infty \Rightarrow h_{tt'} \to 1$ means that shear does not affect the system, such that one ends up with the sMCT equation without any shear effects. For a constant $\dot{\gamma}$ the model is known as the F12-($\dot{\gamma}$) model [18]. The functional dependence $[\underline{\underline{B}}]$ is conveniently dropped in the notation and one only writes $h_{tt'}$ instead of $h_{tt'}[\underline{\underline{B}}]$.
The final two-time sMCT equation for time dependent shear reads:

$$\partial_t\phi(t,t') + \phi(t,t') + h_{tt'}\int_{t'}^{t} h_{tt''}m(t,t'')\partial_{t''}\phi(t'',t')\mathrm{d}t'' = 0 \tag{1.37}$$

with a two-time convolution-like integral, visualized in the following schematic picture.

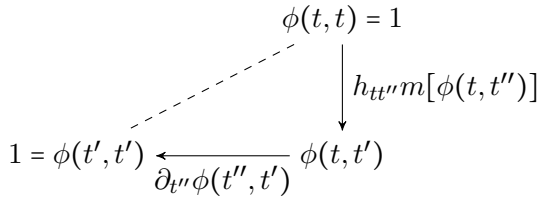

Figure 1.11: Schematic picture of the two-time convolution-like integral to calculate a specific $\phi(t,t')$.

In the upcoming second chapter of this thesis an integral constitutive equation (an integral equation to calculate the stress tensor σ) will be derived. This integral equation will be of the form $\sigma(t) \propto \int_0^t \dot{\gamma}(t')\phi^2(t,t')\mathrm{d}t'$ and therefore one needs $\phi(t,t')$ on a linear grid in t because most standard computational fluid dynamics simulations step linear in time t. For computational speed of the stress integral ($\sigma(t) \propto \int_0^t \dot{\gamma}(t')\phi^2(t,t')\mathrm{d}t'$) one would like to have a (quasi) logarithmic grid in the references times t'.

1.4.2 Numerical Details, Linear/Logarithmic Grid (for CFD)

Later on in this thesis – in the study of non-Newtonian fluid flow – one will encounter constitutive / material equations for the (polymeric) stress similar (but in tensorial form) to the construction

$$\sigma(t) = G_0\int_0^t \dot{\gamma}(t')\phi^2(t,t')\mathrm{d}t',$$

with $\phi(t,t')$ determined by the shear dependent sMCT equation.
Therefore the first time argument t needs to be compatible with the time stepping requirements of

the computational fluid dynamics (CFD). A CFD simulation usually progresses linear in time, which implies that one would like to have $\phi(t, t')$ on a linear grid in the first time argument t. For a fast computation of this extensive (polymeric) stress integral it is desirable to perform the numerical approximation on a (quasi-) logarithmic grid which is relatively fine for small $t - t'$ and gets larger for bigger $t - t'$. The physical intepretation is again that the latest deformations have the biggest influence on the stress of a material element and should therefore have the best resolution. This quasi-logarithmic grid – allowing fast computations of the memory integrals in the sMCT equation – is done by doubling the step size Δt after a certain number of steps. This number of steps using the same Δt is called the block size and will be denoted N_A). So for every fixed i (therefore t) one uses the step size $\Delta_0 t = 2^0 dt = dt$ for the zeroth block of the j indices (connected to t') and then $\Delta_1 t = 2dt$ for the first, $\Delta_2 t = 2^2 dt = 4dt$ for the second an so on, until one arrives at $t' < \Delta_{N_B - 1} t$. The total number of blocks is denoted N_B, starting at block 0 up to block $N_B - 1$.
The grid on which the (discretized version of the) sMCT equation is solved, looks the following way: the wider t and t' are apart from each other (or in other words: the further we are away from the diagonal $t = t'$ in Fig. 1.11) the less accurate the discretization gets.

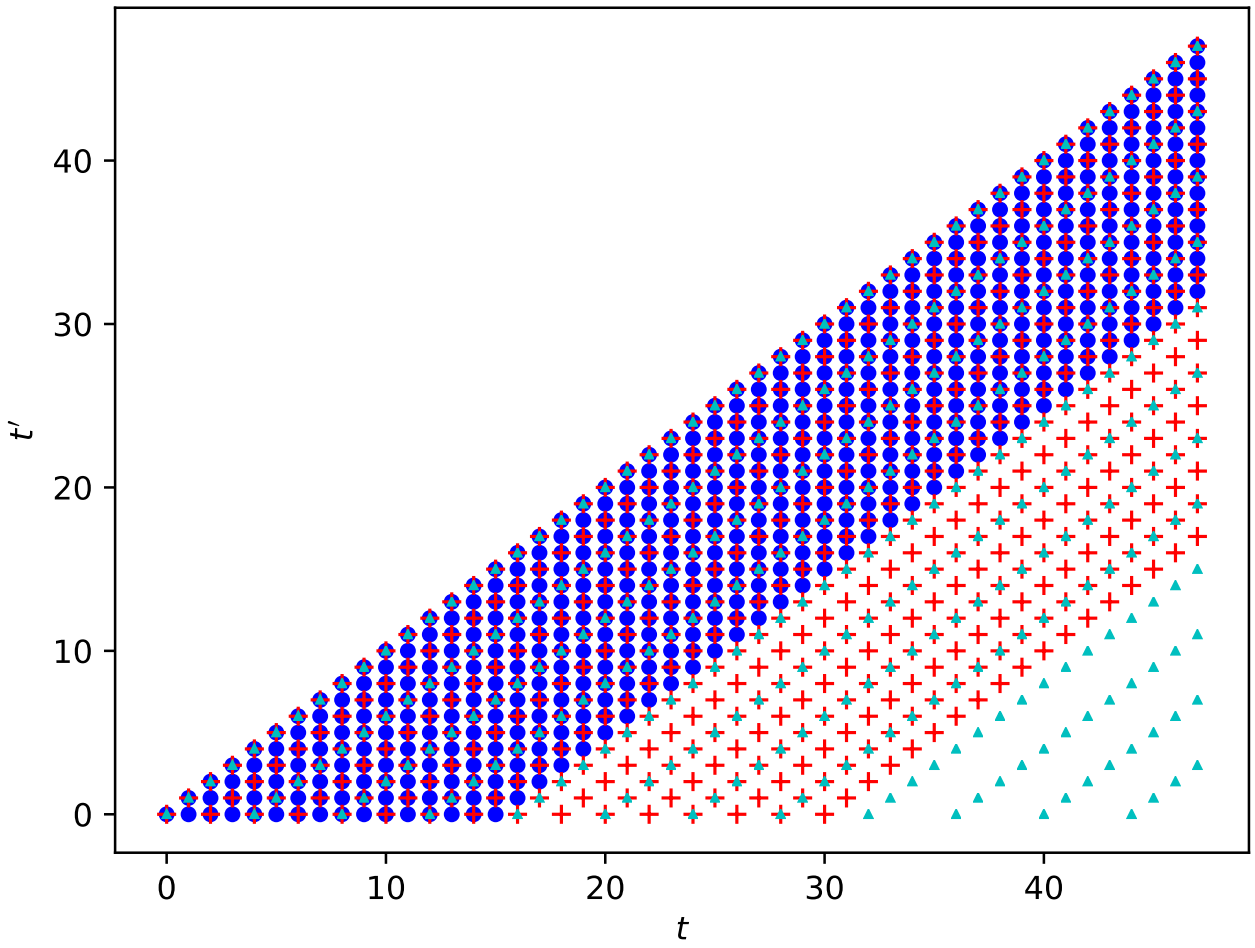

Figure 1.12: Schematic sketch of the discretization grid. Blue points are the finest level ($b = 0$), red pluses are the points corresponding to $b = 1$, cyan triangles correspond to $b = 2$.

Algorithm

The two-time sMCT equation in its discretized version ($(t,t') \to (i,j)$) using the implicit Euler method is given by

$$\frac{\phi_{i,j} - \phi_{i-1,j}}{\Delta t} + \phi_{i,j} + h_{i,j} \sum_{k=j}^{i-1} h_{i,k} m_{i,k} \left[\phi_{k+1,j} - \phi_{k,j}\right] = 0. \tag{1.38}$$

Now set

$$\begin{aligned} A &:= 1/\Delta t + 1 + h_{i,j} h_{i,i-1} m_{i,i-1} \\ B &:= h_{i,j}^2 (\phi_{j+1,j} - 1)/A \\ C &:= \left[(1/\Delta t + h_{i,j} h_{i,i-1} m_{i,i-1}) \phi_{i-1,j} - h_{i,j} \sum_{k=j+1}^{i-2} h_{i,k} m_{i,k} \left[\phi_{k+1,j} - \phi_{k,j}\right] \right] / A. \end{aligned}$$

This leads to the simple implicit equation:

$$\phi_{i,j} = -B m_{i,j} + C, \tag{1.39}$$

which one could solve by the following iterative procedure:

1. start by $\phi_{i,j}^{(0)} \leftarrow \phi_{i-1,j}$,
2. calculate a first Ansatz for $m_{i,j}^{(0)} = m[\phi^{(0)}]$,
3. with this $m_{i,j}^{(0)}$ calculate a new $\phi_{i,j}^{(1)}$ via the implicit equation 1.39,
4. iterate this procedure (steps 1. to 3.) to calculate new $m_{i,j}^{(1)}, ..., m_{i,j}^{(n)}$ and $\phi_{i,j}^{(2)}, ..., \phi_{i,j}^{(n+1)}$,
5. continue this procedure until $|\phi_{i,j}^{(n+1)} - \phi_{i,j}^{(n)}| < \varepsilon_1$ and $\frac{|\phi_{i,j}^{(n+1)} - \phi_{i,j}^{(n)}|}{|\phi_{i,j}^{(n+1)}|} < \varepsilon_2$ are reached,
6. set $\phi_{i,j} \leftarrow \phi_{i,j}^{(n+1)}$.

The threshold parameters ε_1 and ε_2 determine the desired absolute and relative tolerance of the iterative procedure.

Long Time Limit of the Two-Time MCT Algorithm

In the special case of zero shear, mathematically described by $h \equiv 1$, the long term limit (here $t - t' \to \infty$ instead of $t \to \infty$ in the one-time MCT discussed in section 1.3.4) of system is given by the bifurcation equation

$$f = \frac{m}{1+m},$$

with $\lim_{t-t'\to\infty} \phi(t,t') = f$ and $\lim_{t-t'\to\infty} m(t,t') = m$. This means that for a fixed t and therefore i in the discretized version one needs to assume that one step back in t' and therefore j is already in the long time limit. This also implies that the step size $\Delta t \to \infty$, which leads to:

$$\begin{aligned} A &= 1 + m, \\ B &= (f-1)/A = \frac{f-1}{1+m}. \end{aligned}$$

Since it is assumed that $\phi_{j+1,j}$ is already in the long term limit ($\phi_{j+1,j} = f$) the sum $\sum_{k=j+1}^{i-2} \ldots$ in C vanishes, such that:

$$C = mf/A = \frac{mf}{1+m}.$$

This leads to an implicit equation (obtained form 1.39):

$$f = -B \cdot m + C = \frac{m}{1+m},$$

which is exactly the desired bifurcation equation given above (and in 1.24).
This calculation proves that the proposed algorithm to solve the two-time schematic MCT equation does predict – in the special case of $h \equiv 1$ – the correct long time limits.

1.4.3 Solution of F12 Model under Time-Dependent Shear

Let us now look at some numerical solutions of the shear-dependent two-time sMCT equation 1.37 obtained by the previously described algorithm. One can already assume, that the correlation function decays quicker under stronger shear because the memory kernel decreases stronger, resulting in less coupling. In the limit $\dot{\gamma} \to \infty$ the memory kernel vanishes, resulting in an exponential decay.
The following graphics will show $\phi(t,t')$ versus $t-t'$. In a system without shear this is equal to $\phi(t-t',0)$ because $\phi(t_2,t_1)$ is only dependent on t_2-t_1. In an oscillatory sheared system, with

$$\dot{\gamma}(s) = \gamma_0 f \cos(fs),$$

this is not the case because $h_{t_1 t_2}$ depends on $\gamma(t_2,t_1) = \gamma_0 [\sin(ft_2) - \sin(ft_1)] \neq \gamma(t_2-t_1,0)$.
The inner memory kernel (without the h-factors) should be in F12 Model form $m[\phi] = v_1\phi + v_2\phi^2$, with parameters $v1 = 2(\sqrt{2}-1)$, $v2 = 2$, which is – as previously discussed – in the glassy regime ($\epsilon = 0$ so exactly at the critical point) and therefore the correlation function would not decay to zero for $t-t' \to \infty$ without shear.

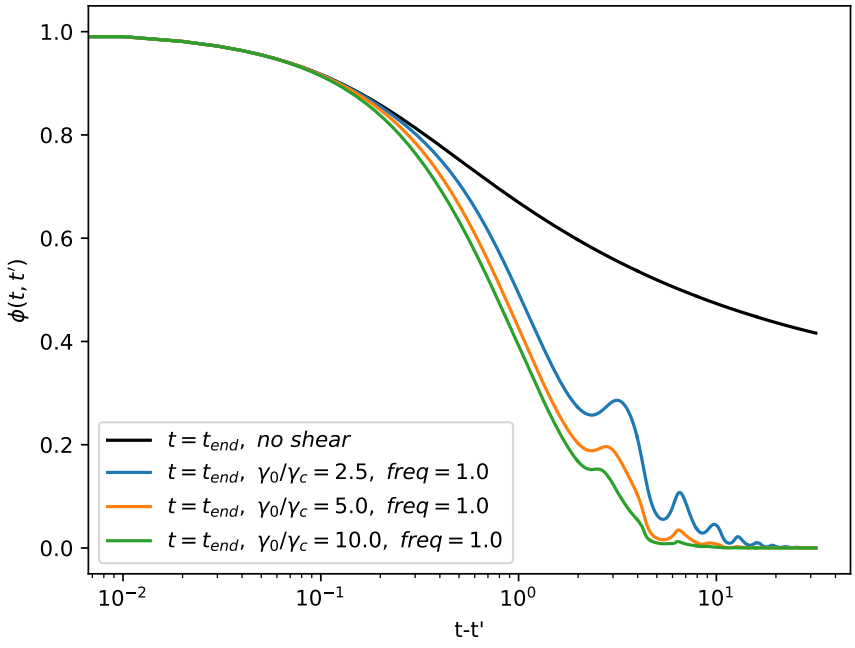

Figure 1.13: $\phi(t,t')$ versus $t-t'$ for various γ_0/γ_c on a logarithmic grid in time t'.

One can see that – as expected – the correlation functions decays much quicker with stronger shear (γ_0/γ_c bigger). Please note that an increase in the correlation function ϕ does not violate the second law of thermodynamics since the external strain-rate does provide energy to the system.
Next one can vary t and see that we get different correlation function, except for time shifts of factor $2\pi f$. In this case the h-factor is the same due to the periodicity of the sinus function.

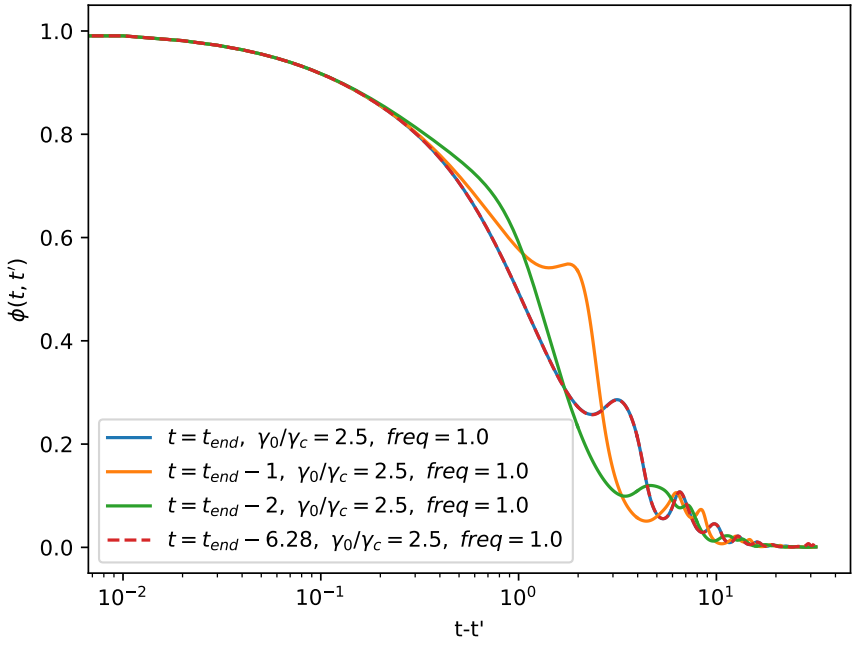

Figure 1.14: $\phi(t, t')$ versus $t - t'$ for various t with the same critical $v_1,\ v_2$ as above.

One can see that qualitatively all correlation functions decay on the same timescale. The small difference is induced by smaller or bigger strains $\gamma(t, t')$ at the different points in the two time plane t, t'.

Chapter 2

Continuum Mechanics

This chapter presents the basic equations, mainly the incompressible Navier-Stokes equation, of continuum mechanics (which can of course also be found in many textbooks, for example [31, 59]) and introduces some material laws (also called constitutive equations) for viscoelastic and viscoelastoplastic fluids. Furthermore some analytical observations in simple flow geometry (an infinitely long rectangular channel) are recalled to gain basic understanding of the behavior of viscoelastic and viscoelastoplastic (yield stress) fluids.

2.1 Navier-Stokes Equation for incompressible Fluids

To derive the famous Navier[1]-Stokes[2] equation (NSE) one might start by remembering some basic conservation rules

$$\frac{\mathrm{d}m}{\mathrm{d}t} = 0 \;\rightarrow\; \text{conservation of total mass,} \tag{2.1}$$

$$\frac{\mathrm{d}}{\mathrm{d}t}\vec{P} = \vec{F}_{ext} + \vec{F}_{surface} \;\rightarrow\; \text{conservation of total momentum,} \tag{2.2}$$

where $\vec{F}_{ext}$ is the total external force (for example a gravitational or electric force) and $\vec{F}_{surface} = \int_{\partial V(t)} \underline{\underline{\Sigma}}(\vec{r},t)\cdot d\vec{s}$ is the friction force at the surface of the control volume. The total mass m is defined by integrating the particle density $\rho(\vec{r},t)$ over the control volume $V(t)$ that moves along with the flow. A similar statement for the total momentum leads to:

$$m(t) := \int_{V(t)} \rho(\vec{r},t)\mathrm{d}\vec{r},$$
$$\vec{P}(t) := \int_{V(t)} \rho(\vec{r},t)\vec{v}(\vec{r},t)\mathrm{d}\vec{r}.$$

Inserting the definitions of total mass and momentum into the conservation laws and applying the Gauss[3] theorem onto the surface force term produces continuity equations for mass and momentum:

$$\partial_t\rho + \vec{\nabla}\cdot[\rho\vec{v}] = 0, \tag{2.3}$$

$$\partial_t\rho\vec{v} + \vec{\nabla}\cdot[\rho\vec{v}\otimes\vec{v}] = \rho\vec{f}_{ext} + \vec{\nabla}\cdot\underline{\underline{\Sigma}}\,. \tag{2.4}$$

[1] Claude Louis Marie Henri Navier (10 February 1785 – 21 August 1836) was a French mechanical engineer and physicist.

[2] Sir George Gabriel Stokes (13 August 1819 – 1 February 1903) was an Irish physicist and mathematician.

[3] Johann Carl Friedrich Gauss (30 April 1777 – 23 February 1855) was a German mathematician, geodesist, and physicist who made significant contributions to many fields in mathematics and science.

Incompressible Fluids

These universal equations can be reduced if one assumes the flow to be incompressible, which means that the density does not change along the streamlines. Mathematically this leads to

$$\frac{D}{Dt}\rho := \partial_t \rho + [\vec{v} \cdot \vec{\nabla}]\rho = 0.$$

In this thesis the density is assumed to even be constant, which is a slightly stronger condition. In a sense that otherwise there could be for example a bubble in the flow that is transported along the flow lines and $\frac{D}{Dt}\rho = 0$ would be fulfilled, even though ρ is not constant.
The differential operator $\frac{D}{Dt}* := \partial_t * + [\vec{v} \cdot \vec{\nabla}]*$ is called the material (or advective) derivative. It describes the time rate of change of some scalar or vector physical quantity $*$ of a material element that is subjected to a space-and-time-dependent macroscopic velocity field $\vec{v}$. Combined with the mass conservation

$$\partial_t \rho + \vec{\nabla} \cdot [\rho \vec{v}] = \partial_t \rho + \rho[\vec{\nabla} \cdot \vec{v}] + [\vec{v} \cdot \vec{\nabla}]\rho = 0$$

this leads to the incompressiblility equation

$$\vec{\nabla} \cdot \vec{v} = 0.$$

The so called Euler stress tensor $\underline{\underline{\Sigma}}$ can be splitted into its trace, the "volumetric stress" and the "deviatoric stress" $\underline{\underline{\Sigma}} = -p\underline{\underline{1}} + \underline{\underline{\sigma}}$. Using this splitting and combining the two equations leads to the incompressible Navier-Stokes equation, which are a set of partial differential equations:

$$\begin{aligned} \partial_t \rho + [\vec{v} \cdot \vec{\nabla}]\rho &= 0, \\ \rho\left(\partial_t \vec{v} + [\vec{v} \cdot \vec{\nabla}]\vec{v}\right) &= \rho \vec{f}_{ext} - \vec{\nabla} p + \vec{\nabla} \cdot \underline{\underline{\sigma}}, \\ \vec{\nabla} \cdot \vec{v} &= 0. \end{aligned}$$

Under the assumption of a constant density, which for convenience can be set to unity ($\rho = 1$), the first equation becomes redundant and the set of equations reduces to:

$$\partial_t \vec{v} + [\vec{v} \cdot \vec{\nabla}]\vec{v} = \vec{f}_{ext} - \vec{\nabla} p + \vec{\nabla} \cdot \underline{\underline{\sigma}}, \tag{2.5}$$

$$\vec{\nabla} \cdot \vec{v} = 0. \tag{2.6}$$

Incompressible Stokes Flow

For the special case of viscoelatic and viscoelastoplastic fluid flow one might neglect the $[\vec{v} \cdot \nabla]\vec{v}$ term, because these advective inertial forces are small (and therefore neglectable) compared to the viscous forces. The Navier-Stokes equation for the momentum reduces to the so-called time-dependent Stokes equation

$$\partial_t \vec{v} = \vec{f}_{ext} - \nabla p + \nabla \cdot \underline{\underline{\sigma}}. \tag{2.7}$$

One also calls this equation the Stokes flow or creep flow.

Need for Constitutive Equations

In two spatial dimensions the momentum balance gives two equations, plus the additional equation from the incompressibility condition leads to three equations in total. However, the system has six unknowns, since $\underline{\underline{\sigma}}$ consists of three independent unknowns because of the symmetry ($\sigma_{ij} = \sigma_{ji}$). The velocity $\vec{v}$ consists of two components (x and y direction), plus the scalar pressure variable. To solve

this underdetermined set of equations is in general of course mathematically impossible.
Therefore one needs additional equations to close the system. These additional equations are called constitutive equations or material laws, and specify the stress tensor $\underline{\underline{\sigma}}$. Constitutive equations are usually emprical, the aim of this thesis is to incorporate more sophisticated constitutive equations that are closer to them being found in statistical physics.

2.2 Differential Constitutive Equations

As discussed in the last section the Navier-Stokes equations are underdetermined and need closure by adding an external material law, also called a constitutive equation (CE). Here a couple of more or less ad-hoc constitutive equation in differential form (DCE) are presented. Note that neither of them has a "first-principles" starting point, but at least some heuristics.
One defines the velocity gradient $\underline{\underline{\kappa}}$ and its symmetrized version, the strain-rate (sometimes also deformation-rate) tensor $\underline{\underline{D}}$ by

$$\underline{\underline{\kappa}}(t) := (\vec{\nabla} \otimes \vec{v}(t))^T \equiv (\vec{\nabla}\vec{v}(t))^T, \tag{2.8}$$

$$\underline{\underline{D}}(t) := \frac{1}{2}(\underline{\underline{\kappa}}(t) + \underline{\underline{\kappa}}^T(t)). \tag{2.9}$$

2.2.1 Newtonian Model

The Newtonian model assumes an instantaneous linear relation between the stress and the strain-rate. This linear relation defines the so called (dynamic) viscosity η of the Newtonian fluid. The model assumes that η is constant during all deformations.
The constitutive equation for the Newtonian incompressible fluid is given by

$$\underline{\underline{\sigma}}(t) = 2\eta\underline{\underline{D}}(t), \tag{2.10}$$

and leads to the Laplace-operator $\Delta := \vec{\nabla}^2$ acting on the velocity such that the momentum balance in the NSE reads:

$$\partial_t\vec{v} + [\vec{v}\cdot\vec{\nabla}]\vec{v} - \eta\Delta\vec{v} = \vec{f}_{ext} - \vec{\nabla}p.$$

In the following the Newtonian model is used to describe a solvent background (for example water or ethanol) in which a polymer / colloidal suspension is dissolved. Since most colloidal suspensions or polymeric melts are diluted in a Newtonian (incompressible) solvent it is customary to split the stress tensor into a Newtonian solvent part and polymeric part:

$$\underline{\underline{\sigma}} = \underline{\underline{\sigma_S}} + \underline{\underline{\sigma_P}},$$

with the solvent stress tensor $\underline{\underline{\sigma_S}}$ given by $\underline{\underline{\sigma_S}}(t) = 2\eta_S\underline{\underline{D}}(t)$.

2.2.2 Maxwell Model

The observations that many fluids (including honey for example) behave viscoelastic, which means that they show elastic properties on short time scales and viscous properties on long times scales, lead to the famous Maxwell model – proposed by James Clark Maxwell himself in 1867 [40].
The Maxwell model assumes that the total strain of a material is the sum of a purely viscous dashpot and a purely elastic spring which are in serial connection, such that the strains of both elements add up: $\gamma = \gamma_D + \gamma_S$. As damper and spring are connected in series, the total stress is equal to the stress

on the damper and equal to the stress on the spring (similar to the current in a series connection) $\sigma = \sigma_D = \sigma_S$.

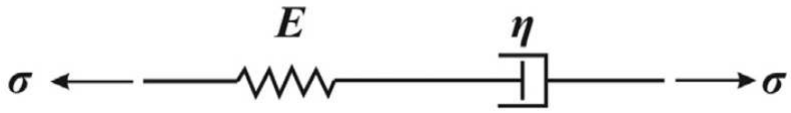

Figure 2.1: Schematic idea of the Maxwell element: a serial connection of an elastic spring to a viscous dashpot. Figure from [25]

.

With the Newtonian fluid approximation / assumption $\sigma_D = \eta\dot{\gamma}_D$ where η is the viscosity of the dashpot and Hooke's law $\sigma_S = G_\infty\gamma_S$ as a model for the spring one gets the (differential) constitutive equation

$$\dot{\gamma} = \frac{\dot{\sigma}}{G_\infty} + \frac{\sigma}{\eta}. \tag{2.11}$$

This differential equation with initial condition $\sigma(t = 0) = 0$ (no initial stress) is solved by

$$\sigma(t) = G_\infty \int_0^t \dot{\gamma}(t')e^{\frac{-(t-t')}{\lambda}}\mathrm{d}t', \tag{2.12}$$

with $\lambda = \eta/G_\infty$ being a characteristic relaxation time of the system. Some literature also uses τ instead of λ for the relaxation time.

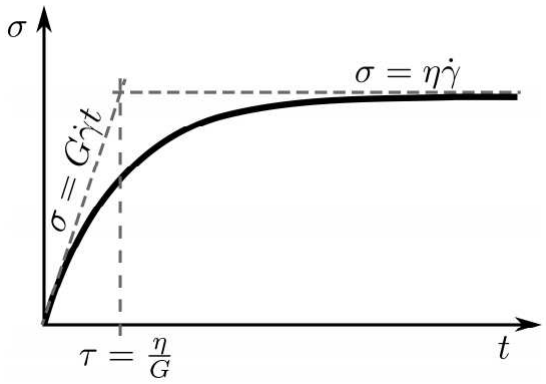

Figure 2.2: Stress versus time for constant strain-rate $\dot{\gamma}$ obtained from the Maxwell model. Figure from Ref.[13].

This was the simple one-dimensional case, in higher dimensions one uses the previously defined velocity gradient $\underline{\underline{\kappa}} = (\vec{\nabla}\vec{v})^T$ and its symmetrized version $\underline{\underline{D}} = \frac{1}{2}(\underline{\underline{\kappa}} + \underline{\underline{\kappa}}^T)$, instead of the scalar strain-rate $\dot{\gamma}$. However, the simple partial time derivative does not take the advection of the fluid element into account, neither is it rotation invariant. Therefore it needs to be replaced by a suitable "covariant" derivate. The most common choice to do so is the so called upper convected derivative. The upper convected derivative correctly describes the rate of change of some tensor property in a laboratory fixed (also called Eulerian) reference frame.

Upper Convected Maxwell Model

To formulate the upper convected version of the Maxwell model for the polymeric stress tensor $\underline{\underline{\sigma_P}}$ (also called Oldroyd[4] B model for the total stress tensor $\underline{\underline{\sigma}} = \underline{\underline{\sigma_S}} + \underline{\underline{\sigma_P}}$) one first needs to define the upper convected (or Oldroyd B) derivative[42] – which fulfills tensorial transformation properties – for an arbitrary tensor $\underline{\underline{A}}$:

$$\overset{\triangledown}{\underline{\underline{A}}} := \partial_t \underline{\underline{A}} + [\vec{v} \cdot \vec{\nabla}]\underline{\underline{A}} - \underline{\underline{\kappa}} \cdot \underline{\underline{A}} - \underline{\underline{A}} \cdot \underline{\underline{\kappa}}^T. \tag{2.13}$$

By simply exchanging the partial time derivative $\partial_t \underline{\underline{\sigma}}(t)$ from the simple Maxwell model with the upper convected derivative $\overset{\triangledown}{\underline{\underline{\sigma}}}(t)$ one obtains the upper convected Maxwell model (UCM model) given by

$$\overset{\triangledown}{\underline{\underline{\sigma_P}}}(t) + \frac{1}{\lambda}\underline{\underline{\sigma_P}}(t) = 2G_\infty \underline{\underline{D}}(t). \tag{2.14}$$

Finger Tensor

To be actually able to formulate an integral solution formula (similar to the variation of constant formula previously) one needs to furthermore define the Finger tensor $\underline{\underline{B}}(t, t')$, which is a rotation-invariant measure of occurring deformations of a given material / fluid element between times t' and t. The Finger tensor is defined as the solution of:

$$\overset{\triangledown}{\underline{\underline{B}}}(t, t') := \partial_t \underline{\underline{B}}(t, t') + [\vec{v}(t) \cdot \vec{\nabla}]\underline{\underline{B}}(t, t') - \underline{\underline{\kappa}}(t) \cdot \underline{\underline{B}}(t, t') - \underline{\underline{B}}(t, t') \cdot \underline{\underline{\kappa}}^T(t) = 0, \tag{2.15}$$

with the initial condition that $\underline{\underline{B}}(t', t') = \underline{\underline{\mathrm{Id}}}$ for all times $t' \leq t$.

Define a deformation gradient tensor $\underline{\underline{E}}(t, t')$ by

$$\underline{\underline{E}}(t, t') := \exp_+\Big(\int_{t'}^{t} \underline{\underline{\kappa}}(s) - [\vec{v}(s) \cdot \vec{\nabla}]\mathrm{d}s\Big),$$

such that one can write the Finger tensor

$$\underline{\underline{B}}(t, t') = \underline{\underline{E}}(t, t') \cdot \underline{\underline{E}}(t, t')^T.$$

One can easily check that this expression fulfills the defining equation 2.15 from above.
Further note that

$$-\partial_{t'} \underline{\underline{B}}(t, t')|_{t'=t} = 2\underline{\underline{D}}(t) \tag{2.16}$$

holds true for all times t.

Integral Formula of the UCM

With these properties – equation 2.16 and the defining PDE 2.15 – of the Finger tensor one can show (see 2.2.4 where all the derivatives are actually calculated) that the integral formula or integral constitutive equation (ICE)

$$\underline{\underline{\sigma_P}}(t) = G_\infty \int_0^t [-\partial_{t'} \underline{\underline{B}}(t, t')] e^{\frac{-(t-t')}{\lambda}} \mathrm{d}t'. \tag{2.17}$$

is equivalent to UCM model defined by equation 2.14 above.

[4] James Gardner Oldroyd (25 April 1921 – 22 November 1982) was a British applied mathematician.

2.2.3 Excursion: Upper Convected Derivative and Finger Tensor

In the subsection before it was mentioned that the upper convected derivative is the proper way – that the correct tensor transformation behaviour from Lagrangian ξ^α (Greek letters) to Eulerian coordinates x^i (Roman letters) is fulfilled – to define the rate of change for tensorial quantities (such as the stress tensor for example) in the Eulerian reference frame. So far there was no destinction between upper (contravariant) and lower (covariant) indices for the components of the vectors and tensors, as done very often outside of the field of general relativity (GR). If one looks very carefully into some course (e.g. [59]) on classical field theory one finds that components of vectors (as opposed to those of covectors) are said to be contravariant. Therefore (only for this excursion!) one should use upper indices for vectors and especially tensors (such as the Finger tensor which will be the main focus of this subsection) and calculate so-called covariant derivative (objects in geometry should be independent of their description and in particular of the chosen coordinate system).

Why the Material Derivative is not sufficient

Before that one could first verify why it is not sufficient to simply change the partial derivative ∂_t to a material derivative $\frac{D}{Dt}$. To do so one could consider a motion / flow in which a given material element has a "worldline" $\vec{x}(t)$, and a second motion where just the whole fluid is rotated by $\underline{\underline{Q}}(t)$ such that the very same material has a "worldline" $\vec{x}^*(t) = \underline{\underline{Q}}(t)\vec{x}(t)$. If the constitutive equation respects material frame indifference, stresses in a material element should only arise from deformations. Especially these stresses should not change even if the material is under a time-dependent rotation [48]. This however is not the case if one would just naively exchange the partial derivative ∂_t with the material derivative $\frac{D}{Dt}$, as the following calculation (from [48])

$$\begin{aligned}
\underline{\underline{T}}^*(\vec{x}^*,t) &= \underline{\underline{Q}}(t)\underline{\underline{T}}(\vec{x},t)\underline{\underline{Q}}^{-1}(t) \\
\frac{D}{Dt}\underline{\underline{T}}^*(\vec{x}^*,t) &= \underline{\underline{Q}}(t)\left[\frac{D}{Dt}\underline{\underline{T}}(\vec{x},t)\right]\underline{\underline{Q}}^{-1}(t) + \dot{\underline{\underline{Q}}}(t)\underline{\underline{Q}}^{-1}(t)\underline{\underline{T}}^*(\vec{x}^*,t) + \underline{\underline{T}}^*(\vec{x}^*,t)\dot{\underline{\underline{Q}}}(t)\underline{\underline{Q}}^{-1}(t)
\end{aligned}$$

shows.

Covariant Derivatives and Christoffel Symbols

Now it is clear why it is insufficient to simply exchange ∂_t with $\frac{D}{Dt}$, but so far it is still unclear why the upper convected derivative

$$\overset{\triangledown}{\underline{\underline{A}}} := \partial_t\underline{\underline{A}} + [\vec{v}\cdot\vec{\nabla}]\underline{\underline{A}} - \underline{\underline{\kappa}}\cdot\underline{\underline{A}} - \underline{\underline{A}}\cdot\underline{\underline{\kappa}}^T.$$

of a tensor $\underline{\underline{A}}$ fulfills the right tensorial transformation behaviour.
From the classical field theory it is known that the covariant derivatives with respect to k (written with a lower $;k$ in contrast of $,k$ for the partial derivative) of a contravariant vector a^i and tensor (of the second order) A^{ij}, using the Einstein[5] summation convention, are

$$\begin{aligned}
a^i{}_{;k} &= a^i{}_{,k} + \Gamma^i_{mk}a^m, \\
A^{ij}{}_{;k} &= A^{ij}{}_{,k} + \Gamma^i_{mk}A^{mj} + \Gamma^j_{mk}A^{im},
\end{aligned}$$

[5] Albert Einstein (14 March 1879 – 18 April 1955) was a German-born theoretical physicist, widely acknowledged to be one of the greatest and most influential physicists of all time.

with the Christoffel[6] symbols Γ of the Levi-Civita[7] connection, commonly known from GR. In the Euclidean geometry these Christoffel symbols describe how the local coordinate basis changes from point to point [30]. The covariant derivative is designed to obey the correct tensor coordinate transformation behaviour, therefore it is sufficient to prove that the upper convected derivative can be written with only covariant and no partial derivatives (other than a partial time derivative ∂_t). To do so one writes the upper convected derivative of a tensor A^{ij} in index notation using the fact that $\kappa^i{}_j \equiv v^i{}_{,j}$ and $\vec{v} \cdot \vec{\nabla} = v^k \partial_k$:

$$\begin{aligned}
\overset{\triangledown}{A}{}^{ij} &= \partial_t A^{ij} + v^k A^{ij}{}_{,k} - v^i{}_{,k} A^{kj} - A^{ik} v^j{}_{,k} \\
&= \partial_t A^{ij} + \left(v^k A^{ij}{}_{;k} - v^k \Gamma^i_{mk} A^{mj} - v^k \Gamma^j_{mk} A^{im} \right) - v^i{}_{,k} A^{kj} - A^{ik} v^j{}_{,k} \\
&= \partial_t A^{ij} + v^k A^{ij}{}_{;k} - \left(v^i{}_{,k} A^{kj} + v^k \Gamma^i_{mk} A^{mj} \right) - \left(A^{ik} v^j{}_{,k} + v^k \Gamma^j_{mk} A^{im} \right) \\
&= \partial_t A^{ij} + v^k A^{ij}{}_{;k} - \left(v^i{}_{,k} A^{kj} + \Gamma^i_{mk} v^m A^{kj} \right) - \left(A^{ik} v^j{}_{,k} + A^{ik} v^m \Gamma^j_{mk} \right) \\
&= \partial_t A^{ij} + v^k A^{ij}{}_{;k} - v^i{}_{;k} A^{kj} - A^{ik} v^j{}_{;k}
\end{aligned}$$

where in the second last step one first renames the indices k and m and then uses the symmetry property $\Gamma^i_{mk} = \Gamma^i_{km}$.
One can see that the upper convected derivative can be written using only covariant derivatives and is therefore covariant itself. However, this is not the only covariant derivative, a similar derivation but with covariant (lower indices) instead of contravariant (upper indices) tensors leads the so-called lower convected derivative (corresponding to the Oldroyd A model). From a mathematical perspective it is hard to decide which version to use on a basis of Euclidean space and Navier-Stokes equation alone. The extensive use of the upper convected version is due to experiments that show that polymeric fluids climb a rotating rod, favoring the upper convected version (B). The lower convected version (A) would predict the opposite effect [29].

Finger Tensor

The fact that the Finger tensor $B^{ij}(t, t')$ fulfills the equation

$$\begin{aligned}
\overset{\triangledown}{B}{}^{ij}(t, t') &= 0 \\
B^{ij}(t', t') &= \delta^{ij}
\end{aligned}$$

makes B^{ij} a covariant second rank tensor in the Eulerian reference system that does not contain any rigid-body rotations. Therefore only deformations – but no translations or rotations – of a material element do enter the Finger tensor.

2.2.4 Fluidity Model

Finally one might consider a more general type of differential constitutive equation for viscoelastic material. This more general fluidity model – in contrast to the Maxwell Model – consists of a set of two partial differential equations instead of only one differential equation for the stress tensor $\underline{\underline{\sigma_P}}(t)$. The first differential equation still describes the evolution of the stress tensor. This differential equation needs a so called "fluidity", which is an inverse timescale in order to describe the memory / relaxation

[6] Elwin Bruno Christoffel (10 November 1829 – 15 March 1900) was a German mathematician and physicist who worked on fundamental concepts of differential geometry, which would later provide the mathematical basis for theory of general relativity.

[7] Tullio Levi-Civita (29 March 1873 – 29 December 1941) was an Italian mathematician, most famous for his work on differential geometry.

of a viscoelastic or glassy fluid as a parameter instead of a constant timescale λ in the Maxwell Model. The fluidity $f(t)$ itself is given by another differential equation in which also other details such as the shear of the system are taken into account.
Some microscopic arguments such as the cage-breaking phenomena under shear (or shear-thinning) which shortens relaxation time massively can be explained within this fluidity model. The set of differential equations for the fluidity model reads the following way (here the spatial dependence is written explicitly because of the spatial derivatives):

$$\underline{\underline{\overset{\triangledown}{\sigma_P}}}(\vec{r},t) + f(\vec{r},t)\underline{\underline{\sigma_P}}(\vec{r},t) = 2G_\infty \underline{\underline{D}}(\vec{r},t), \tag{2.18}$$

$$\lambda_f \frac{D}{Dt} f(\vec{r},t) - \xi^2 \Delta f(\vec{r},t) = \frac{1}{\lambda_M(|\dot{\gamma}(\vec{r},t)|)} - f(\vec{r},t). \tag{2.19}$$

The second equation is a diffusive partial differential equation with a characteristic diffusive / fluidity timescale λ_f and a cooperativity length ξ, leading to a diffusion coefficient $D_f = \xi^2/\lambda_f$. The flow induced timescale $\lambda_M(|\dot{\gamma}|)$, which includes a shear-thinning effect, is defined by

$$\frac{1}{\lambda_M(|\dot{\gamma}|)} = \frac{1}{\lambda} + \frac{|\dot{\gamma}|}{\gamma_c}, \tag{2.20}$$

with a scalar strain-rate defined by

$$|\dot{\gamma}| := \sqrt{2 \cdot tr(\underline{\underline{D}}^2)}. \tag{2.21}$$

Note that this is still an ad-hoc expression for the relaxation time and cannot be calculated out of any basic physical assumptions.
If dealing with homogeneous simple shear flow, which means that $\kappa_{xy}(t) = \dot{\gamma}(t)$ and other entries are zero, the fluidity equation reduces to

$$\lambda_f \dot{f}(t) + f(t) = \frac{1}{\lambda} + \frac{|\dot{\gamma}(t)|}{\gamma_c}, \tag{2.22}$$

which is a simple ordinary differential equation and can be solved by the variation of constant formula:

$$f(t) = \left(f(0) - \frac{1}{\lambda}\right) e^{-t/\lambda_f} + \frac{1}{\lambda} + \int_0^t e^{-(t-t')/\lambda_f} \frac{|\dot{\gamma}(t)|}{\gamma_c \lambda_f} \mathrm{d}t'.$$

The equation for the (polymeric) stress reduces to another ordinary differential equation:

$$\dot{\sigma}_{P,xy}(t) + f(t)\sigma_{P,xy}(t) = G_\infty \dot{\gamma}(t), \tag{2.23}$$

which can also be solved by the variation of constant formula (but here it is very likely that the integral over the fluidity cannot be calculated analytically):

$$\sigma_{P,xy}(t) = \sigma_{P,xy}(0) \mathrm{e}^{-\int_0^t f(s)\mathrm{d}s} + \int_0^t \mathrm{e}^{-\int_{t'}^t f(s)\mathrm{d}s} G_\infty \dot{\gamma}(t')\mathrm{d}t'. \tag{2.24}$$

Reduction to the White Metzner Model

This fluidity model reduces to the so-called White-Metzner model by simply setting both the fluidity timescale τ_f and the cooperativity length ξ to zero, in which case the fluidity $f(\vec{r},t)$ is immediately given by

$$f(\vec{r},t) = \frac{1}{\lambda_M(|\dot{\gamma}(\vec{r},t)|)}. \tag{2.25}$$

Therefore the differential constitutive equation of the White-Metzner model is:

$$\overset{\triangledown}{\underline{\underline{\sigma_P}}}(\vec{r},t) + \frac{1}{\lambda_M(|\dot{\gamma}(\vec{r},t)|)}\underline{\underline{\sigma_P}}(\vec{r},t) = 2G_\infty \underline{\underline{D}}(\vec{r},t). \tag{2.26}$$

Note that the White-Metzner model can also be written in a variation of constant formula like style:

$$\underline{\underline{\sigma_P}}(t) = \int_0^t \left[-\partial_{t'}\underline{\underline{B}}(t,t')\right] G(t,t')\mathrm{d}t', \tag{2.27}$$

very similar to the UCM model solution given in equation 2.17, with a DE for the shear modulus $G(t,t')$. This and other connections, for example between the White-Metzner and UCM model, can be observed by explicitly taking the upper convected derivative of the integral formula 2.27 above. Therefore first calculate the partial time derivative and the effect of the advection term $\vec{v}\cdot\vec{\nabla}$ on 2.27:

$$\begin{aligned}
\partial_t\underline{\underline{\sigma_P}}(t) &= 2G_\infty\underline{\underline{D}}(t) + \int_0^t \left[-\partial_{t'}\underline{\underline{B}}(t,t')\right]\partial_t G(t,t') \; + \left[-\partial_{t'}\partial_t\underline{\underline{B}}(t,t')\right] G(t,t')\mathrm{d}t', \\
[\vec{v}\cdot\vec{\nabla}]\underline{\underline{\sigma_P}}(t) &= \int_0^t \left[-\partial_{t'}\underline{\underline{B}}(t,t')\right][\vec{v}\cdot\vec{\nabla}]G(t,t') \; + \left[-\partial_{t'}[\vec{v}\cdot\vec{\nabla}]\underline{\underline{B}}(t,t')\right] G(t,t')\mathrm{d}t'.
\end{aligned}$$

If one now calculates $\overset{\triangledown}{\underline{\underline{\sigma_P}}}$ with the use of $\overset{\triangledown}{\underline{\underline{B}}} \equiv 0$ one ends up with:

$$\overset{\triangledown}{\underline{\underline{\sigma_P}}}(t) = 2G_\infty\underline{\underline{D}}(t) + \int_0^t \left[-\partial_{t'}\underline{\underline{B}}(t,t')\right][\partial_t + \vec{v}\cdot\vec{\nabla}]G(t,t')\mathrm{d}t'. \tag{2.28}$$

One can see that the White Metzner Model is obtained if $G(t,t')$ fulfills the PDE:

$$[\partial_t + \vec{v}\cdot\vec{\nabla}]G(t,t') = -\frac{1}{\lambda_M(|\dot{\gamma}(t)|)}G(t,t'). \tag{2.29}$$

Thus one can write the White-Metzner (and the UCM) model in the spirit of an integral equation for the stress which needs "weights" $G(t,t')$ determined by a differential equation. This is due to the mathematical fact that every differential equation can be transformed into an integral equation, but of course not vice versa.

Further Reduction to the UCM Model

The reduction to the UCM Model can be done by simply letting $\gamma_c \to \infty$ such that $\lambda_M \equiv \lambda$. We see that 2.26 reduces to 2.14 and more interestingly that 2.29 reduces to:

$$[\partial_t + \vec{v}\cdot\vec{\nabla}]G(t,t') = -\frac{1}{\lambda}G(t,t'). \tag{2.30}$$

This differential equation, with initial condition $G(t,t) = G_\infty$, has a spatially homogeneous solution (exponential decay):

$$G(t,t') = G_\infty \mathrm{e}^{\frac{-(t-t')}{\lambda}},$$

which proves that 2.17 is indeed the solution to 2.14 as boldly claimed in subsection 2.2.2.

2.3 Integral Constitutive Equations

Of course one can write every differential equation into an integral equation (most times by using the variation of constant formula) but not vice versa. In mathematical terms one could say that the set of differential equation is a subset of the bigger set of integral equations. Constitutive equations that only exist in an integral formulation are often called (true) ICEs.

2.3.1 Generalized Maxwell Model

As a first example for a true ICE for $\underline{\underline{\sigma_P}}$ one could consider the generalized Maxwell model, which can be introduced as a slight modification of the White-Metzner (differential) model:

$$\underline{\underline{\sigma_P}}(t) = \int_0^t \left[-\partial_{t'}\underline{\underline{B}}(t,t')\right] G(t,t')\mathrm{d}t',$$
$$[\partial_t + \vec{v}\cdot\vec{\nabla}]G(t,t') = -\frac{1}{\lambda_M(|\dot{\gamma}(t)|)}G(t,t'),$$

by changing the time at which τ_M is evaluated in the lower equation from t to t'.
Therefore the generalized Maxwell model for the polymeric stress is given by:

$$\underline{\underline{\sigma_P}}(t) = \int_0^t \left[-\partial_{t'}\underline{\underline{B}}(t,t')\right] G(t,t')\mathrm{d}t',$$
$$[\partial_t + \vec{v}\cdot\vec{\nabla}]G(t,t') = -\frac{1}{\lambda_M(|\dot{\gamma}(t')|)}G(t,t'). \tag{2.31}$$

In contrast to the White-Metzner model (shown in 2.2.4) the generalized Maxwell model cannot be transformed into a differential equation. The reason is that if one calculates the derivative of $\underline{\underline{\sigma}}(t)$ the $\lambda_M(|\dot{\gamma}(t')|)$ term obtained from 2.31 cannot be pulled out of the integral 2.28 like in the White-Metzner (or upper convected Maxwell) model. Therefore this is a true ICE.
The generalized Maxwell Model was successfully introduced in [49] in its simple shear version where $\vec{v}\cdot\vec{\nabla} = 0$. The vanishing advection term leads to the fact that 2.31 can be homogeneously solved by:

$$G(t,t') = G_\infty e^{-(t-t')/\lambda_M(|\dot{\gamma}(t')|)},$$

resulting in the integral equation

$$\underline{\underline{\sigma_P}}(t) = G_\infty \int_0^t [-\partial_{t'}\underline{\underline{B}}(t,t')] e^{-(t-t')/\lambda_M(|\dot{\gamma}(t')|)}\mathrm{d}t'. \tag{2.32}$$

The generalized non-linear Maxwell model has been used in the past to reproduce important and central features predicted by MCT since it is able to mimic the physics of glass-forming liquids rheology [13, 43].

2.3.2 MCT-ITT Model

Within the framework of Mode-Coupling-Theory one can derive a much more complicated constitutive equation which has a microscopic "first-principles" starting point with well understood approximations, in contrast to the other more or less ad-hoc constitutive equations shown previously. This extension of (schematic) MCT to describe glass-forming liquids under shear using the integration-through-transient formalism was first introduced by Fuchs and Cates in [17] and [19]. Later refinements of their work lead to first-principles constitutive equations using MCT in [5, 7] and schematic MCT in [8].
The integration through transient (short: ITT) framework is a way of calculating non-equilibrium averages from a Green-Kubo relation of equilibrium averages.

However, the first question one should discuss is why it is appropriate to close the (Navier-) Stokes equations, that arise from Newtonian dynamics, with a constitutive equation that arises from Brownian dynamics. The underlying idea is that our Brownian MCT is already a temporal coarse-grained model. Additionally the full stress tensor should always contain a Newtonian solvent (or background) viscosity.

Further it should be mentioned that the upcoming derivation is only valid for (locally) homogeneous flow. Since in later finite elements simulations we are going to use a low order scheme the Finger tensor $\underline{\underline{B}}$ and therefore the shear is indeed constant per finite element cell and the derived equations can be used without further modification. In other word the local homogeneity per FEM node will be given.

Smoluchowski Equation

For dense colloidal particles one usually describes the system by a probability distribution function Ψ for the positions of the particles. The time evolution of the probability distribution function $\Psi(\vec{r}, t)$ is given by the Smoluchowski equation:

$$\partial_t \Psi(t) = \Omega(t)\Psi(t), \tag{2.33}$$

with $\Omega(t) = \Omega_0 + \delta\Omega(t)$ the (forward) Smoluchowski operator, here split into a stationary equilibrium operator Ω_0 and a time-dependent pertubation $\delta\Omega(t)$. Assume that there is an equilibrium solution $\Omega_0\Psi_{eq} = 0$ and that the system has been in equilibrium up to time $t = 0$ (which means that $\delta\Omega(t < 0) \equiv 0$), then one can write down a formal solution:

$$\Psi(t) = \exp_+\left(\int_0^t \Omega(t')\mathrm{d}t'\right)\Psi_{eq}, \tag{2.34}$$

with $\exp_+$ the positiv time-ordered exponential. Using the basic exponential property:

$$\exp_+(x(t)) = 1 + \int_0^t \dot{x}(t')\exp_+(x(t'))\mathrm{d}t',$$

which can be shown by taking the time derivative on both sides (one obtains the chain rule and therefore LHS and RHS have the same derivative) and plugging in $t = 0$ (one obtains the simple true statement $1 = 1$ which means that LHS and RHS are equal at $t = 0$ and therefore, because of the first property, for all t), one ends up with:

$$\Psi(t) = \Psi_{eq} + \int_0^t \Omega(t')\exp_+\left(\int_0^{t'} \Omega(t'')\mathrm{d}t''\right)\Psi_{eq}\mathrm{d}t'. \tag{2.35}$$

Now one is tempted to switch the order of the Smoluchowski operator and the ordered exponential, such that $\Omega(t') = \Omega_0 + \delta\Omega(t')$ acts first onto the equilibrium probability distribution function. However, since these two operators do not commute with each other this switch cannot be done.
First define the time evolution operator and its adjoint operator by:

$$U_{t,t'} := \exp_+\left(\int_{t'}^t \Omega(t'')\mathrm{d}t''\right), \tag{2.36}$$

$$U^\dagger_{t,t'} := \exp_-\left(\int_{t'}^t \Omega^\dagger(t'')\mathrm{d}t''\right). \tag{2.37}$$

To now work out how the Smoluchowski and time evolution operators commute with each other, it is helpful to first note that:

$$\partial_{t'''}\Omega(t'')U_{t'',t'''} = -\partial_{t''}U_{t'',t'''}\Omega(t''').$$

This leads to the following calculation:

$$\begin{aligned}\int_{t'}^{t''} \Omega(t'')U_{t'',t'''}\mathrm{d}t''' &= \Omega(t'')U_{t'',t''} - \Omega(t'')U_{t'',t'} \\ &= -\int_{t'}^{t''} \partial_{t''}U_{t'',t'''}\Omega(t''')\mathrm{d}t''' \\ &= -\partial_{t''}\int_{t'}^{t''} U_{t'',t'''}\Omega(t''')\mathrm{d}t''' + \Omega(t'')U_{t'',t''},\end{aligned}$$

and therefore:

$$\Omega(t')U_{t',0} = \partial_{t'} \int_0^{t'} U_{t',t'''}\Omega(t''')\mathrm{d}t'''. \tag{2.38}$$

Now one can see that the Smoluchowski operator $\Omega(t''')$ is right from the time evolution operator $U_{t',t'''}$ and therefore directly acts onto the equilibrium probability distribution function Ψ_{eq}.

Nonequilibrium Distribution Function

Combining the equation 2.38 with the formal solution 2.35 for the Smoluchowski equation, one obtains

$$\Psi(t) = \Psi_{eq} + \int_0^t \partial_{t'} \left[\exp_+(\int_{t'''}^{t'} \Omega(t'')) \ \Omega(t''') \right] \Psi_{eq}\mathrm{d}t'''\mathrm{d}t'.$$

By the application of the fundamental theorem of calculus, followed by renaming t''' to t' and finally switching to the adjoint operators (due to anti-distributivity $(AB)^\dagger = B^\dagger A^\dagger$ the order of the exponential also changes) one finds

$$\Psi(t) = \Psi_{eq} + \int_0^t \Omega(t')\Psi_{eq} \exp_-(\int_{t'}^t \Omega^\dagger(t'')\mathrm{d}t'')\mathrm{d}t'. \tag{2.39}$$

One can now specify the Smoluchowski operator $\Omega(t) = \Omega_0 + \delta\Omega(t)$ to be

$$\Omega_0 = \sum_i D_0 \vec{\nabla}_i \cdot (\vec{\nabla}_i - \beta \vec{F}_i), \ \delta\Omega(t) = -\sum_i D_0 \vec{\nabla}_i \cdot \underline{\underline{\kappa}}(t) \cdot \vec{r}_i \tag{2.40}$$

with the diffusion constant D_0 and the inverse thermal energy $\beta = \frac{1}{k_B T}$ set to unity. $\underline{\underline{\kappa}}(t)$ denotes the flow velocity gradient tensor, which was defined in subsection 2.2.1. Note that for the incompressible fluid flow $\underline{\underline{\kappa}}$ is traceless because of $tr(\underline{\underline{\kappa}}) \equiv \vec{\nabla} \cdot \vec{v} = 0$. With this property of the velocity gradient tensor $\underline{\underline{\kappa}}$ in mind, one is able to calculate how the pertubation operator acts onto the equilibrium probability density function:

$$\begin{aligned} \Omega(t')\Psi_{eq} = \delta\Omega(t')\Psi_{eq} &= -\sum_i \vec{\nabla}_i \cdot \underline{\underline{\kappa}}(t') \cdot \vec{r}_i \Psi_{eq} = -\sum_i \vec{F}_i \cdot \underline{\underline{\kappa}}(t') \cdot \vec{r}_i \Psi_{eq} \\ &= \underline{\underline{\kappa}}(t') : \underline{\underline{\hat{\sigma}}} \ \Psi_{eq}, \end{aligned} \tag{2.41}$$

with $\underline{\underline{A}} : \underline{\underline{B}} = \sum_{i,j} A_{ij}B_{ij}$ the contraction of tensors $\underline{\underline{A}}$ and $\underline{\underline{B}}$ and $\hat{\sigma}_{ab} = \sum_i F_i^a r_i^b$ the microscopic stress of the fluid.
This means when acting on the equilibrium distribution Ψ_{eq} the nonequilibrium Smoluchowski operator $\Omega(t')$ generates a term proportional to the stress tensor. Note that $\mathrm{tr}(\underline{\underline{\kappa}}) = 0$ was used to eliminate the first term of the product rule.
The full non-equilibrium distribution function, which is therefore given by combining the result 2.41 and equation 2.39 into

$$\Psi(t) = \Psi_{eq} + \int_0^t \left[\underline{\underline{\kappa}}(t') : \underline{\underline{\hat{\sigma}}} \right] \Psi_{eq} \exp_-(\int_{t'}^t \Omega^\dagger(t'')\mathrm{d}t'')\mathrm{d}t'. \tag{2.42}$$

Equation 2.42 is the central result of the integration through transients (ITT) formalism and will provide a very convenient starting point for analysis of the non-equilibrium dynamics of colloidal suspensions. A fundamental advantage of 2.42 over 2.35 or 2.39 is that it enables non-equilibrium averages to be expressed in terms of equilibrium averages, under the sole assumption that the system has been in equilibrium up to $t = 0$ [7].

Exact Green-Kubo Relation

The full non-equilibrium distribution function allows to calculate non-equilibrium averages $\langle ... \rangle^{neq}$ from Green-Kubo relations out of only regular equilibrium Boltzmann averages $\langle ... \rangle^{eq}$. For the non-equilibrium average of arbitrary (not necessary scalar) f one obtains

$$\langle f \rangle_t^{neq} = \langle f \rangle^{eq} + \int_0^t \langle \underline{\underline{\kappa}}(t') : \hat{\underline{\underline{\sigma}}} \ \exp_-\left(\int_{t'}^t \Omega^\dagger(t'') \mathrm{d}t'' \right) f \rangle^{eq} \mathrm{d}t', \tag{2.43}$$

which states that time development of the observable f is, thus, generated by the adjoint operator. With this equation and the assumption that in equilibrium the system is unstressed one derives the exact non-equilibrium Green-Kubo relation for the stress tensor:

$$\underline{\underline{\sigma}}(t) = \frac{1}{V} \int_0^t \langle \underline{\underline{\kappa}}(t') : \hat{\underline{\underline{\sigma}}} \ \exp_-\left(\int_{t'}^t \Omega^\dagger(t'') \mathrm{d}t'' \right) \hat{\underline{\underline{\sigma}}} \rangle^{eq} \mathrm{d}t'. \tag{2.44}$$

Unfortunately this exact generalized Green-Kubo expression for the stress tensor 2.44 requires approximation before explicit calculations can be performed.

Exact Projection

In order to be able to perform the necessary approximations to the exact generalized Green-Kubo expression for the stress tensor – given by equation 2.44 – one first needs to construct a still exact reformulation of 2.43 in which slow fluctuations are explicitly projected out. To do so one must first note (a proof is given in [7]) that

$$\langle \underline{\underline{\kappa}}(t') : \hat{\underline{\underline{\sigma}}} \ \exp_-\left(\int_{t'}^t \Omega^\dagger(t'') \mathrm{d}t'' \right) \hat{\rho}(\vec{q}) \rangle^{eq} = 0 \tag{2.45}$$

is true for all wave vectors $\vec{q}$. Remember that the Fourier transformed density $\hat{\rho}(\vec{q}, t)$ is defined – like in the first chapter – by

$$\hat{\rho}(\vec{q}) = \sum_{k=1}^{N} \mathrm{e}^{\mathrm{i}\vec{q}\cdot\vec{r}_k} / \sqrt{N}.$$

Introduce the density projection operator $\mathcal{P}$ and its orthogonal $\mathcal{Q}$ by

$$\begin{aligned} \mathcal{P} &:= \sum_{\vec{q}} \frac{|\hat{\rho}(\vec{q})\rangle^{eq} \langle \hat{\rho}^*(\vec{q})|}{S(\vec{q})}, \\ \mathcal{Q} &:= \mathrm{Id} - \mathcal{P}, \end{aligned} \tag{2.46}$$

where the normalization factor $S(\vec{q}) := \langle \hat{\rho}(\vec{q}) \hat{\rho}^*(\vec{q}) \rangle^{eq}$ is the static structure factor.
Because of 2.45 and $f = \mathcal{P}f + \mathcal{Q}f$ one can (still exact!) smuggle in a $\mathcal{Q}$ projector into 2.43, such that:

$$\langle f \rangle_t^{neq} = \langle f \rangle^{eq} + \int_0^t \langle \underline{\underline{\kappa}}(t') : \hat{\underline{\underline{\sigma}}} \ \mathcal{Q} \exp_-\left(\int_{t'}^t \Omega^\dagger(t'') \mathrm{d}t'' \right) \mathcal{Q} f \rangle^{eq} \mathrm{d}t'.$$

By using the idempotency $\mathcal{Q}^2 = \mathcal{Q}$ of the (and of course any other) projection operator one is able to smuggle in even more $\mathcal{Q}$'s (details in [7] and [61]) and obtains the following still exact formulation:

$$\langle f \rangle_t^{neq} = \langle f \rangle^{eq} + \int_0^t \langle \underline{\underline{\kappa}}(t') : \hat{\underline{\underline{\sigma}}} \ \mathcal{Q} \exp_-\left(\int_{t'}^t \mathcal{Q}\Omega^\dagger(t'') \mathcal{Q} \mathrm{d}t'' \right) \mathcal{Q} f \rangle^{eq} \mathrm{d}t'. \tag{2.47}$$

Note that the reformulation relies on the incompressibility condition $\mathrm{tr}(\underline{\underline{\kappa}}) = 0$.

MCT-like Approximation

As previously mentioned the exact Green-Kubo relation of the (polymeric) stress tensor 2.44 is not suitable to perform explicit calculations and that approximations must be made. To make these approximations it is desirable to use the also exact formulation 2.47 to obtain

$$\underline{\underline{\sigma_P}}(t) = \frac{1}{V}\int_0^t \langle \underline{\underline{\kappa}}(t') : \hat{\underline{\underline{\sigma}}}\ \mathcal{Q}\exp_-\Big(\int_{t'}^t \mathcal{Q}\Omega^\dagger(t'')\mathcal{Q}\mathrm{d}t''\Big)\mathcal{Q}\hat{\underline{\underline{\sigma}}}\rangle^{eq}\mathrm{d}t'$$

in the $\mathcal{Q}$ projected dynamics. Due to the projector $\mathcal{Q}$ the lowest non-zero order of density fluctuations must be pair-density fluctuations $\hat{\rho}(\vec{q}_1)\hat{\rho}(\vec{q}_2)$ with two distinct wave vectors. We thus define a projection operator

$$\mathcal{P}_2 = \sum_{\vec{q}_1,\vec{q}_2} |\hat{\rho}^*(\vec{q}_1)\hat{\rho}^*(\vec{q}_2)\rangle^{eq}\chi(\vec{q}_1,\vec{q}_2)\langle\hat{\rho}(\vec{q}_1)\hat{\rho}(\vec{q}_2)| \tag{2.48}$$

onto density pairs. The factors $\chi(\vec{q}_1,\vec{q}_2)$ should be designed to ensure normalization. The Green-Kubo relation projected onto pair-density fluctuations, which is no longer exact, is given by

$$\underline{\underline{\sigma_P}}(t) = \frac{1}{V}\int_0^t \langle \underline{\underline{\kappa}}(t') : \hat{\underline{\underline{\sigma}}}\ \mathcal{Q}\mathcal{P}_2\exp_-\Big(\int_{t'}^t \mathcal{Q}\Omega^\dagger(t'')\mathcal{Q}\mathrm{d}t''\Big)\mathcal{P}_2\mathcal{Q}\hat{\underline{\underline{\sigma}}}\rangle^{eq}\mathrm{d}t'. \tag{2.49}$$

One can rewrite this approximative Green-Kubo relation of the stress tensor by defining vertex functions:

$$V^{(1)}_{\vec{k}'\vec{p}'} := \frac{\underline{\underline{\kappa}}(t') : (\vec{k}'\otimes\vec{p}')}{NS(\vec{k}')S(\vec{p}')}\frac{1}{k}\frac{\mathrm{d}S(\vec{k}')}{\mathrm{d}k'}\delta_{\vec{k}',-\vec{p}'}, \tag{2.50}$$

$$V^{(2)}_{\vec{k}\vec{p}} := \frac{\vec{k}\otimes\vec{p}}{NS(\vec{k})S(\vec{p})}\frac{1}{k}\frac{\mathrm{d}S(\vec{k})}{\mathrm{d}k}\delta_{\vec{k},-\vec{p}}, \tag{2.51}$$

to the form

$$\underline{\underline{\sigma_P}}(t) = \sum_{\vec{k},\vec{p},\vec{k}',\vec{p}'}\frac{1}{V}\int_0^t V^{(1)}_{\vec{k}'\vec{p}'}V^{(2)}_{\vec{k}\vec{p}}\cdot\langle\hat{\rho}^*(\vec{k}')\hat{\rho}^*(\vec{p}')\exp_-\Big(\int_{t'}^t \mathcal{Q}\Omega^\dagger(t'')\mathcal{Q}\mathrm{d}t''\Big)\hat{\rho}(\vec{k})\hat{\rho}(\vec{p})\rangle^{eq}\mathrm{d}t'. \tag{2.52}$$

By applying an MCT-like approximation the four-point correlation function with the reduced dynamics will be replaced by a product of two-point correlation functions with the full dynamics:

$$\langle\hat{\rho}^*(\vec{k}')\hat{\rho}^*(-\vec{k}')\mathrm{e}_-^{\int_{t'}^t \mathcal{Q}\Omega^\dagger(t'')\mathcal{Q}\mathrm{d}t''}\hat{\rho}(\vec{k})\hat{\rho}(-\vec{k})\rangle^{eq} \approx \Big(\langle\hat{\rho}^*(\vec{k}')\mathrm{e}_-^{\int_{t'}^t \Omega^\dagger(t'')\mathrm{d}t''}\hat{\rho}(\vec{k})\rangle^{eq}\Big)^2. \tag{2.53}$$

By using the essential observation from [7]: $\vec{k}' = \exp_+\big(\int_{t'}^t \underline{\underline{\kappa}}(s)\big)\vec{k} =: \vec{k}(t,t')$, which means $\vec{k}'$ is the forward advected wave vector of $\vec{k}$.
One now (re-)defines the two-time transient density correlation function

$$\Phi_{\vec{k}}(t,t') := \frac{\langle\hat{\rho}^*(\vec{k}(t,t'))\mathrm{e}_-^{\int_{t'}^t \Omega^\dagger(t'')\mathrm{d}t''}\hat{\rho}(\vec{k})\rangle^{eq}}{S(\vec{k}(t,t'))}.$$

If one further remembers that the Finger tensor is given by

$$\underline{\underline{B}}(t,t') = \underline{\underline{E}}(t,t')\cdot\underline{\underline{E}}(t,t')^T$$

the full MCT-ITT forumla for the (polymeric) stress tensor simplifies to

$$\underline{\underline{\sigma_P}}(t) = \int_0^t \mathrm{d}t'\int_{\mathbb{R}^2}\mathrm{d}\vec{k}\left[-\partial_{t'}(\vec{k}\cdot\underline{\underline{B}}(t,t')\cdot\vec{k})\right]\mathcal{G}_{\vec{k}}(t,t'), \tag{2.54}$$

where for the generalized shear modulus one can see that

$$\mathcal{G}_{\vec{k}}(t,t') \propto \Phi_{\vec{k}}(t,t')^2 \tag{2.55}$$

holds true. For the full detailed version of the generalized shear modulus $\mathcal{G}_{\vec{k}}$ one might redirect to the work of Brader et al. [7] where the whole discussion of the MCT-ITT formula for the stress tensor can be found in great detail.

Schematic Version of the MCT-ITT Formula

By doing further approximations to eliminate the wavevector dependence (details in [8]) one gets the desired version of the ITT formula for the stress tensor:

$$\underline{\underline{\sigma_P}}(t) = \int_0^t \left[-\partial_{t'} \underline{\underline{B}}(t,t')\right] G(t,t') \mathrm{d}t', \tag{2.56}$$

where $\underline{\underline{B}}(t,t')$ is again the Finger tensor and $G(t,t')$ is a generalized shear modulus which relates to MCT-like dynamical density correlations. In the full MCT-ITT formula (with wave vector dependence) one observed that the wave vector dependent generalized shear modulus $\mathcal{G}_{\vec{k}}$ is proportional to the squared transient density correlation function $\Phi^2_{\vec{k}}$. Therefore it is a reasonable and commonly used choice (see [8]) to set

$$G(t,t') =: G_0 \phi^2(t,t'). \tag{2.57}$$

So the equation 2.56 is structurally identical to the (generalized) Maxwell Model, but the shear modulus $G(t,t')$ is "microscopically calculated" with the help of the sMCT instead of an exponential decay differential equation.

2.4 Analytical Observations of a Pressure Driven Channel Flow

The standard example in the field of rheology is the pressure driven channel flow:
One assumes an infinitely long rectangular channel of height h directed in the x-direction. By looking at infinitly long channels (or in a simulation: a channel of length L with periodic boundary conditions in the x direction) one does not have to worry about in- and outlet effects. In addition one only has to consider velocities in the x direction and changes (mathematically speaking non-vanishing partial derivatives) in the y direction. Further one assumes the pressure to drop linearly by Δp over each length unit L, such that $\vec{\nabla} p = \frac{\Delta p}{L} \hat{e}_x$.
This allows the Navier-Stokes equation to be reduced to the time-dependent Stokes equation:

$$\partial_t v_x = -\frac{\Delta p}{L} + \partial_y \sigma_{xy}, \tag{2.58}$$

with zero Dirichlet[8] boundary conditions

$$v_x(y = \{0, h\}, t) = 0, \tag{2.59}$$

often referred to as 'no-slip' boundary conditions.
Since $v_y \equiv 0$ and the fact that one does not have to consider any partial derivatives in the x direction, one gets the following matrix representation of the velocity gradient tensor:

$$\underline{\underline{\kappa}} = \begin{pmatrix} 0 & \partial_y v_x \\ 0 & 0 \end{pmatrix}. \tag{2.60}$$

[8] Johann Peter Gustav Lejeune Dirichlet (13 February 1805 – 5 May 1859) was a German mathematician who made contributions to number theory (including creating the field of analytic number theory), and to the theory of Fourier series and other topics in mathematical analysis.

Since this matrix is nilpotent with index 2 for all times t_1, t_2 (which means that $\underline{\underline{\kappa}}(t_1)\underline{\underline{\kappa}}(t_2) = 0$ for any two times t_1 and t_2) and the $\vec{v} \cdot \vec{\nabla}$ term vanishes in the channel flow, one can easily write down

$$\underline{\underline{E}}(t, t') = \underline{\underline{\mathrm{Id}}} + \int_{t'}^{t} \underline{\underline{\kappa}}(s)\mathrm{d}s$$

and further calculate the Finger tensor

$$\underline{\underline{B}}(t, t') = \underline{\underline{E}}(t, t')\underline{\underline{E}}(t, t')^T = \underline{\underline{\mathrm{Id}}} + \begin{pmatrix} (\int_{t'}^{t} \partial_y v_x(s)\mathrm{d}s)^2 & \int_{t'}^{t} \partial_y v_x(s)\mathrm{d}s \\ \int_{t'}^{t} \partial_y v_x(s)\mathrm{d}s & 0 \end{pmatrix}. \tag{2.61}$$

With the Maxwell-like constitutive equations shown previously one is able to close the set of equations and make at least some analytical observations in simple flow situations.

2.4.1 Steady State of the Upper Convected Maxwell Model

With the variation of constant formula for the upper convected Maxwell model (in the case of $\lambda > 0$) one obtains

$$\sigma_{xy}(y, t) = G_\infty \int_0^t \partial_y v_x(y, t')\ e^{-\frac{t-t'}{\lambda}} dt', \tag{2.62}$$

which can be plugged in into the time-dependent Stokes equation of the pressure driven channel flow to achieve the final integro-differential equation

$$\partial_t v_x = -\frac{\Delta p}{L} + G_\infty \int_0^t \partial_y^2 v_x(y, t')\ e^{-\frac{t-t'}{\lambda}} dt', \tag{2.63}$$

with the boundary condition $v_x(y = \{0, h\}, t) = 0$.

Stationary Solution

A stationary solution $v_x^{ss}(y)$ would mean that the right hand side vanishes and that one could pull the stationary velocity $v_x^{ss}(y)$ out of the integral, such that

$$\begin{aligned} \frac{\Delta p}{L} &= \partial_y^2 v_x^{ss}(y) \cdot G_\infty \int_0^\infty e^{-\frac{s}{\lambda}} ds = \partial_y^2 v_x^{ss}(y) \cdot \eta \\ \Rightarrow v_x^{ss}(y) &= \frac{\Delta p}{2L\eta} y(y - h), \end{aligned} \tag{2.64}$$

with $\eta = G_\infty \lambda$ the viscosity of the fluid.
One can easily check that this is the same profile as for a Newtonian fluid with viscosity $\eta = G_\infty \lambda$. Parabola profiles like this are often called Hagen-Poiseuille profiles in literature.
The next thing one can show is that any initial condition $v_x(y, t = 0)$ will be driven into v_x^{ss} when $t \to \infty$. To do so, one uses the Laplace transformed version of 2.63, in which the convolution is transformed to a multiplication. Furthermore one multiplies the whole equation by a factor s:

$$s^2 \hat{v}_x(y, s) - s v_x(y, 0) = -\frac{\Delta p}{L} + G_\infty \frac{1}{s + \lambda^{-1}} \cdot \partial_y^2 \hat{v}_x(y, s) s, \tag{2.65}$$

$$s \to 0,\ \Rightarrow 0 = -\frac{\Delta p}{L} + \eta \cdot \partial_y^2 v_x(y, t \to \infty),$$

$$v_x(y, t \to \infty) = \frac{\Delta p}{2L\eta} y(y - h) = v_x^{ss}(y), \tag{2.66}$$

where the final value theorem of the Laplace transformation is used to get back to real time space.

2.4.2 Stationary Solutions for the White-Metzner and generalized Maxwell Models

To calculate stationary solutions v_x^{ss} of either WMM or genMM one first needs to calculate the stationary stress tensor $\underline{\underline{\sigma}}^{ss}$. One can already guess that both models will share the same stationary stress tensor since the only difference between the two models is the time at which λ_M is taken and in the stationary regime this time dependence becomes irrelevant.

White-Metzner Model

In the steady state the partial time derivative in equation 2.26 vanishes, therefore one can reformulate it to

$$-\underline{\underline{\kappa}} \cdot \underline{\underline{\sigma}}^{ss} - \underline{\underline{\sigma}}^{ss} \cdot \underline{\underline{\kappa}}^T = G_\infty \underline{\underline{\kappa}} + G_\infty \underline{\underline{\kappa}}^T - \frac{1}{\lambda_M^{ss}(|\dot{\gamma}^{ss}|)} \underline{\underline{\sigma}}^{ss}, \tag{2.67}$$

with

$$\underline{\underline{\kappa}} = \begin{pmatrix} 0 & \dot{\gamma}^{ss} \\ 0 & 0 \end{pmatrix}.$$

Since $\underline{\underline{\kappa}}^2 = 0$, one can see and quickly check that

$$\underline{\underline{\sigma}}^{ss} = G_\infty \lambda_M^{ss}(|\dot{\gamma}^{ss}|) \left[\underline{\underline{\kappa}} + \underline{\underline{\kappa}}^T + 2\lambda_M^{ss}(|\dot{\gamma}^{ss}|) \underline{\underline{\kappa\kappa}}^T \right] \tag{2.68}$$

solves the equation above. Insert the stress tensor into the right hand side:

$$\begin{aligned} -\underline{\underline{\kappa}} \cdot \underline{\underline{\sigma}}^{ss} - \underline{\underline{\sigma}}^{ss} \cdot \underline{\underline{\kappa}}^T &= G_\infty \lambda_M^{ss}(|\dot{\gamma}^{ss}|) \left[-\underline{\underline{\kappa\kappa}} - \underline{\underline{\kappa\kappa}}^T - 2\lambda_M^{ss}(|\dot{\gamma}^{ss}|) \underline{\underline{\kappa\kappa\kappa}}^T - \underline{\underline{\kappa\kappa}}^T - \underline{\underline{\kappa}}^T \underline{\underline{\kappa}}^T - 2\lambda_M^{ss}(|\dot{\gamma}^{ss}|) \underline{\underline{\kappa\kappa}}^T \underline{\underline{\kappa}}^T \right] \\ &= G_\infty \lambda_M^{ss}(|\dot{\gamma}^{ss}|) \left[-2\underline{\underline{\kappa\kappa}}^T \right] \\ &= -G_\infty \left[2\lambda_M^{ss}(|\dot{\gamma}^{ss}|) \underline{\underline{\kappa\kappa}}^T \right] \\ &= G_\infty \underline{\underline{\kappa}} + G_\infty \underline{\underline{\kappa}}^T - \frac{1}{\lambda_M^{ss}(|\dot{\gamma}^{ss}|)} \underline{\underline{\sigma}}^{ss}. \end{aligned}$$

Generalized Maxwell Model

First one assumes that the system is in the steady state since forever, such that the lower integral limit can be set to $-\infty$. Further one knows that in the channel geometry the deformation gradient tensor is given by

$$\underline{\underline{E}}(t, t') = \underline{\underline{\mathrm{Id}}} + \underline{\underline{\kappa}}(t - t')$$

for a stationary velocity gradient $\underline{\underline{\kappa}}$. This leads to

$$\begin{aligned} \underline{\underline{B}}(t, t') = \underline{\underline{E_{tt'}}} \cdot \underline{\underline{E_{tt'}}}^T &= \underline{\underline{\mathrm{Id}}} + \left[\underline{\underline{\kappa}} + \underline{\underline{\kappa}}^T \right] (t - t') + \underline{\underline{\kappa\kappa}}^T (t - t')^2 \\ -\partial_{t'} \underline{\underline{B}}(t, t') &= \underline{\underline{\kappa}} + \underline{\underline{\kappa}}^T + 2\underline{\underline{\kappa\kappa}}^T (t - t'), \end{aligned} \tag{2.69}$$

which one can plug into 2.32 with the integral starting from $-\infty$. By setting $t - t' = s$ and with the use of the integral

$$\int_0^\infty s e^{-s/\lambda} ds = \lambda,$$

one obtains

$$\underline{\underline{\sigma}}^{ss} = G_\infty \int_0^\infty \left[\underline{\underline{\kappa}} + \underline{\underline{\kappa}}^T + 2\underline{\underline{\kappa\kappa}}^T s \right] e^{-s/\lambda_M^{ss}} ds = G_\infty \lambda_M^{ss}(|\dot{\gamma}^{ss}|) \left[\underline{\underline{\kappa}} + \underline{\underline{\kappa}}^T + 2\underline{\underline{\kappa\kappa}}^T \right], \tag{2.70}$$

which is the exact same stationary stress tensor as for the WMM.

Stationary Velocity Profile

Since the (mathematical) intuitive statement that the WMM and genMM are stationary identical is now proved by having explicitly calculated both, one can further calculate the stationary velocity profile from the (Navier-) Stokes equation. Again all calculations are restricted to no-slip boundary conditions $v_x(y = \{0, h\}, t) = 0$.
In order to physically model a polymer melt or colloidal suspension one often adds a Newtonian viscosity part to the stress tensor (called solvent part of the stress tensor).

$$\underline{\underline{\sigma}} = \underline{\underline{\sigma_P}} + \underline{\underline{\sigma_S}}$$

This corresponds to the idea that the viscoelastic material (a polymer melt for example) is diluted in a Newtonian / viscous solvent with viscosity $\eta_S = G_\infty \lambda_S$. Correspondingly we replace the structural relaxation time λ of the polymeric part by $\lambda_P = \eta_P / G_\infty$. This leads to the Navier-Stokes x-equation

$$\frac{\Delta p}{L} = \partial_y \left(\left[\eta_S + G_\infty \lambda_M (|\dot{\gamma}^{ss}|) \right] \dot{\gamma}^{ss} \right). \tag{2.71}$$

Integrating both side with respect to y and writing out all the terms leads to

$$\frac{\Delta p}{L} \cdot (y - \frac{h}{2}) = \left[\eta_S + \frac{\eta_P}{1 + \frac{\lambda_P}{\gamma_c} |\partial_y v_x^{ss}(y)|} \right] \partial_y v_x^{ss}(y)$$

which one only needs to solve for $0 < y < \frac{h}{2}$ where $\partial_y v_x^{ss}(y) > 0$. The other half is then known by its symmetry property around the middle axes $y = \frac{h}{2}$.
Without the loss of generality one can set some constants to unity to fix scales, for example $h = 1$ to fix the length scale, $\lambda_S = 1$ to fix the time scale and $G_\infty = 1$ to fix the pressure scale. Further one defines $d := \frac{y - \frac{h}{2}}{h}$, $\hat{\gamma_c} := \frac{L}{\Delta p} \gamma_c$ and sets $\partial_y v_x^{ss} =: \frac{\Delta p}{L} u'$, such that the integrated NSE reduces to

$$d = \left[1 + \frac{\lambda_P}{1 + \frac{\lambda_P}{\hat{\gamma_c}} u'} \right] u' \tag{2.72}$$

in the region $-\frac{1}{2} \leq d \leq 0$ where u' is non-negative. This equation leads to a quadratic equation (multiply by $1 + \frac{\lambda_P}{\hat{\gamma_c}} u'$) in u' which is solved by two solutions. The physically reasonable solution is the one that obeys $u'(d = 0) = 0$, because the velocity profile should have its maximum in the middle of the channel (by symmetry reasons). Therefore one has

$$u' = -\frac{\hat{\gamma_c}}{2} \left[\left(\frac{d}{\hat{\gamma_c}} + \frac{1 + \lambda_P}{\lambda_P} \right) - \sqrt{\left(\frac{d}{\hat{\gamma_c}} + \frac{1 + \lambda_P}{\lambda_P} \right)^2 + \frac{4}{\hat{\gamma_c} \lambda_P} d} \right] \tag{2.73}$$

in the lower half of the channel (d is negative or zero).
Now one needs to integrate this and fit the integration constant to the no-slip Dirichlet boundary condition $u(d = -\frac{1}{2}) = 0$. Since this integration (especially the second term with the $\sqrt{\ldots}$) is very tedious details are left out.
Further define $t = \frac{\lambda_P - 1}{\lambda_P}$ and $s^2 = \frac{4}{\lambda_P}$ to obtain

$$\begin{aligned} \hat{u}(d) = -\frac{d^2}{4} - \frac{1 + \lambda_P}{\lambda_P} \frac{\hat{\gamma_c}}{2} d - \frac{\hat{\gamma_c}^2}{4} \left(t + \frac{d}{\hat{\gamma_c}} \right) \sqrt{\left(t + \frac{d}{\hat{\gamma_c}} \right)^2 + s^2} \\ - \frac{\hat{\gamma_c}^2 s^2}{4} \ln \left(\sqrt{\left(t + \frac{d}{\hat{\gamma_c}} \right)^2 + s^2} + \left(t + \frac{d}{\hat{\gamma_c}} \right) \right) \end{aligned} \tag{2.74}$$

for the indefinite integral of u'. To now fulfill the no-slip boundary condition one needs to set

$$u(d) = \hat{u}(d) - \hat{u}(d = -\frac{1}{2}) \tag{2.75}$$

for the lower half of the channel and the mirror-symmetrical (around $d = 0$) continuation for the upper half of the channel.

The glassy solution

In the glassy limit one considers $\lambda_P \to \infty$ and therefore $t \to 1$ and $s^2 \to 0$, such that

$$\hat{u}(d) \xrightarrow{\lambda_P \to \infty} -\frac{\hat{\gamma_c}^2}{4}\left[\frac{1}{\hat{\gamma_c}^2}d^2 + \frac{2}{\hat{\gamma_c}}d - (1 + \frac{d}{\hat{\gamma_c}})|1 + \frac{d}{\hat{\gamma_c}}|\right]. \tag{2.76}$$

One can now separate this into two different regimes $|d| > \hat{\gamma_c}$, called "outer regime" and $|d| < \hat{\gamma_c}$, called "inner regime".
For the "outer regime" one finds (note that all calculations are done for the lower part of the channel where $d < 0$)

$$\hat{u}(d) \xrightarrow{\lambda_P \to \infty} \frac{\hat{\gamma_c}^2}{4}\left[1 - 2(1 + \frac{d}{\hat{\gamma_c}})^2\right] \tag{2.77}$$

which means that in the 'outer regime' one receives a parabolic shaped velocity profile.
However for the "inner regime" one obtains

$$\hat{u}(d) \xrightarrow{\lambda_P \to \infty} \frac{\hat{\gamma_c}^2}{4} \tag{2.78}$$

which means that in the "inner regime" the velocity is constant. This yields to the observation that a velocity-plug is expressed.
Further one recognizes that $|\frac{d}{\hat{\gamma_c}}| > 1$ takes the role of a yield criterion, where $|\frac{d}{\hat{\gamma_c}}| = 1$ defines a so called yield surface. Viscoelastic fluids that have a non vanishing yield stress are often called viscoelastoplastic fluids. Note that in $\hat{\gamma_c} = \frac{L}{\Delta p}\gamma_c$ the pressure difference plays a major role, such that if the pressure difference Δp is to small $\hat{\gamma_c}$ gets to big to fulfill the yield criterion anywhere inside the channel, resulting in no flow at all.

2.5 Residual Stresses from a Simple Shear Experiment, analytical Observations

Another analytically solvable situation is the simple shear flow through an infinitely long rectangular channel. Like the pressure driven channel flow the system is quasi one dimensional ($\vec{v}(\vec{r}, t) = \vec{v}(y, t)$). Here, instead of a pressure gradient, the movement of the fluid is induced by a "moving upper wall" in the infinitely long channel, which precisely means that the boundary conditions are changed to $\vec{v}(y = h) = v_0\hat{\vec{e}}_x$ and $\vec{v}(y = 0) = 0$. Since there is no pressure gradient the (non-trivial part of the) Navier-Stokes equation reduces to

$$\partial_t v_x = \partial_y \sigma_{xy}, \tag{2.79}$$

which immediately implies that the shear stress σ_{xy} must be a constant in the steady state.
The question now is whether this constant is zero or if there is a remaining shear stress (so-called residual stress) after flow cessation. The experiment is to stop the upper wall at given time (commonly one sets this to $t = 0$) and see weather the stress relaxes to zero or if a residual stress remains. Since

the system is dissipative one can assume that the velocity relaxes to zero when the energy supply by the moving upper boundary is set to zero.
Experimental work on glass-forming and viscoelastoplastic fluids have found residual stresses $\underline{\underline{\sigma}}^{res}$ that show three main features [1]:

(1) partial relaxation of $\underline{\underline{\sigma}}^{res}$ from the steady state stress $\underline{\underline{\sigma}}^{ss}$,

(2) $\underline{\underline{\sigma}} = \underline{\underline{\sigma}}^{res} \neq 0$ for $t \to \infty$,

(3) the residual stress $\underline{\underline{\sigma}}^{res}$ depends on the deformation history.

To be able to make analytical predictions one further simplifies the whole setup by directly setting $\partial_y v_x(y,t) = \dot{\gamma}(t)$. This assumption corresponds to a infinitely thin channel, such that the shear rate $\dot{\gamma}$ and therefore the velocity $\vec{v}(y)$ die down to zero immediately at $t = 0$. This means that one can assume the shear rate to be a step function:

$$\dot{\gamma}(t) = \dot{\gamma} \cdot \theta(-t). \tag{2.80}$$

2.5.1 White-Metzner Model

For the White-Metzner model in the infinitely long channel one has to solve the ordinary differential equation

$$\dot{\sigma}_{xy}(t) + \frac{1}{\lambda_M(t)}\sigma_{xy}(t) = G_\infty \dot{\gamma}(t).$$

Note that for $t > 0$ the right hand side vanishes and that $\frac{1}{\lambda_M(t)} = \frac{1}{\lambda}$, reducing the equation to a standard exponential decay differential equation:

$$\dot{\sigma}_{xy}(t) + \frac{1}{\lambda}\sigma_{xy}(t) = 0, \tag{2.81}$$

which leads to $\sigma_{xy}(t \to \infty) = 0$ for finite relaxation time λ.
However in the glassy limit in which $\frac{1}{\lambda}$ vanishes and the equation reduces to $\dot{\sigma}_{xy}(t > 0) = 0$ the solution must be constant $\sigma_{xy}(t \to \infty) = \sigma_{xy}(0)$.
The constant $\sigma_{xy}(0)$ can be calculated with the variation of constant formula:

$$\sigma_{xy}(0) = G_\infty \dot{\gamma} \int_{-\infty}^{0} \exp(\frac{\dot{\gamma} t'}{\gamma_c}) \mathrm{d}t' = G_\infty \gamma_c. \tag{2.82}$$

This indicates that in the glassy limit $\frac{1}{\lambda} \to 0$ the White-Metzner model forms "trivial" residual stresses, which are not history dependent. Therefore the White-Metzner model does not predict feature (1) and (3) correctly.

2.5.2 Generalized Maxwell Model

In this simplified one dimensional setup the generalized or nonlinear Maxwell model is, in contrast to the differential equation of the previous White-Metzner model, given by the integral equation

$$\sigma_{xy}(t) = G_\infty \int_{-\infty}^{t} \dot{\gamma}(t') \exp(\frac{-(t-t')}{\lambda_M(|\dot{\gamma}(t')|)}) \mathrm{d}t'.$$

If one now plugs in $\dot{\gamma}(t) = \dot{\gamma} \cdot \theta(-t)$, the integral is cut off at $t' = 0$:

$$\begin{aligned} \sigma_{xy}(t > 0) &= G_\infty \dot{\gamma} \int_{-\infty}^{0} \exp(\frac{-(t-t')}{\lambda_M(|\dot{\gamma}|)}) \mathrm{d}t' \\ &= G_\infty \dot{\gamma} \lambda_M(|\dot{\gamma}|) \exp(-\frac{t}{\lambda_M(|\dot{\gamma}|)}), \end{aligned} \tag{2.83}$$

which implies that $\sigma_{xy}(t \to \infty) \to 0$, regardless of the structural relaxation time λ. So in contrast to the White-Metzner model the generalized Maxwell model does not form any residual stresses in the glassy limit $\frac{1}{\lambda} \to 0$. Obviously features (2) and (3) are not correctly predicted by the generalized Maxwell model.

2.5.3 MCT-ITT Model

Analytical observations in terms of a analytical calculation of the one dimensional stress integral

$$\sigma(t > 0) = G_0 \dot{\gamma} \int_{-\infty}^{0} \phi^2(t, t') \mathrm{d}t' \tag{2.84}$$

for the MCT-ITT model are not possible. However, numerical calculations of exactly this integral, where $\phi(t, t')$ is given by the schematic two-time MCT under time-dependent shear, do show non-trivial residual stresses [1]. The MCT-ITT model is the only model that fulfills (1), (2) and (3).

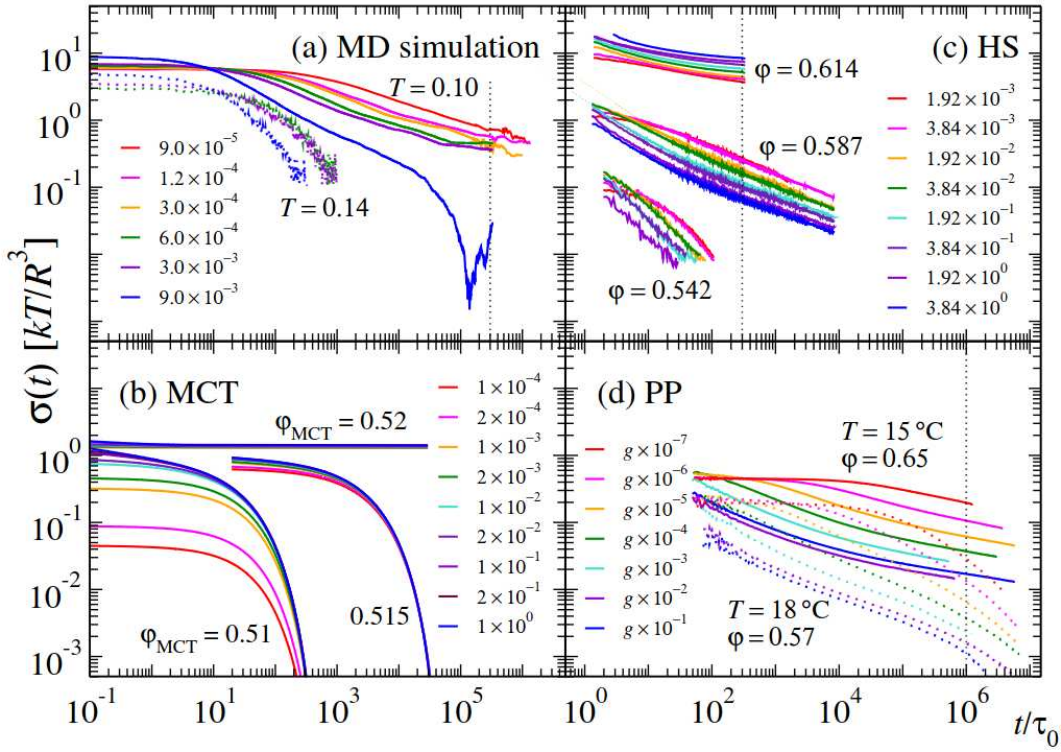

Figure 2.3: Stress decay $\sigma(t)$ after cessation of steady shear, for various strain-rates $\dot{\gamma}$ (increasing from red to blue) and control parameters, as labeled. (a) MD simulation: $T = 0.14$ in the liquid, $T = 0.1$ in the glass. (b) Isotropic hard-sphere model of ITT-MCT, packing fraction $\varphi_{\mathrm{MCT}} = 0.51$, 0.515(liquid), and 0.52(glass). (c) HS colloidal suspension: $\varphi = 0.542$, 0.587 (liquid), and 0.614 (glass). (d) PS-PNIPAM particles: $T = 18$C ($\varphi \approx 0.57$, liquid, $\dot{\gamma}$ as labeled, with $g = 3.4$) and $T = 15$C ($\varphi \approx 0.65$, glass, $g = 4.0$). Figure from Ref. [1].

Chapter 3

Theory of the Finite Element Method and FEniCS

This chapter provides a general introduction of the finite element method (FEM) and of the FEniCS environment to create such finite elements (FE) simulations for the numerical approximation of (systems of) partial differential equations in the Python3 programming language. For a better understanding first a brief general introduction into the mathematical theory – including also weak derivatives and Sobolev[1] spaces from the theory of partial differential equations – and technical aspects of the finite element method is given.

3.1 FEM Basics

This section is written to shortly cover the basics of the finite elements method, a simulation technique to numerically solve (simulate) partial differential equations. For a more in-depth discussion of the mathematical principles of the finite element method the reader is referred to the excellent literature [10, 33] for the mathematical aspects, [38] for technical aspects and [15] explicitly for flow problems.

3.1.1 Concept of Weak Derivatives and Sobolev Spaces

The finite element method does not aim to numerically solve the partial differtial equation directly, instead it numerically solves the weak formulation of the problem and delivers an approximation of the so-called weak solution.
To get a first idea of the concept of weak solutions consider the Poisson[2] problem

$$\begin{aligned} -\Delta u &= f \quad in\ \Omega, \\ u &= u_D \quad on\ \delta\Omega, \end{aligned}$$

where Ω is any open (real) subspace of $\mathbb{R}^d$ and $\delta\Omega$ the boundary of this subspace. The equations above require that $u \in C^2(\Omega)$ if $f \in C^0(\Omega)$ is given. Recall that by definition $C^n(\Omega)$ is the space of functions living on Ω which have continuous (partial) derivatives up to order n, therefore C^0 or C is the space of continuous functions. If one multiplies the first equation of the Poisson problem with any so-called test-function $\varphi \in C_0^\infty(\Omega)$ (here the lower index 0 indicates that the functions φ vanish at the boundary $\delta\Omega$) and integrates over the whole space Ω – using the integration by parts formula – to obtain

$$\int_\Omega (\nabla u) \cdot (\nabla v) \mathrm{d}x = \int_\Omega f v \mathrm{d}x, \quad \forall \varphi \in C_0^\infty(\Omega). \tag{3.1}$$

[1] Sergei Lvovich Sobolev (6 October 1908 – 3 January 1989) was a Soviet mathematician working in mathematical analysis and partial differential equations.

[2] Siméon Denis Poisson (21 June 1781 – 25 April 1840) was a French mathematician and physicist.

Because φ vanishes at the boundary $\delta\Omega$ there is no boundary term on the left hand side. We note that this equation does not require u to be at least two times differentiable, it only requires u to be "weakly differentiable" once and the integral to exist. First one needs to the define what a weak derivative is: One calls a function v the α-th (with $\alpha = (\alpha_1, ..., \alpha_d)$ and $|\alpha| = \alpha_1 + ... + \alpha_d$) weak derivative of function u if

$$\int_\Omega u\varphi^{(\alpha)} \mathrm{d}x = (-1)^{|\alpha|} \int_\Omega v\varphi \mathrm{d}x, \quad \forall \varphi \in C_0^\infty(\Omega)$$

holds true for all test-functions. One often denotes the α-th weak derivative by $v = D^\alpha u$, in contrast to the normal (or strong) derivative $u^{(\alpha)}$.
The concept of a weak derivative is obviously an extension to the normal derivative, since the equation above holds by the integration by parts formula if v is the normal derivative $u^{(\alpha)}$ of the function u. Also if two functions v, w are weak derivatives of the same function u, they must be equal (up to a set of points with measure zero). Therefore the weak derivative is unique.
The two conditions given above (u is once weakly differentiable and all integrals do exist) are fulfilled by functions in a space that the mathematicans call the Sobolev space $H^1(\Omega)$, which is defined as

$$H^1(\Omega) := \{u : \Omega \to \mathbb{R} \mid D^\alpha u \in L^2(\Omega), \ \forall \ |\alpha| \leq 1\}.$$

The integral equation 3.1 is called the weak formulation of the Poisson problem. Finally note that every solution of the differentiable problem automatically is also a solution of the weak formulation but not vice versa. We call the solution of the weak formulation the weak solution of the PDE. For a detailed mathematical introduction to weak derivatives, Sobolev spaces and weak solutions the reader is referred to the classic literature on partial differetial equation by L.C. Evans [16].

3.1.2 Idea of Trial- and Test-function Space and their Approximations

The main idea of the finite element method is to approximate the exact solution by a linear combination of basis functions, historically called "trial-functions" ("Ansatzfunktionen" or "Ritz-Ansätze" by the swiss mathematican Ritz[3]). To numerically approximate or solve the weak problem one needs to define a trial-function space $V = \{u \in H^1(\Omega) | u = u_D \ on \ \delta\Omega\}$ and a test-function space $\hat{V} = \{v \in H^1(\Omega) | v = 0 \ on \ \delta\Omega\}$ and approximate these to do numerical simulations.
The need for further approximations is needed because the function space H^1 is a space of infinite dimension and therefore one would need to numerically solve an infinite amount of equations for the basis coefficients, which is obviously not possible. Therefore one needs to approximate the infinite spaces V and $\hat{V}$ by finite function spaces V_h and $\hat{V}_h$ on which one can calculate an approximative solution $u_h \in V_h$ to the weak problem by numerically solving only a finite amount of equations. To understand the basic idea it might be helpful to visit a very simple example in one dimension first.

Linear Polynomials in 1D, Hatfunctions

In one dimension the connected set Ω must be an interval. Without loss of generality one can set this interval to $I = [0, L]$ which can be divided into n sub-intervals $I_i = [x_{i-1}, x_i]$, such that $x_0 = 0$ is the start of I and $x_n = L$ is the end of I. In 1D one often does this in an equidistant way, but this is not necessary for FEM. On each sub-interval one now defines the space of continuous piecewise linear polynomials which is called P1 (or CG1 for continuous Galerkin of order 1):

$$P_1(I_i) := \{p(x) = c_0 + c_1 x, \ x \in I_i\}. \tag{3.2}$$

[3]Walther Heinrich Wilhelm Ritz (22 February 1878 – 7 July 1909) was a Swiss mathematican and theoretical physicist.

With this space of linear functions one can define finite-dimensional trial- and test-function spaces V_h and $\hat{V}_h$ on the whole grid such that every function v out of these spaces is in $P_1(I_i)$ if v is restricted to I_i. Therefore:

$$V_h = \{v \in C(I), v|_{I_i} \in P_1(I_i) \ \wedge \text{b.c.}\}, \tag{3.3}$$

$$\hat{V}_h = \{v \in C(I), v|_{I_i} \in P_1(I_i) \ \wedge \ v(0) = v(L) = 0\}, \tag{3.4}$$

where b.c. means that v fulfills the given boundary conditions of the problem.

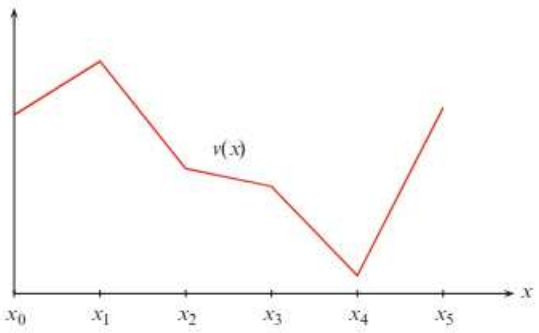

Figure 3.1: A continuous piecewise linear function v. Figure from Ref. [33].

To design a FEM simulation one must be able to convert the weak problem (which arises from the PDE) into a system of algebraic equations (not necessary linear). To do so one needs a finite dimensional basis of these function spaces to set up equations. Obviously every function out of these spaces V_h and $\hat{V}_h$ is uniquely determined by its nodal values $v(x_i)$ (with $i = 0, 1, ..., n$). This implies that for every set of nodal values $\{a_i; i = 0, 1, .., n\}$ there is only one v which shares these nodal values, so it is an obvious choice to set

$$\varphi_i(x) = \begin{cases} (x - x_{i-1})/(x_i - x_{i-1}), & x \in (x_{i-1}, x_i) \\ (x_{i+1} - x)/(x_{i+1} - x_i), & x \in [x_i, x_{i+1}) \\ 0, & \text{else} \end{cases} \tag{3.5}$$

and call these set of basis functions $\{\varphi_i\}$ the nodal basis. Since these functions look like hats (see figure below) one often calls them hat functions.

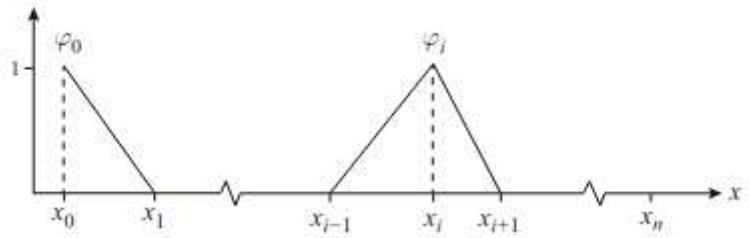

Figure 3.2: Nodal basis in 1D, also called hat functions. Figure from Ref. [33].

For a given continuous function f on the interval I its continuous piecewise linear approximation (πf) is easily calculated as:

$$(\pi f)(x) = \sum_i f(x_i)\varphi_i(x).$$

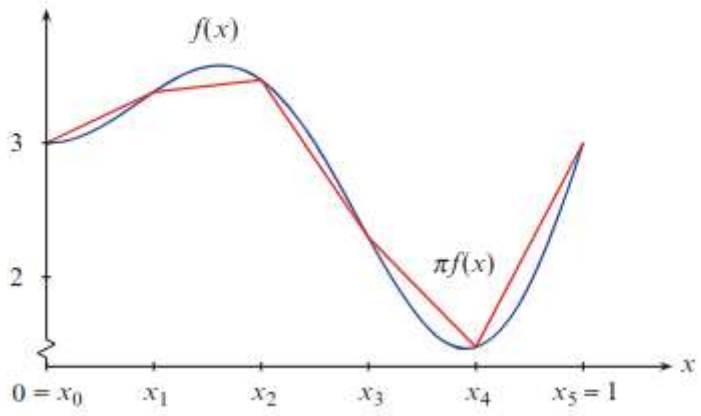

Figure 3.3: Approximation (πf) of $f(x) = 2x\sin(2\pi x) + 3$ over $[0,1]$ on a uniform mesh/grid with 6 nodes x_i ($i = 0, 1, ...5$). Figure from Ref. [33].

Minimal Example in 1D

Consider the Poisson problem in 1D with zero Dirichlet boundary condition over the unit interval $[0,1]$:

$$\begin{aligned} -u'' &= f \quad in\ (0,1), \\ u &= 0 \quad on\ \{0,1\}. \end{aligned}$$

For simplicity one might choose an equidistant grid / mesh $0 = x_0 < .. < x_i = i/n < ... < x_n = 1$ and set $h = 1/n$. From above one knows that the weak formulation of this problem is given by

$$\int_0^1 u'v' \mathrm{d}x = \int_0^1 fv \mathrm{d}x.$$

Now u and v should be constructed as a linear combination of hat functions, for example

$$\begin{aligned} u(x) &= \sum_{i=0}^{n} \mu_i \varphi_i(x), \\ v(x) &= \sum_{j=0}^{n} \nu_j \varphi_j(x), \end{aligned}$$

because of the zero Dirichlet boundary condition $V_h = \hat{V}_h$ and therefore also $\varphi_i = \hat{\varphi}_i$. Further one could define the coefficient vectors $\mu = (\mu_i)_{i=0}^n$ and $\nu = (\nu_j)_{j=0}^n$ to simplify further writing. Since

$$\varphi_i'(x) = \begin{cases} 1/h, & x \in (x_{i-1}, x_i) \\ -1/h, & x \in [x_i, x_{i+1}) \\ 0, & \text{else} \end{cases}$$

the weak formulation from above reduces to

$$\begin{aligned} \sum_{i,j} \mu_i \nu_j \underbrace{\int_0^1 \varphi_i' \varphi_j' \mathrm{d}x}_{=:A_{ij}} &= \sum_j \nu_j \underbrace{\int_0^1 f \varphi_j' \mathrm{d}x}_{=:b_j}, \\ \sum_{i,j} \mu_i \nu_j A_{ij} &= \sum_j \nu_j b_j, \\ \nu^T A \mu &= \nu^T b. \end{aligned}$$

This is equivalent to the system of linear equations

$$A\mu = b. \tag{3.6}$$

Because A is a symmetric and positive-definite matrix one knows from textbook linear algebra that A is invertible (A^{-1} exists). Therefore one can find a unique solution vector $\mu(= A^{-1}b)$ of the system of linear equations, which leads to a unique (approximative) solution $u_h = \sum_i \mu_i \varphi_i \in V_h$.
From calculating the integrals in the definition of the (later called: stiffness-) matrix A one finds that:

$$A_{ij} = \int_0^1 \varphi_i' \varphi_j' \mathrm{d}x = \frac{1}{h} \begin{bmatrix} 2 & -1 & & & \\ -1 & 2 & -1 & & \\ & -1 & 2 & -1 & \\ & \ddots & \ddots & \ddots & \\ & & -1 & 2 & -1 \\ & & & -1 & 2 \end{bmatrix}$$

which is (up to factor $-h$) the well-known first order finite difference approximation of the second derivative. The generalization of this procedure is called the standard Galerkin[4] method and will be discussed in the next subsection.

3.1.3 Standard Galerkin Method

The standard Galerkin method converts a continuous operator problem, such as a differential equation (commonly in weak formulation like here in the finite element method), to a discrete algebraic problem by applying linear constraints determined by finite sets of basis functions. Suppose that infinite trial- and test-function spaces V and $\hat{V}$ are already successfully reduced to finite-dimensional approximations V_h and $\hat{V}_h$, for example consisting out of continuous piecewise linear functions, with (nodal) basis $\{\varphi_i\}_{i=1}^{n_{Nodes}}$ and $\{\hat{\varphi}_i\}_{i=1}^{n_{Nodes}}$. One can calculate a system of algebraic equations for the basis coefficients which leads to an approximative solution of the weak problem.
It is important to note that even if the PDE itself is nonlinear it is sufficient to use the basis functions $\hat{\varphi}_i$ as test-functions. This can be seen at the very beginning of creating the weak problem from the PDE: one multiplies with v and therefore the whole equation is linear in v. Consider for example, the nonlinear part of the Navier-Stokes-Equation:

$$(u \cdot \nabla)u = f$$
$$\int [(u \cdot \nabla)u] v dx - \int f v dx = 0$$

where the second equation is obviously linear in v.

Linear problems

If the PDE is linear, one arrives at a weak problem of the form:

$$a(u, v) = L(v), \ \forall v \in \hat{V} \tag{3.7}$$

with a bilinear form a and a linear form L. In the case of the Poisson problem one is able to identify $a(u, v) = \int (\nabla u) \cdot (\nabla v) \mathrm{d}x$ and $L(v) = \int f v \mathrm{d}x$. Since $a(\cdot, -)$ is a bilinear form it is sufficient to calculate the 'stiffness matrix' $A_{ij} = a(\varphi_i, \hat{\varphi}_j)$ and the 'load vector' $b_j = L(\hat{\varphi}_j)$ and solve the linear equation

$$A\mu = b \tag{3.8}$$

[4]Boris Grigoryevich Galerkin (4 March [O.S. 20 February] 1871–12 July 1945) was a Soviet mathematician and engineer.

to obtain the approximative solution

$$u_h(x) = \sum_i \mu_i \varphi_i(x). \tag{3.9}$$

The existence of a solution $u \in V$ to the problem 3.7 is guaranteed – under the assumption that a is a continuous coercive bilinear form and L a continuous linear functional – by the Lax-Milgramm theorem [10, 33].

Nonlinear problems

For nonlinear problems equation 3.7 changes to

$$F(u, v) = 0 \tag{3.10}$$

with F only linear in the second argument (as discussed previously). Due to this linearity in the second argument one ends up with the nonlinear system of equations

$$F(\sum_j \mu_j \varphi_j, \varphi_i) = 0 \quad \forall i = 1, ..., n_{Nodes} \tag{3.11}$$

for our degrees of freedom or (unknown coefficients) μ_j.
This nonlinear system of equations then needs to be plugged into a non-linear solver, for example using Newton's method (mathematical details on the Newton method can be found in [52]). However the existence or even uniqueness of a solution u_h can not be guaranteed and is an open research topic for mathematicians.

3.1.4 Finite Elements in 2D

In the above discussion in one dimension, one was able to easily construct a discrete subspace $V_h \subset V$ of the infinite-dimensional function spaces. However, in two (or even more) dimensions this is no longer that straightforward, because it is no longer trivial how to divide Ω (which was just an interval in the one dimensional case) into smaller sets K on which one could afterwards define finite-dimensional basis functions. A central aspect of the finite element method is the construction of such subspaces by patching together local function spaces defined by a set of finite elements.

Triangulation

The first step one needs to do is to decompose our subspace Ω into a set $\mathcal{K} = \{K\}$ (also very often called $\mathcal{T}_h$) of open cells K (simplices) such that

1. $\overline{\Omega} = \cup_{K \in \mathcal{K}} \overline{K}$,
2. any nonempty intersection between two different cells K_i, K_j is either a vertex, an edge or a face of both cells.

If both of these conditions are fulfilled the mathematical literature [10, 33, 38] defines $\mathcal{K}$ to be a valid triangulation.
In practice the whole decomposition of space is usually called the "mesh". In 2D (which is the only case covered in this work) this is mainly done with triangles (therefore this process is often called triangulation), but could also be done by squares. In 3D one uses prisms, pyramids or tetrahedrons. If one restricts the triangulation conditions to only triangles in two dimensions the second condition could also be reformulated to

2. no vertex of any triangle lies in the interior of an edge of another.

With this condition one can directly tell that the left decomposition in the figure below is a valid triangulation while the right one is not.

Figure 3.4: Two subdivisions: the one on the left is a valid triangulation and the one on the right is not because of the hanging node in the center. Figure from Ref. [10].

As a full two dimensional example a channel is shown with right orientated diagonals (default in FEniCS) and crossed diagonals (better to keep certain symmetries, for example in the channel flow)

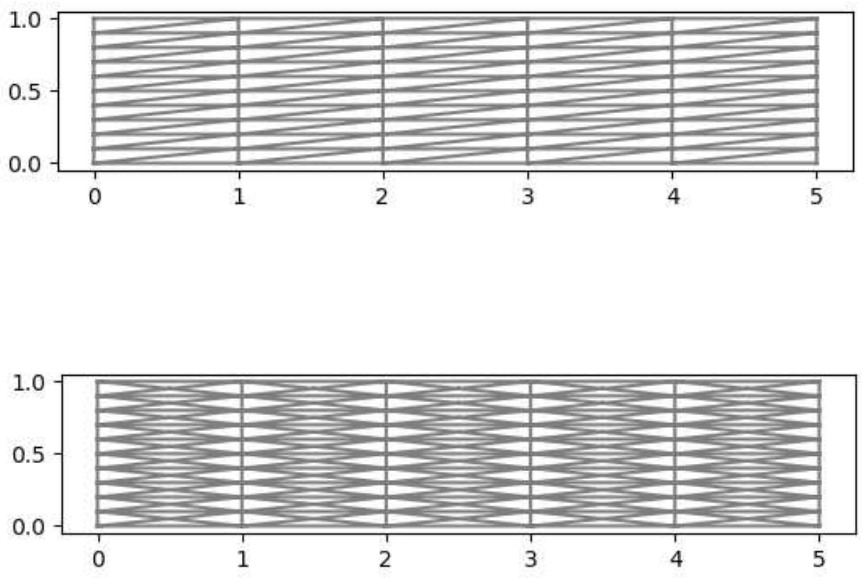

Figure 3.5: Decomposition (or mesh) of a channel with right (default) and crossed diagonals.

In the mesh creation (or triangulation) of Ω lies one of the major advantages of the FEM over other method such as finite differences or Lattice Boltzmann, because it is much more flexible in terms of overall simulation geometry but also in terms of refinement towards for example a certain edge as shown in the figure below.

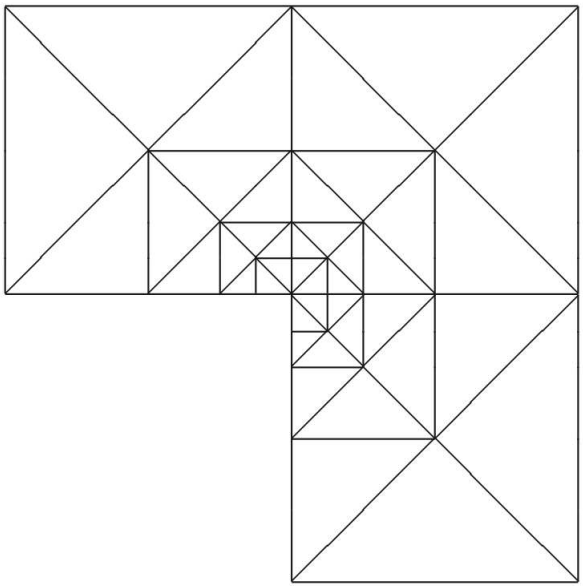

Figure 3.6: Refinement towards the recessed edge in the center. Figure from Ref. [9].

On the open cells K from a valid triangulation one can now define finite-dimensional function spaces which will be used as trial- and test-function spaces. To keep it simple and fitting to this thesis we will only look into polynomials with degree less or equal to $n \in \mathbb{N}$ living on these cells K that are defined in the following way:

$$P_n(K) := \{p(x) = \sum_{|\alpha| \leq n} c_\alpha x^\alpha,\ x \in K\}. \tag{3.12}$$

The Finite Element

Similar to the one dimensional case, discussed earlier, one can look at the space of continuous piecewise linear functions in two spatial dimensions. Previously we have discussed how to decompose our 2D space, on which we want to solve a PDE, into triangles K. A linear function on a triangle K is defined by:

$$p_1^K(x, y) = c_{(0,0)} + c_{(1,0)}x + c_{(0,1)}y,\ (x, y) \in K.$$

There are three coefficients ($R = 3$) that need to be fixed by three equations, consequently one could use the three edges of the triangle to fix values. For comparison, a constant element would only need one value (usually the center of mass of the triangle) and a quadratic element would need six values (usually the three edges and the three midpoints of the sides).
Let us first consider K to be the elementary triangle with edges $N_1^K = (0, 0)$, $N_2^K = (1, 0)$ and $N_3^K = (0, 1)$ (do not confuse with the multi-indices above) from the figure below.

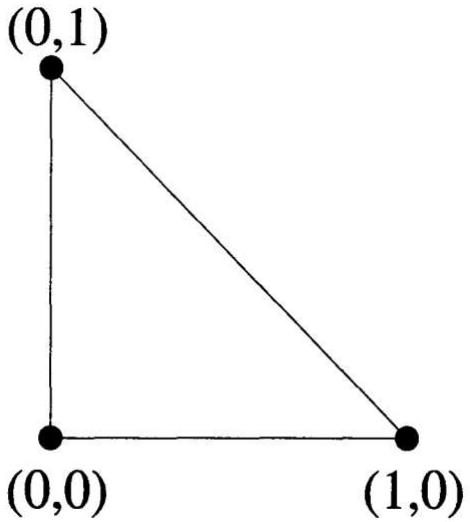

Figure 3.7: Elementary triangle with edges $N_1^K = (0,0)$, $N_2^K = (1,0)$ and $N_3^K = (0,1)$. Figure from Ref. [10].

The local basis functions $\{\varphi_i^K\}_{i=1}^3$ corresponding to a linear element need to fulfill $\varphi_i^K(N_j^K) = \delta_{ij}$, hence

$$\varphi_1^K(x,y) = 1 - x - y,$$
$$\varphi_2^K(x,y) = x,$$
$$\varphi_3^K(x,y) = y.$$

$\{\varphi_i^K\}_{i=1}^3$ are sufficient to write every linear function on the elementary triangle K as a linear combination of these basis functions: $p_1 = \sum_{i=1}^3 l_i\varphi_i$. The triple $(K, P_1(K), \{l_i\})$ consisting of the cell K, the finite dimensional function space (the "Ansatzfunktionen") $P_1(K)$ (linear polynomials on K) and the degrees of freedom $\{l_i\}$ which is a basis of its dual space $P_1(K)'$ is what is called a "finite element". The properties of this example on the elementary triangle can be generalized to the definition (for example [38] or [10]) that one says, if

1. the domain K is a bounded, closed subset of $\mathbb{R}^d$ with nonempty interior and piecewise smooth boundary,
2. the space of "Ansatzfunktionen" $\mathcal{V}$ is a finite dimensional function space on K of dimension n,
3. the set of degrees of freedom (nodes) $\mathcal{L} = \{l_1, ..., l_{n_K}\}$ is a basis for the dual space $\mathcal{V}'$,

are fulfilled, then $(K, \mathcal{V}, \mathcal{L})$ is a finite element.

Hatfunctions in 2D

Again very similar to the one dimensional case one can construct a linear global nodal basis $\{\varphi_i\}_{i=1}^{n_{Nodes}}$ with $\varphi_i(N_j) = \delta_{ij}$ and $V_h = \text{span}\{\varphi_i | i = 1, ..., n_{Nodes}\}$, where N_j denotes the j-th node of the mesh. This construction leads to the two dimensional hat functions shown in the figure below.

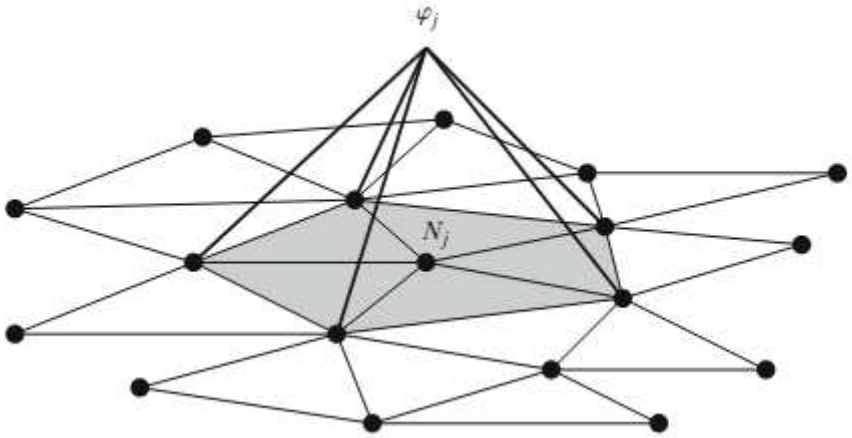

Figure 3.8: 2D hat function φ_j on a general triangle mesh. Figure from Ref. [33].

Assembly of the Stiffness Matrix and Load Vector

For the sake of simplicity the discussion of the assembly is restricted to the case of zero Dirichlet boundary conditions, such that one does not need to distinguish between V_h and $\hat{V}_h$ or their (global nodal) basis functions given by $\{\varphi_i\}_{i=1}^{n_{Nodes}}$ (for example the 2D hat functions from figure 3.8). The local basis functions on triangle K should be given by $\{\varphi_i^K\}_{i=1}^{R}$, with R the number of the local degrees of freedom (for example $R = 3$ in the the case of the linear hat functions in figure 3.8).
Goal of the finite element method when applied to linear PDEs is to be able to calculate a numerical solution $u_h = \sum_i \mu_i \varphi_i$ by solving a system of linear equations

$$A\mu = b$$

with a stiffness matrix A and a load vector b. The organization of the calculation of the stiffness matrix A and the load vector b is what is called the "assembly". The assembly process can be done in the following way:

- Let the total number of triangles be given by n_T such that there exist a global numeration of the triangles $K_1, K_2, ..., K_{n_T}$. The local nodes of triangle K_l should be numerated by $N_1^{K_l}, ..., N_R^{K_l}$. Further give all the nodes (for the whole mesh) a global numeration $N_1, N_2, ..., N_{n_{Nodes}}$ which corresponds to the numeration of the global nodal basis $\{\varphi_i\}_{i=1}^{n_{Nodes}}$.

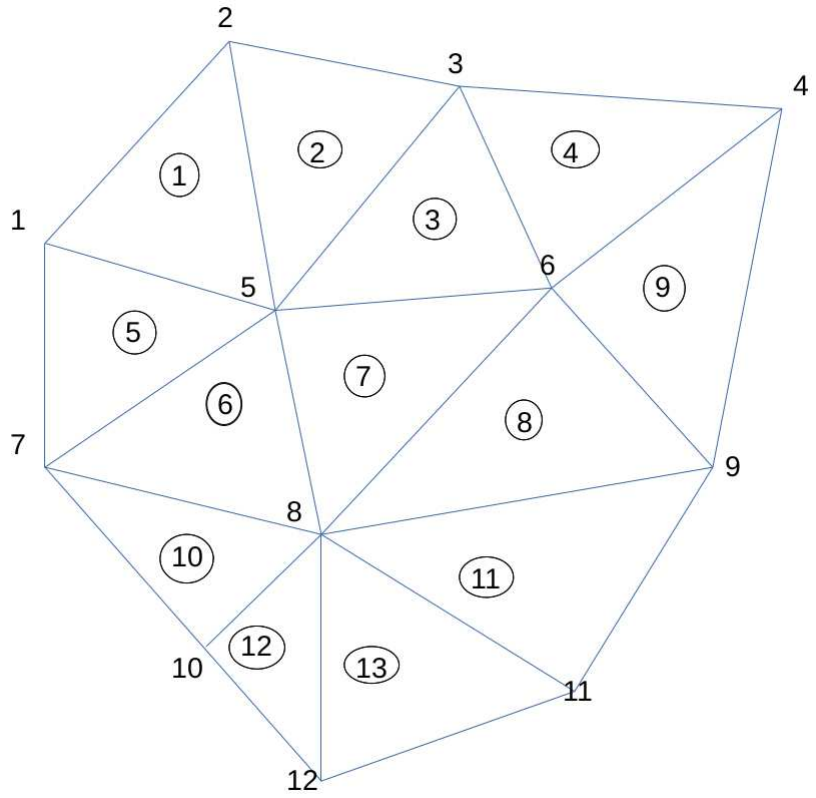

Figure 3.9: Triangle 8 has nodes (or edges) (9,6,8).

- Define a local to global mapping by: $i^l(r)$ is the global number of the node which has the local number $N_r^{K_l}$ in triangle K_l. Then for $i = i^l(r)$

$$\varphi_i\big|_{K_l} = \varphi_r^{K_l}$$

holds true for all $l = 1, ..., n_T$ and all $r = 1, ..., R$.

- Algorithm to assemble the stiffness matrix A (for the Poisson equation example):

$A_{ij} = 0$;
for $l = 1, ..., n_T$ **do** (Loop over all n_T triangles.)
for $r, s = 1, ..., R$ **do** (Loop over the local degrees of freedom.)
$A_{rs}^{K_l} \leftarrow a(\varphi_r^{K_l}, \varphi_s^{K_l})$; (= $\int_{K_l} \nabla\varphi_r^{K_l} \cdot \nabla\varphi_s^{K_l} \mathrm{d}x$ in the Poisson equation example.)
$i \leftarrow i^l(r)$;
$j \leftarrow i^l(s)$;
$A_{ij} \leftarrow A_{ij} + A_{rs}^{K_l}$;
end for
end for

- Assembly of the load vector can be done in similar fashion.

Remarks concerning the generalization of the assembly process:

1. Note that the assembly process for A and b from above covers only linear PDEs. However, in the nonlinear case one needs to solve a set of nonlinear equations

$$F(u_h, \varphi_i) = 0, \ \forall i = 1, ..., n_{Nodes}$$

in order to optain a numerical approximation u_h of the nonlinear PDE. Still the assembly process for a set of nonlinear equations works very similar also using the local to global mapping $i^l(r)$ to set up the set of equations.

2. If one does not have zero Dirichlet boundary conditions one needs to distinguish between V_h and $\hat{V}_h$ and use $\hat{\varphi}_i$ as the second argument to assemble the stiffness matrix A and also for the load vector b.

3.1.5 Discontinuous Galerkin Method

This final subsection is written to briefly present some very basic aspects of the discontinuous Galerkin (DG) method, which will be used later on in our simulations. This method is based on finite element spaces that consist of discontinuous piecewise polynomials defined on a partition of the computational domain.

Motivation

The DG method generalizes the FEM by eliminating continuity constraints and providing the tools to handle potential jumps via numerical fluxes. In this respect it transfers a classical advantage of the finite volume methods to a finite element approach. Hence, it provides additional flexibility in designing the shape functions that are discontinuous, and means to stabilize discontinuities or steep gradient regions. DG methods are inherently local requiring less communication between neighbouring mesh cells. This facilitates the enforcement of local mass conservation (i.e., per mesh cell).

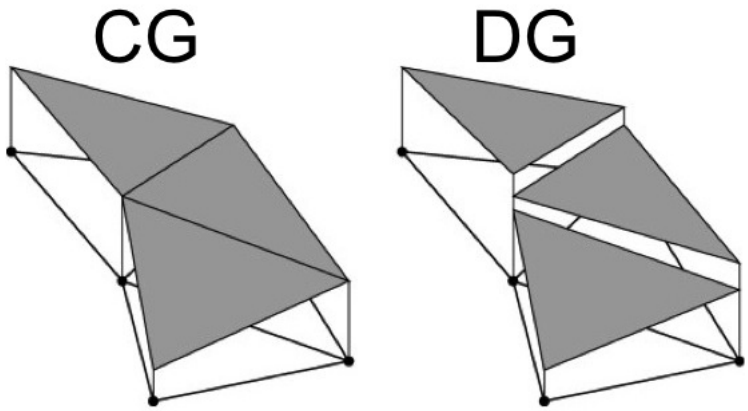

Figure 3.10: Visualization of the difference between CG and DG methods. DG allows steps, while CG methods are constraint on continuity.

Basic Definitions

In contrast to the previously defined V_h the condition that the functions $v \in V_h$ are continuous ($v \in C(\Omega)$ or better $V_h \subset C(\Omega)$) will be dropped (or better: reduced to being square integrable). Therefore let $\mathcal{K} = \{K\}$ be a mesh of our domain Ω and define the trial-function space of discontinuous piecewise polynomial functions with degree less or equal to $n \in \mathbb{N}$ by

$$V_h = \{v \in L^2(\Omega), v|_K \in P_n(K), \ \forall K \in \mathcal{K} \ \wedge \ b.c.\}. \tag{3.13}$$

Thus, the functions $v \in V_h$ are polynomials (up to degree n) on each element K, but (can be) discontinuous across the element boundaries ∂K. Let $\mathcal{E}_I$ denote the set of interior edges and with each interior edge $\mathcal{E}$ we associate a fixed unit normal vector n. We denote by $K^{\pm}$ the element for which $\pm n$ is the exterior normal. Accordingly we define

$$v^{\pm} := \lim_{\epsilon \to 0^+} v(x \pm \epsilon n).$$

For edges on the boundary $\partial\Omega$ we let n be the exterior unit normal vector. Further, we define the "jump" $[v]$ and the "average" $\langle v \rangle$ of a function v by

$$[v] := v^+ - v^-,$$
$$\langle v \rangle := \frac{v^+ + v^-}{2},$$

and note that the following identity

$$[uv] = [u]\langle v \rangle + \langle u \rangle [v] \tag{3.14}$$

can be quickly be proven by multiplying out the right-hand side.

Example Problem: Transport Equation

In 1973 Reed and Hill first introduced a DG method to solve the hyperbolic neutron transport equation [46], here also a hyperbolic transport equation will be used as an example. We consider the following problem modeling convection and reaction: given a divergence-free vector field $b(x)$ find u such that

$$u + b \cdot \nabla u = f \quad in\ \Omega, \tag{3.15}$$
$$u = g \quad on\ \partial\Omega_-, \tag{3.16}$$

where

$$\partial\Omega_- := \{x \in \partial\Omega; n(x) \cdot b(x) < 0\} \tag{3.17}$$

is the so-called "inflow part" of the boundary. Further we define the "outflow part" of the boundary by $\partial\Omega_+ := \partial\Omega \setminus \partial\Omega_-$.

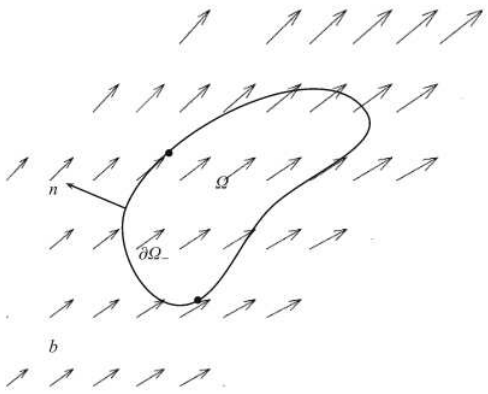

Figure 3.11: "inflow part" $\partial\Omega_-$, where $n \cdot b < 0$. Figure from Ref.[33]

The first step to derive a DG method is – similar to the standard CG method – to multiply the equation with a test-function $v \in V_h$ and perform integration by parts. This time we need to perform

the integration by parts on element-wise (for each $K \in \mathcal{K}$) because of the discontinuities. This procedure gives us

$$
\begin{aligned}
(f, v) &= \sum_{K \in \mathcal{K}} (u + b \cdot \nabla u, v)_K && (3.18)\\
&= \sum_{K \in \mathcal{K}} (u, v)_K - (u, b \cdot \nabla v)_K + (n \cdot bu, v)_{\partial K} \\
&= \sum_{K \in \mathcal{K}} (u, v)_K - (u, b \cdot \nabla v)_K && (3.19)\\
&\quad + \sum_{E \in \mathcal{E}_I} (n \cdot bu, [v])_E + (n \cdot bg, v)_{\partial\Omega_-} + (n \cdot bu, v)_{\partial\Omega_+}
\end{aligned}
$$

where we have used the inflow boundary condition and $\nabla \cdot b \equiv 0$ (divergence free). With $(.,-)$ we denote the L^2 scalar product (integration of the product over the given set). In order to make use of this form for $u \in V_h$ we replace u by $\langle u \rangle + \gamma[u]$, where γ is a jump parameter on interior edges. Choosing $\gamma = \text{sign}(n \cdot b)/2$ leads to the traditional DG method for first order problems where

$$
\langle u \rangle + \gamma[u] = \begin{cases} u^+, & \text{if } n \cdot b > 0 \\ u^-, & \text{if } n \cdot b < 0 \end{cases} \tag{3.20}
$$

is precisely the upstream value at the face.
Using element-wise integration by parts, together with the identity 3.14, we end up with

$$
\begin{aligned}
(f, v) - (n \cdot bg, v)_{\partial\Omega_-} &= \sum_{K \in \mathcal{K}} (u, v)_K + (b \cdot \nabla u, v)_K && (3.21)\\
&\quad - \sum_{E \in \mathcal{E}_I} (n \cdot b[u], \langle v \rangle)_E + (\gamma n \cdot b[u], [v])_E - (n \cdot bu, v)_{\partial\Omega_-}.
\end{aligned}
$$

From the right-hand side of 3.21 we can define the bilinear form $a(u, v)$ ("stiffness") and from the left-hand side of 3.21 we define the linear form $l(v)$ ("load"). Now we may formulate the following discontinuous Galerkin (DG) method: find $u_h \in V_h$ such that

$$
a(u_h, v) = l(v), \quad \forall v \in V_h. \tag{3.22}
$$

From now on we can solve this similar to the CG method.

3.2 Introduction to the FEniCS Software

This section is meant to be a very short introduction to the FEniCS software in the Python3 programming language. We will only discuss the absolute minimum to understand how a finite element method simulation is structured in FEniCS. Therefore we will revise the simple Poisson problem.

3.2.1 Poisson Problem in FEniCS

The material covered in this subsection can be found in great detail in the FEniCS Tutorial book [32], which is highly recommend as a practical starting point to learn how to implement numerical simulations of partial differential equations – such as the Poisson equation – with the finite element method in the FEniCS environment of the Python3 programming language.
Recall that the weak formulation of the Poisson problem

$$
\begin{aligned}
-\Delta u &= f \quad \text{in } \Omega, \\
u &= u_D \quad \text{on } \delta\Omega,
\end{aligned}
$$

is given by

$$\int_\Omega (\nabla u) \cdot (\nabla v) dx = \int_\Omega f v dx, \quad \forall \varphi \in C_0^\infty(\Omega). \tag{3.23}$$

For the sake of simplicity let $\Omega = [0,1]^2$ and manufacture some exact solution $u_e(x,y)$ by calculating f and setting $u_D = u_e$. Here we choose $u_e(x,y) = 1 + x^2 + 2y^2$, by taking the $-\Delta$ of u_e we get $f(x,y) = -6$. Now we want to solve this Poisson problem to get a numerical solution u that can be compared to the exact solution $u_e \equiv u_D$.
Now we need to do the following step to perform a FEM simulation in Python using the FEniCS software[5]:

1. import FEniCS and Numpy (for further calculations):

```
from fenics import *
import numpy as np
```

2. define / load the mesh and function space approximation (for example piecewise linear polynomials P_1):

```
# Create mesh and define function space
mesh = UnitSquareMesh(8, 8)
V = FunctionSpace(mesh, 'P', 1)
```

3. Implement the boundary conditions (here: Dirichlet boundary conditions):

```
# Define boundary condition
u_D = Expression('1+x[0]*x[0]+2*x[1]*x[1]', degree=2)
# Define the boundary itself
def boundary(x, on_boundary):
return on_boundary
# Dirichlet boundary conditions
bc = DirichletBC(V, u_D, boundary)
```

4. Define the trial- and test-function spaces, FEniCS takes care of constructing the basis functions:

```
# Define trial- and test-function spaces
u = TrialFunction(V)
v = TestFunction(V)
f = Constant(-6.0)
a = dot(grad(u), grad(v))*dx
L = f*v*dx
```

5. Implement the weak formulation of the problem you want to solve. FEniCS takes care of the assembly process:

```
# Define the weak problem
f = Constant(-6.0)
a = dot(grad(u), grad(v))*dx
L = f*v*dx
# Assembly system
A, b_vec = assemble_system(a, L, bc)
```

[5] code can be found on `https://jorgensd.github.io/dolfinx-tutorial/` and in the FEniCS Tutorial Book [32]

6. Use a FEniCS solver for example by LU decomposition (mathematcial details on the LU decomposition can be found in [52]) or Newton's method to solve the algebraic equations FEniCS has set up in the background:

```
# Solve system
u = Function(V)
solve(A, u, b_vec)
```

7. Plot and save obtained simulation data:

```
# Plot solution and mesh
plot(u)
plot(mesh)

# Save solution to file in VTK format
vtkfile = File('poisson/solution.pvd')
vtkfile << u
```

8. Compute errors (only possible since the analytic solution is known!):

```
# Compute error in L2 norm
error_L2 = errornorm(u_D, u, 'L2')

# Compute maximum error at vertices
vertex_values_u_D = u_D.compute_vertex_values(mesh)
vertex_values_u = u.compute_vertex_values(mesh)
error_max = np.max(np.abs(vertex_values_u_D - vertex_values_u))

# Print errors
print('error_L2  =', error_L2)
print('error_max =', error_max)
```

Since the analytical solution is known, one is able to calculates two types of errors: the L^2-norm error and the maximal error of a degree of freedom.
The widely used L^2-norm error is given by

$$E_{L^2} = \left(\int_\Omega (u - u_e)^2 dx \right)^{\frac{1}{2}}, \tag{3.24}$$

while the maximal error of a degree of freedom is

$$E_{max} = \max(|u(N_j) - u_e(N_j)|; N_j \in \text{mesh}).$$

A note on the Accuracy of Integration

An excellent explanation of integration accuracy can be given by a direct citation from [32]:
As seen before, FEniCS expressions must be defined using a particular degree. The degree tells FEniCS into which local finite element space the expression should be interpolated when performing local computations (integration). As an illustration, consider the computation of the integral $\int_0^1 \cos(x)\mathrm{d}x = \sin(1)$. This may be computed in FEniCS by

```
mesh = UnitIntervalMesh(1)
I = assemble(Expression('cos(x[0])', degree=degree)*dx(domain=mesh))
```

Note that one must here specify the argument domain=mesh to the measure dx. This is normally not necessary when defining forms in FEniCS but is necessary here since cos(x[0]) is not associated with any domain (as is the case when we integrate a function from some function space defined on some mesh).
FEniCS also allows expressions to be expressed directly as part of a form. This requires the creation of a 'SpatialCoordinate'. In this case, the accuracy is dictated by the accuracy of the integration, which may be controlled by a degree argument to the integration measure dx. The degree argument specifies that the integration should be exact for polynomials of that degree.
The following code snippet shows how to compute the integral $\int_0^1 \cos(x)\mathrm{d}x = \sin(1)$ using this approach:

```
mesh = UnitIntervalMesh(1)
x = SpatialCoordinate(mesh)
I = assemble(cos(x[0])*dx(degree=degree))
```

Varying the degree between 0 and 5, the value of $|\sin(1) - \mathrm{I}|$ is 0.036, 0.036, 0.00020, 0.00020, $4.3E-07$, $4.3E-07$. Note that the quadrature degrees are only available for odd degrees so that degree 0 will use the same quadrature rule as degree 1, degree 2 will give the same quadrature rule as degree 3 and so on.

3.2.2 Stationary Stokes Flow Problem of a shear-thinning Fluid

Highly inspired by the article of Tunc et al. [55] we want to look at stationary flow first. While Tunc et al. have implemented the Oldroyd-B Model, which is the UCM Model plus a Newtonian term for the stress tensor, we will "upgrade" the UCM Model to the shear-thinning White Metzner Model. In the computational fluid dynamics community it is very common to denote the relaxation time with λ instead of τ, while τ is sometimes used for the polymeric (UCM or other) part of the stress tensor.

Set of Partial Differential Equations

We want to solve the conservation laws for a homogeneous incompressible fluid under isothermal steady-state conditions (often called Stokes equation):

$$\begin{aligned} \nabla \cdot \vec{v} &= 0, \\ -\nabla p + \nabla \cdot \underline{\underline{\sigma}} &= 0. \end{aligned}$$

As mentioned before the stress tensor should be a superposition of a Newtonian solvent and a White-Metzner Fluid, such that:

$$\begin{aligned} \underline{\underline{\sigma}} &= 2\eta_S \underline{\underline{D}} + \underline{\underline{\sigma_P}}, \\ \overset{\triangledown}{\underline{\underline{\sigma_P}}} + \frac{1}{\lambda_M(|\dot{\gamma}|)} \underline{\underline{\sigma_P}} &= 2G_\infty \underline{\underline{D}}. \end{aligned}$$

Here η_S is the Newtonian solvent viscosity and $G_\infty \lambda_M =: \eta_P$ is the polymeric viscosity. Note that under steady-state conditions the upper convected derivative changes to $[\vec{v} \cdot \nabla] * - \kappa * - * \kappa^T$ because ∂_t vanishes.

Weak forms

Since the FEM does not use the PDE itself but its weak formulation we need to define test-functions $\hat{p}, \hat{\vec{v}}, \underline{\underline{\hat{\sigma}_P}}$ corresponding to the unknown $p, \vec{v}, \underline{\underline{\sigma_P}}$. The weak formulations are obtained by multiplying these test-functions to the corresponding equations above and performing integration by parts. When

we denote the domain on which the problem is defined by Ω and its boundary by $\partial\Omega$ the weak equations that we are going to solve are given by

$$\int_\Omega (\nabla \cdot \vec{v})\hat{p} dV = 0, \tag{3.25}$$

$$-\int_\Omega p(\nabla \cdot \hat{\vec{v}})dV + \int_\Omega (2\eta_S \underline{\underline{D}} + \underline{\underline{\sigma_P}}) : \nabla\hat{\vec{v}} dV - \int_{\partial\Omega} (\underline{\underline{T}} \cdot \vec{n}) \cdot \hat{\vec{v}} dA = 0, \tag{3.26}$$

$$\int_\Omega \Big[\underline{\underline{\sigma_P}} + \lambda_M(|\dot{\gamma}|)([\vec{v}\cdot\nabla]\underline{\underline{\sigma_P}} - \underline{\underline{\kappa}}\cdot\underline{\underline{\sigma_P}} - \underline{\underline{\sigma_P}}\cdot\underline{\underline{\kappa}}^T) - 2\mu_p(|\dot{\gamma}|)\underline{\underline{D}}\Big] : \underline{\underline{\hat{\sigma}_P}} dV = 0. \tag{3.27}$$

Note that $\cdot$ denotes the contraction over one index (scalar product or matrix multiplication) and is implemented in FEniCS using "dot", while : denotes the contraction over both indices ($A : B \equiv \sum_i \sum_j A_{ij}B_{ij}$) and is implemented in FEniCS using "inner". (If there is just one index "dot" and "inner" are identical.) With $\vec{n}$ the outer normal unit vector to the boundary $\partial\Omega$ is denoted.

Approximation of Trial- and Testfunctions

To perform a FEM simulation in FEniCS we must specify trial- and test-function spaces. For the mesh (specified later) we use – as always – triangular elements, the functions on the triangular elements are approximated by so called Taylor-Hood (P2 P1) elements which means

- 'CG2' (continuous polynomials of degree two) elements for the velocity $\vec{v}$ (in FEniCS language: "VectorElement('CG', triangle, 2)"),
- 'CG1' (continuous polynomials of degree one) elements for the pressure p (in FEniCS language: "FiniteElement('CG', triangle, 1)"),
- 'CG1' (continuous polynomials of degree one) elements for the stress $\underline{\underline{\sigma_P}}$ (in FEniCS language: "TensorElement('CG', triangle, 1)").

The test-functions $\hat{p}, \hat{\vec{v}}, \underline{\underline{\hat{\sigma}_P}}$ are chosen to coincide with the corresponding basis of the trial-functions (see Standard Galerkin Method).

Mesh

After all equations are implemented we now need to specify the area / domain on which our system of equations (incompressible Stokes equation plus stationary White Metzner model) should be solved, further we need to define boundary conditions.
The areas / geometries on which the simulations take place should be:

- a simple channel,

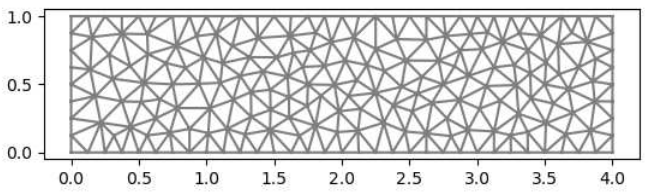

- a channel with a sphere as an obstacle (very common CFD example in the applied mathematics community, "classical TU Dortmund benchmark example"),

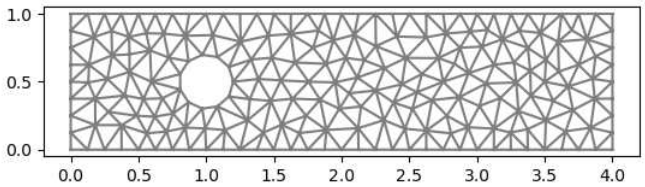

- the so called "4:1 contraction" (very common CFD example in the rheology community).

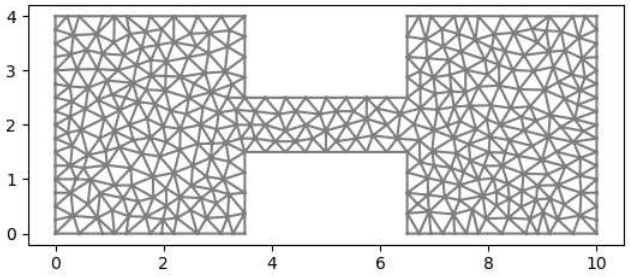

All of these geometries can be created using the "mshr" extension to FEniCS using a superposition of predefined commands such as "Rectangle(point1, point2)" and "Circle(point, radius, number of edges)". The mesh is created by using the "generate_mesh(domain, cells across its diameter)" function of the mshr extension, where in these examples above we used 15 cells across the channel width (diameter) to see the mesh, in simulations these meshs will be much finer. "mshr" and many other meshing tools also allow local refinements of the mesh in areas where higher spatial precision is needed. This flexibility is one of the major benefits of the FE Method over LB Method or finite differences (FD) Method.
For the boundary conditions we use "no-slip" conditions which mean that $\vec{v}(\vec{x}) \equiv 0$ for $\vec{x} \in wall$. In addition we want to have a pressure drop of Δp between the inflow (left) and outflow (right) resulting in $\nabla p = \frac{\Delta p}{L}\vec{e}_x$.

Numerical Results for $\lambda = 1$

Let us look at the numerical results of this Stokes problem for solvent viscosity $\eta_S = 1$, pressure scale $G_\infty = 1$ and structural relaxation time $\lambda = 1$ for the channel flow, channel flow with spherical obstacle and the 4:1 contraction, all driven by a pressure gradient $\frac{\Delta p}{L} = 1$. The critical strain parameter γ_c is set to 0.1 (= 10%) For all simulations 64 elements across the diameter of the simulation area are used. To visualize the numerical results we use the FEniCS build-in plot function to show the magnitude of the velocity $|\vec{v}|$, the xy component of the total stress tensor σ_{xy} and the first normal stress difference $N_1 = \sigma_{xx} - \sigma_{yy}$.

Channel without obstacle

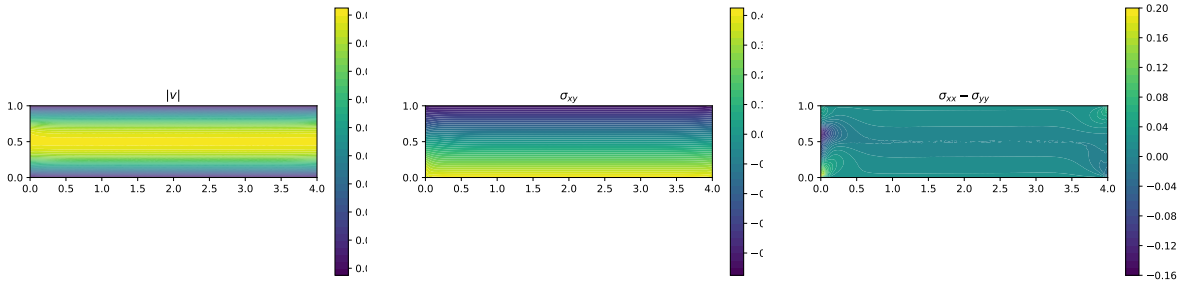

Figure 3.12: FEM Simulation result $|\vec{v}|$, σ_{xy} and N_1 of the Stokes problem for a White-Metzner model fluid with $\lambda = 1$ in a simple rectangular channel.

Channel with a spherical obstacle

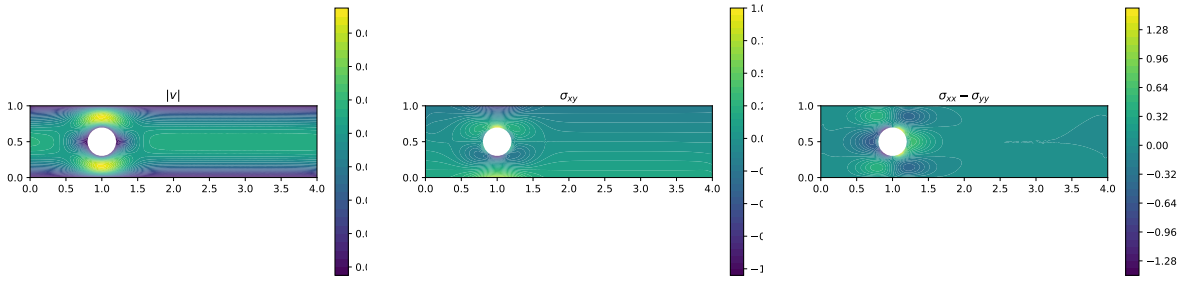

Figure 3.13: FEM Simulation result $|\vec{v}|$, σ_{xy} and N_1 of a Stokes flow past a spherical obstacle in a rectangular channel for a White-Metzner Model fluid with $\lambda = 1$..

4:1 Contraction

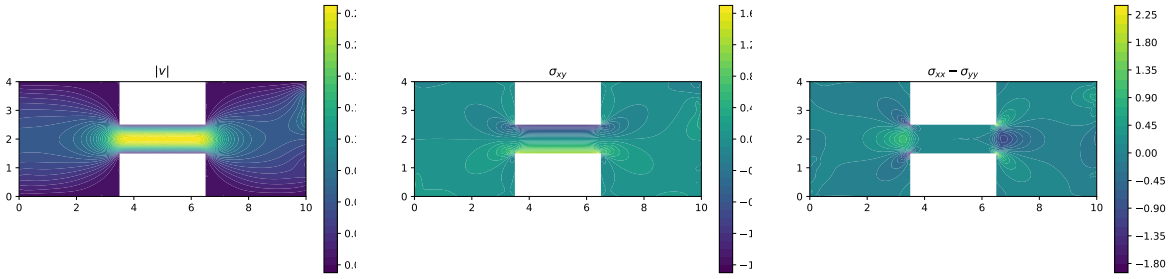

Figure 3.14: FEM Simulation result $|\vec{v}|$, σ_{xy} and N_1 of the Stokes problem for a White-Metzner Model fluid with $\lambda = 1$ in 4:1 contraction / extension channel.

Chapter 4

FEM Simulation of non-Newtonian Fluid Flow

Having now discussed the basic principles of FEM simulations, we can use these concepts to numerically solve non-Newtonian flow problems for the previously introduced integral constitutive equations (ICE), especially the ITT-MCT but also the generalized Maxwell constitutive equations. This leads to large memory demands to store the entire deformation history. The large memory demand poses a major computational challenge and asks for a discretization strategy focused on economical use of degrees of freedom. To this end, we propose a low-order discontinuous Galerkin scheme, which additionally respects the physical conservation laws inherent in incompressible fluid flow problems. It is worth mentioning that (Brownian) MCT is a microscopic theory based on stochastic equation of motions. All the atomic interactions between particles are encoded in the Smoluchowski operator. Using a FEM simulation to determine of the the macroscopic quantities, especially the Finger-Tensor, provides a link between the microscopic first-principle MCT and the macroscopic flow geometry. These simulations open new fields of application and promise a better understanding of non-Newtonian effects.

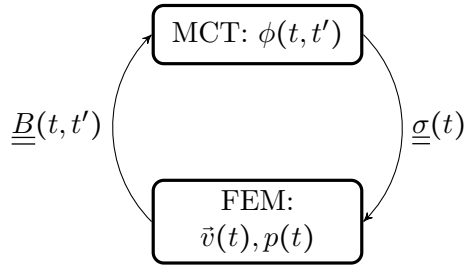

Figure 4.1: Schematic idea of the interplay between microscopic MCT and macroscopic FEM simulation.

4.1 Development of FEM Code for Integral Constitutive Equations

In contrast to many of the commonly used ad-hoc constitutive equations, aim of this thesis is to simulate the flow of non-Newtonian fluids described by strongly history depended constitutive equations. This history dependence leads to the mathematical form of an integral (constitutive) equation instead of a differential equation. In a differential equation the change of a quantity at time t is only dependent of its state at the very same time t but not of all previous times denoted by $t' \leq t$.

4.1.1 FEM/FEniCS Setup

CG2-DG0 Setup

For any given geometry / mesh (for example one the rectangular channel) one needs to fix the trial- and test-function spaces for the velocity $\vec{v}(t)$, the pressure $p(t)$, and the polymeric stress tensor $\hat{\underline{\underline{\sigma}}}_P(t)$. This thesis presents a discontinuous Galerkin finite elements approach which is the lowest order stable approximation of the pressure and the stress. Their approximation will be done by a superposition of piece-wise constant and discontinuous basis functions. It is desirable to have a lower order for the stress elements because one has to solve the schematic MCT equations on every stress node in the grid in order to calculate the polymeric stress tensor. This lowest order LBB stable DG approximation are the so called 'CG2-DG0' elements [34] and have the following form:

- 'CG2' (continuous polynomials of degree two) elements for the velocity $\vec{v}$ (in FEniCS language: "VectorElement('CG', mesh.ufl_cell(), 2)"),
- 'DG0' (discontinuous polynomials of degree zero) elements for the pressure p (in FEniCS language: "FiniteElement('DG', mesh.ufl_cell(), 0)"),
- 'DG0' (discontinuous polynomials of degree one) elements for the stress $\underline{\underline{\sigma_P}}$ (in FEniCS language: "TensorElement('DG', mesh.ufl_cell(), 0)"),

where the FEniCS command "mesh.ufl_cell()" just returns the cell type (for example "triangle" or "interval").
The LBB (named after mathematicians Ladyzhenskaya, Babuska and Brezzi) criterion is a sufficient condition for a saddle point problem to have a unique solution that depends continuously on the input data, for mathematical detail see [15]. Note that this setting does not secure that the imcompressibility condition $\nabla \cdot \vec{v} = 0$ holds point-wise, but of course cell-wise (since this equation is solved on each cell). This means that the suggested setup ensures that both mass- and momentum-conservation hold cell-wise and that the problem is well-posed and LBB-stable.

Alternative Setup

To even ensure pressure-robustness and point-wise mass-conservation one could (simulations presented in this thesis are performed using the 'CG2-DG0' code version) change to the slightly more computational expensive linear BDM elements [11] for the velocity leading to the FEM setup:

- 'BDM1' ($H(\mathrm{div}, \Omega)$-conforming[1] vector elements of degree one) elements for the velocity $\vec{v}$ (in FEniCS language: "VectorElement('BDM', mesh.ufl_cell(), 1)"),
- 'DG0' (discontinuous polynomials of degree zero) elements for the pressure p (in FEniCS language: "FiniteElement('DG', mesh.ufl_cell(), 0)"),
- 'DG0' (discontinuous polynomials of degree one) elements for the stress $\underline{\underline{\sigma_P}}$ (in FEniCS language: "TensorElement('DG', mesh.ufl_cell(), 0)").

Note that both 'BMD1' and 'CG2' elements have 6 degrees of freedom (in the case of a two dimensional triangulation) and have lead to the same results in all test simulations we have performed. For further details on 'BDM' elements one can consult references [11, 38].

[1] $H(\mathrm{div}, \Omega)$ is the Sobolev space of vector functions with square-integrable divergence on the set Ω.

Boundary Conditions

Our choice of boundary conditions are the "no-slip" boundary conditions which means that we have no velocity at the walls ($\vec{v}(\vec{x}) \equiv 0$ for $\vec{x} \in wall$) in the case of a fixed wall and $\vec{v}(\vec{x}) \equiv \vec{v}_{wall}$ if a wall is moving (for example the lid-driven cavity simulation or the simple shear, where typically the upper wall "moves" with a velocity $\vec{v}_{wall} = v_0\vec{e}_x$ in the x-direction). In both cases it means, that there is no velocity difference between the fluid and the walls at the boundaries. Towards the x-direction of the flow we usually use periodic boundary conditions, such that the values on the inlet will be overwritten with the values on the outlet of the flow.

4.1.2 Operator-Splitting by the Marchuk-Yanenko Method

The goal of any numerical simulation is to propagate a system – here given by $(\underline{\underline{\sigma}}[\underline{\underline{B}}, G], \vec{v}, p)$ – from one time-step $t - \Delta t$ to another time-step t. The problem in this specific case is that the equations describing the time evolution of the system are coupled. This means, that for example the equations for $\vec{v}(t)$ and $p(t)$ (Stokes equations) need the stress tensor $\underline{\underline{\sigma}}(t)$. But to be able to calculate the stress tensor $\underline{\underline{\sigma}}(t)$ one needs to know $\underline{\underline{B}}(t, t')$ and therefore the velocity field $\vec{v}(t)$ itself.
One possible solution would be to use a fully explicit method to update some of this variables (for example $\underline{\underline{\sigma}}$ and therefore ϕ and $\underline{\underline{B}}$) and then calculate the other variable with a (often more stable) implicit method (in this example $\vec{v}$). A more refined and widely used alternative is the so-called Marchuk-Yanenko operator-splitting method (see [39] or [21]). This method allows to implicitly update all variables by splitting the propagation operator into two propagation operators which will be used successively. The idea here is to update $\underline{\underline{B}}$ implicitly (more stable [12]) but with the old $\vec{v}(t - \Delta t)$ as a zeroth order approximation for the correct $\vec{v}(t)$.
So the whole numerical algorithm using the Marchuk-Yanenko method is given by the following steps

1. calculate $\underline{\underline{B}}(t, :)$ from $\vec{v}(t - \Delta t)$,
2. from this calculate $\phi(t, :)$ or rather $G(t, :)$,
3. with that $\underline{\underline{\sigma}}(t)$ (discretized integral),
4. finally calculate $\vec{v}(t)$, $p(t)$ (solving the Stokes problem) implicitly.

4.1.3 Numerics of the Finger Tensor

As hinted in the schematic image at the very beginning of this chapter the link between the macroscopic FEM simulation and the microscopic MCT calculations of correlation functions is done via the Finger-Tensor $\underline{\underline{B}}(t, t')$. The Finger tensor is determined by the partial differential equation 2.15:

$$\mathring{\underline{\underline{B}}}(t, t') := \partial_t \underline{\underline{B}}(t, t') + [\vec{v}(t) \cdot \nabla]\underline{\underline{B}}(t, t') - \underline{\underline{\kappa}}(t) \cdot \underline{\underline{B}}(t, t') - \underline{\underline{B}}(t, t') \cdot \underline{\underline{\kappa}}^T(t) = 0$$

and needs to be discretized both in time and space. The FEniCS environment will take care of the spatial discretizations if one sets $\underline{\underline{B}}(t, t')$ to be a DG0 tensor element. It is practical to use the same finite elements for both the Finger tensor $\underline{\underline{B}}$ and the polymeric stress tensor $\underline{\underline{\sigma_P}}$ because the polymeric stress tensor $\underline{\underline{\sigma_P}}$ is calculated from an integral over the Finger tensor $\underline{\underline{B}}$ and a generalized shear modulus G, this way no interpolations or projections must be made.

Basic Discretization

The time derivative will be discretized with the implicit Euler method such that one obtains

$$\underline{\underline{B}}(t, t') + \Delta t \left([\vec{v}(t) \cdot \nabla]\underline{\underline{B}}(t, t') - \underline{\underline{\kappa}}(t) \cdot \underline{\underline{B}}(t, t') - \underline{\underline{B}}(t, t') \cdot \underline{\underline{\kappa}}^T(t) \right) = \underline{\underline{B}}(t - \Delta t, t'). \tag{4.1}$$

Now perform the zeroth order approximation for the unknown $\vec{v}(t)$, which is to simply replace it by $\vec{v}(t-\Delta t) =: \vec{v}_{old}$:

$$\underline{\underline{B}}(t,t') + \Delta t\left([\vec{v}_{old}\cdot\nabla]\underline{\underline{B}}(t,t') - \underline{\underline{\kappa}}_{old}\cdot\underline{\underline{B}}(t,t') - \underline{\underline{B}}(t,t')\cdot\underline{\underline{\kappa}}^{T}_{old}\right) = \underline{\underline{B}}(t-\Delta t,t'), \tag{4.2}$$

for all (discrete) $t' \le t$, with $\underline{\underline{B}}(t',t') = \underline{\underline{1}}$ as an initial condition. This means that one has to solve this implicit equation for the whole set off previous times up to the youngest Finger-Tensor $\underline{\underline{B}}(t,t) = \underline{\underline{1}}$.

Transformation from Reference Time t' to Age $a = t - t'$

Unfortunately one has to deal with a more complicated grid (see the section on two-time MCT) which is not linear in t', therefore sometimes one does not have the right hand side value $\underline{\underline{B}}(t-\Delta t,t')$ available. One possible solution – proposed by Hulsen et al. in [27] – is to define a new Finger-Tensor with arguments time t and age $a = t - t'$ such that $\underline{\underline{b}}(t,a) := \underline{\underline{B}}(t,t-a)$.
By applying the chain-rule one derives

$$\partial_t B(t,t'=t-a) = \partial_t b(t,a) + \partial_a b(t,a),$$

hence that the upper convected derivative is no longer zero, but:

$$\overset{\triangledown}{\underline{\underline{b}}}(t,a) = -\partial_a \underline{\underline{b}}(t,a). \tag{4.3}$$

Note that the additional term $-\partial_a *$ is just because of the chain rule, which needs to be applied when differentiating with respect to t, and has nothing to do with any properties of the Finger tensor itself or the upper convected derivative.
The transformation from reference time variable t' to the age variable $a = t - t'$ and the defining equation of the Finger tensor (notation: drop the distinction between $\underline{\underline{B}}$ and $\underline{\underline{b}}$) are sketched in the figure below.

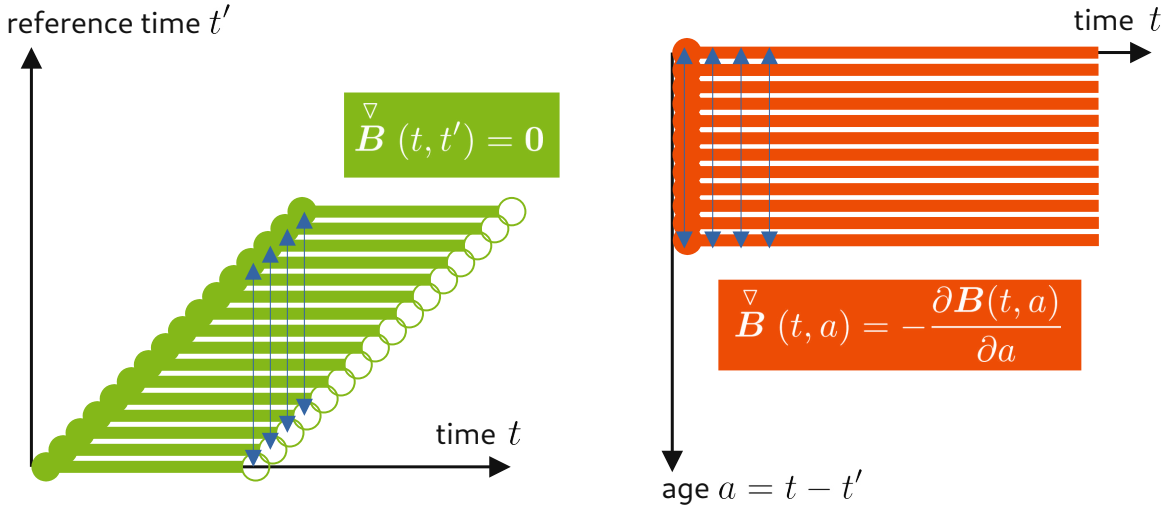

Figure 4.2: Sketch of the transformation from reference time variable t' to the age variable $a = t - t'$. The blue arrows describe a change in age $a = t - t'$ at a given fixed time t. Figure courtesy of Dr. Timm Treskatis.

To achieve good numerical stability one uses the implicit Euler scheme for both the time derivative ∂_t as well as for the additional derivative ∂_a. Interestingly the implicit Euler scheme (often called backward Euler) is actually forward in a (since a grows while t' decreases) and makes sure that the information

is transported the correct temporal way (otherwise it will cause strong oscillatory artifacts).
For notational convention one may now drop the distinction between $\underline{\underline{B}}$ and $\underline{\underline{b}}$ and just write $\underline{\underline{B}}(t,a)$ to formulate the new (temporal discretized) new evolution equation for the Finger-Tensor:

$$\begin{aligned}&\underline{\underline{B}}(t,a) + \Delta t \left([\vec{v}_{old} \cdot \nabla] \underline{\underline{B}}(t,a) - \underline{\underline{\kappa}}_{old} \cdot \underline{\underline{B}}(t,a) - \underline{\underline{B}}(t,a) \cdot \underline{\underline{\kappa}}_{old}^T \right) \\ &= \underline{\underline{B}}(t-\Delta t, a) - \frac{\Delta t}{\Delta a} \left[\underline{\underline{B}}(t-\Delta t, a) - \underline{\underline{B}}(t-\Delta t, a-\Delta a) \right]. \end{aligned} \tag{4.4}$$

This can also be viewed as an interpolation from $\underline{\underline{B}}(t-\Delta t, a)$ to $\underline{\underline{B}}(t-\Delta t, a-\Delta t)$, which corresponds to the "old" right hand side $\underline{\underline{B}}(t-\Delta t, t')$.
Note that if $\Delta t \equiv \Delta a$ the first two terms on the right hand side would cancel each other and we would directly have $\underline{\underline{B}}(t-\Delta t, a-\Delta t)$ (corresponding to a grid which is linear in both arguments t, t' or t, a). For time grids used during this thesis, which are linear in the time t but logarithmic in the age a to save memory and achieve fast computation of the integral constitutive equation for the polymeric part of the stress tensor, this cancellation is unfortunately not the case.

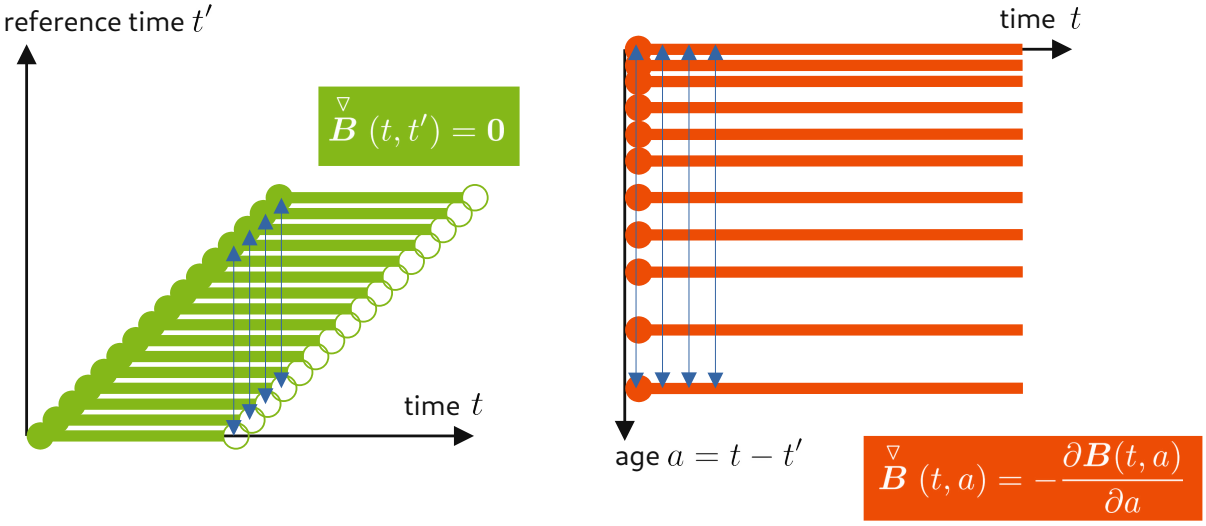

Figure 4.3: Sketch of the transformation from reference time variable t' to the age variable $a = t - t'$ on a grid logarithmic in age a. Figure courtesy of Dr. Timm Treskatis.

DG-Method

To be able to use any FE method the equations need to be in their weak formulation. Therefore – as always – the above equation must be multiplied with a test-function / -tensor $\underline{\underline{C}}$ and integrated by using the DG-method similar to the classic example problem from Reed and Hill 3.21. If one defines

$$\begin{aligned} v_n &= \vec{v}_{old} \cdot \vec{n}, \\ v_{n,\pm} &= (v_n \pm |v_n|)/2, \end{aligned}$$

with $\vec{n}$ denoting the outer unit normal vector, one can formulate the weak formulation of the deformation problem:

$$\begin{aligned}&\sum_{K \in \mathcal{K}} \int_K \underline{\underline{B}}(t,a) \cdot \underline{\underline{C}} - \Delta t \cdot \underline{\underline{B}}(t,a) \cdot \operatorname{div}(\underline{\underline{C}} \cdot \vec{v}_{old}) + \Delta t \cdot \left(-\underline{\underline{\kappa}}_{old} \cdot \underline{\underline{B}}(t,a) - \underline{\underline{B}}(t,a) \cdot \underline{\underline{\kappa}}_{old}^T \right) \cdot \underline{\underline{C}} \, \mathrm{d}x \\ &+ \sum_{K \in \mathcal{K}} \int_{\partial K} \Delta t \left(v_{n,+} \cdot \underline{\underline{B}}^+(t,a) + v_{n,-} \cdot \underline{\underline{B}}^-(t,a) \right) \cdot [\underline{\underline{C}}] \mathrm{d}S + \sum_{E \in \mathcal{E}_I} \int_E \Delta t (v_n \cdot \underline{\underline{B}}(t,a)) \cdot \underline{\underline{C}} \, \mathrm{d}s \\ &= \sum_{K \in \mathcal{K}} \int_K \left(\underline{\underline{B}}(t-\Delta t, a) - \frac{\Delta t}{\Delta a} (\underline{\underline{B}}(t-\Delta t, a) - \underline{\underline{B}}(t-\Delta t, a-\Delta a)) \right) \cdot \underline{\underline{C}} \, \mathrm{d}x. \end{aligned} \tag{4.5}$$

(The very first "−" in the equation 4.5 above is from integrating by parts and $[\underline{\underline{C}}] = \underline{\underline{C}}^{+} - \underline{\underline{C}}^{-}$ defines the "jump", like in 3.1.5.)
Since the equation is linear in both the new $\underline{\underline{B}}(t,a)$ and the test function / tensor $\underline{\underline{C}}$ one can assemble a system of linear equations and solve it using the "mumps" LU (decomposition) solver provided by the FEniCS environment.
It is worth to mention that the left hand side (corresponding to the stiffness matrix) of 4.5 needs to be assembled only once for every discrete time step in t. To solve – when t is fixed – for every a on the quasi-logarithmic grid only a new right hand side (corresponding to the load vector) needs to be assembled in order to solve the system of linear equations.

4.1.4 Integral Constitutive Equation

In the subsection 2.3 we have seen that all of the integral constitutive equations – considered in this thesis – for the polymeric part $\underline{\underline{\sigma_P}}$ of the stress tensor $\underline{\underline{\sigma}} = 2\eta_S \underline{\underline{D}} + \underline{\underline{\sigma_P}}$ have the same integral construction

$$\underline{\underline{\sigma_P}}(t) = \int_0^t \left[-\partial_{t'} \underline{\underline{B}}(t,t')\right] G(t,t') \, \mathrm{d}t',$$

but with different generalized shear moduli $G(t,t')$ depending on the exact constitutive model. For the upper-convected Maxwell Model, generalized (sheer-thinning) Maxwell model and the MCT-ITT model revisit equations 2.17, 2.32, 2.56.
The last subsection focused on the calculation of the Finger tensor on a grid linear in t but non-linear (quasi logarithmic) in the historical time t' and therefore the age $a := t - t'$ to which the Finger-Tensor $\underline{\underline{B}}(t,t') \to \underline{\underline{B}}(t,a)$ was transformed in the second variable. Accordingly one has to carry out the same variable transformation $t' \to a := t - t'$ for the the polymeric stress integral constitutive equation.
Therefore note that

$$t' \to a := t - t' \;\Rightarrow\; \frac{da}{dt'} = -1,$$

which leads to

$$\underline{\underline{\sigma_P}}(t) = \int_0^t \left[\partial_a \underline{\underline{B}}(t,a)\right] G(t,a) \, \mathrm{d}a. \tag{4.6}$$

Here $G(t,a)$ is defined in the exact the same procedure as done previously with the Finger-Tensor $\underline{\underline{B}}(t,a)$ (defining a new $g(t,a) := G(t,t-a)$ and then renaming from small to capital letter again).

For now suppose that $G(t,a)$ is already given and that also the calculation of the Finger tensor $\underline{\underline{B}}(t,a)$ is already carried out as discussed in the previous subsection. To find the polymeric stress tensor $\underline{\underline{\sigma_P}}(t)$ one needs to numerically approximate the integral formula 4.6. This rather standard numerical task is done using the trapezoidal rule (for example [52]) for a non uniform grid $0 = a_0 < a_1 < \ldots < a_N = t$:

$$\int_0^t f(a)\mathrm{d}a \approx \sum_{k=1}^{N} \frac{f(a_k) + f(a_{k-1})}{2} (a_k - a_{k-1}).$$

One can simplify this by making use of the fact that in each block the grid is uniform (with step-size $\Delta a^b = 2^b dt$), such that $a_k^b = a_0^b + k \cdot \Delta a^b$ with $a_0^0 = 0$ and $a_0^b = N_a \sum_{l=0}^{b-1} \Delta a^l$:

$$\int_0^t f(a)da \approx \sum_{b=0}^{N_B-1} \Delta a^b \sum_{k=1}^{N_A} \frac{f(a_k^b) + f(a_{k-1}^b)}{2}.$$

In the specific case of $f(a) = \left[\partial_a \underline{\underline{B}}(t,a)\right] G(t,a)$ this leads to the following numerical approximation of the stress integral 4.6:

$$\underline{\underline{\sigma_P}}(t) \approx \sum_{b=0}^{N_B-1} \sum_{k=1}^{N_A} \left[\underline{\underline{B}}(t,a_k^b) - \underline{\underline{B}}(t,a_{k-1}^b)\right] \frac{G(t,a_k^b) + G(t,a_{k-1}^b)}{2}, \tag{4.7}$$

where the Δa^b from the integral approximation cancels out with the $1/\Delta a^b$ from the numerical approximation of the partial derivative ∂_a.

Error of the Trapazoidal Rule

For every block the error is known (again [52]) to be of order $\mathcal{O}(f^{(2)}(\xi^b)(\Delta a^b)^2)$ and would therefore – disregarding $f^{(2)}(\xi^b)$ – grow by a factor of 4 with each doubling of the step size $\Delta a^b \to \Delta a^{b+1}$. Fortunately the generalized shear moduli $G(t,a)$ are roughly known to be functions that decay at least exponentially or build a plateau (in the glassy limit). In the case of exponential decay the integral is dominated by the the first blocks with the small error. In the case of a plateau one basically has to solve the integral over a derivative and is exact anyway (by the main theorem of calculus).

4.1.5 Stokes Problem

At this point the numerical implementation of the Finger tensor and the integral constitutive equation are done. According to the Marchuk-Yanenko splitting method one further needs to solve the fluid mechanical (Stokes) problem to determine the velocities $\vec{v}(\vec{x},t)$ and pressures $p(t)$ to be able to iterate the whole procedure.
The general momentum time evolution for an incompressible (which mathematically provides $\nabla \cdot \vec{v} = 0$) fluid without external forces is given by the famous Navier-Stokes equation (with density $\rho \equiv 1$):

$$\partial_t \vec{v} + [\vec{v} \cdot \nabla]\vec{v} = -\nabla p + \nabla \cdot \underline{\underline{\sigma}}.$$

Since this thesis aims to study the rheology of extremely viscous (viscoelatic or even viscoelastoplastic) fluids it is very common to neglect the $[\vec{v} \cdot \nabla]\vec{v}$ term. On can assume, that advective inertial forces are small compared with viscous forces, resulting in the Stokes problem (also called "creep flow"):

$$\partial_t \vec{v} = -\nabla p + \nabla \cdot \underline{\underline{\sigma}}. \tag{4.8}$$

To numerically solve the Stokes problem in the FEniCS environment one has to discretize the partial time derivative $\partial_t \vec{v}$ on the right hand side of 4.8. For similar flow problems the mathematical theory (for example [53]) indicates that the implicit Euler method is again (like for the Finger-Tensor) a reasonable choice.
Using the implicit Euler scheme results in the temporal discretized equation

$$\vec{v}(t) + \Delta t \left[\nabla p(t) - \nabla \cdot \underline{\underline{\sigma}}(t)\right] = \vec{v}(t - \Delta t), \tag{4.9}$$

which needs to be transformed into its weak form to be solved with the finite element method. This is – as always – done by multiplying with test-functions $\hat{\vec{v}}$ and $\hat{p}$ (for the incompressibility equation) and integrating by parts. Note that $\underline{\underline{\sigma}} = 2\eta_S \underline{\underline{D}} + \underline{\underline{\sigma_P}}$ is written out explicitly and that $\mathcal{D}$ denotes the symmetrized gradient operator:

$$\begin{aligned} &\sum_{K \in \mathcal{K}} \int_K \vec{v} \cdot \hat{\vec{v}} + \Delta t \cdot \left[2\eta_S \mathcal{D}(\vec{v}) \cdot \mathcal{D}(\hat{\vec{v}}) + \underline{\underline{\sigma_P}} \cdot \mathcal{D}(\hat{\vec{v}}) - p \cdot \mathrm{div}(\hat{\vec{v}}) - \hat{p} \cdot \mathrm{div}(\vec{v})\right] \mathrm{d}x \\ &= \sum_{K \in \mathcal{K}} \int_K \vec{v}_{old} \cdot \hat{\vec{v}}\ dx + \sum_{K \in \mathcal{K}} \int_{\partial K} \Delta t \cdot (\langle \underline{\underline{\sigma_P}} \rangle \vec{n} \cdot [\vec{v}]) \mathrm{d}S + \sum_{E \in \mathcal{E}_I} \int_E \Delta t \cdot (\underline{\underline{\sigma_P}} \vec{n} \cdot \hat{\vec{v}} + p\vec{n} \cdot \hat{\vec{v}}) \mathrm{d}s. \end{aligned} \tag{4.10}$$

The $\hat{p} \cdot \mathrm{div}(\vec{v})\ dx$ term ensures the incompressibility of flow, while the $p\vec{n} \cdot \hat{\vec{v}}\ ds$ term is providing a pressure gradient on the inlet and outlet. The linear variational problem is assembled and solved by the FEniCS environment using the "mumps" LU solver.

4.2 Numerical Details of Integral Constitutive Equations

Integral constitutive equations need a much more complicated memory management compared to standard differential models. The main reason for this is that for every time step (fixed variable t) one needs to know the whole history, stored in the age variable a, of both the Finger tensor $\underline{\underline{B}}(t,a)$ and the generalized shear modulus $G(t,a)$.
In the MCT-ITT model one even needs to store all the old correlation functions $\phi(t'',t')$ for $t'' \in [t',t]$ to be able to calculate the memory integral in the two-time sMCT equation (see section 1.4).

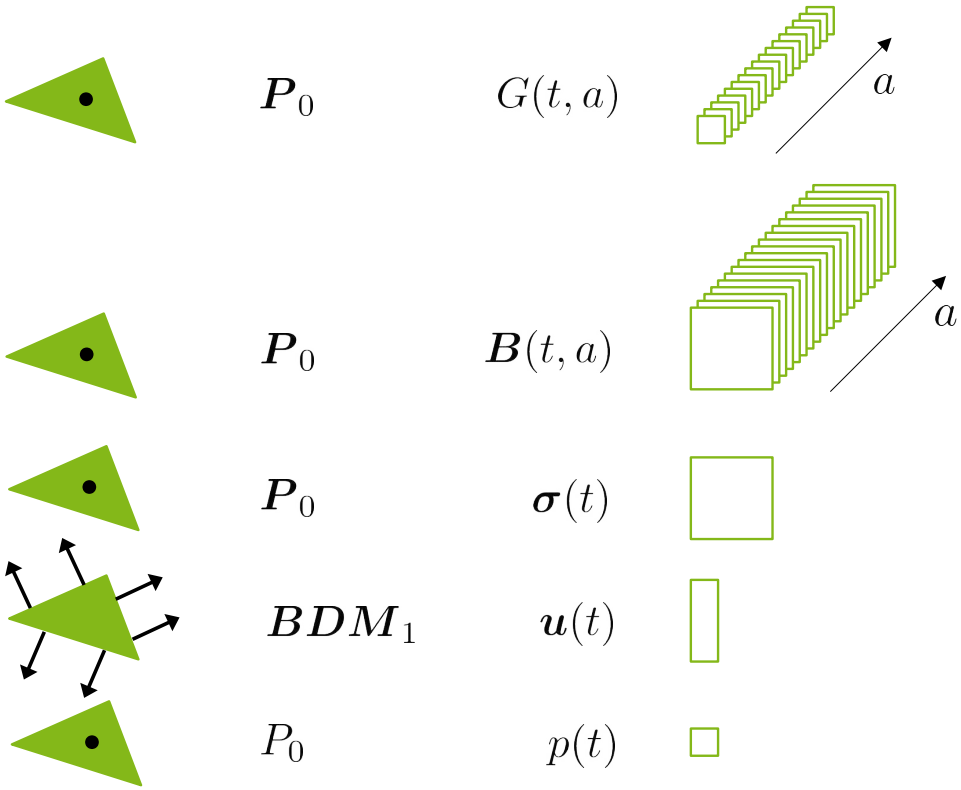

Figure 4.4: Schematic picture to visualize the general memory management of the ICE Stokes simulations. In this sketch a small square represents one scalar variable at a given time t, the rectangle (size of two small squares) represents a two dimensional vector variable at a given time t and the large square (size of four small squares) represents a 2×2 tensorial variable at a given time t. A series of these squares (or ractangles) menas that one needs to store the whole history of that quantity. Figure courtesy of Dr. Timm Treskatis.

4.2.1 Generalized (integral) Maxwell Model

The first integral constitutive equation for the polymeric stress tensor $\underline{\underline{\sigma_P}}$ shall be the generalized Maxwell model which is a real ICE model (such that there is no way to reduce it into a differential model) but computationally a bit more generous than the MCT-ITT model. The main difference in computational effort lies in the fact that one does not need to solve an integral equation (for example the schematic MCT equation) to obtain the generalized dynamic shear modules $G(t,a)$, $a := t - t'$ which is essential to be able to perform any numerical approximations of the polymeric stress tensor:

$$\underline{\underline{\sigma_P}}(t) = \int_0^t \left[\partial_a \underline{\underline{B}}(t,a)\right] G(t,a)\, \mathrm{d}a$$

known from the subsection 2.3. In the generalized Maxwell model one can calculate the dynamical shear modulus $G(t,a)$ by solving:

$$\frac{D}{Dt}G(t,t') = -\frac{1}{\lambda_M(|\dot{\gamma}(t')|)}G(t,t'), \tag{4.11}$$

with $|\dot{\gamma}| = \sqrt{2 \cdot tr(\underline{\underline{D}}^2)}$ a scalar strain-rate that needs to be stored for every historical time step t'. Afterwards one transforms to $G(t, a = t-t')$ (and interpolate if necessary). A slightly better way (done in the simulations presented in this thesis) is to change the second variable to age $a = t - t'$ straight away and note (as seen in the Finger tensor) that an additional $-\partial_a$ occurs on the right hand side. This is due to the chain-rule since the second variable is no longer independent of the first one. The equation – in its strong formulation – is given by:

$$\frac{D}{Dt}G(t,a) = -\left(\frac{1}{\lambda_M(|\dot{\gamma}(t-a)|)} + \partial_a\right)G(t,a) \tag{4.12}$$

To be able to numerically solve this PDE with the finite element method in the FEniCS environment one needs the weak formulation for appropriate DG0 elements (because the Finger tensor is approximated by DG0 elements as well).

Weak Formulation, DG0-Method

With the same DG-method as previously used for the Finger tensor $\underline{\underline{B}}(t,a)$ one can write down a weak formulation that can be numerically solved on DG0 elements. The scalar test-function multiplied to equation 4.12 will be denoted by H. The notations $v_n = \vec{v}_{old} \cdot \vec{n}$ for the (old) flow in outer normal ($\vec{n}$) direction and $v_{n,\pm} = (v_n \pm |v_n|)/2$ for the jumps in tangential direction are kept consistent. With these notations one can formulate the weak problem using the integration by parts formula:

$$\begin{aligned}
&\sum_{K\in\mathcal{K}} \int_K G(t,a)\cdot H - \Delta t \cdot G \cdot \mathrm{div}(H\cdot\vec{v}_{old}) + \frac{G(t,a)\cdot H}{\lambda_M(|\dot{\gamma}(t-a)|)}\ \mathrm{d}x \\
&+ \sum_{K\in\mathcal{K}} \int_{\partial K} \Delta t \cdot (v_{n,+}\cdot G^+(t,a) + v_{n,-}\cdot G^-(t,a))\cdot[H]\ \mathrm{d}S \\
&+ \sum_{E\in\mathcal{E}_I} \Delta t\cdot(v_n\cdot G(t,a))\cdot H\ \mathrm{d}s \\
&= \sum_{K\in\mathcal{K}} \int_K \left(G(t-\Delta t,a) - \frac{\Delta t}{\Delta a}\{G(t-\Delta t,a) - G(t-\Delta t, a-\Delta a)\}\right)\cdot H\ \mathrm{d}x.
\end{aligned} \tag{4.13}$$

Similar to the case of the Finger tensor one one needs to assemble the stiffness matrix only once for every time step t and just use different load vectors for every age a. The assembled system of linear equations can be solved using the "mumps" LU solver provided by the FEniCS environment.
Note that for the integral form of the White-Metzner model the weak equation is almost identical to 4.13, with the only difference that in the first line one needs to exchange $\lambda_M(|\dot{\gamma}(t-a)|)$ by $\lambda_M(|\dot{\gamma}(t)|)$. With the dynamical shear modulus G one can easily perform a numerical approximation of the polymeric stress integral (for example with the help of the trapazoidal rule as discussed previously) and perform the whole simulation by solving the equations for $\underline{\underline{B}}$ and $\vec{v}, p$ implicitly using the operator-splitting scheme by Marchuck and Yanenko as described in subsection 4.1.2.

4.2.2 MCT-ITT Integral Constitutive Equation

In comparison to the previously discussed generalized Maxwell ICE model the calculation of the dynamical shear modulus $G(t,a) = G_\infty \phi^2(t,a)$ from the MCT-ITT model is far more complicated. Here $\phi(t,a)$ is the solution of the schematic two-time MCT equation under shear. So to simulate the MCT-ITT model one needs to to solve another integral equation for $G(t,a)$ in every time step. Recall that the schematic (two-time) MCT equation under shear is given by:

$$\partial_t \phi(t,t') + \phi(t,t') + h_{tt'} \int_{t'}^{t} h_{tt''} m(t,t'') \partial_{t''} \phi(t'',t') \mathrm{d}t'' = 0.$$

This makes it necessary to store $\phi(t,a) := \phi(t,t-t')$ in both variables on a linear/logarithmic grid as discussed in section 1.4.

Even though the correlation function ϕ itself should by transformed to the (t,a) variables, the inner part (previously stored in the variable C, see 1.4) of the convolution-like memory integral $h_{tt'} \int_{t'}^{t} h_{tt''} m(t,t'') \partial_{t''} \phi(t'',t') \mathrm{d}t''$ will be performed on the (t,t') grid. The partial time derivative on the very left of the sMCT equation will be performed on the (t,a) grid. Therefore one first recalls the $(t,t') \to (i,j)$ discretized version (see section 1.4 or equation 1.38)

$$\begin{aligned} \partial_t \phi_{i,j} + \phi_{i,j} + h_{i,j} \sum_{k=j}^{i-1} h_{i,k} m_{i,k} \left[\phi_{k+1,j} - \phi_{k,j} \right] = \\ \left(\hat{\partial}_t + 1 + h_{i,j} h_{i,i-1} m_{i,i-1} \right) \phi_{i,j} + h_{i,j}^2 m_{i,j} \left[\phi_{j+1,j} - 1 \right] + \tilde{R}_{i,j} = 0, \end{aligned} \tag{4.14}$$

where $\hat{\partial}_t$ should be the implicit Euler operator, such that $\hat{\partial}_t \phi_{i,j} = \frac{\phi_{i,j} - \phi_{i-1,j}}{\Delta t}$. While the new $\tilde{R}_{i,j}$ should contain all the reminder terms not containing either $\phi_{i,j}$ nor $m_{i,j}$.
If one now switches the temporal coordinates from (t,t') to $(t, a = t - t')$, which means from (i,j) to $(i, l = i - j)$ in the discretized equation reads

$$\left(\hat{\partial}_t + \hat{\partial}_a + 1 + h_{i,l} h_{i,1} m_{i,1} \right) \phi_{i,l} + h_{i,l}^2 m_{i,l} \left[\phi_{i-l+1,1} - 1 \right] + \tilde{R}_{i,l} = 0.$$

With writing out the partial derivatives one obtains

$$\frac{\phi_{i,l} - \phi_{i-1,l} + \frac{\Delta t}{\Delta a} \left(\phi_{i-1,l} - \phi_{i-1,l-1} \right)}{\Delta t} + \left(1 + h_{i,l} h_{i,1} m_{i,1} \right) \phi_{i,l} + h_{i,l}^2 m_{i,l} \left[\phi_{i-l+1,1} - 1 \right] + \tilde{R}_{i,l} = 0,$$

which one can further manipulate by absorbing all the terms that do not contain either $\phi_{i,l}$ nor $m_{i,l}$ into a new $R_{i,l} = \tilde{R}_{i,l} + \frac{-\phi_{i-1,l} + \frac{\Delta t}{\Delta a} \left(\phi_{i-1,l} - \phi_{i-1,l-1} \right)}{\Delta t}$.
This leads to the final discretized equation

$$\left(\frac{1}{\Delta t} + 1 + h_{i,l} h_{i,1} m_{i,1} \right) \phi_{i,l} + h_{i,l}^2 m_{i,l} \left[\phi_{i-l+1,1} - 1 \right] + R_{i,l} = 0. \tag{4.15}$$

One can again think of interpolating the point $\phi(t - \Delta t, a - \Delta t)$ out of $\phi(t - \Delta t, a)$ and $\phi(t - \Delta t, a - \Delta a)$ to construct the partial time derivative in the very beginning of the sMCT equation.

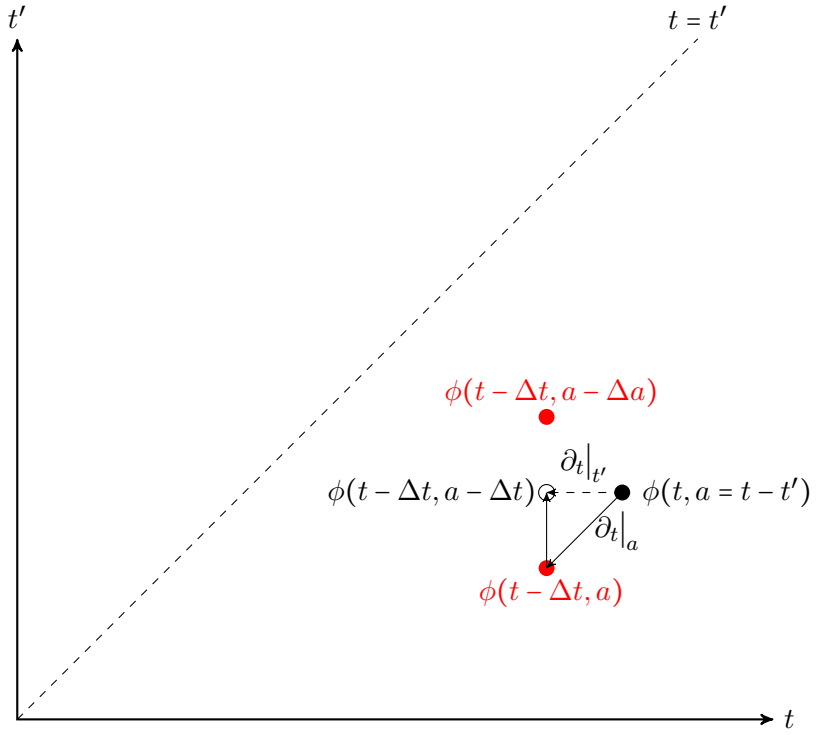

Figure 4.5: Schematic picture of the partial derivative on the very left of the sMCT equation. The black filled circle represents the $\phi(t, a = t - t')$ that one wants to calculate, the empty circle represents the missing $\phi(t - \Delta t, a)$ with that one would wish to approximate the partial time derivative $\partial_t|_{t'}$ with fixed t' in the (t, t') coordinate representation and the red filled circles represent $\phi(t - \Delta t, a)$ and $\phi(t - \Delta t, a - \Delta a)$ which approximate the needed ∂_a derivative in the (t, a) coordinates. One can observe that first 'stepping' form $\phi(t, a)$ to $\phi(t-\Delta t, a)$ $(\partial_t|_a)$ and then $\frac{\Delta t}{\Delta a}$ in the $\partial_a|_t$ direction (towards $\phi(t-dt, a-da)$ would correspond to the whole $\partial_a|_t$-step) leads to $\phi(t-\Delta t, a-\Delta t)$. Therefore one can think of this, such as interpolating the desired – but often missing – $\phi(t-\Delta t, a-\Delta t)$ out of $\phi(t-\Delta t, a)$ and $\phi(t - \Delta t, a - \Delta a)$.

Newton's Method

With the explicit knowledge that the schematic memory kernel is the F12 model $m_{i,l} = m[\phi_{i,l}] = v_1\phi_{i,l} + v_2\phi_{i,l}^2$ one can reformulate the problem 4.15 to a root-search problem of a polynomial $P(\phi_{i,l})$. Given the fact that one has an excellent initial guess by using the previous time step $\phi_{i-1,l}$ a fast and reliable way of solving $P(\phi_{i,l}) = 0$ is to use Newton's method:

$$\phi_{i,l}^{(n+1)} = \phi_{i,l}^{(n)} - \frac{P(\phi_{i,l})}{P'(\phi_{i,l})}, \tag{4.16}$$

where $P'(\phi_{i,l})$ is the derivative of 4.15, in which one uses $m'_{i,l} = m'[\phi_{i,l}] = v_1 + 2v_2\phi_{i,l}$. The Newton iteration is done until certain thresholds $|\phi_{i,l}^{(n+1)} - \phi_{i,l}^{(n)}|_{L^2} < \epsilon_1$ (absolute tolerance, in the simulation this is set to 10^{-9}) and $\frac{|\phi_{i,l}^{(n+1)} - \phi_{i,l}^{(n)}|_{L^2}}{|\phi_{i,l}^{n+1}|_{L^2}} < \epsilon_2$ (relative tolerance, in the simulation this is set to 10^{-6}) or a maximum number of iterations (set to 25) are reached. The maximum number of iteration is only a necessary criterion to ensure that the Newton method does not "get stuck" or diverge. For example if $P(x) = x^3 - 2x + 2$, therefore $P'(x) = 3x^2 - 2$ and one chooses the staring point $x^{(0)}$ to be either 0 or 2 one ends up in an oscillation between these two point $x^{(n)} = 0$ and $x^{(n+1)} = 2$ [52]. Therefore if the simulation reaches this maximum iteration criterion, one can not trusts its results and should consider

re-tuning the parameters. Fortunately all simulations performed during this thesis never reached more than 5 Newton iterations.
Since on has to calculate up to $N_A \cdot N_B$ correlation functions on each cell during each time step of the simulation it is very helpful that the Newton method does provide quadratic convergence instead of only linear convergence such as for the standard Picard iteration method [52].

4.3 Channel Flow

The previously discussed numerical implementation can be tested to study the non-Newtonian fluid flow provided by MCT-based integral constitutive equations for some exemplary cases and geometries. To first test the numerics the simple rectangular channel flow is tested.

4.3.1 Pressure driven Channel Flow of MCT-ITT and generalized Maxwell Model

The pressure driven channel flow is one of the standard examples one wants to simulate. One assumes that the channel is infinitely long and therefore provides translational invariance in the flow (here x) direction. This yields to the fact that $\partial_x \equiv 0$ inside the whole channel. Since the fluid is incompressible one can deduct that all flow will be in the x-direction and that $v_y \equiv 0$ will hold true during the whole simulation. As a consequence of these two facts the $\vec{v}\cdot\nabla$ term will vanish (this means that all changes - mathematically captured by the gradient ∇ - are perpendicular to the flow direction $\hat{e}_x$). Nonetheless the channel flow setup is still able to tell whether some of the typical behavior of viscoelastic flow which is experimentally and for easier models even analytically (see 2.4) well known. These classical effects, for example the existence of a plug in the flow profile, are recovered with the MCT-Integral constitutive model. Like in the whole thesis no-slip Dirichlet boundary conditions are used, which means that $\vec{v}(\vec{x}) \equiv \vec{0},\ \forall \vec{x} \in wall$. The initial condition at which every simulation starts (at time $t = 0$) is that all material is at rest, unstressed and without any deformation history (short said: is has been at rest since forever), mathematically precise: $\vec{v}(t = 0) = \vec{0}$, $\underline{\underline{\sigma}}(t = 0) = 0$ and $\underline{\underline{B}}(t = 0, a) = \mathrm{Id}\ \forall a \geq 0$.
Note that the second condition $\underline{\underline{\sigma}}(t = 0) = 0$ is implied by the other two conditions, because $\vec{v}(t = 0) = \vec{0}$ immediately leads to zero strain-rate and therefore the solvent (or Newtonian) stress is zero. In addition $\underline{\underline{B}}(t = 0, a) = \mathrm{Id}\ \forall a \geq 0$ leads to $\partial_a \underline{\underline{B}}(t = 0, a) = 0\ \forall a \geq 0$ which implies that the polymeric stress is zero as well. Thus one obtains that the total stress ($\underline{\underline{\sigma}} = \underline{\underline{\sigma_S}} + \underline{\underline{\sigma_P}}$) vanishes: $\underline{\underline{\sigma}}(t = 0) = 0$.
During all simulations, if not stated otherwise, both the constants $G_\infty = 1$ in the generalized Maxwell model or $G_0 = 1$ in the MCT-ITT model and the solvent viscosity $\eta_S = 1$ are set to unity. This sets the pressure scale and the relaxation time of the solvent liquid. The numerical time-step size of the implicit Euler scheme (of both the Stokes problem and the Finger tensor partial differential equation $\overset{\triangledown}{\underline{\underline{B}}} = 0$) is set to $\Delta t = 0.05$.
A single simulation of the MCT-ITT model, using these parameters, takes around 10 days utilizing 24 cores of a dual Xeon E5-2650v4 workstation and needs around 45 GB of memory. The same simulation, but using the generalized Maxwell model only takes around 1 day on the same machine and just needs memory in the order of 1 GB.

Plug Flow

The pressure driven channel flow simulation of both the generalized Maxwell model and the more complicated, but microscipical reasoned, MCT model both show very similar plug flow velocity profiles in the steady state. Of course the height v_{max} of these plug profiles is very different since the MCT (without any shear) builds plateaus at $f < 1$ and therefore shows faster velocity profiles (since the polymeric stress is at least by a factor of f^2 smaller that the genMM one). To correct for this, one can simply scale the velocity profile to unit height (by dividing each profile with its maximum value in the

middle). As discussed earlier the plug width is determined by the pressure gradient, which is $\Delta p/L$ where L is the periodic channel length ($L = 5$ in this case), the critical yield parameter γ_c which is (when not explicitly stated otherwise) always set to $\gamma_c = 0.1$. The structural (polymeric) relaxation time is either given by a constant λ_c in the genMM or by the schematic coupling coefficients v_1, v_2 in the F12 sMCT model. In the MCT case one often looks at the specific transition point at $v_1 = 2(\sqrt{2}-1), v_2 = 2$ and tunes this with an additional parameter ϵ such that $v_1 = 2(\sqrt{2}-1) + \epsilon/(\sqrt{2}-1), v_2 = 2$ (as in the [8] reference), so for $\epsilon < 0$ the undeformed material would be in the liquid regime and for $\epsilon \geq 0$ the undeformed material would be in the glassy regime. Of course also for $\epsilon \geq 0$ one can observe a flow since the cages that the particles build in the glassy regime can be broken by the pressure gradient or by shear / deformation of the material.

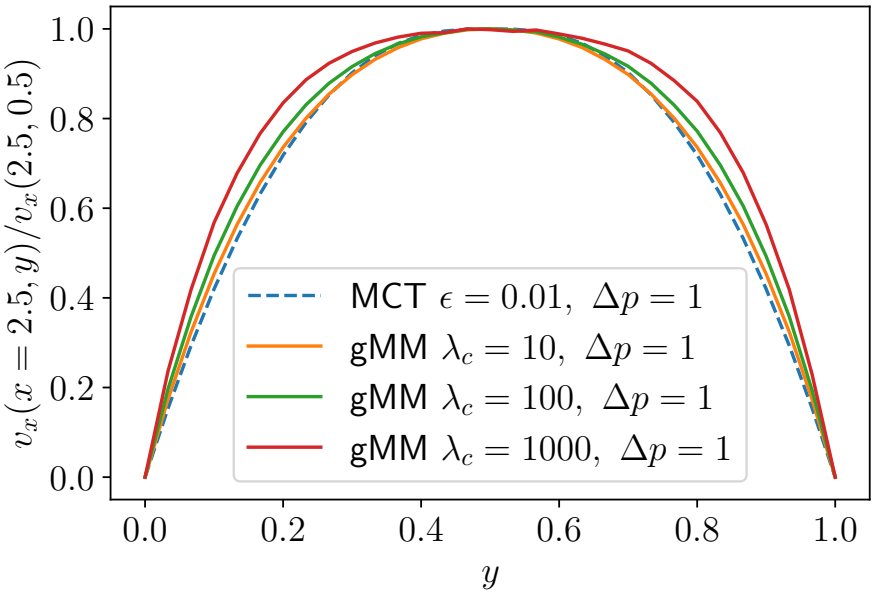

Figure 4.6: Plug flow velocity profiles for MCT and generalized Maxwell model with different parameters.

As one can see in the picture above one can find a parameter set for ϵ in the MCT model and λ_c in the generalized Maxwell model such that their profiles are very similar in their scaled shapes. The absolute plug profiles one can map onto each other by using different (higher G_0 for the MCT model) G_∞ and G_0 for both models. This observation is a good first indication that the MCT model converges in the steady state to similar characteristics. Furthermore one can observe that the deeper – in terms of bigger ϵ-parameter – the unperturbed system would be in the glassy state the more pronounced is the plug flow. This observaton is very intuitive and explained by the caging effect. The deeper the system is in the glassy regime the more shear is needed to break the cages. Since the (absolute value of the) shear increases linearly from the channel center (where $\sigma_{xy}(y = 0) = 0$) to the walls (where $\sigma_{xy}(y = 0, 1) = \pm\frac{\Delta p}{2L}$), as shown in an upcoming calculation (and numerically), the plug gets wider as ϵ increases.

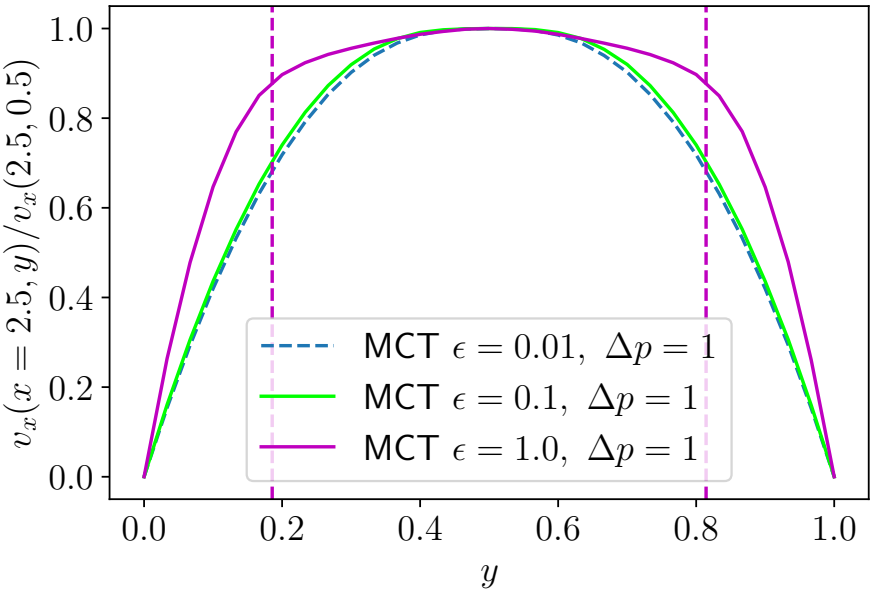

Figure 4.7: Plug flow velocity profiles for MCT with different ϵ-parameters. The larger ϵ is the deeper is the system in the glassy state. For the $\epsilon = 1.0$ simulation the positions where $|\sigma_{xy}| = \sigma_{yield}$ (see 4.18) are indicated by the vertical dashed lines.

However, the interesting new physics should be inside the transient dynamics behavior of the flow, for example whether there are velocity and stress overshoots in the start up phase and how does the cessation of the flow look, especially in more complex geometries that the FE methods is able to solve.

Total Stress and Polymeric Stress

As a reminder and a good numerical test as well, let us briefly recapture that in the pressure driven channel the (Navier-)Stokes equation alone (and nothing else) determines the steady state off-diagonal total stress σ_{xy}, totally independent of the material laws and parameters. Therefore one only needs to integrate the first (x-related) momentum equation in the steady state, respecting the symmetry condition that $\sigma_{xy}(y = \frac{H}{2})$ vanishes:

$$\begin{aligned} -\Delta p/L &= \partial_y \sigma_{xy} \\ \Rightarrow \sigma_{xy}(y) &= (\Delta p/L)(\frac{H}{2} - y). \end{aligned} \tag{4.17}$$

This means that $\sigma_{xy}(y)$ is linear from $\frac{\Delta p H}{2L}$ at $y = 0$ to $-\frac{\Delta p H}{2L}$ at $y = H$. Since this simple condition is totally independent of the constitutive model one should use this to check whether the numerical simulations are at least trustworthy or inconsistent in itself (not actually"'solving" the fluid mechanics correctly).
First one can observe that the simulations actually rediscover y-linear relation 4.17 of the total stress tensor numerically.

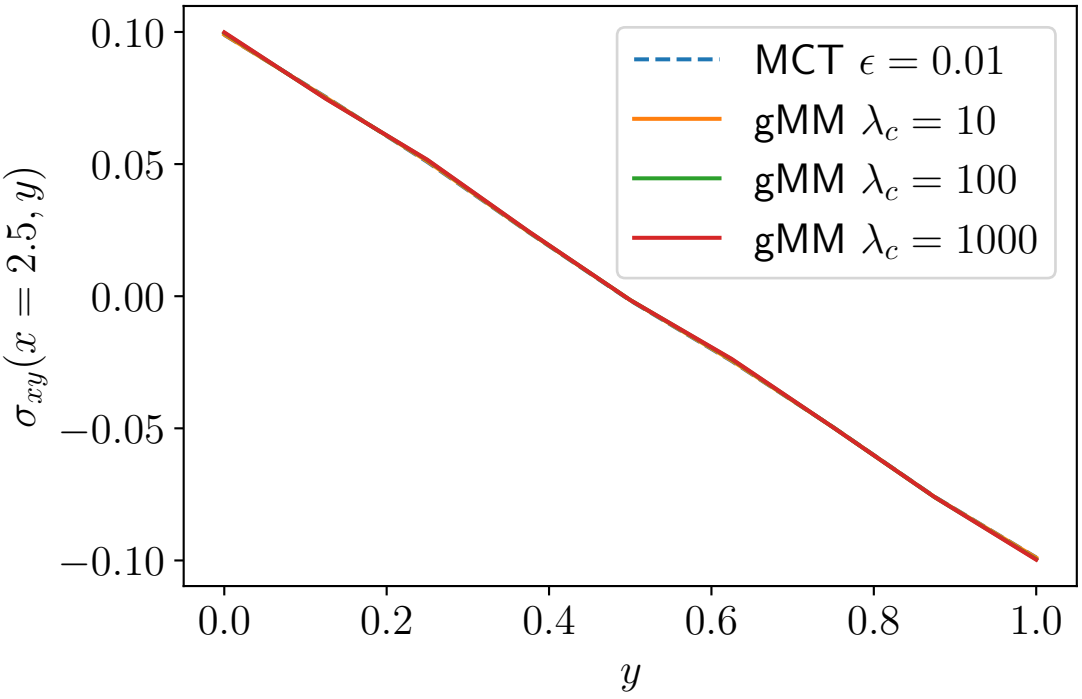

Figure 4.8: xy-component of the total stress versus the height position y for MCT and generalized Maxwell model with different parameters. One can see that the linear relation required from the fluid mechanics (independent of the constitutive model) is correctly found.

The more interesting stress property is the polymeric part which - in contrast to the xy total stress which is fully given by the fluid mechanics - is determined by the constitutive equation. It is worth mentioning that a higher polymeric stress must result in a lower strain-rate. Since the solvent viscosity η_S is fixed this is the reason why the (maximum) mid-channel velocity is dependent on the constitutive equation even though the total stress is not. One will see that the constitutive equations leading to the least polymeric stress will show the largest mid-channel velocities and vice versa. Also one can explain the plug profile with the relation of the polymeric stress and strain-rate. In the region around the middle of the channel ($y = 0.5 \pm \epsilon$) the polymeric stress has (about) the same slope / gradient as the total stress. Hence, the strain-rate must be (very close to) zero and therefore there must be a plug region. If one sets $\sigma_{xy} = \sigma_{yield}$, where σ_{yield} is the yield stress, defined as $\sigma_{yield} = G_0 f^2 \gamma_c$ in the MCT-ITT model [44] and $\sigma_{yield} = G_\infty \gamma_c$ in the generalized Maxwell model [43], one finds the plug area to be:

$$y = 0.5 \pm \frac{\sigma_{yield}}{\Delta p / L}. \tag{4.18}$$

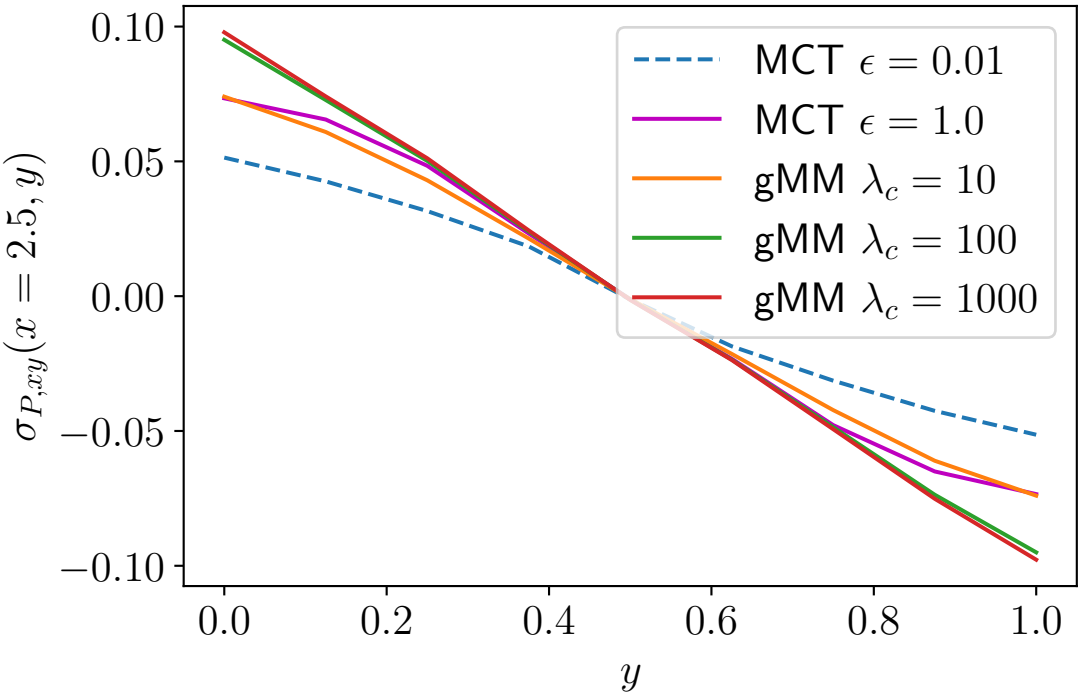

Figure 4.9: xy-component of the polymeric stress versus the height position y for MCT and generalized Maxwell model with different parameters.

So far the focus was only on the off-diagonal component of the (polymeric) stress tensor. Even though (since $\partial_x \equiv 0$ in the infinite channel geometry) σ_{xx} has no influence on the fluid flow, the Finger tensor growths quadratic in the time difference / age. One could be worried about this growth because in the integral formula of our ICEs there is only one time derivative applied ($\partial_a B_{xx}$ still growths linear in a). However luckily the generalized shear moduli $G(t, a)$ decays rapidly enough such that also σ_{xx} reaches a steady state profile and does not diverge towards ∞. Analytically that was already observed in 2.4.2 for the genMM and WMM, in which $G(t, a)$ decays exponentially.

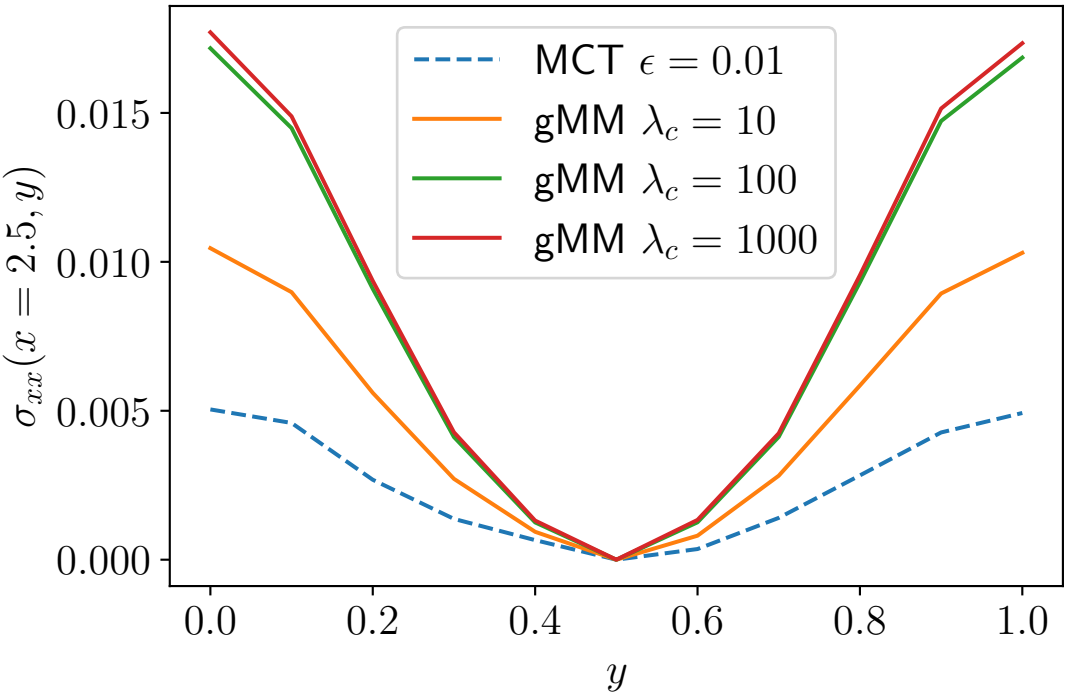

Figure 4.10: xx-component of the polymeric stress versus the height position y for MCT and generalized Maxwell model with different parameters.

Start-Up Flow Dynamics

To be able to observe the transient dynamics of the start-up flow one has to start with a material that is and has been at rest since forever, such that there is no deformation history (start with unity Finger tensors at time $t = 0$). Apply an external force or a pressure gradient for $t \geq 0$ to initiate flow of the material. The start-up flow will reach a steady state – like in the figure above – when all external forces or pressure gradients are balanced by the divergence of the stress (tensor) of the material. The phase until the material reaches its steady state one calls the transient dynamics of the start-up flow. Let us first have a look on the evolution of the mid-channel velocity after application of a constant pressure gradient $\nabla p = (\Delta p/L)\hat{e}_x$ for the generalized Maxwell model and the MCT-ITT model. As previously, the simulation setup is a periodic channel of length $L = 5$ and height $H = 1$, the pressure drop is $\Delta p = 1$ and for the material specific parameter one sets the critical yield stress parameter to $\gamma_c = 0.1$, the solvent viscosity to $\eta_S = 1$ and the shear modulus constant to $G_\infty = G_0 = 1$. For the generalized Maxwell model one could also set a constant (shear independent) structural relaxation time λ_c and in the MCT model the schematic parameter ϵ, as described previously.

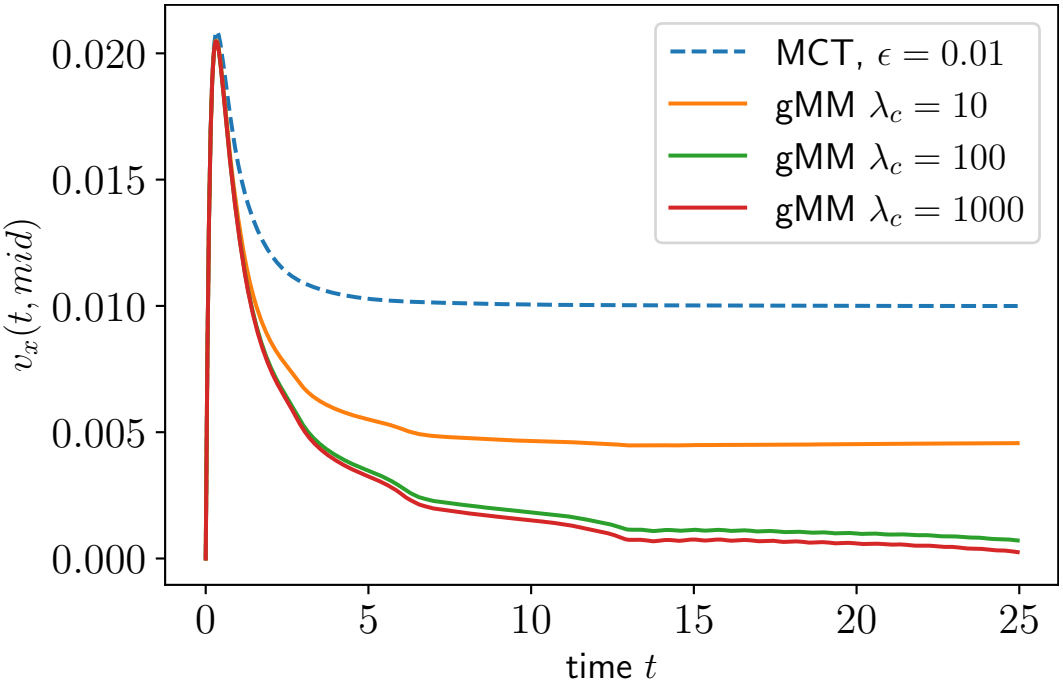

Figure 4.11: Evolution of the mid channel velocity in the start-up flow for the MCT and generalized Maxwell model with different parameters.

Again one can see that the generalized Maxwell model with $\lambda_c = 10$ and the MCT model with $\epsilon = 0.01$ behave qualitatively very similar. All models show drastic velocity overshoots which is a phenomenon typical for viscoelastic fluid flow and not present in Newtonian fluid flow.

4.3.2 Accuracy of Integral Formulation compared to Differential Formulation

To observe the amount of error that the way more complicated integral formulation of constitutive equations has over simpler differential models, we have compared the integral to the classical differential formulation of the White-Metzner model. The White-Metzner model was taken because it can be formulated in both integral and differential form and has some shear-thinning effect included, which the classical upper convected Maxwell model (or Oldroyd B) does not have. So in the integral formulation the polymeric part of the stress tensor is given by

$$\underline{\underline{\sigma_P}}(t) = \int_0^t \left[\partial_a \underline{\underline{B}}(t,a)\right] G(t,a)\, \mathrm{d}a$$

known from the subsection 2.2.4, with the dynamical shear modulus $G(t,a)$ determined from the solution of

$$\frac{D}{Dt} G(t,a) = -\left(\frac{1}{\lambda_M(|\dot\gamma(t)|)} + \partial_a\right) G(t,a). \tag{4.19}$$

Note that the extra $-\partial_a$ term on the right hand side arises – like before – from the variable change from t' to $a = t - t'$ and the chain rule (see [27] or 4.1.3). In the differential formulation of the White-Metzner model the polymeric stress is given by

$$\overset{\triangledown}{\underline{\underline{\sigma}}}(t) + \frac{1}{\lambda_M(|\dot\gamma(t)|)} \underline{\underline{\sigma}}(t) = 2G_\infty \underline{\underline{D}}(t).$$

Simulation Setup

The simulation geometry (or mesh) that was used is the simple periodic rectangular channel with $L = 5H$ and N_x cells in length and N_y cells in height. To achieve symmetry around the central axis ($y = H/2 \equiv 1/2$) a crossed triangulation was used. The parameters in the White-Metzner model are set to $G_\infty = 1$, $\lambda_c = 10$, $\gamma_c = 0.1$ and the solvent viscosity is set to $\mu_S = 1$. In both cases the pressure drop over one (periodic) channel lenght ($L = 5$) was set to be $\Delta p = 2.5$. All temporal (time t and in the integral model also age a) discretizations are done using the stable implicit Euler scheme using a simulation time step of $\Delta t = 0.1$. In the integral formulation 6 blocks with 16 steps in each blocks were used (such that there is no cut-off), in the differential formulation this procedure is of course not used, since there is no need to calculate Finger tensors $\underline{\underline{B}}(t,a)$ or shear modulus $G(t,a)$, because it is a Markovian process and therefore described by an (in our case implicit) update rule.

Error Analysis

The L^2-norm difference (see 3.24 for the definition of the L^2-norm error) of the euclidean norm of the velocity field, the strain-rate, the pressure and the polymeric stress tensor for different N_x, N_y and therefore different cell diameters h_{max} are calculated after 250 time steps when the system has reached its steady state and shown in the following table. Note that for spatial reasons not the whole machine precision but only the first five non vanishing digits are shown (so the last digits are not rounded, but floored).

h_{max}	N_x	N_y	$\|\|v_{diff} - v_{int}\|\|_{L^2}$	$\|\|D_{diff} - D_{int}\|\|_{L^2}$	$\|\|p_{diff} - p_{int}\|\|_{L^2}$	$\|\|\sigma_{P,diff} - \sigma_{P,int}\|\|_{L^2}$
0.25	20	5	0.0012037	0.0085258	0.0032912	0.0098730
0.125	40	10	0.00043930	0.0028918	0.00069851	0.0047115
0.0625	80	20	0.00011846	0.00077666	0.00015710	0.0038658
0.03125	160	40	2.5999E-05	0.00020212	4.4661E-05	0.0036716
0.015625	320	80	5.0194E-06	6.7118E-05	1.7455E-05	0.0036314

In addition to the tabular representation one can plot the L^2-norm error versus the inverse cell diameter h_{max} ('mesh.hmax()' in FEniCS). In this visual representation one can directly observe that the error in the polymeric stress tensor plateaus at approximately 0.0036 which is a relative error of about 0.1% is due to the temporal discretization scheme of the integration.

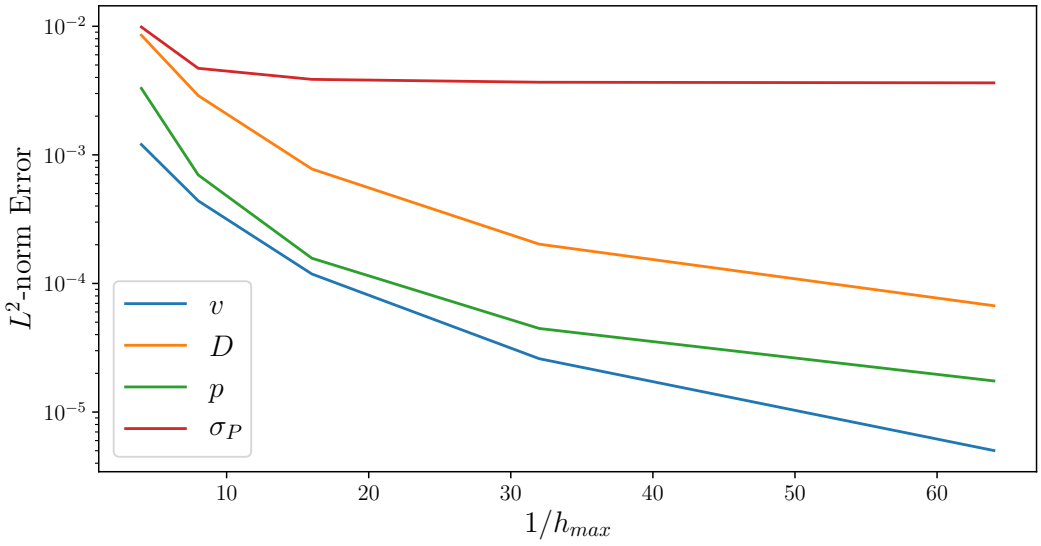

Figure 4.12: Visualization of the L^2-norm error versus the inverse cell diameter h_{max}.

Discretization of the Leibniz Integral Rule

It can be shown that the discretized version of the integral formulation does not exactly solve the implicit Euler discretized version of the differential formulation. In the analytic continuum case in section 2.2.4 one uses the Leibniz integral rule

$$\frac{\mathrm{d}}{\mathrm{d}t}\int_{t_0}^{t} f(t,s)\mathrm{d}s = f(t,t) + \int_{t_0}^{t} \partial_t f(t,s)\mathrm{d}s$$

to show that the integral formulation does fulfill the differential formulation. However in exactly this Leibniz integral rule the order of discretization of the derivative and the integral matters up to an error of order $\mathcal{O}(\Delta t)$
For example if one first discretizes the integral on the right hand side with a given quadrature formula with weights w_i and applies the implicit Euler derivative – using linear grid with $n+1$ nodes, such that $\Delta t = t/n$ – one obtains (w.l.o.g. $t_0 = 0$)

$$\int_0^t \partial_t f(t,s)\mathrm{d}s \approx \sum_{i=0}^{n} w_i \partial_t f(t, i\Delta t)\Delta t \approx \sum_{i=0}^{n} w_i \left[f(t,i\Delta t) - f(t-\Delta t, i\Delta t)\right],$$

such that the full discretized statement of the the right hand side is given by:

$$f(t,t) + \sum_{i=0}^{n} w_i \left[f(t,i\Delta t) - f(t-\Delta t, i\Delta s)\right].$$

In constrast one could start by discretizing the left hand side of the Leibniz integral rule

$$\begin{aligned}\frac{\mathrm{d}}{\mathrm{d}t}\int_0^t f(t,s)\mathrm{d}s &\approx \frac{\int_0^t f(t,s)\mathrm{d}s - \int_0^{t-\Delta t} f(t-\Delta t,s)\mathrm{d}s}{\Delta t} \\ &\approx \int_{t-\Delta t}^{t} \frac{f(t,s)\mathrm{d}s}{\Delta t} + \int_0^{t-\Delta t} \frac{f(t,s) - f(t-\Delta t,s)}{\Delta t}\mathrm{d}s \\ &\approx \sum_{i=n-1}^{n} \hat{w}_i f(t, i\Delta s) + \sum_{i=0}^{n-1} \hat{\hat{w}}_i \left[f(t,i\Delta s) - f(t-\Delta t, i\Delta s)\right],\end{aligned}$$

which is not identical to the discretized statement of the right hand side if uses a consistent quadrature rule (for example the trapazoidal rule where all $w, \hat{w}, \hat{\hat{w}} = 1/2$.
This mathematical fact leads to an additional systematic error of $\mathcal{O}(\Delta t)$ which is independent of the spatial mesh cell diameter h_{max} and therefore contributes to the error plateau in σ_P.

4.4 Channel with Spherical Obstacle, Geometry-Dependent Residual Stresses

The MCT model is able to show flow-induced residual stresses (self balanced internal stresses that remain after the flow has come to rest). The theoretical study of these residual stresses dates back to at least the early 1930's, but first experimental knowledge / observations dates even further back to the spectacular exploding Prince Rupert glass droplets in the 1660's and even further to the images produced by "magic mirrors" of the Western Han dynasty around 200 B.C.. The ability to calculate them in a numerical fluid flow simulation is one of the major achievements in this work. Because of the large role they play in determining the mechanical properties and failure behaviour the controlled use of residual stresses can massively improve material stability to build for example crack resistant cover glasses for modern smartphones or safety glasses in general.

Theory of Geometry-Dependent Residual Stresses

To be able to observe residual stresses the geometry must be suitable to find a non-trivial solution of the Stokes equation without external pressure gradients or other forces, which is just that the stress tensor is divergence free:

$$\nabla \cdot \underline{\underline{\sigma}} = 0.$$

Since the stress tensor is always symmetric ($\sigma_{xy} = \sigma_{yx}$) this reduces to the following two equations:

$$\partial_x \sigma_{xx} = -\partial_y \sigma_{xy}, \tag{4.20}$$

$$\partial_x \sigma_{xy} = -\partial_y \sigma_{yy}. \tag{4.21}$$

If one now goes back to the simple channel flow where $\partial_x \equiv 0$ holds true for the whole channel one notices that σ_{xy} must be constant and because of the symmetry properties around the middle this constant must be zero $\Rightarrow \sigma_{xy} = 0$. This means that only the volumetric part of the stress tensor can remain after the flow has come to rest in the simple channel flow geometry. If however the x-invariance is broken (which means $\partial_x \neq 0$) by an obstacle (or a contraction) inside the channel, the equations above (especially the first one) allow $\sigma_{xy} \neq 0$ balanced by a non vanishing $\partial_x \sigma_{xx}$ term.

A geometrical setup which fulfills this x-invariance breaking is the usual rectangular channel with $L = 5H$ but tuned with a little spherical obstacle around a point in the vertical middle of the channel (diameter is 40% of the channel width) and can be seen (as the actual mesh used for simulations) in the figure 4.13 below. The mesh used in this simulations is build with the help of the "mshr" FEniCS extension and consists of 128 cells across its diameter and 18911 cells in total, which leads to a $h_{max} \approx 0.0358$ therefore, since $|\vec{v}|_max \leq 0.1$, leads to Courant-Friedrichs-Lewy (CFL) number $C < 1$.

Simulation Details

The simulation is started with a pressure gradient $(\Delta p/L)\hat{e}_x$ (with $L = 5$ as before) from an at rest initial condition ($\vec{v}(t = 0) = \vec{0}$, $\underline{\underline{\sigma}}(t = 0) = 0$ and $\underline{\underline{B}}(t = 0, a) = \underline{\underline{\mathrm{Id}}}$) with no-slip Dirichlet boundary conditions at the walls as well as at the obstacle. After 1/4 of the simulation time $t_{end} = 101.6$ (7 blocks with 16 steps and a time step of $\Delta t = 0.05$, such that there is no cut-off in history) the pressure gradient is set to zero (at $t_{off} = \frac{1}{4} t_{end} = 25.6$ on changes $\Delta p = 0$).

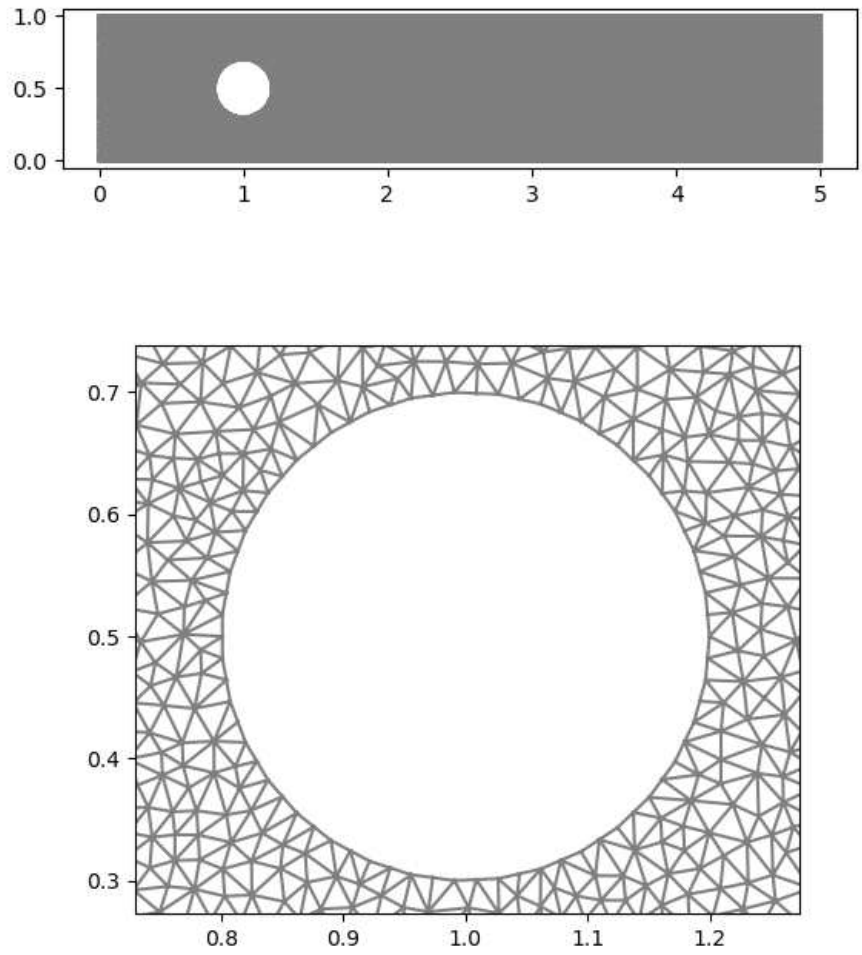

Figure 4.13: Mesh (and a zoom in) used in the simulation with a maximum cell diamater of $h_{max} \approx 0.0358$.

Simulations of the MCT constitutive equation model with ϵ = +0.01 and the other parameters unchanged (G_0 = 1, γ_c = 0.1 and the solvent viscosity to η_S = 1) - therefore slightly in the glassy regime if unsheared - show that after the removal of the pressure gradient $\Delta p/L$ stresses undergo a fast initial drop, while the velocities display a pronounced undershoot. This can be rationalized as another viscoelastic effect [43],[44]: the presence of stresses causes the fluid to be driven in the direction opposite of the initial flow direction, until the stresses have sufficiently relaxed.

4.4.1 Steady State

First one can observe the streamlines of the velocity filed $\vec{v}^{ss}(\vec{r})$ in the steady state phase of the simulation (just before switching off the driving pressure gradient) which of course confirm that the x symmetry is indeed broken by the flow around the obstacle.

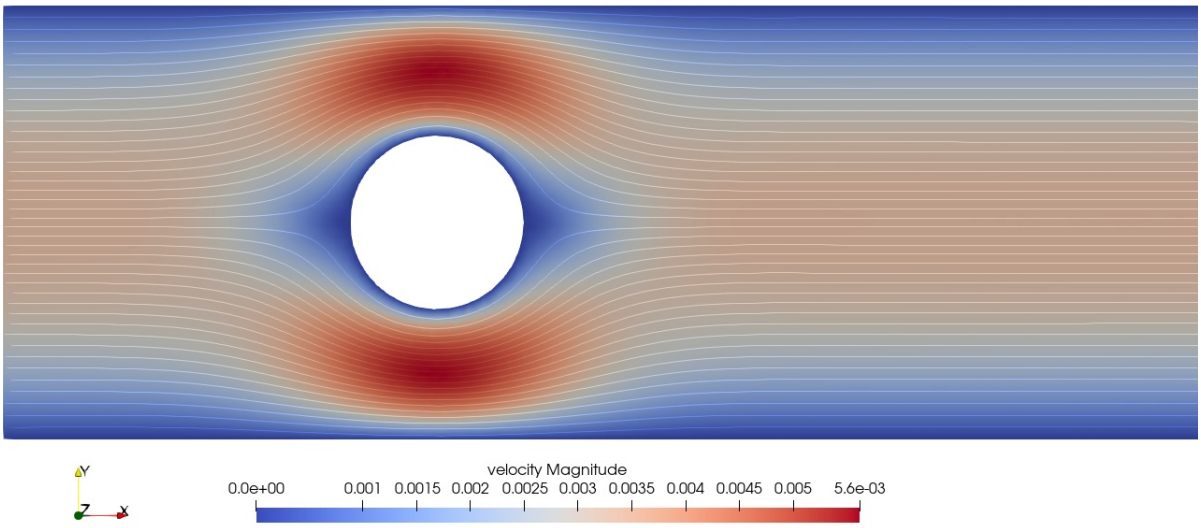

Figure 4.14: Steady state velocity field $\vec{v}^{ss}(\vec{r})$ and streamlines around the obstacle for a pressure drop of $\Delta p = 1.0$ over the channel length of $L = 5$.

Due to the obstacle also the shear stress σ_{xy} is no longer linear in y, like in the normal rectangular channel geometry. One can guess that in the $x = 1$ plane, where the center of the obstacle is located, the shear stress must vanish in the two symmetrical points $(1, 0.2)$ and $(1, 0.8)$ between the obstacle and the walls. Further one can guess that far away from the spherical obstacle one can observe that shear stress is again linear in y.

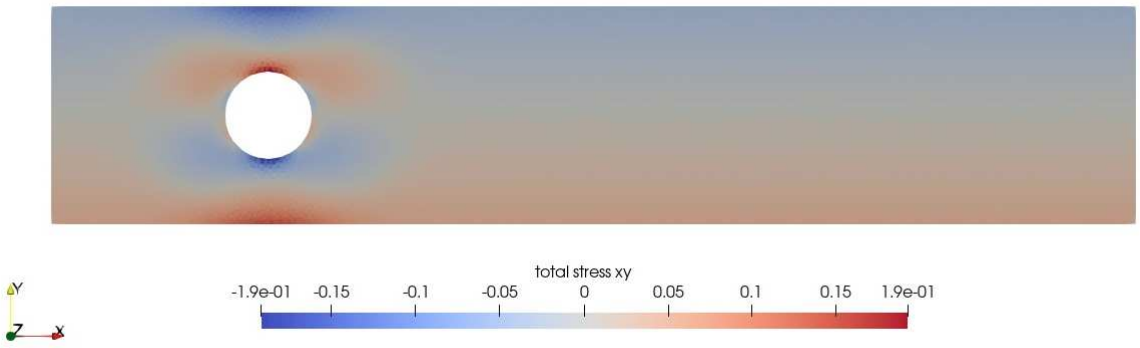

Figure 4.15: Steady state shear stress σ^{ss}_{xy} for a pressure drop of $\Delta p = 1.0$ over the channel length of $L = 5$.

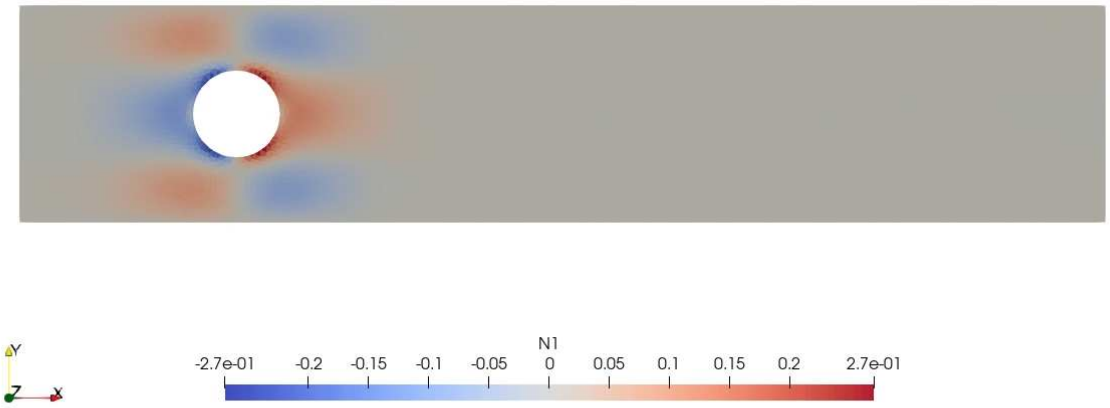

Figure 4.16: Steady state normal stress difference N_1^{ss} for a pressure drop of $\Delta p = 1.0$ over the channel length of $L = 5$.

4.4.2 Geometry-Dependent Residual Stresses from the MCT-ITT Model

Crucially, we observe the shear stress $\sigma_{xy}(t)$ to completely relax in the channel without obstacle (green line in Fig. 4.17 below), while in the presence of the obstacle, the velocity back-leash is much less pronounced, and finite shear stresses remain even for times where the velocity has already decayed to zero. These are geometry-dependent residual stresses [51].

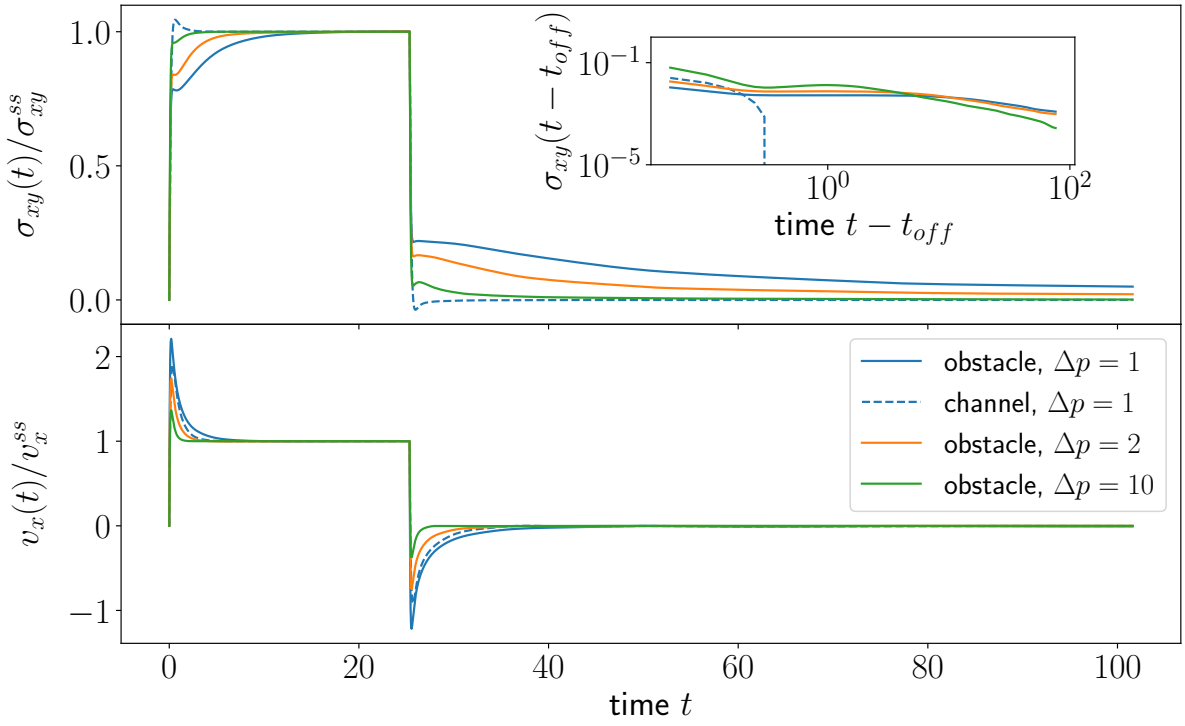

Figure 4.17: Shear stress $\sigma_{xy}(t)$ and velocity $v_x(t)$ as a function of time in the 5:1 rectangular channel with and without the spherical obstacle. Switched on at $t = 0$, off at $t = t_0 = 25.4$. Inset provides a logarithmic zoom.

A further notable observation of the geometry-dependent residual stress phenomena is that around the obstacle the sign of the stress pattern does flip. This means for example that the the negative valued (blue) area below the obstacle changes to a positive valued (red) area. A possible reason for this could be the previously mentioned viscoelastic undershoot / pullback after removing the pressure gradient which one can see in the velocity plot of figure 4.17. This viscoelastic undershoot may change the signs in the most relevant and more recent Finger tensors in the the integral constitutive equation which leads to an exchange of signs in the stress tensor as well.

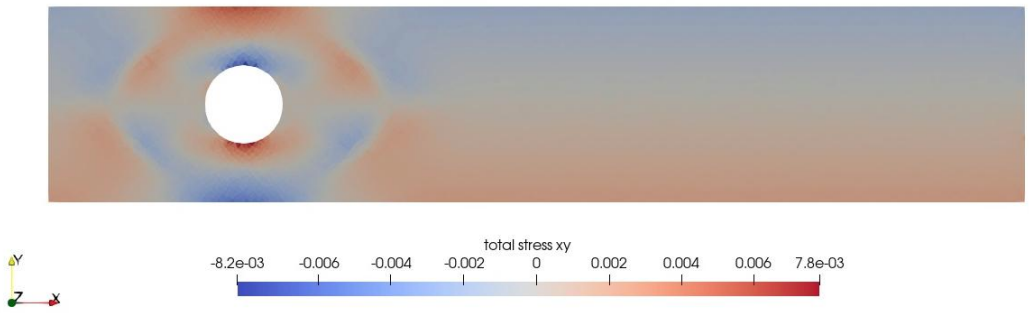

Figure 4.18: Residual shear stress σ_{xy}^{res} of the $\Delta p = 1.0$ simulation.

Generalized Maxwell Model

As comparison to the MCT-ITT residual stress results above the exact same simulations, of a pressure driven channel ($L = 5H$) flow with a spherical obstacle of diameter covering 40% of the channel height, are done for the generalized Maxwell model with a very high structural relaxation time scale of $\lambda_c = 10^3$ and the critical yield parameter is – as usual – set to $\gamma_c = 0.1$. Like previously with the MCT-ITT model different pressure drops ($\Delta p = \{1, 2\}$) across the (periodic) channel are simulated. As before the numerical time step for the implicit Euler scheme is $\Delta t = 0.05$ and also the resolution in age is kept identical, which means 7 blocks of 16 steps in each block and no cut-off in history. The mesh is also the same "mshr" FEniCS extension mesh with 128 cells across the diameter with $h_{max} = 0.0358$, like in figure 4.13.
The shear stress σ_{xy} relaxes on a much smaller time scale ($\approx 10^1$, depending on the pressure gradient applied previously) compared to its structural relaxation time scale $\lambda_c = 10^3$. This means that unlike the MCT-ITT model the generalized Maxwell model is not able to predict geometry-dependent residual stresses when the spherical obstacle is put in the rectangular channel. This is a major advantage of the more complicated and statstical physics based MCT-ITT model over the simpler generalized Maxwell model.

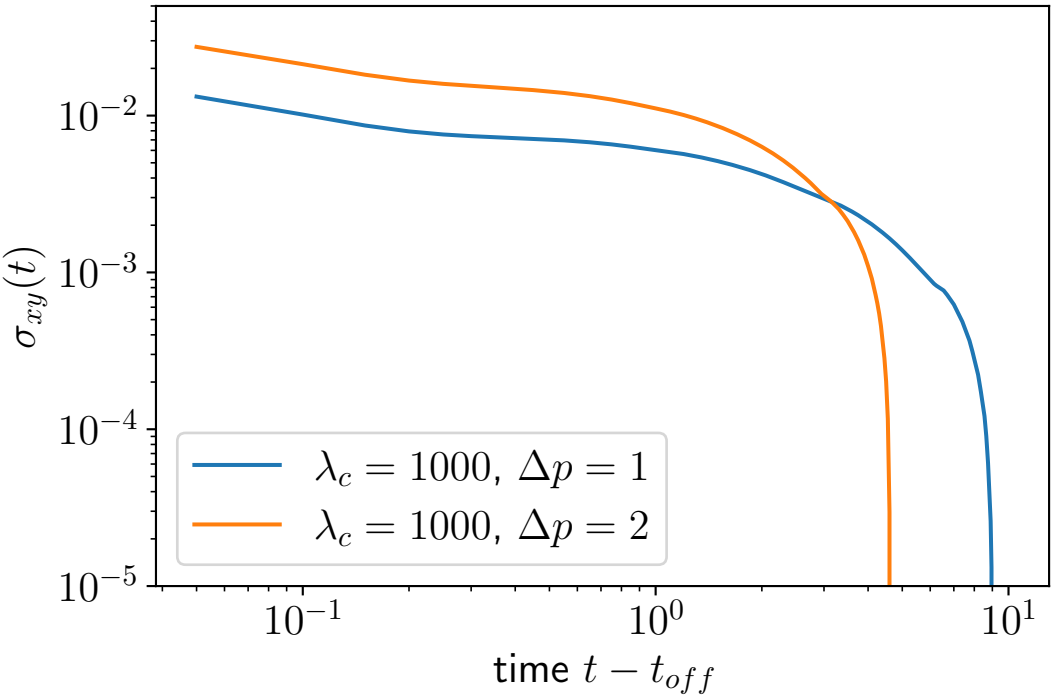

Figure 4.19: Shear stress $\sigma_{xy}(t)$ and velocity $v_x(t)$ of the generalized Maxwell model as a function of time in the 5:1 rectangular channel with the spherical obstacle.

Normal Stresses and Influence of the Periodic Boundary Condition

Another effect, which is already known from the rectangular channel flow [44], is that the the normal stress σ_{xx} and also the first normal stress difference $N_1 = \sigma_{xx} - \sigma_{yy}$ remain non-zero after the cessation of flow is also present in the channel tuned with the spherical obstacle. The N_1 pattern changes drastically (in x) from the one in the ordinary channel around the obstacle. Away from the obstacle the N_1 pattern becomes locally constant in x. However one observes that away from the obstacle in the normal channel are small residual shear stresses.
This effect is due to the periodic boundary conditions which forces σ_{xx} to vary slowly in x direction also in the channel region and therefore induce residual shear stresses in order to fulfill the Stokes equation $\partial_x \sigma_{xx} = -\partial_y \sigma_{xy}$. In the channel flow σ_{xx} is not directly effected by the Stokes equation $\partial_x \sigma_{xx} = -\partial_y \sigma_{xy}$ because of $\partial_x \equiv 0$ due to the x symmetry. In the geometry with the obstacle $\partial_x \neq 0$ and $\partial_x \sigma_{xx}$ needs to balance the residual shear stress $\partial_y \sigma_{xy}$ which is strongest in the $x = 1$ plane around the obstacle and therefore one can observe that $\partial_x \sigma_{xx}$ is also strongest around the $x = 0$ plane. This can be seen very nicely in figure 4.21 by looking at the color changing from red (+) to blue (−) around the the $x = 1$ plane. But also far away from the obstacle, for example at roughly $x = 4$ one can see that σ_{xy} is linear in y and that in order to balance this σ_{xx} changes in x, which is not the case in the channel, because of the x symmetry and the therefore lacking residual shear stresses changing in the y direction.

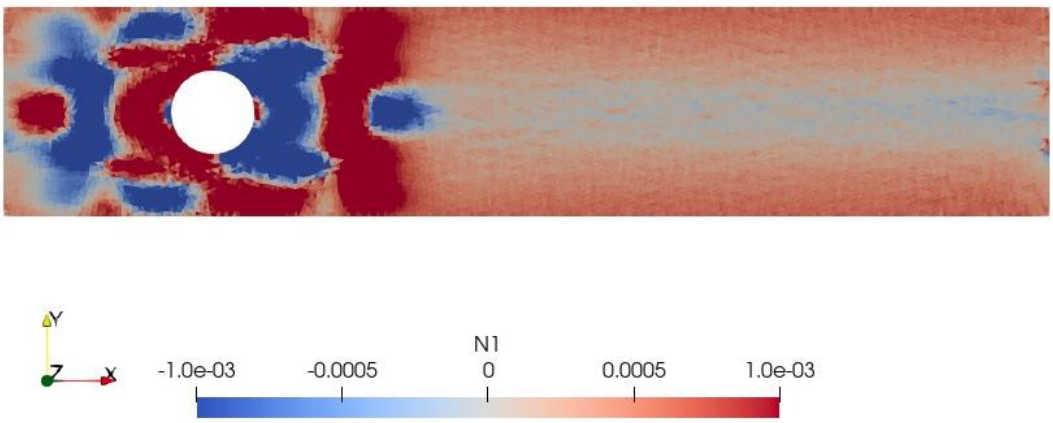

Figure 4.20: Residual first normal stress difference N_1 of the $\Delta p = 1.0$ simulation. Color bar is chosen to show that N_1 is locally changing around the obstacle and constant in the channel away from the obstacle.

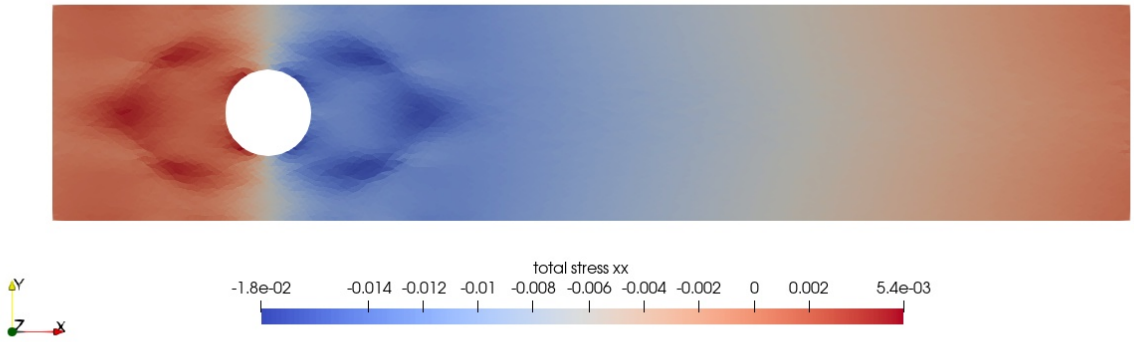

Figure 4.21: Residual normal stress σ_{xx}^{res} of the $\Delta p = 1.0$ simulation.

To further investigate the effect of the periodic boundary condition in the x-direction the channel length is doubled, while the pressure gradient is kept constant (so Δp is doubled as well). With this setup one can now observe how σ_{xx} changes in the x-direction. The first plausible guess is, that due to the incompressibility, that σ_{xx} inside the channel part away from the obstacle varies only roughly half as quick as in the original half length channel. Then in the limit of $L \to \infty$ one can expect to have no residual shear stresses except around the obstacle.
The following plots do verify this expectation and show that one can indeed expect the shear residual inside the channel part away from the obstacle to scale with $1/L$ and therefore vanish as $L \to \infty$.

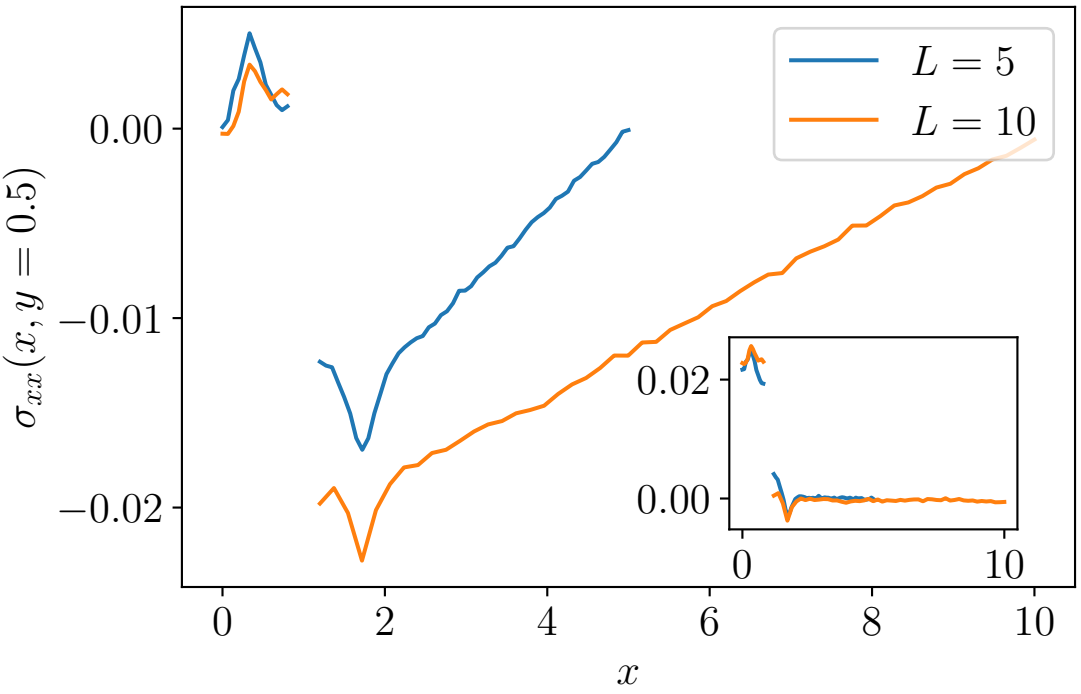

Figure 4.22: $\sigma_{xx}(x, y = 0.5)$ for both the standard $L = 5$ channel with obstacle and for the longer $L = 10$ channel. In the inlet view the periodicity is subtracted.

Short Summary

To summarize the discussion on residual stresses so far, it can be said that the the geometrical setup needs to allow $\partial_x \neq 0$ in order to make it possible that $\partial_y \sigma_{xy}$ is not zero, but balanced by $\partial_x \sigma_{xx}$ which is clearly non vanishing because of the geometry (for example with an obstacle like done in this thesis). The second observation, that away from the obstacle, in the normal channel one has small residual shear stresses might be because of the periodic boundary conditions which forces σ_{xx} to vary slowly in x direction also in the channel region and therefore induce residual shear stresses in order to fulfill the Stokes equation $\partial_x \sigma_{xx} = -\partial_y \sigma_{xy}$ [51].
In the next subsection it will be seen that the residual stresses that might be induces by the periodic boundary conditions take a minor role in experimental realizations because they are to small to be visualized by stress-optical effects between crossed polarizers.

4.4.3 Stress-Optical Visualization of the Residual Stresses

For transparent materials, a non-destructive method to observe residual stresses employs the stress-optical effect: otherwise non-birefringent materials are observed to become optically birefringent in

response to mechanical stress. This led Maxwell to postulate the stress-optical law [40], $\Delta n = n_o - n_e = C(\sigma_1 - \sigma_2)$, where $\sigma_{1,2}$ are the stress eigenvalues in the plane perpendicular to the propagation of light, and $n_{o,e}$ are the refractive indices along the optical axes defined by the corresponding stress eigenvalues. C is called the stress-optical coefficient. Assuming a slab of material whose properties are invariant along the light-propagation direction (taken to be along z), a textbook calculation shows that the transmitted light intensity when placing the sample between two circular polarizers, is (only here λ_w is once used as the wavelength!):

$$I(\lambda_w, \delta) = I_0(\lambda_w)\cos(\delta/2)^2,$$

where

$$\delta = (2\pi z/\lambda_w)\Delta n$$

is the (stress-dependent) optical retardation. If we assume illumination by a white-light source (I_0 constant across the visible spectrum $\lambda_w \in [360, 830]$nm), a colorful transmission spectrum will be recorded by the observer. This spectrum $I(\lambda, \delta)$ can be converted to empirical RGB values of colors as perceived by the human eye [50]. This is the color bar used in the figure below.

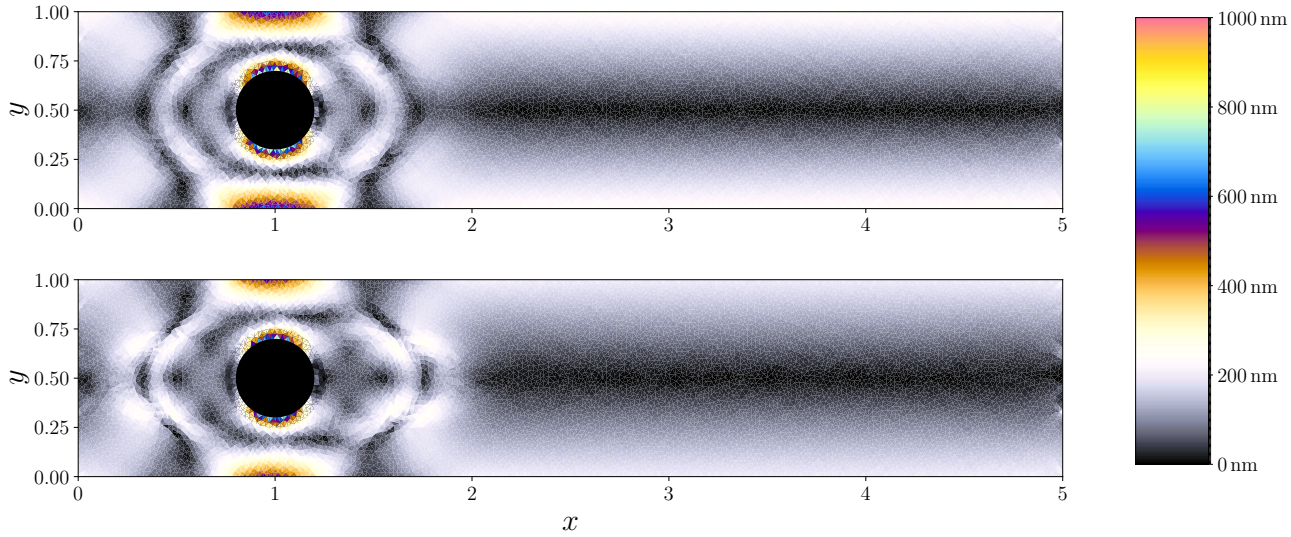

Figure 4.23: Residual-stress induced birefringence in a 5:1 rectangular channel with a circular obstacle, after cessation of a pressure-driven flow with pressure drops (a) $\Delta p/G_\infty = 1$, (b) $\Delta p/G_\infty = 2$ per channel length $L = 5H$. Colors represent optical path lengths for white-light illumination (as indicated by the color bar) assuming sample thickness h and stress-optical coefficient C such that $Ch = 1\text{mm}/G_\infty$.

4.4.4 Linear Elasticity Theory of Residual Stresses

The analysis of structures and their deformations is one of the major activities of modern engineering, a framework often used is linear elasticity theory which linearly relates small deformations $\vec{u}$ of a body Ω to the internal stresses σ. To study the influence of residual stresses to the shape of the body when cut free we set the full internal stress $\underline{\underline{\sigma}} = \underline{\underline{\hat{\sigma}}} + \underline{\underline{\sigma}}_{res}$, with $\hat{\sigma}$ the stresses that arise from linear elasticity and σ_{res} the residual stresses frozen in the material. Under the assumption that there are no external forces acting on either the bulk of the material or the surfaces and denoting the deformation field of

the material with $\vec{u}$ the governing equations of linear elasticity are given by

$$\begin{aligned}\vec{\nabla} \cdot \underline{\underline{\sigma}} &= 0,\\ \underline{\underline{\hat{\sigma}}} &= \lambda \mathrm{tr}(\underline{\underline{\varepsilon}})\mathrm{Id} + 2\mu\underline{\underline{\varepsilon}},\\ \underline{\underline{\varepsilon}} &= \frac{1}{2}\left(\vec{\nabla} \otimes \vec{u} + (\vec{\nabla} \otimes \vec{u})^T\right),\end{aligned}$$

together with the mixed boundary conditions that the total internal stress $\underline{\underline{\sigma}}$ is perpendicular to the free surfaces Γ_1, which are both the upper and lower surface and the hole in our case and that on the fixed surfaces Γ_2 there is no deformation

$$\begin{aligned}\underline{\underline{\sigma}} \cdot \vec{n} &= 0 \quad \text{on } \Gamma_1,\\ \vec{u} &= 0 \quad \text{on } \Gamma_2.\end{aligned}$$

Even though the residual stress is of course divergence-free ($\vec{\nabla} \cdot \underline{\underline{\sigma}}^{res} = 0$) its influence is expressed in the first boundary condition at the free surfaces in a way that the elastic stresses have to balance the residual stress $\underline{\underline{\hat{\sigma}}} \cdot \vec{n} = -\underline{\underline{\sigma}}^{res} \cdot \vec{n}$. To quantify the influence of the residual stress through the boundary conditions we used another FEM simulation with parameters λ, μ and simple linear continuous elements ('CG1' or sometimes called 'P1') for the displacements $\vec{u}$ to calculate the the shape (given by the deformations) and the resulting relaxed residual stresses $\underline{\underline{\hat{\sigma}}}$. The observation from this simulation is that the body shrinks around the hole in order to balance the residual stresses normal to the free surfaces.

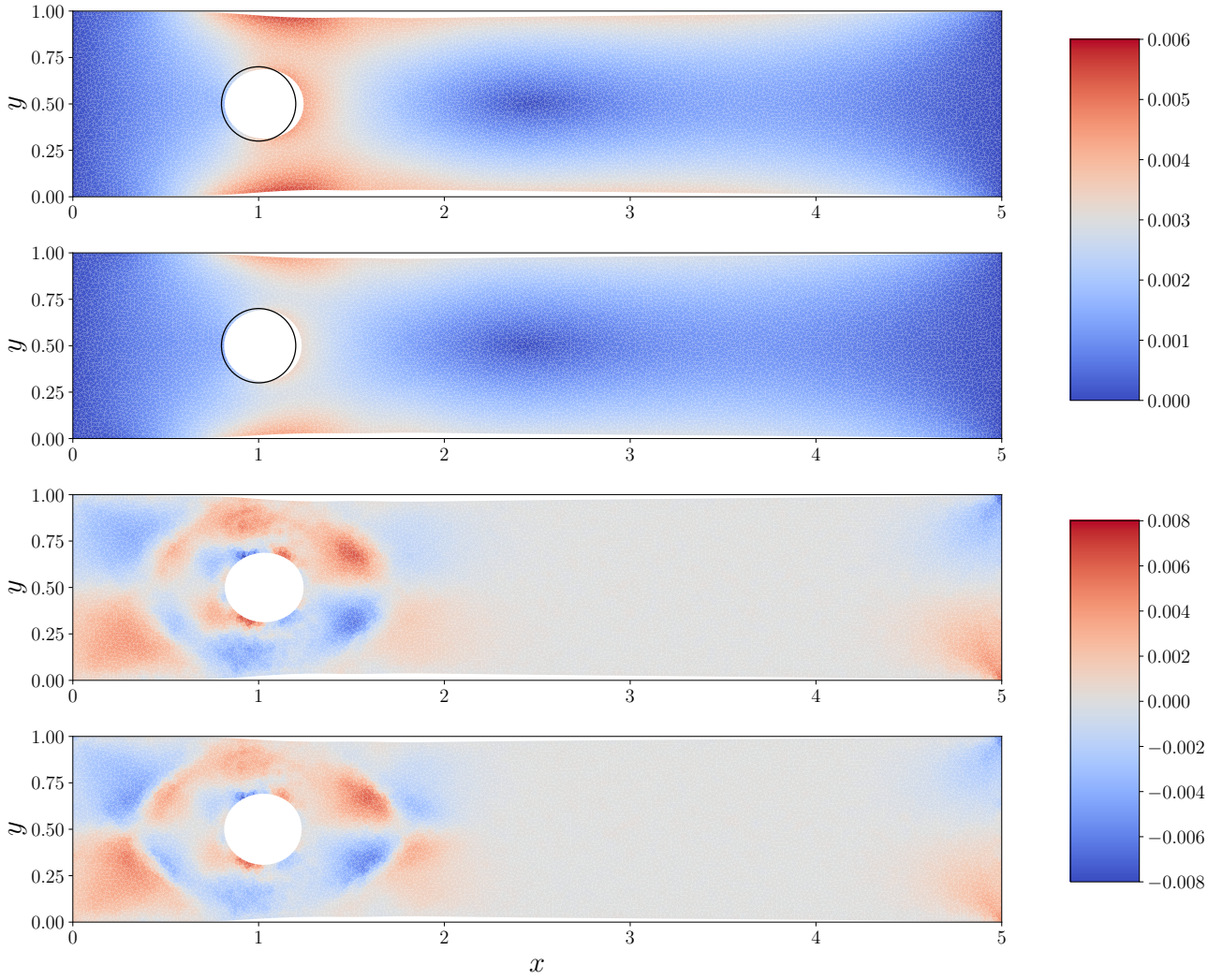

Figure 4.24: Magnitude of the eigenstrain caused by the residual stresses (top: $\Delta p = 1$, bottom: $\Delta p = 2$). Also shown are the relaxed residual shear stresses σ_{xy}.

4.5 4:1 Contraction / Extension Flow

Another classical benchmark geometry that is well established for over 30 years [3],[35] is the 4:1 contraction – already mentioned in the last chapter – where the channel abruptly contracts to one quarter of its width (or height). The popularity of this geometry is reasoned because the contraction of flow is of great importance in many processing operations, such as molding and extrusion of viscoelastic (polymeric) materials. Furthermore, the 4:1 planar contraction is a suitable benchmark problem for the evaluation of new models or codes [26]. The ability to be able to simulate the viscoelastic flow of integral constitutive models in such a slightly more complicated geometry (compared to the classical rectangular channel) does show the advanced ability and versatility that the finite element simulation technique has over other methods such as lattice Boltzmann or simple finite difference schemes.
This versatility can be seen in the following figure, where the mesh used for the simulations in this subsection is shown. Note that the cell diameter decreases by a factor of 4 from $h = 0.025$ in the wide are towards $h = 0.00625$ in the contracted area, such that in both the wide and contracted area are 40 cells from bottom to top. The total number of cells is 65974. As in the previous simulations periodic boundary conditions in the x-direction are used.

A single simulation of the MCT-ITT model, using these parameters, takes around 20 days utilizing 24 cores of a dual Xeon E5-2650v4 workstation and needs around 120 GB of memory. The same simulation, but using the generalized Maxwell model only takes around 2 day on the same machine and just needs memory in the order of 3 GB.

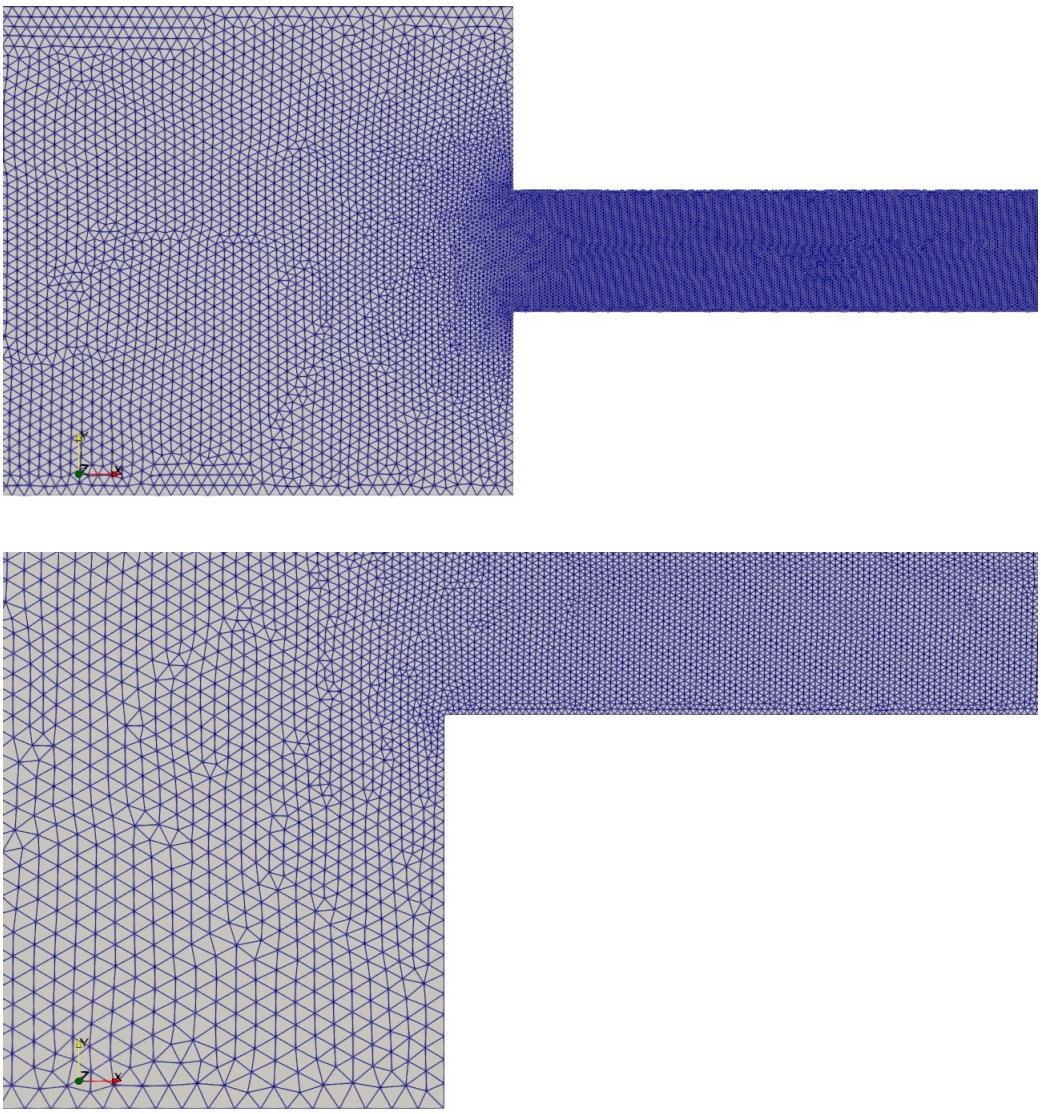

Figure 4.25: Parts of the 4:1 contraction mesh used in the simulations. Cells diameter decreases from $h = 0.025$ in the wide are towards $h = 0.00625$ in the contracted area.

4.5.1 Pressure Driven Flow and transient Cessation in the 4:1 Contraction

The pressure driven flow through the periodic 4:1 contraction has been simulated for both the MCT-ITT and the generalized Maxwell model using the implicit Euler scheme with a time step $\Delta t = 0.05$ and 7 blocks of 16 steps in age, which again results in the fact that there is no cut-off in history / age. For the high pressure simulations a pressure drop of $\Delta p = 20$ over the periodic length of $L = 10$ (which means $|\nabla p| = \Delta p / L = 2$ in the wide area) was used. The MCT glass transition parameter was set to $\epsilon = 0.01$, while in the generalized Maxwell model $\lambda_c = 10$ was used, both models where simulated with

the standard critical yield parameter $\gamma_c = 0.1$.
Similar to previous simulations using the rectangular channel with the spherical obstacle the pressure drop is removed after 1/4 of the total simulation time of $t_{end} = 101.6$ to study the cessation of flow and whether or not residual shear stresses remain after the material has come to rest. In the figure below the velocity field and streamlines of both the MCT-ITT and the generalized Maxwell model are shown in the steady state at $t = t_{off} - dt$ and at $t = t_off + \{1, 2, 3, 5, 7, 9\}$.

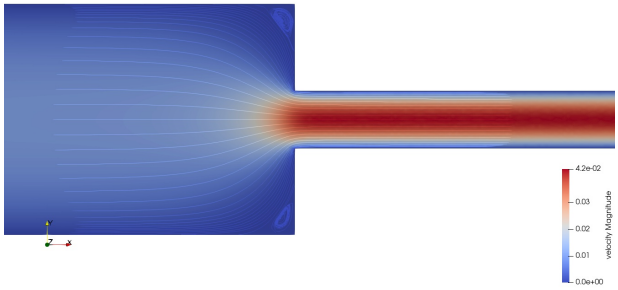

(a) MCT-ITT model: velocity field and streamlines at $t = t_{off} - dt$.

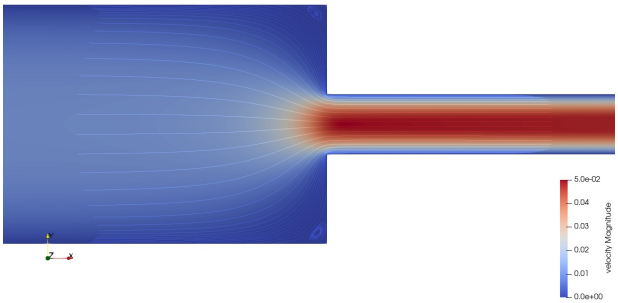

(b) Generalized Maxwell model: velocity field and streamlines at $t = t_{off} - dt$.

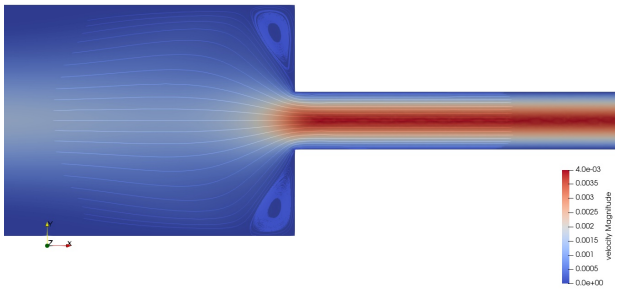

(c) MCT-ITT model: velocity field and streamlines at $t = t_{off} + 1$.

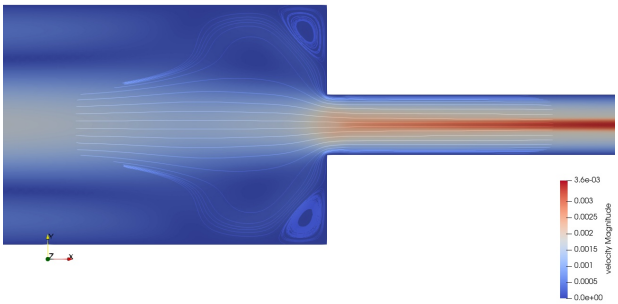

(d) Generalized Maxwell model: velocity field and streamlines at $t = t_{off} + 1$.

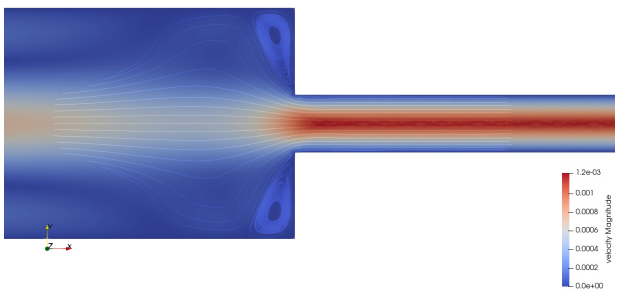

(e) MCT-ITT model: velocity field and streamlines at $t = t_{off} + 2$.

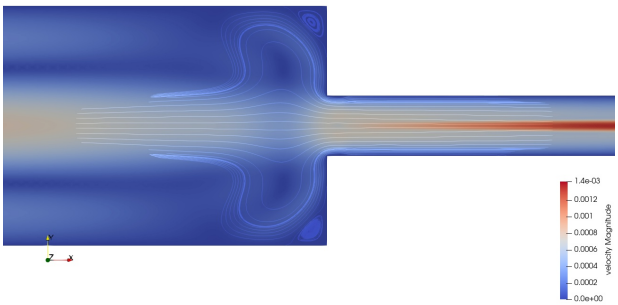

(f) Generalized Maxwell model: velocity field and streamlines at $t = t_{off} + 2$.

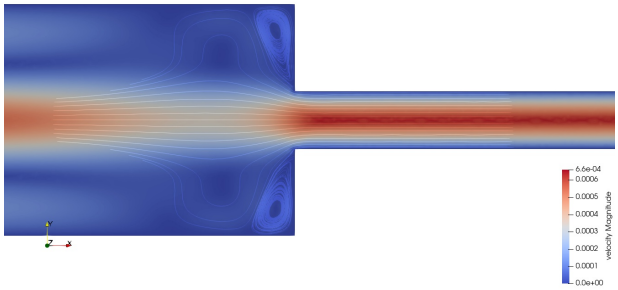

(a) MCT-ITT model: velocity field and streamlines at $t = t_{off} + 3$.

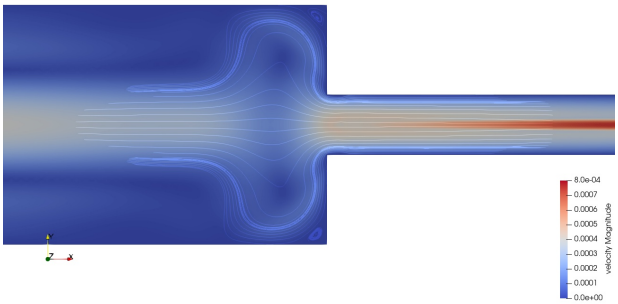

(b) Generalized Maxwell model: velocity field and streamlines at $t = t_{off} + 3$.

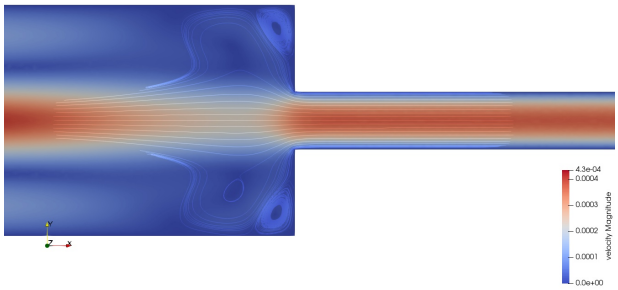

(c) MCT-ITT model: velocity field and streamlines at $t = t_{off} + 5$.

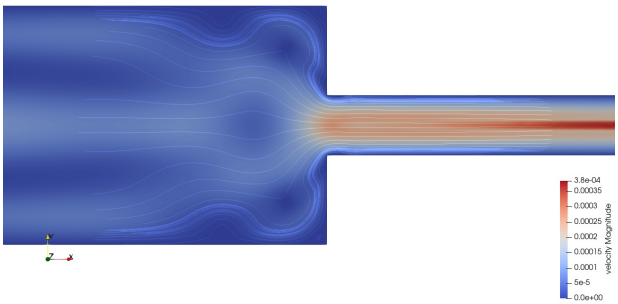

(d) Generalized Maxwell model: velocity field and streamlines at $t = t_{off} + 5$.

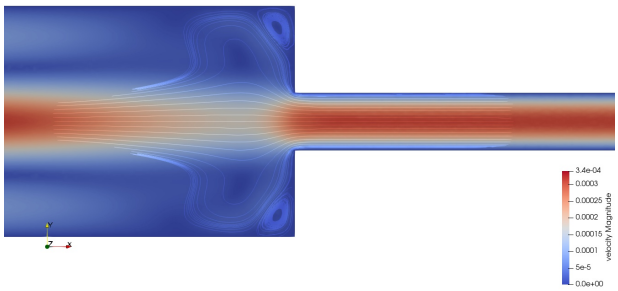

(e) MCT-ITT model: velocity field and streamlines at $t = t_{off} + 7$.

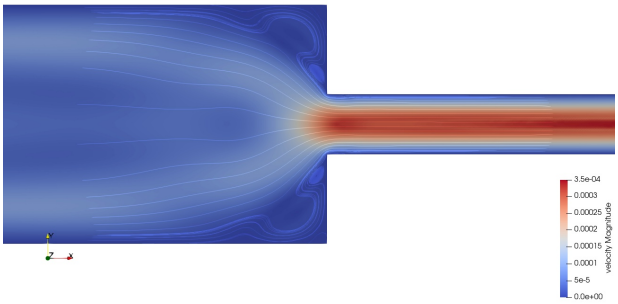

(f) Generalized Maxwell model: velocity field and streamlines at $t = t_{off} + 7$.

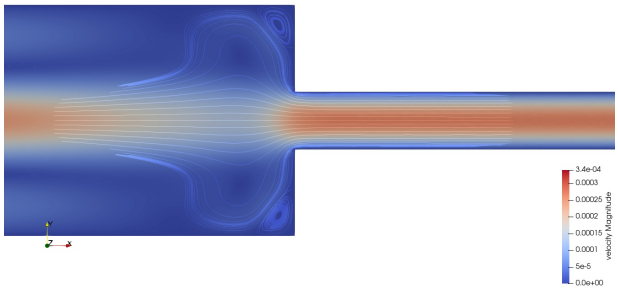

(g) MCT-ITT model: velocity field and streamlines at $t = t_{off} + 9$.

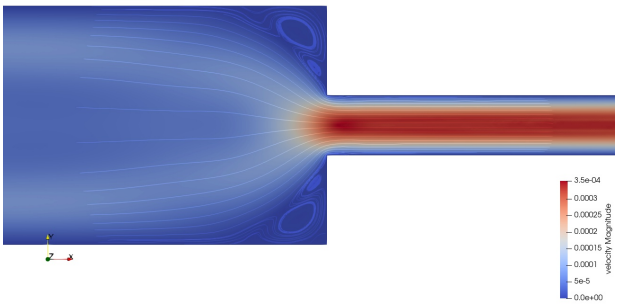

(h) Generalized Maxwell model: velocity field and streamlines at $t = t_{off} + 9$.

One can see that in the transient phase after switching off the driving pressure gradient both models show a strong vortex formation in the corners, this is clearly an non-Newtonian phenomenon since the overall velocity magnitude is decreasing (because it is a dispersive system with friction). A both possible and plausible explanation is that the material near the contraction edges – which is more sheared and therefore has a lower viscosity – gets pushed back (due to the elasticity) against higher viscosity material resulting in a flow into the corners and this vortex formation.

Steady State Shear Stresses predicted by the MCT-ITT Model

To study steady state shear stresses in the 4:1 contraction the same simulation setups (MCT-ITT model with parameters $\epsilon = 0.01$ and $\gamma_c = 0.1$) are used (only the pressure drop is chosen differently as $\frac{\Delta p}{L} = 1$).
In the steady state one observes the standard linear shear stress pattern inside the wide ($x < 4$ or $x > 6$) and narrow ($4 < x < 6$) channels and a more complicated, but familiar pattern around see edges (see [13] to compare to a differential viscoelastic constitutive model). The following images show the steady state shear stress pattern, on the left side the colorbar is restricted to have a better visualization of the pattern around the edges while on the right side the colorbar is adjusted to fit the whole range of found values.

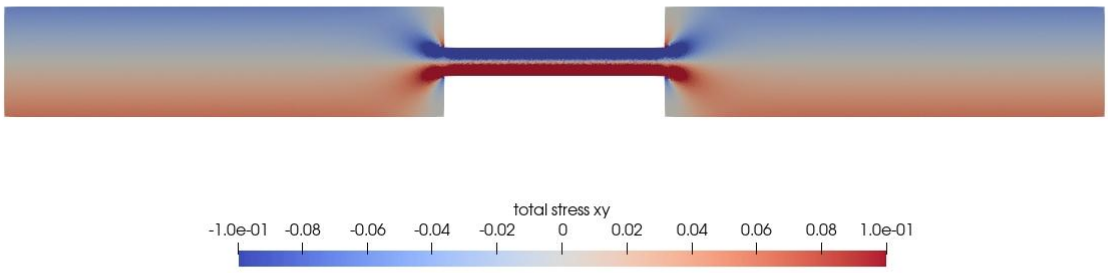

(a) Steady state σ_{xy} for the standard MCT-ITT system driven by $\frac{\Delta p}{L} = 1$ with a restricted colorbar.

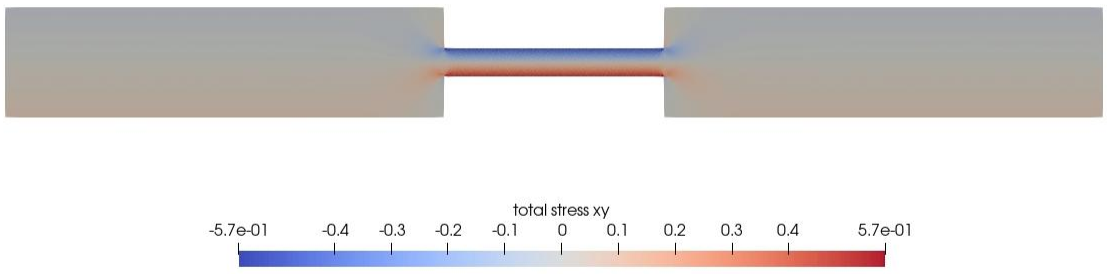

(b) Steady state σ_{xy} for the standard MCT-ITT system driven by $\frac{\Delta p}{L} = 1$ with full colorbar (showing the whole range of found values).

4.5.2 Residual Stresses in 4:1 Contraction Flow predicted by the MCT-ITT Model

The geometry of the abrupt 4:1 contraction allows flow-induced residual shear stresses since $\partial_x \neq 0$ is valid in the contraction region.
After turning off the driving pressure gradient the system comes to rest, similar to the geometrical setup with the spherical obstacle one finds that there are remaining residual shear stresses. One also finds a similar sign flip in the narrow channel as the one around the spherical obstacle. Further one can observe a stress free region directly in front (and also directly after) the contraction area.

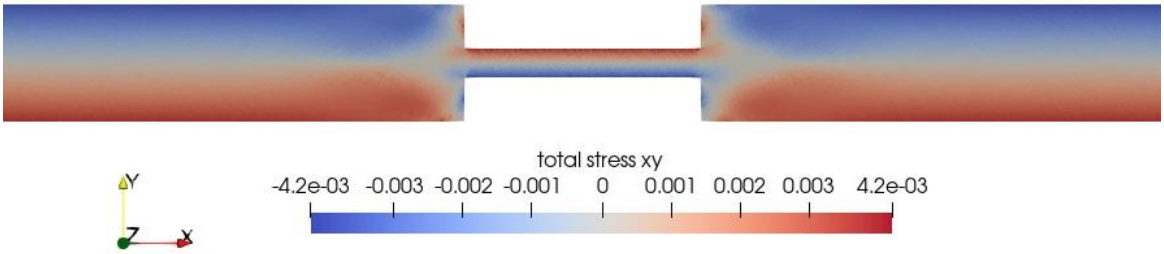

Figure 4.29: Residual shear stresses of the standard MCT-ITT model previously driven by a pressure gradient of by $\frac{\Delta p}{L} = 1$.

Another effect one observes after cessation of the system is that the residual shear stresses in the wide channel area are relatively (compared to the stresses in the stronger narrow channel) much stronger than the shear stresses in the steady state pressure driven system. This effect and the sign-flipping can be seen best in a line plot of σ_{xy} over the x-position of the (periodic) simulation domain for a fixed y value. Here $y = 0.4$ is chosen, which is in the lower half, where $\sigma_{xy} > 0$ in the steady state of the pressure driven system.

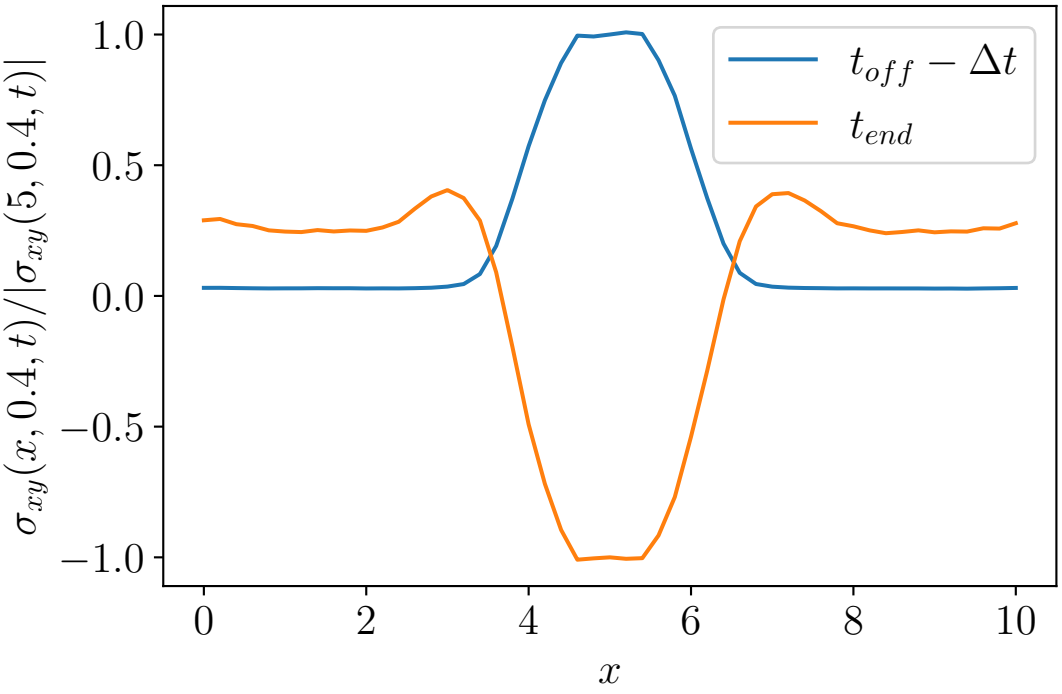

Figure 4.30: Line plot of $\frac{\sigma_{xy}(x,0.4)}{|\sigma_{xy}(5,0.4)|}$ is shown for both the pressure driven steady state (so just before the switch-off at $t = t_{off} - \Delta t$) and after cessation of the flow (at the end of the simulation, $t = t_{end}$).

Because of the first component of the Stokes equation $\partial_x \sigma_{xx} + \partial_y \sigma_{xy} = 0$ – and the geometrical symmetry around the the $y = 0.5$ line – one can already know that also the residual normal stress σ_{xx} must have a negative slope (regarding the x-positional variable for $y = 0.4$ fixed) inside the narrow ($4 < x < 6$) part of the simulation domain, while the steady state normal stress in the pressure driven phase of the simulation must have a positive slope.

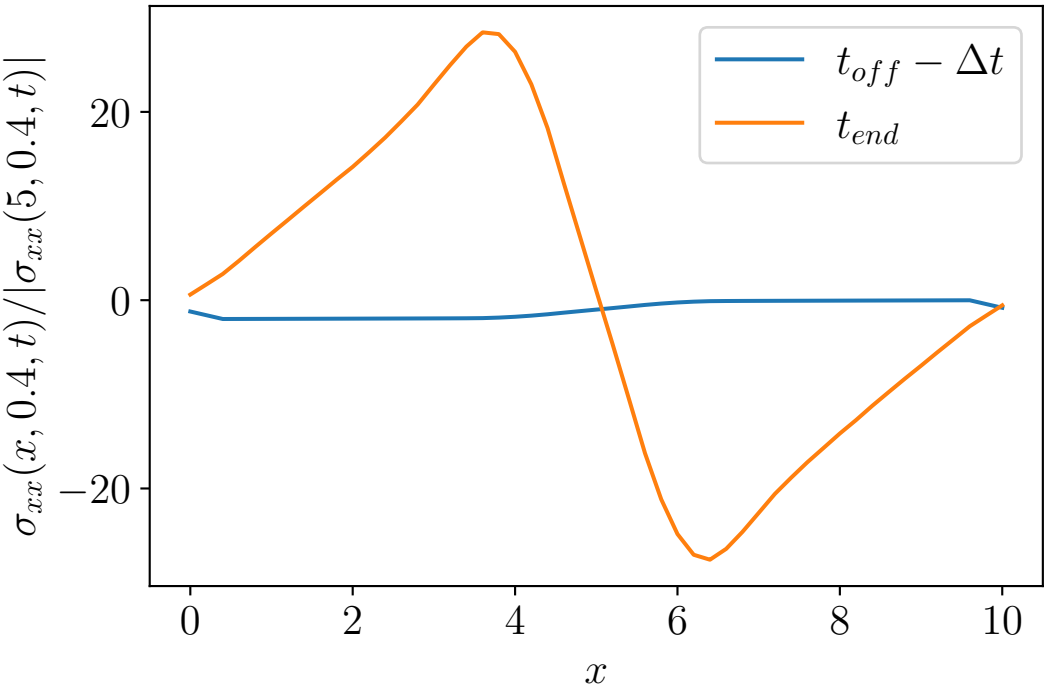

Figure 4.31: Line plot of $\frac{\sigma_{xx}(x,0.4)}{|\sigma_{xx}(5,0.4)|}$ is shown for both the pressure driven steady state (so just before the switch-off at $t = t_{off} - \Delta t$) and after cessation of the flow (t the end of the simulation ($t = t_{end}$).

We expect the same finite-size effects as discussed above for the channel with a spherical obstacle (see 4.4.2).

Line Plots of Residual Stresses

Another property worth looking at is the residual first normal stress difference N_1 at the end of the simulation. As in the previous simulation concerning viscoelastoplastic flow past the spherical obstacle N_1 tends to be constant away from the x-invariance breaking areas, which are in this geometrical setup the contraction areas. The normal stress σ_{xx} seems to be affected by the periodical boundaries in x-direction in the same way as the simulations concerning the flow around the spherical obstacle done in the previous subsection (see the dedicated sub-subsection in 4.4.2).

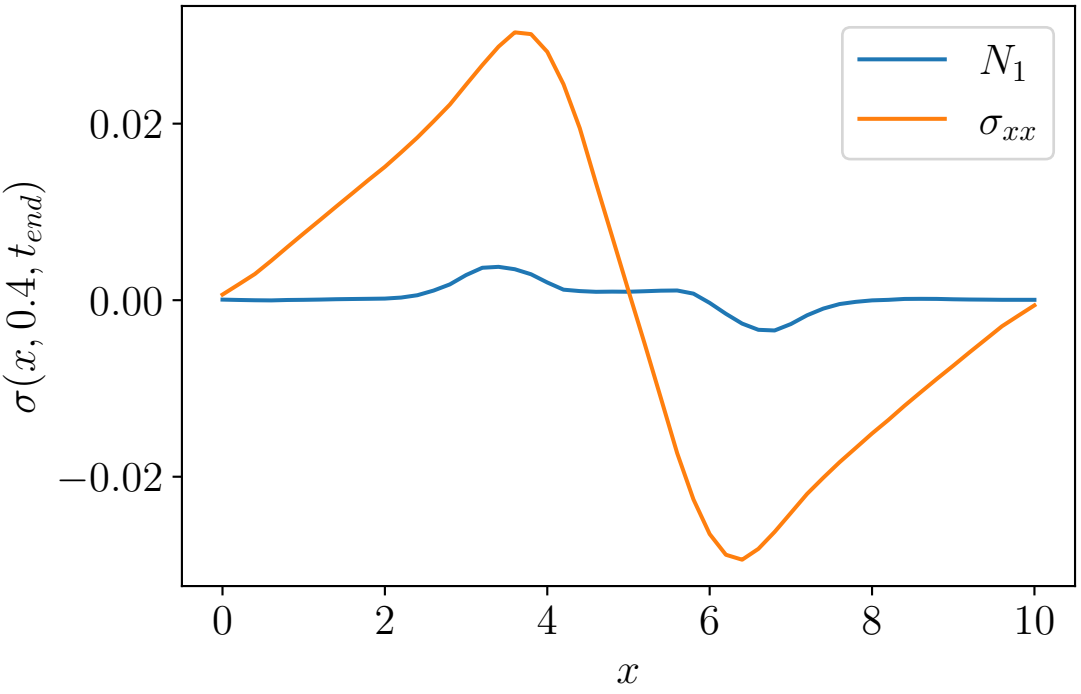

Figure 4.32: Line plot at constant $y = 0.4$ of the residual normal stress σ_{xx} and the residual first normal stress difference N_1 at the end of the simulation ($t = t_{end}$).

Further one can have a look on line plots of the residual shear stress and the first normal stress difference (at the end of the simulation at $t = t_{end}$) for fixed values of x, for example $x = 3.5$ and $x = 3.9$ (contraction at $x = 4$). Note that due to the geometrical symmetry around the $y = 0.5$ axis the shear stress σ_{xy} must be (approximately) zero at $y = 0.5$, which is the case as one can see from the following two line plots. For the first normal stress difference N_1 this is not the case as one can already see from the surface plot of the first normal stress difference shown below.

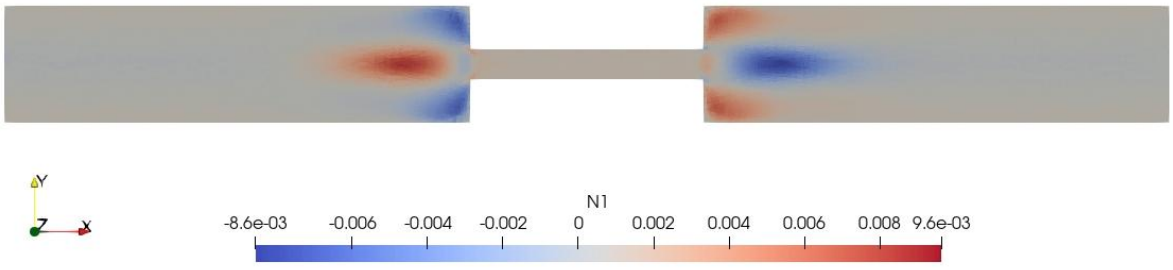

Figure 4.33: Residual first normal stress difference N_1 of the standard MCT-ITT model previously driven by a pressure gradient of by $\frac{\Delta p}{L} = 1$.

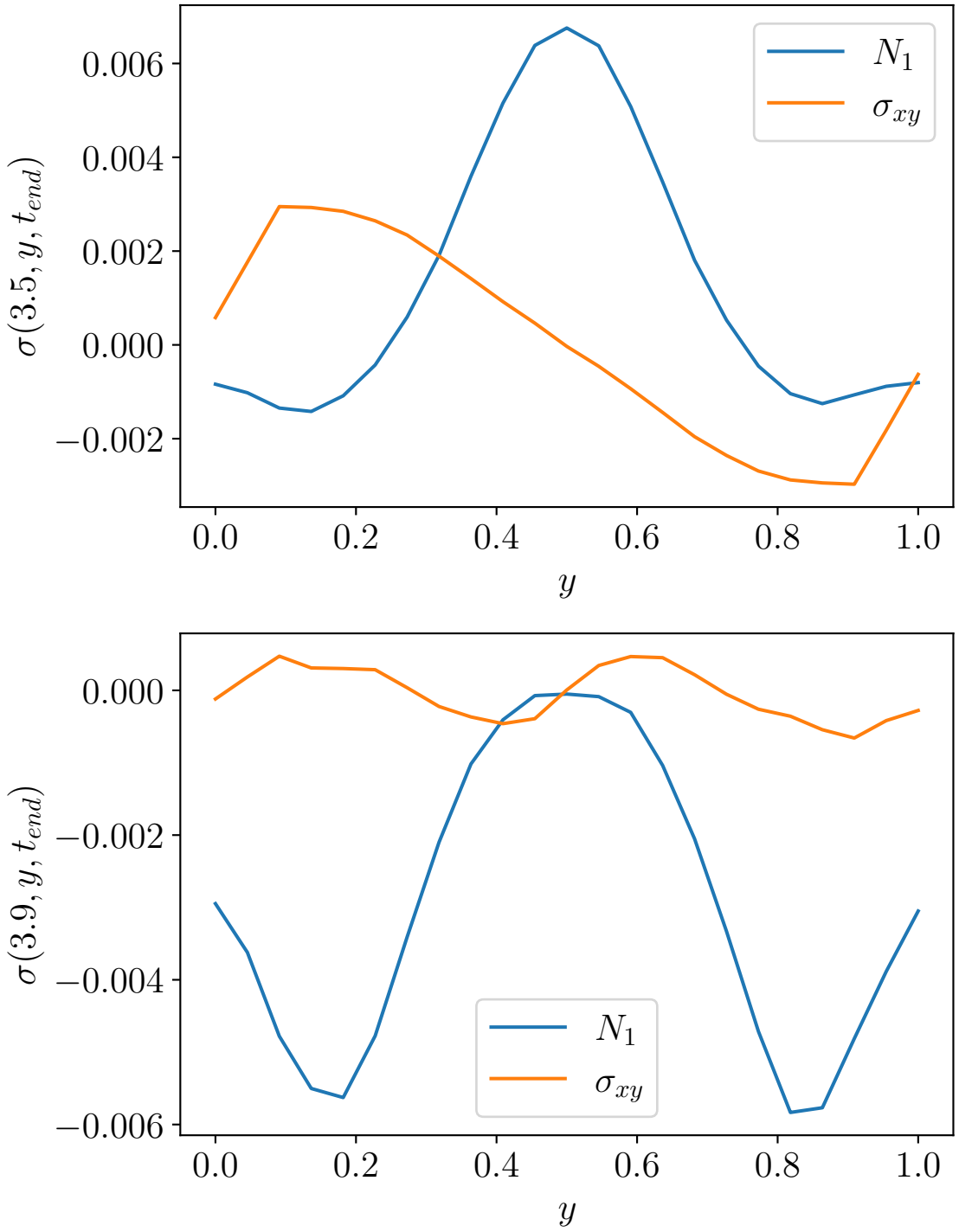

Figure 4.34: Line plot at constant $x = 3.5$ and $x = 3.9$ of the residual normal stress σ_{xy} and the residual first normal stress difference N_1 at the end of the simulation ($t = t_{end}$).

Chapter 5

Advectional Extension to the Schematic Mode-Coupling Theory

This chapter will provide an advectional extension to the schematic MCT equation. This means that the partial time derivatives will be exchanged by material derivatives which continuum mechanics desires to correctly describe the rate of change of any scalar quantity in the Eulerian reference frame. One could consider this a similar approach as the upper convected (or Oldroyd derivative version B) done by Oldroyd [42] to correctly describe the rate of change of a tensorial quantity in the Eulerian reference frame. Of course this exchange of the partial time derivative with the material derivative is a rather heuristic approach and has no statistical physics based derivation yet, however there are existing efforts by Alexandre Nicolas and Matthias Fuchs [41] towards this direction.

5.1 Reasoning of the Advectional Extension

In the MCT equation

$$\partial_t \phi(t,t') + \phi(t,t') + h_{tt'} \int_{t'}^{t} h_{tt''} m(t,t'') \partial_{t''} \phi(t'',t') \mathrm{d}t'' = 0$$

all spatial information is encoded in the h-factors and therefore come from the Finger tensor $\underline{\underline{B}}$. Since the equation of the Finger tensor $\underline{\underline{B}}$ is formulated in the laboratory fixed Eulerian reference frame and therefore contains the advected (or material) derivative (the upper convected derivative is the tensorial extension of the material derivative) one could argue that the correlation function ϕ is also formulated in Eulerian coordinates. According to continuum mechanics the correct temporal rate of change of any scalar quantity in the Eulerian system is the material derivative $\frac{D}{Dt}$, so one might exchange the partial time derivatives in the schematic version of the MCT equation with material derivatives. This leads the above equation to change to

$$\frac{D}{Dt}\phi(t,t') + \phi(t,t') + h_{tt'} \int_{t'}^{t} h_{tt''} m(t,t'') \frac{D}{Dt''} \phi(t'',t') \mathrm{d}t'' = 0, \tag{5.1}$$

where all the partial time derivatives have been replaced by material derivatives.

Reduction to the Maxwell Model

If one thinks of a Markovian process the memory kernel should be δ-function like

$$m(t,t'',t') = 2\hat{\lambda}\delta(t-t''),$$

such that the MCT equation reduces to

$$2\lambda\frac{D}{Dt}\phi(t,t') + \phi(t,t') = 0, \tag{5.2}$$

with $2\lambda = \Gamma + \hat{\lambda}$, where Γ is the intrinsic time scale from MCT that has always been set to unity previously. If one now sets $G(t,t') = \phi^2(t,t')$ one obtains the known differential equation of the Maxwell model:

$$\frac{D}{Dt}G(t,t') = -\frac{1}{\lambda}G(t,t'). \tag{5.3}$$

In the same spirit one could also think of the White-Metzner and generalized Maxwell Model as a reduced form of the MCT equation, where basically the integral is removed by a δ-like approach to the memory kernel.

5.2 Numerical Details of the Advected MCT-ITT Model

5.2.1 Outer Advection

The implementation of the first (called outer, because it is outside the memory integral) advected derivative $\frac{D}{Dt}$ on the very left of equation 5.1 can be done without changing the memory setup. One simply uses $\vec{v}_{old} \coloneqq \vec{v}(t-\Delta t)$ as the same zeroth order approximation to $\vec{v}(t)$ as in the numerical method to calculate the Finger tensor (see 4.1.3). The additional error is of the order $\mathcal{O}(\Delta t)$ which is the same order as the implicit Euler scheme.
By only taking the into account the outer advection term the disctretized two-time sMCT equation 4.15 changes to:

$$\left(\frac{1}{\Delta t} + [\vec{v}_{old}\cdot\vec{\nabla}] + 1 + h_{i,l}h_{i,1}m_{i,1}\right)\phi_{i,l} + h_{i,l}^2 m_{i,l}\left[\phi_{i-l+1,1} - 1\right] + R_{i,l} = 0, \tag{5.4}$$

where the term $R_{i,l}$ is unchanged.

DG0 Method

However, in contrast to the algebraic equation 4.15 this is a partial differential equation, therefore a DG0 (it is convenient that ϕ and $\underline{\underline{B}}$, $\underline{\underline{\sigma}}$ are all approximated the same way to avoid interpolations or projections) weak formulation must be derived. The weak formualtion of 5.4 can be found in similar fashion as described in subsections 3.1.5 or 4.1.3. Denoting the test-function by ψ the weak formulation reads

$$\begin{aligned} F[\phi_{i,l}] = &\sum_{K\in\mathcal{K}}\int_K\left(\frac{1}{\Delta t} + 1 + h_{i,l}h_{i,1}m_{i,1}\right)\phi_{i,l}\cdot\psi - \phi_{i,l}\cdot\operatorname{div}(\psi\vec{v}_{old})\ \mathrm{d}x \\ &+ \sum_{K\in\mathcal{K}}\int_K\left(h_{i,l}^2 m_{i,l}\left[\phi_{i-l+1,1}-1\right] + R_{i,l}\right)\cdot\psi\ \mathrm{d}x \\ &+ \sum_{K\in\mathcal{K}}\int_{\partial K}\left(v_{n,+}\cdot\phi_{i,l}^{+} + v_{n,-}\cdot\phi_{i,l}^{-}\right)\cdot[\psi]\ \mathrm{d}S + \sum_{E\in\mathcal{E}_I}\int_E(v_n\cdot\phi_{i,l})\cdot\psi\ \mathrm{d}s \overset{!}{=} 0. \end{aligned}$$

To solve $F[\phi_{i,l}] = 0$ for all valid test-functions ψ one uses the Newton scheme in an operator sense. This is quite similar to the multidimensional Newton scheme to numerically solve $f(x) = 0$ for a given $f : \mathbb{R}^n \to \mathbb{R}^m$ via iterativly solving

$$\begin{aligned} J_f(x^{(n)})\Delta x^{(n)} &= -f(x^{(n)}), \\ x^{(n+1)} &= x^{(n)} + \Delta x^{(n)}, \end{aligned}$$

where $J_f(x^{(n)})$ is the Jacobian evaluated at the n-th iteration point $x^{(n)}$ [52]. However instead of a finite dimensional (Jacobi-) matrix the functional derivative $DF(\phi_{i,l}^{(n)})[\Delta\phi_{i,l}^{(n)}]$ is an infinite dimensional (weak differential-) operator acting on $\Delta\phi_{i,l}^{(n)}$.

$$\begin{aligned} DF(\phi_{i,l})[\Delta\phi_{i,l}] = &\sum_{K\in\mathcal{K}} \int_K \left(\frac{1}{\Delta t} + 1 + h_{i,l}h_{i,1}m_{i,1}\right)\Delta\phi_{i,l}\cdot\psi - \Delta\phi_{i,l}\cdot\operatorname{div}(\psi\vec{v}_{old})\ \mathrm{d}x \\ &+ \sum_{K\in\mathcal{K}} \int_K h_{i,l}^2 m'_{i,l}\Delta\phi_{i,l}\left[\phi_{i-l+1,1} - 1\right]\cdot\psi\ \mathrm{d}x \\ &+ \sum_{K\in\mathcal{K}} \int_{\partial K} \left(v_{n,+}\cdot\Delta\phi_{i,l}^{+} + v_{n,-}\cdot\Delta\phi_{i,l}^{-}\right)\cdot[\psi]\ \mathrm{d}S + \sum_{E\in\mathcal{E}_I}\int_E (v_n\cdot\Delta\phi_{i,l})\cdot\psi\ \mathrm{d}s, \end{aligned} \tag{5.5}$$

with $m'_{i,l} = v_1 + 2v_2\phi_{i,l}$ as in the previous chapter, since the F12 model (like proposed in [8]) is used throughout all simulations.
The functional Newton scheme is then given by iterativly solving

$$\begin{aligned} DF(\phi_{i,l}^{(n)})[\Delta\phi_{i,l}^{(n)}] &= -F[\phi_{i,l}^{(n)}], \\ \phi_{i,l}^{(n+1)} &= \phi_{i,l}^{(n)} + \Delta\phi_{i,l}^{(n)}, \end{aligned} \tag{5.6}$$

in its weak form using the "mumps" LU solver provided by the FEniCS environment.
A good initial guess is (similar to the Newton scheme provided by the algebraic equation 4.15) given by $\phi_{i,l}^{(0)} = \phi_{i-1,l}$.

5.2.2 Inner Advection

Memory Management

The advected derivative $\frac{D}{Dt''}$ inside the memory integral of 5.1, referred to as inner advection (term), causes more problems than the outer advection. The reason for this is that one needs the historical velocity field $\vec{v}(t'')$ for all integration points t'' between t' and t. These velocity fields $\vec{v}(t'')$ need to be stored in addition to the the previous memory management.

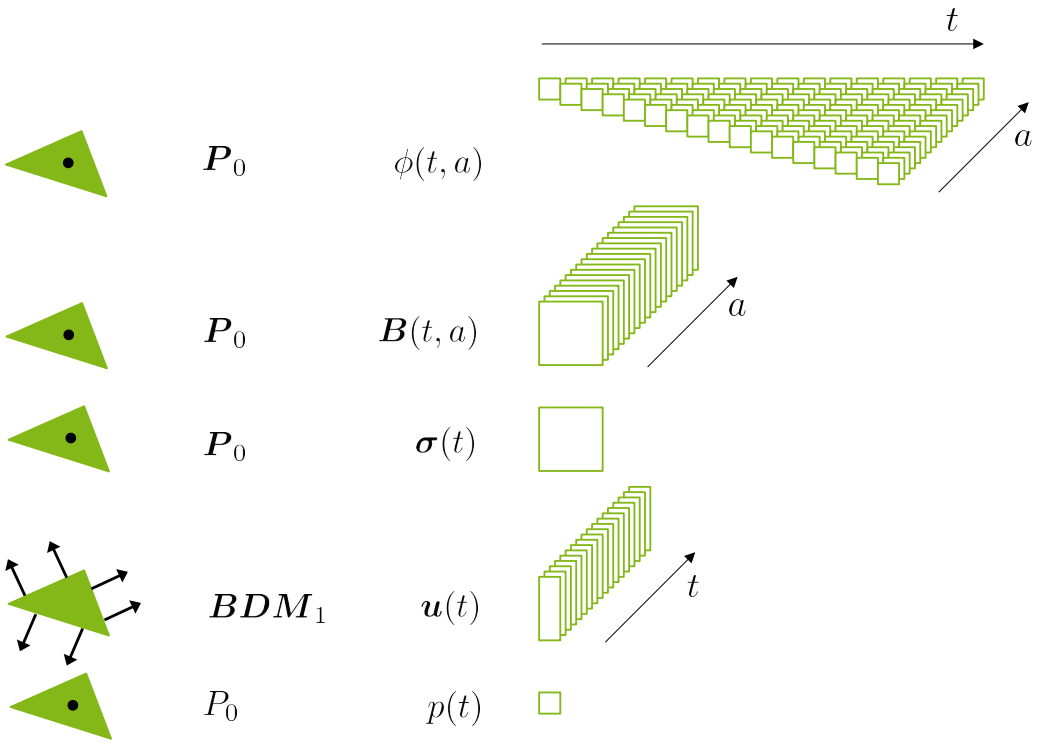

Figure 5.1: Schematic picture to visualize the memory management of the advected MCT-ITT model simulation. Figure courtesy of Dr. Timm Treskatis.

Changes to the Discretized sMCT Equation

The inner advection changes equation 5.4 further from the standard discretized two-time sMCT equation 4.14 in a way that there is an additional sum

$$h_{i,j}\sum_{k=j}^{i-1} h_{i,k}m_{i,k}[\vec{v}_k\cdot\vec{\nabla}]\phi_{k+1,j}(\Delta t)_k$$
$$= h_{i,j}^2 m_{i,j}[\vec{v}_j\cdot\vec{\nabla}]\phi_{j+1,j}(\Delta t)_j + h_{i,j}h_{i,i-1}m_{i,i-1}[\vec{v}_{i-1}\cdot\vec{\nabla}]\phi_{i,j}(\Delta t)_{i-1} + \sum_{k=j+1}^{i-2}\ldots$$

resulting from the additional inner advection term. One now has to be careful when changing from the j (reference time variable) indices to the $l = i - j$ indices (age variable) because the summation order is reversed.
The equation 5.4 changes to

$$\left(\frac{1}{\Delta t} + [\vec{v}_{old}\cdot\vec{\nabla}] + 1 + h_{i,l}h_{i,1}m_{i,1}\right)\phi_{i,l} + h_{i,l}^2 m_{i,l}\left[\phi_{i-l+1,1} - 1\right] + R_{i,l}$$
$$+ h_{i,l}^2 m_{i,l}[\vec{v}_{i-l}\cdot\vec{\nabla}]\phi_{i-l+1,1}(\Delta t)_l + h_{i,l}h_{i,1}m_{i,1}[\vec{v}_{i-1}\cdot\vec{\nabla}]\phi_{i,l}(\Delta t)_1$$
$$+ h_{i,l}\sum_{k=2}^{l-1} h_{i,k}m_{i,k}[\vec{v}_{i-k}\cdot\vec{\nabla}]\phi_{i-k+1,l-k+1}(\Delta t)_k = 0,$$

with the same $R_{i,l}$ as previously, also note that $\vec{v}_{old} \equiv \vec{v}_{i-1}$.
Because of the used DG0 elements the additional terms, which all contain a $\vec{v}\cdot\vec{\nabla}$-operator, do not only enter the second $\mathrm{d}x$ integral of equation 5.5, but also create new $\mathrm{d}S$ (for jumps between cells) and $\mathrm{d}s$

(for cells / edges on the boundaries) integrals:

$$
\begin{aligned}
F[\phi_{i,l}] = &\sum_{K\in\mathcal{K}} \int_K \left(\frac{1}{\Delta t} + 1 + h_{i,l}h_{i,1}m_{i,1}\right)\phi_{i,l}\cdot\psi - \left(1 + h_{i,l}h_{i,1}m_{i,1}(\Delta t)_1\right)\phi_{i,l}\cdot\operatorname{div}(\psi\vec{v}_{old})\ \mathrm{d}x \\
&+ \sum_{K\in\mathcal{K}} \int_K h_{i,l}^2 m_{i,l}\left(\left[\phi_{i-l+1,1} - 1\right]\cdot\psi - \phi_{i-l+1,1}(\Delta t)_l\cdot\operatorname{div}(\psi\vec{v}_{i-l})\right) + R_{i,l}\cdot\psi\ \mathrm{d}x \\
&- \sum_{K\in\mathcal{K}} \int_K h_{i,l}\sum_{k=2}^{l-1} h_{i,k}m_{i,k}\phi_{i-k+1,l-k+1}(\Delta t)_k\cdot\operatorname{div}(\psi\vec{v}_{i-k})\ \mathrm{d}x \\
&+ \sum_{K\in\mathcal{K}} \int_{\partial K} \left(1 + h_{i,l}h_{i,1}m_{i,1}(\Delta t)_1\right)\left(v_{n,+}\cdot\phi_{i,l}^{+} + v_{n,-}\cdot\phi_{i,l}^{-}\right)\cdot[\psi]\ \mathrm{d}S \\
&+ \sum_{E\in\mathcal{E}_I} \int_E \left(1 + h_{i,l}h_{i,1}m_{i,1}(\Delta t)_1\right)(v_n\cdot\phi_{i,l})\cdot\psi\ \mathrm{d}s \\
&+ \sum_{K\in\mathcal{K}} \int_{\partial K} h_{i,l}^2 m_{i,l}(\Delta t)_l\left(v_{i-l,n,+}\cdot\phi_{i-l+1,1}^{+} + v_{i-l,n,-}\cdot\phi_{i-l+1,1}^{-}\right)\cdot[\psi]\ \mathrm{d}S \\
&+ \sum_{E\in\mathcal{E}_I} \int_E h_{i,l}^2 m_{i,l}(\Delta t)_l\left(v_{i-l,n}\cdot\phi_{i-l+1,1}\right)\cdot\psi\ \mathrm{d}s \\
&+ \sum_{K\in\mathcal{K}} \int_{\partial K} h_{i,l}\sum_{k=2}^{l-1} h_{i,k}m_{i,k}(\Delta t)_k\left(v_{i-k,n,+}\cdot\phi_{i-k+1,l-k+1}^{+} + v_{i-k,n,-}\cdot\phi_{i-k+1,l-k+1}^{-}\right)\cdot[\psi]\ \mathrm{d}S \\
&+ \sum_{E\in\mathcal{E}_I} \int_E h_{i,l}\sum_{k=2}^{l-1} h_{i,k}m_{i,k}(\Delta t)_k(v_{i-k,n}\cdot\phi_{i-k+1,l-k+1})\cdot\psi\ \mathrm{d}s \overset{!}{=} 0. \qquad (5.7)
\end{aligned}
$$

To solve $F[\phi_{i,l}] = 0$ for all valid test-functions ψ one agian uses the Newton scheme in an operator sense. To be able to use the Newton scheme one first needs to calculate the functional derivative of $F[\phi_{i,l}]$ applied to $\Delta\phi_{i,l}$:

$$
\begin{aligned}
DF(\phi_{i,l})[\Delta\phi_{i,l}] = &\sum_{K\in\mathcal{K}} \int_K \left(\frac{1}{\Delta t} + 1 + h_{i,l}h_{i,1}m_{i,1}\right)\Delta\phi_{i,l}\cdot\psi - \left(1 + h_{i,l}h_{i,1}m_{i,1}(\Delta t)_1\right)\Delta\phi_{i,l}\cdot\operatorname{div}(\psi\vec{v}_{old})\mathrm{d}x \\
&+ \sum_{K\in\mathcal{K}} \int_K h_{i,l}^2 m'_{i,l}\Delta\phi_{i,l}\left(\left[\phi_{i-l+1,1} - 1\right]\cdot\psi - \phi_{i-l+1,1}(\Delta t)_l\cdot\operatorname{div}(\psi\vec{v}_{i-l})\right)\ \mathrm{d}x \\
&+ \sum_{K\in\mathcal{K}} \int_{\partial K} \left(1 + h_{i,l}h_{i,1}m_{i,1}(\Delta t)_1\right)\left(v_{n,+}\cdot\Delta\phi_{i,l}^{+} + v_{n,-}\cdot\Delta\phi_{i,l}^{-}\right)\cdot[\psi]\ \mathrm{d}S \\
&+ \sum_{E\in\mathcal{E}_I} \int_E \left(1 + h_{i,l}h_{i,1}m_{i,1}(\Delta t)_1\right)(v_n\cdot\Delta\phi_{i,l})\cdot\psi\ \mathrm{d}s \\
&+ \sum_{K\in\mathcal{K}} \int_{\partial K} h_{i,l}^2 m'_{i,l}\Delta\phi_{i,l}(\Delta t)_l\left(v_{i-l,n,+}\cdot\phi_{i-l+1,1}^{+} + v_{i-l,n,-}\cdot\phi_{i-l+1,1}^{-}\right)\cdot[\psi]\ \mathrm{d}S \\
&+ \sum_{E\in\mathcal{E}_I} \int_E h_{i,l}^2 m'_{i,l}\Delta\phi_{i,l}(\Delta t)_l\left(v_{i-l,n}\cdot\phi_{i-l+1,1}\right)\cdot\psi\ \mathrm{d}s \qquad (5.8)
\end{aligned}
$$

with $m'_{i,l} = v_1 + 2v_2\phi_{i,l}$ as previously.
The functional Newton scheme is again given by iterativly solving

$$
\begin{aligned}
DF(\phi_{i,l}^{(n)})[\Delta\phi_{i,l}^{(n)}] &= -F[\phi_{i,l}^{(n)}], \\
\phi_{i,l}^{(n+1)} &= \phi_{i,l}^{(n)} + \Delta\phi_{i,l}^{(n)},
\end{aligned}
$$

with the initial guess $\phi_{i,l}^{(0)} = \phi_{i-1,l}$.

Note that this procedure is still the same Marchuck-Yananko method [39] as previously. One does

not propagate the whole system $(\underline{\underline{\sigma}}[\underline{\underline{B}}, G], \vec{v}, p)$ at once, buts splits the propagation operator to first implicitly propagate $\underline{\underline{\sigma}}$ and therefore $\underline{\underline{B}}$ and $G \propto \phi^2$ with the old velocity field $\vec{v}_{old}$ and then solves the Stokes problem (propagate $(\vec{v}, p)$ from the old time step $t - \Delta t$ to the new time step t).

Note on the Advected Derivative in the Convolution Integral

Note that the $\vec{v}_k \cdot \vec{\nabla}$ was applied to $\phi_{k+1,j}$ in the convolution integral, one also could have applied it onto $\phi_{k,j}$. If it would have been done that way, than it would have no impact on $DF(\phi_{i,l})[\Delta\phi_{i,l}]$ because the term $k = j$ containing $m_{i,j}$ would vanish since $\phi_{j,j} = 1$ and therefore $[\vec{v}_j \cdot \vec{\nabla}]\phi_{j,j} = 0$. So $F[\phi_{i,l}]$ (after transforming to discretized age variable) would not contain additional $m_{i,l}$ terms. The $k = i - 1$ term would lead to $[\vec{v}_{old} \cdot \vec{\nabla}]\phi_{i-1,j}$ instead of $[\vec{v}_{old} \cdot \vec{\nabla}]\phi_{i,j}$ resulting no additional $\phi_{i,l}$ in $F[\phi_{i,l}]$ and therefore would not affect $DF(\phi_{i,l})[\Delta\phi_{i,l}]$. Only the right hand side $-F[\phi_{i,l}^{(n)}]$ in the Newton scheme would change due to the inner advection.

5.2.3 Simulation Setup

Since the Newton method is – as previously discussed in detail – much more complicated for the advected MCT-ITT model, because the schematic MCT equation is no longer local. The standard computational parameters N_B and N_A, for the number of blocks and the number of steps in each blocks that in which the density correlation $\phi(t, t')$ dates back in history, need to be reduced from $N_B = 7$ to $N_B = 6$ and from $N_A = 16$ to $N_A = 8$. Accordingly the number of total time steps, that can be simulated without a cut-off in history (which is $N_t = N_A \cdot (2^{N_B} - 1)$), needs to be reduced by roughly a factor of 4. To compensate the reduced number of time steps the step size Δt of the implicit Euler scheme is doubled to $\Delta t = 0.1$.
All simulations still use the F12 model for the memory kernel with coupling coefficients $v_1 = 2(\sqrt{2} - 1) + \epsilon/(\sqrt{2} - 1)$ and $v_2 = 2$, where $\epsilon = 0.01$ to be slightly in the glassy state. The critical yield parameter γ_c is as previously set to 0.1. The further constants G_0 and η_S are both set to unity (as done in the local MCT version in the previous chapter).
The boundary conditions are identical to the ones in the last chapter, which means: no-slip Dirchlet boundary condition at all walls or obstacle and periodic boundary conditions in the x-direction.
For both simulation geometries, the rectangular channel with spherical obstacle and the 4:1 contraction / extension the exact same meshes (triangulations) as in chapter 4 were used.

5.3 Flow Past a Spherical Obstacle

As a first non-trivial example (this means a geometry that provides $\vec{v} \cdot \vec{\nabla} \neq 0$), the pressure driven flow past a spherical obstacle is simulated. The pressure drop, creating $\vec{\nabla} p = \frac{\Delta p}{L} \hat{e}_x$, is adjusted to $\Delta p = 1.0$ per periodic length of $L = 5$.

5.3.1 Steady State Results

The steady state velocity field and streamlines are visualized in the following graphic. As already mentioned previously the area around ($x \approx 1.0 \pm 0.2$) and in front / past ($x \approx 0.65$ or $x \approx 1.35$) the cylinder is of special interest, because there $\vec{v}$ and $\vec{\nabla}$ point approximately in the same direction (in contrast to the channel area where they are perpendicular).

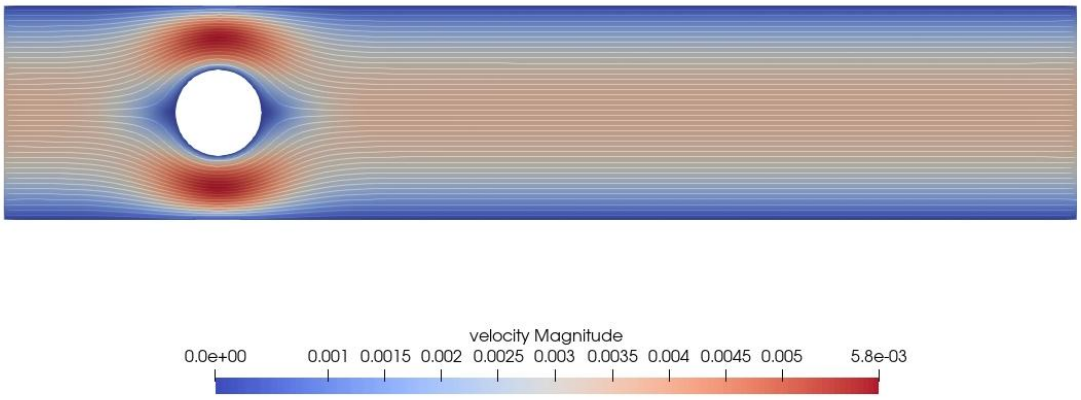

Figure 5.2: Stationary velocity field $|\vec{v}|$ and streamlines of the advected MCT-ITT model driven by a pressure gradient of by $\frac{\Delta p}{L} = 0.2$.

Further one observes identitical patterns of the shear stress σ_{xy} and the first normal stress difference $N_1 = \sigma_{xx} - \sigma_{yy}$ in the steady state.

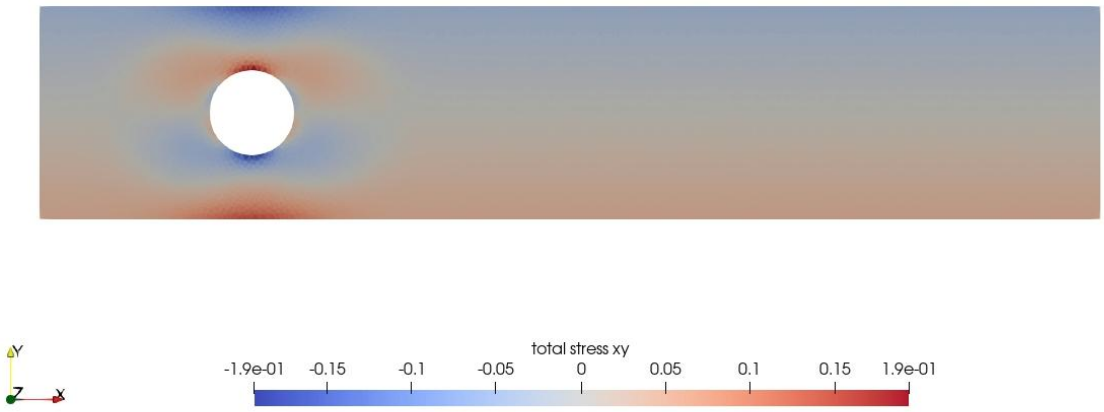

Figure 5.3: Stationary shear stress σ_{xy} of the advected MCT-ITT model driven by a pressure gradient of by $\frac{\Delta p}{L} = 0.2$.

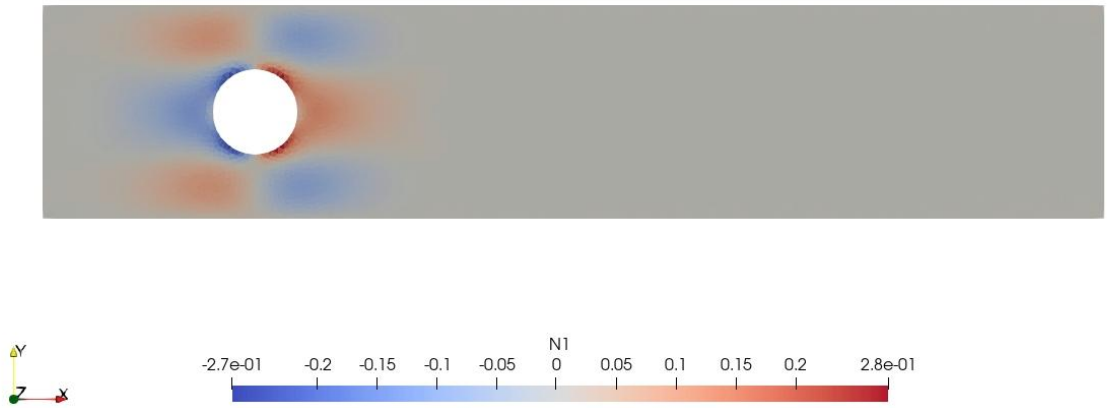

Figure 5.4: Stationary first normal stress difference N_1 of the advected MCT-ITT model driven by a pressure gradient of by $\frac{\Delta p}{L} = 0.2$.

For a better understanding why – so far – the advectional extensional does not change the macroscopic flow behavior one needs to investigate the microscopic transient density correlation functions of both the advected MCT-ITT model and the standard local MCT-ITT model used in the previous chapter.

5.3.2 Transient Density Correlation Functions

Since one can expect the correlation function $\phi(t, t')$ calculated with the advected MCT to be identical to the one calculated with the standard local MCT in areas where $\vec{v} \cdot \vec{\nabla} = 0$, both correlation functions (from the local and advected MCT) are plotted (at the end of the simulation) against their age $t - t'$ in the interesting areas, where neither the shear rate is not zero nor the advection term $\vec{v} \cdot \vec{\nabla}$ does vanish.
One can see that both MCT models (local and advected) lead to very similar transient density correlation functions $\phi(t, t')$ and therefore to similar generalized shear moduli $G(t, t')$ and similar polymeric stress $\underline{\underline{\sigma_P}}(t)$. This is due to the very high viscosity and slow flow of such glass-forming and viscoelasto-plastic fluids, informally speaking: since $|\vec{v}|$ is small $\vec{v} \cdot \vec{\nabla}$ is "small" ("..." since this a differential operator and not a real number like $|\vec{v}|$) as well.

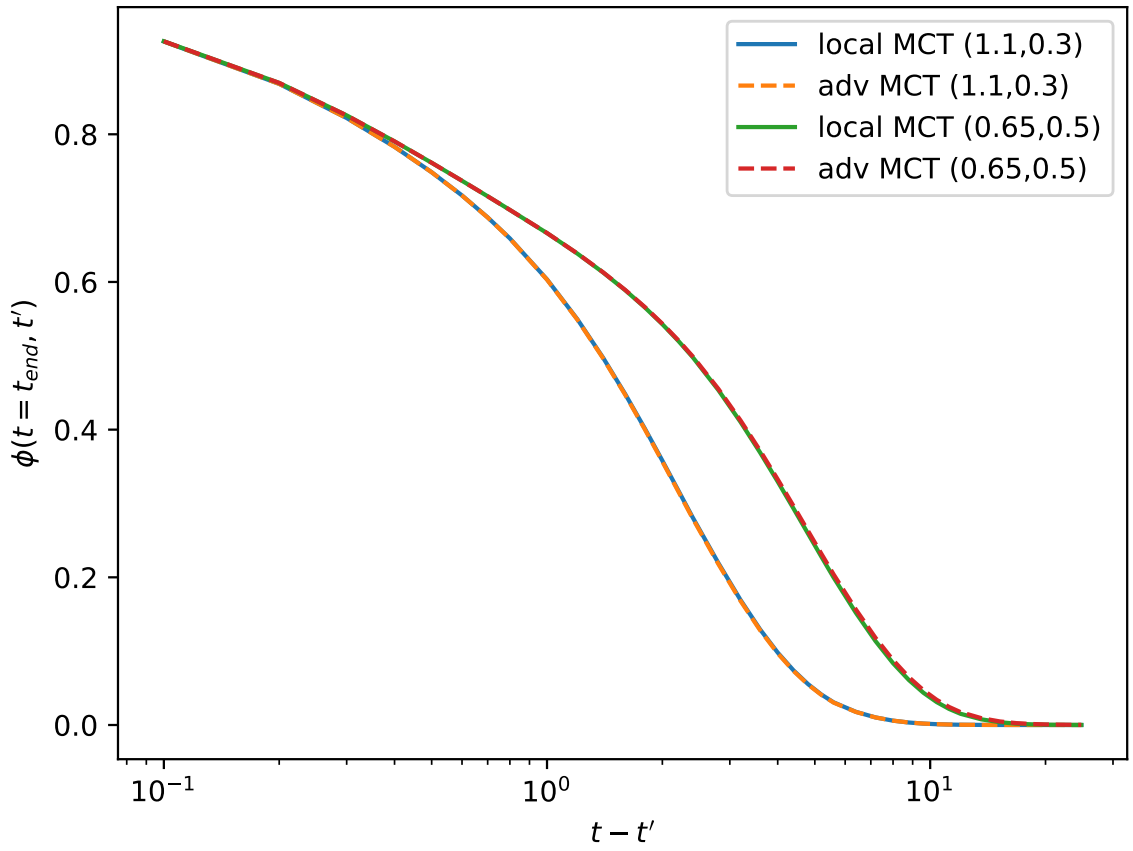

Figure 5.5: Transient density correlation functions $\phi(t, t')$ at positions $(1.1, 0.3)$ and $(0.65, 0.5)$ plotted against $t - t'$ (previously defined as the age a), obtained from both the standard local MCT and the advected MCT, at the end ($t = t_{end}$) of the pressure driven flow past a spherical obstacle simulation.

Heatmap Plots

Furthermore one can visualize the transient density correlation functions ϕ for both the local and the advected MCT-ITT model on the whole mesh for different ages. The following graphics show $\phi(t_{end}, a)$ – with the local MCT on the left (a) and the advected MCT on the right(b) – for ages $a = t_{end} - t' \in \{24.8, 20.0, 16.8, 10.4, 4.0\}$ as a heatmap on the whole mesh.

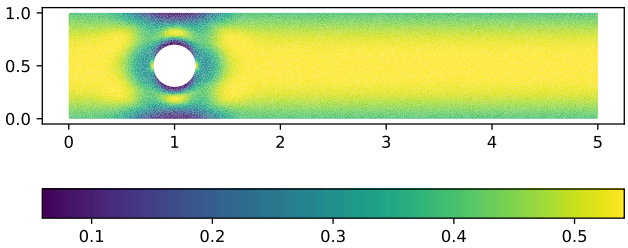

(a) Transient density correlation function $\phi(t_{end}, a = 4.0)$ calculated by the local MCT-ITT model.

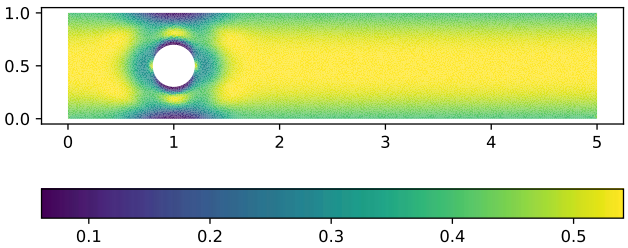

(b) Transient density correlation function $\phi(t_{end}, a = 4.0)$ calculated by the advected MCT-ITT model.

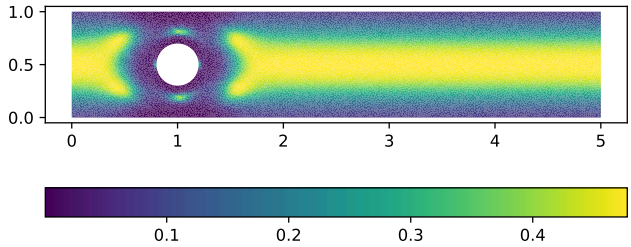

(a) Transient density correlation function $\phi(t_{end}, a = 10.4)$ calculated by the local MCT-ITT model.

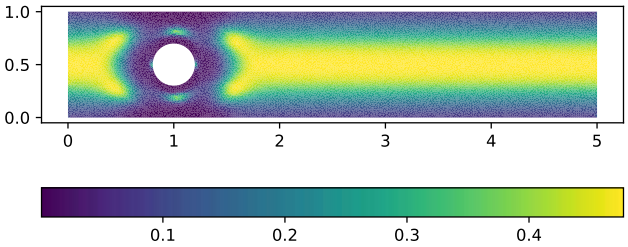

(b) Transient density correlation function $\phi(t_{end}, a = 10.4)$ calculated by the advected MCT-ITT model.

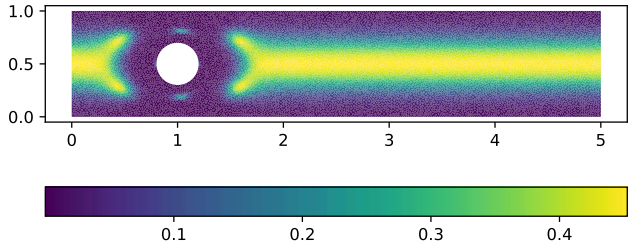

(a) Transient density correlation function $\phi(t_{end}, a = 16.8)$ calculated by the local MCT-ITT model.

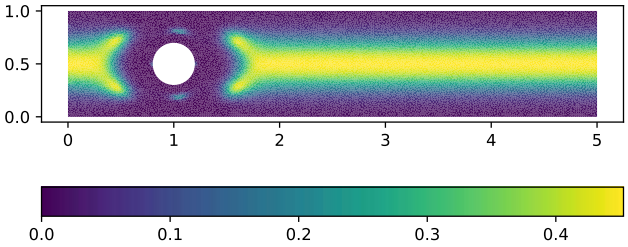

(b) Transient density correlation function $\phi(t_{end}, a = 16.8)$ calculated by the advected MCT-ITT model.

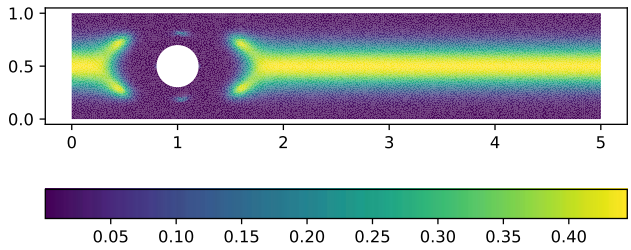

(a) Transient density correlation function $\phi(t_{end}, a = 20.0)$ calculated by the local MCT-ITT model.

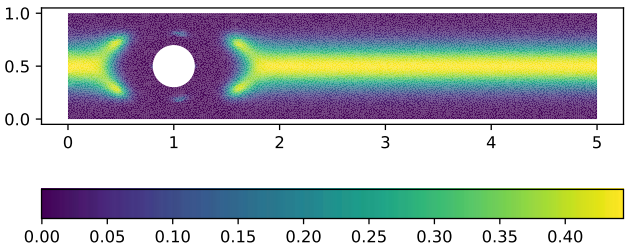

(b) Transient density correlation function $\phi(t_{end}, a = 20.0)$ calculated by the advected MCT-ITT model.

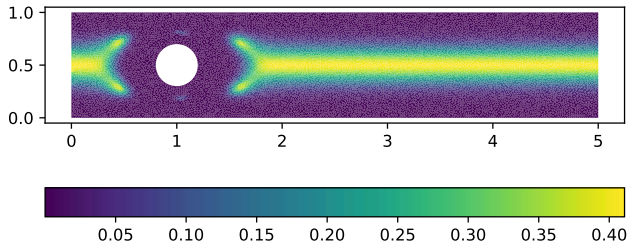

(a) Transient density correlation function $\phi(t_{end}, a = 24.8)$ calculated by the local MCT-ITT model.

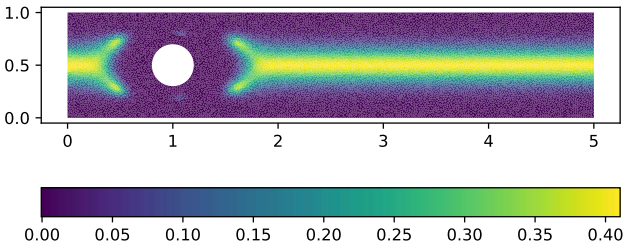

(b) Transient density correlation function $\phi(t_{end}, a = 24.8)$ calculated by the advected MCT-ITT model.

The transient density correlation functions behave nearly identical for both MCT-ITT models, maybe one can spot a minimal difference in the size (smaller for the advected MCT) of the non-decaying (because of the local symmetry) region between the spherical obstacle and the wall for the fully aged ($t' = 0$) correlation function.

Correlation Functions at Switch-Off

So far all the density correlation functions were shown at time $t = t_{end}$ of a simulation with a constant (in time) pressure drop Δp. However it is worth looking at correlation functions of a simulation where at a certain time $t = t_{off} = \frac{t_{end}}{2}$ the pressure drop is set to zero (similar to the simulations in the previous chapter).

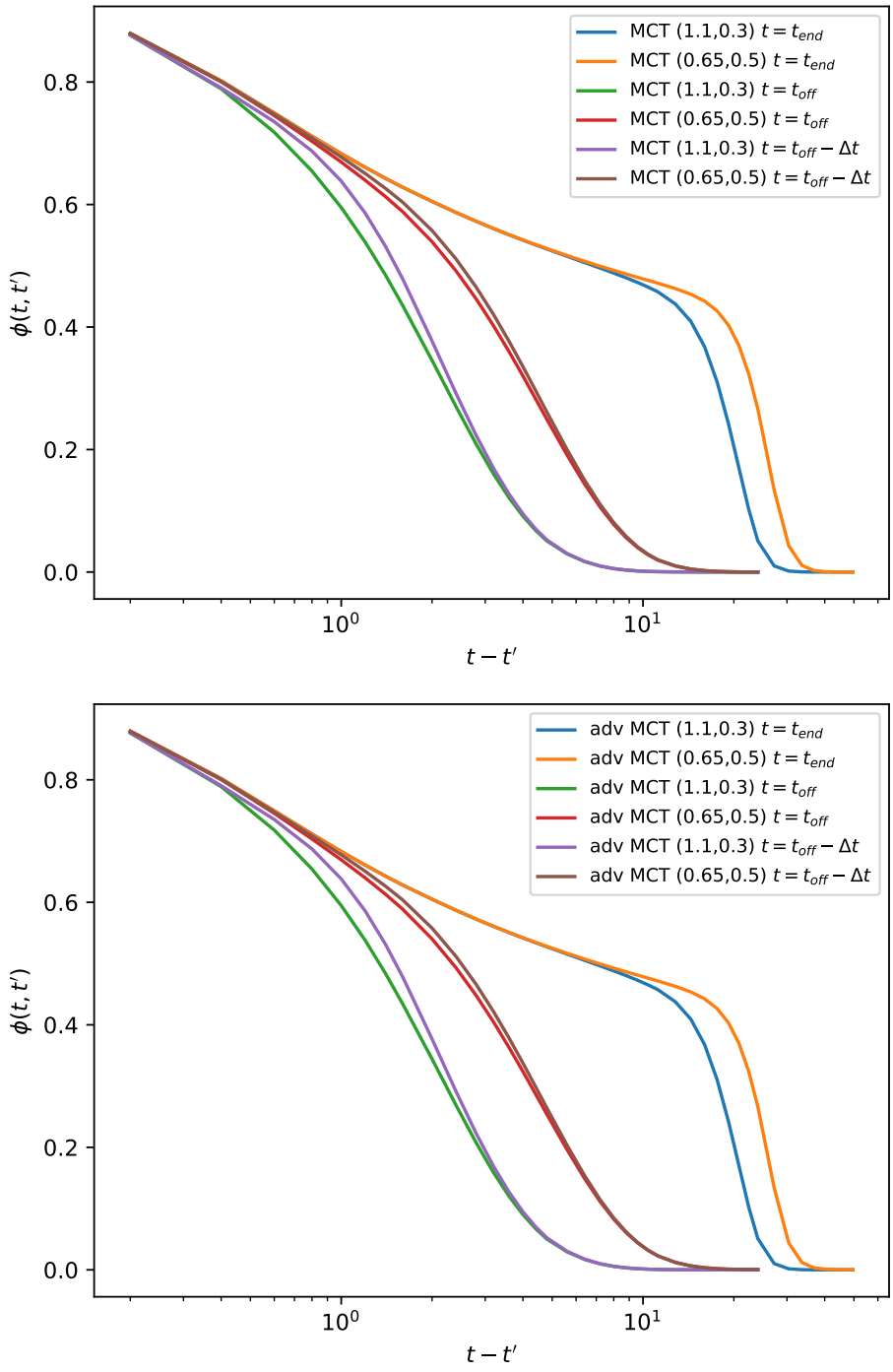

Figure 5.11: Transient density correlation function for different positions and times t calculated by the local MCT model in the upper and by the advected MCT-ITT model in the lower plot.

Finally one can look at the difference $\Delta\phi = \phi_{adv} - \phi_{loc}$ of both transient correlation functions. For times close to to the switch-off $t = \{t_{off} - \Delta t, t_{off}\}$ the advected MCT seems to decay a bit slower right behind the obstacle at position $(0.65, 0.5)$ since the red and brown curves are positive. In contrast, around the obstacle at position $(1.1, 0.3)$ the advected MCT seems to decay slightly faster since the green and purple curves are negative.
However, the correlation functions at $t = t_{end}$ are almost identical with the tendency that the advected MCT decays very slightly slower.

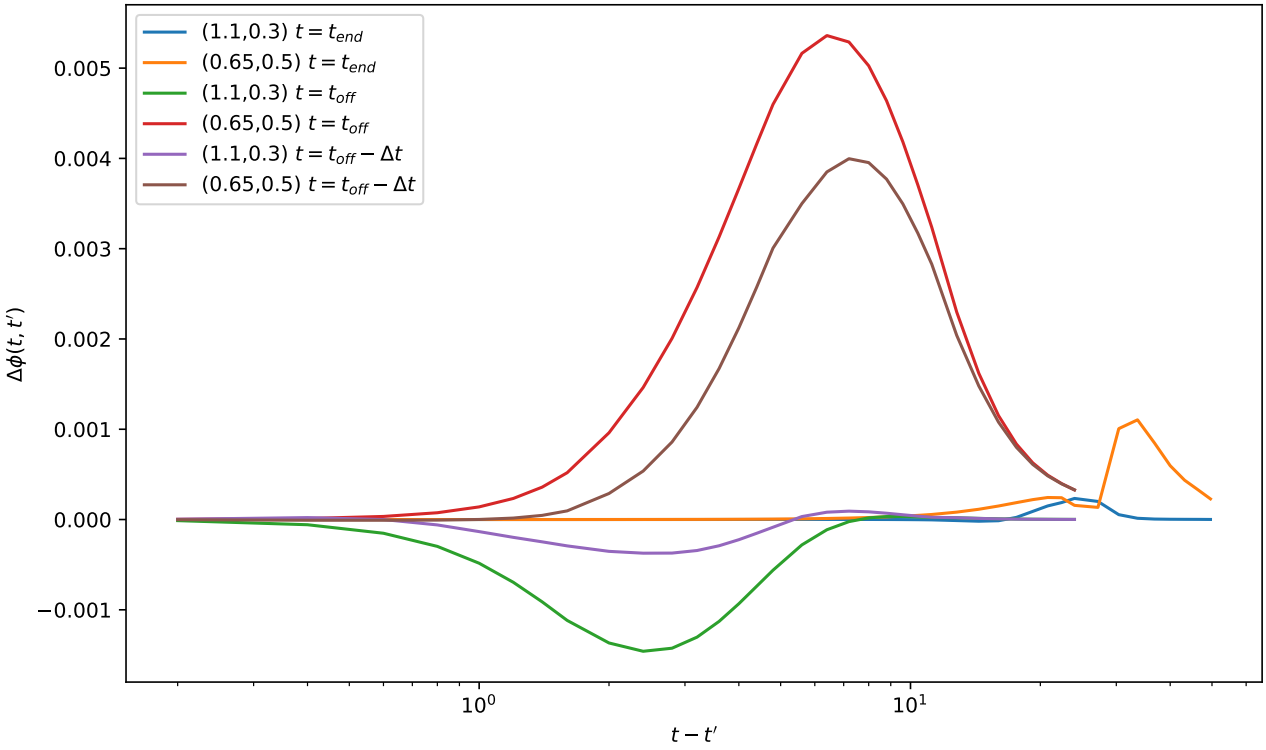

Figure 5.12: Transient density correlation function for different positions and times t calculated by the local MCT model on the left hand side and by the advected MCT-ITT model on the right hand side.

5.3.3 Residual Stresses

If one again removes the driving pressure drop Δp when the system has reached its steady state – like in the previous chapter – also the advected MCT-ITT model predicts residual stresses. The residual stresses are very similar to the local MCT model, and are shown in the following graphics.
One can see that the residual stress (both shear and normal stresses) look qualitatively identical to the ones obtained from the standard local MCT-ITT model (as discussed in chapter 4). However if one looks carefully on the range of values the residual stresses are slightly bigger than the ones presented in the previous chapter. This is due to the fact that the relaxation time $t - t_{off}$ is shorter by a factor of 3, since the advected MCT-ITT model is much more computationally expensive and therefore the simulations are shortened.

Residual Shear Stresses

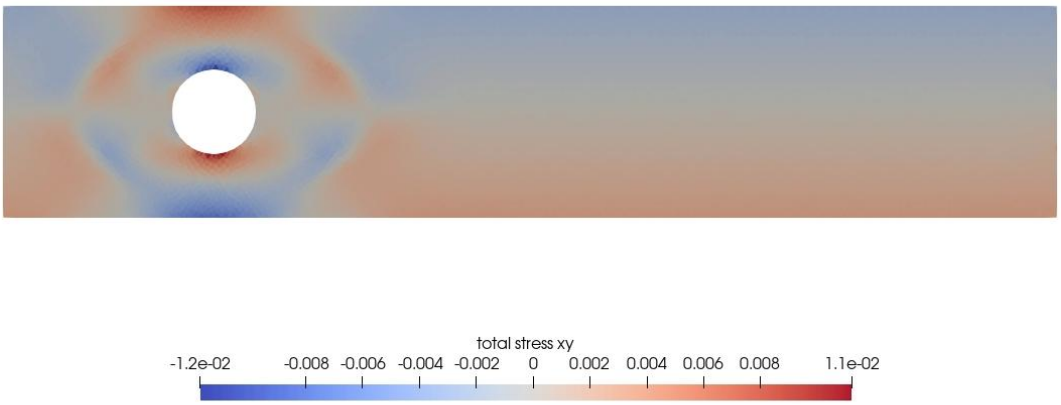

Figure 5.13: Residual shear stresses σ_{xy}^{res} at $t - t_{off} = 25.2$ (25.2 simulation time units after the previous pressure drop of $\Delta p = 1.0$ was turned off).

The same pattern as in the previous chapter can be observed, again around the obstacle the sign of the stresses are flipped compared to the steady state values. Since the correlators $\phi(t, t')$ were (almost) identical to the local MCT-ITT version this was expected and underlines the predicting power of the MCT-ITT model in general since it seems to be very robust to the advection terms where it is unsure to include them or not. From the microscopical derivation of MCT-ITT constitutive laws found in [7] there is no sign to put them in, however from the continuum mechanics perspective they must be included.

Residual Normal Stresses

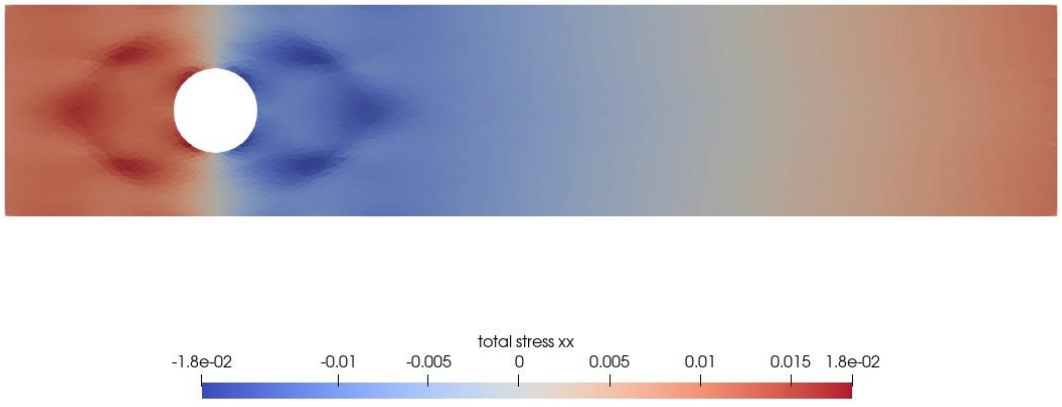

Figure 5.14: Residual normal stresses σ_{xx}^{res} at $t - t_{off} = 25.2$ (25.2 simulation time units after the previous pressure drop of $\Delta p = 1.0$ was turned off).

One can expect the exact same finite-size / periodical boundary effects as extensively discussed in subsection 4.4.2 of the previous chapter.

5.4 Flow in 4:1 Contraction / Extension

As a second example of simulations pressure driven flow in the famous abrupt 4:1 contraction / extension geometry are considered. The pressure drop, creating $\vec{\nabla} p = \frac{\Delta p}{L} \hat{e}_x$, is adjusted to $\Delta p = 10.0$ per periodic length of $L = 10$. Therefore a stronger pressure gradient is applied to the system to achieve higher flow velocities and "bigger" $\vec{v} \cdot \vec{\nabla}$ terms.

5.4.1 Steady State Results

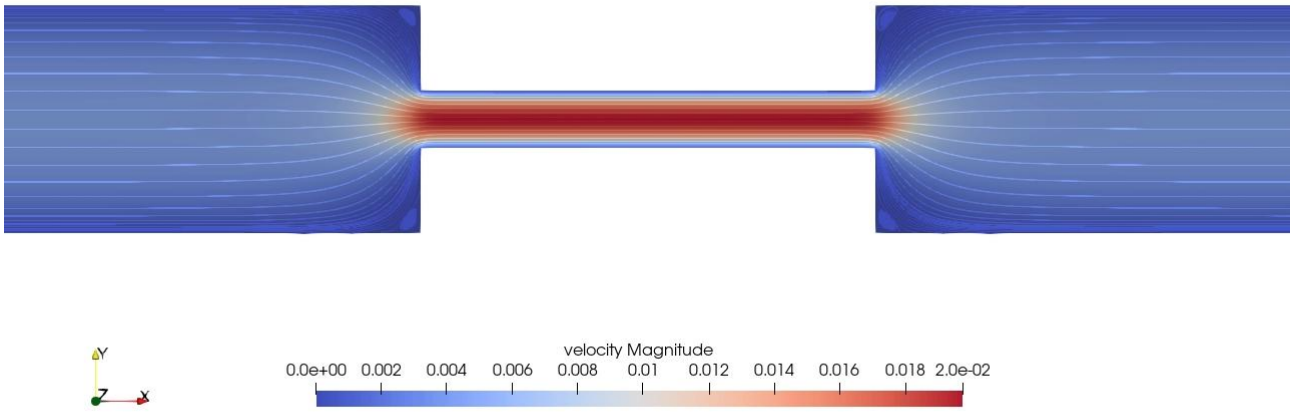

Figure 5.15: Stationary velocity field $|\vec{v}|$ and streamlines obtained from the the advected MCT-ITT model driven by a pressure drop of $\Delta p = 10.0$ per periodic length of $L = 10$.

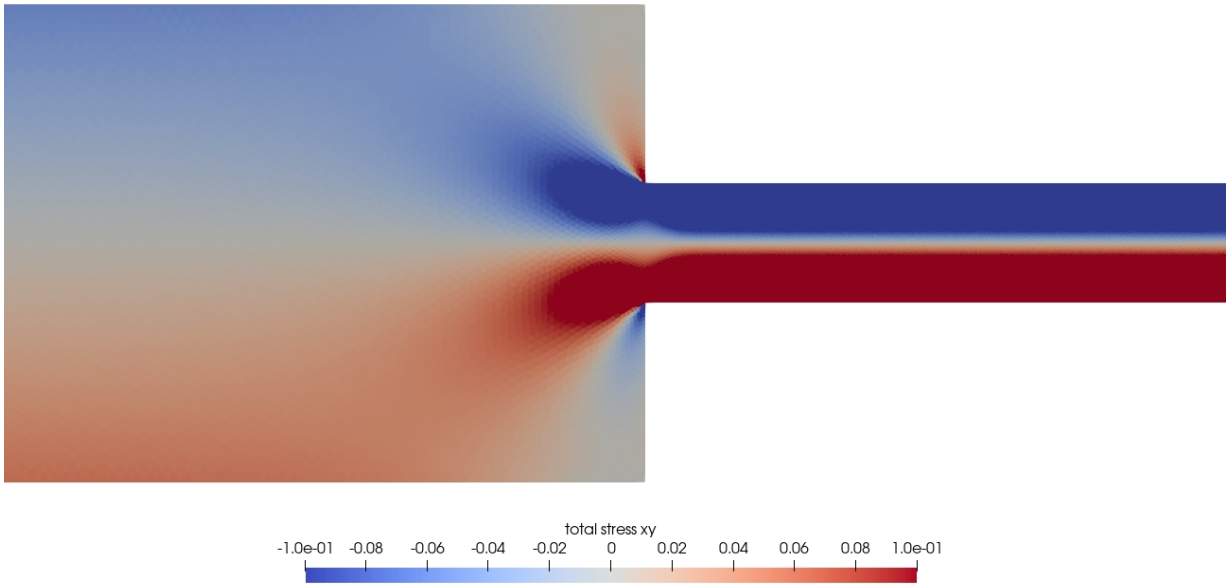

Figure 5.16: Stationary shear stress σ_{xy} obtained from the advected MCT-ITT model driven by a pressure drop of $\Delta p = 10.0$ per periodic length of $L = 10$.

One can observe the same stationary streamline pattern as already discussed in the previous chapter. A very promising point to spot differences between advected and local MCT seems to be $(4.0, 0.5)$ which is directly in the middle of the abrupt contraction. At this point one can see that there should be strong gradients – due to the contraction – and high velocities. Another good point might be near the contraction edges (for example $(3.75, 0.375)$) where also the shear stress is high. In contrast, at points in the edges where almost no flow takes place or at points where $\vec{v} \perp \vec{\nabla}$ and therefore $\vec{v} \cdot \vec{\nabla}$ very small or zero (only done for verification) one cannot expect different correlation function functions since the overall flow seems to be very similar and at these points advection plays no role.

5.4.2 Transient Density Correlation Functions

Again the simulations are modified by adding a switch-off time $t = t_{off} = \frac{t_{end}}{2}$ at which the pressure drop is set to zero and the flow undergoes a cessation process (due to energy dissipation). In the next subsection the residual stresses predicted by the advected MCT-ITT model in the 4:1 contraction / extension are studied using these simulations. The comparison of the transient density correlation function will already tell what to expect in terms of residual stresses since similar correlation functions cause similar stress patterns.

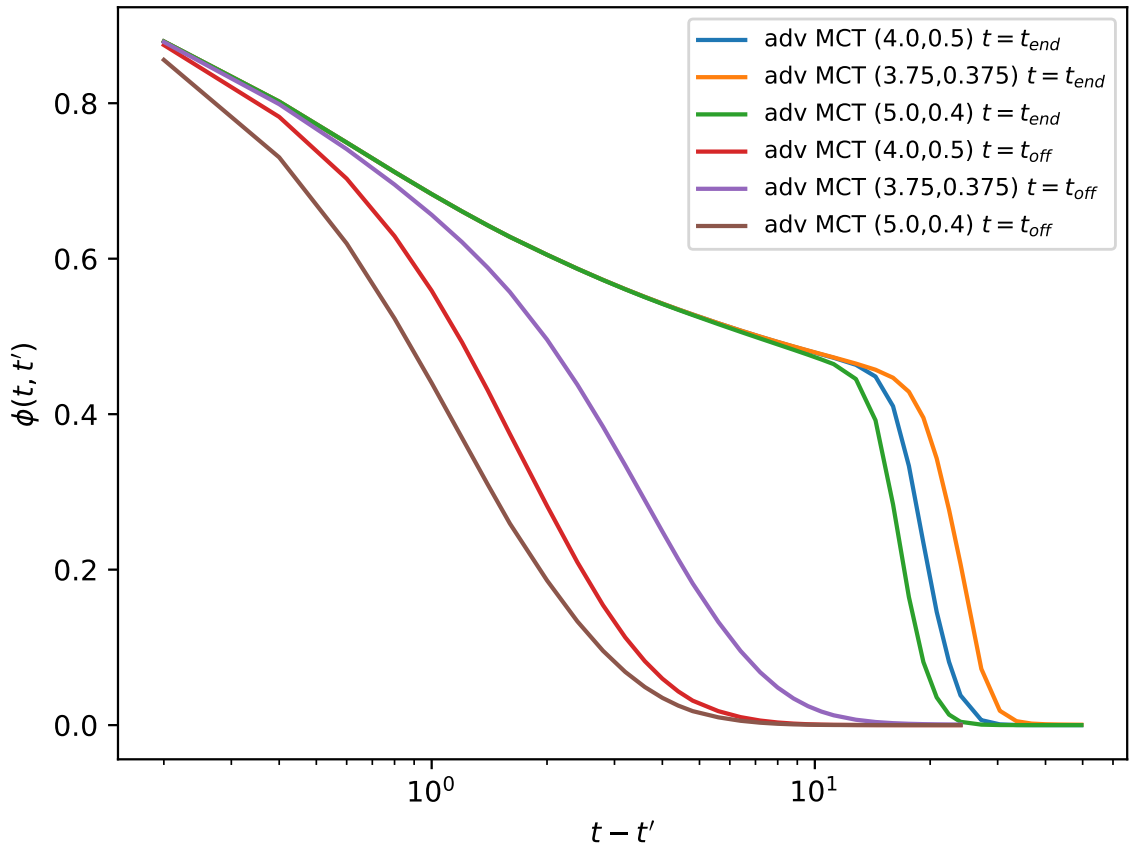

Figure 5.17: Transient density correlation function for different positions – mentioned in the previous subsection – and times t calculated by the advected MCT-ITT model.

Comparison and Heatmap Plots

Next one can compare the local and the advected correlation functions extracted from similar simulations (same number of blocks with the same blocksize, identical pressure drop and switch-off). In this higher pressure simulations one observes bigger differences between the MCT versions (local or advected) than in the corresponding subsection 5.3.2 of previous section on the (lower) pressure driven flow past a spherical obstacle. However these bigger differences only occur in comparisons at time $t = t_{off}$ and – as already seen in 5.3.2 – not systematically in a sense that all correlation functions of the advected model dacay quicker or vice versa.

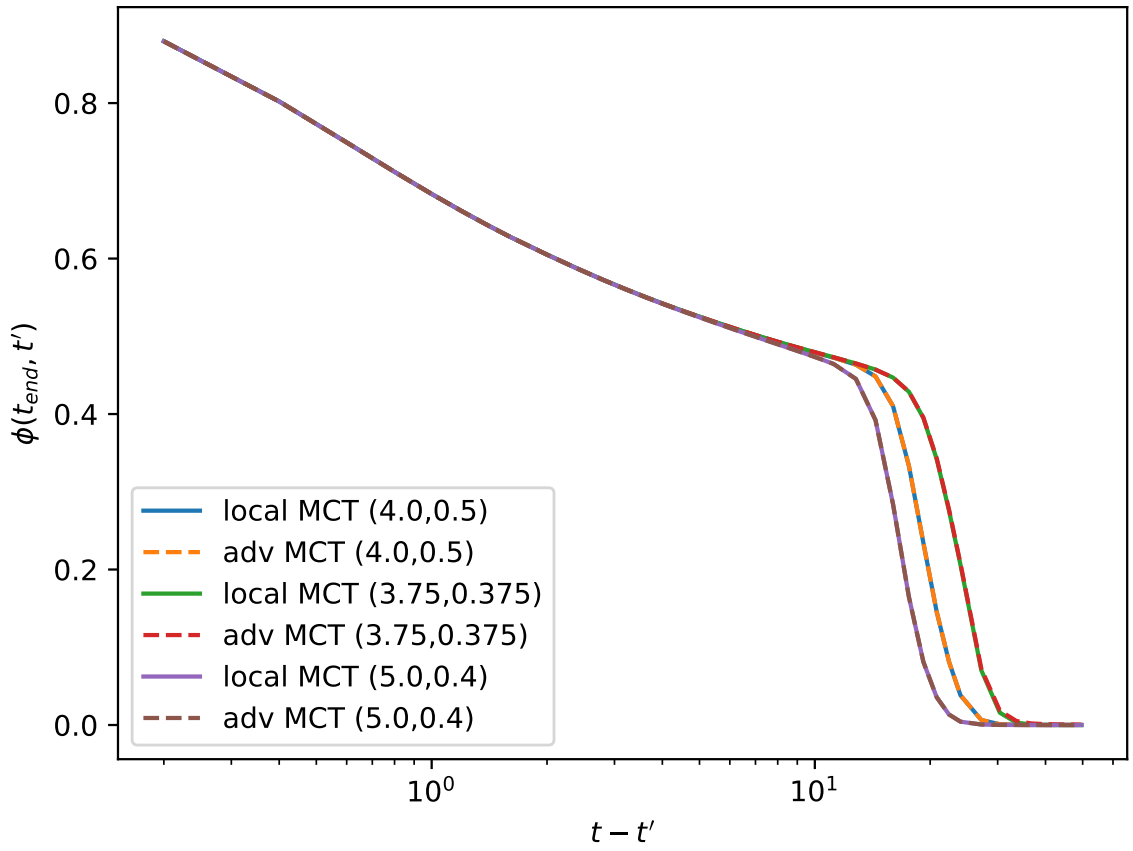

Figure 5.18: Comparison of transient density correlation functions for different positions between the local and the advected MCT-ITT model. All correlation functions evaluated at $t = t_{end}$.

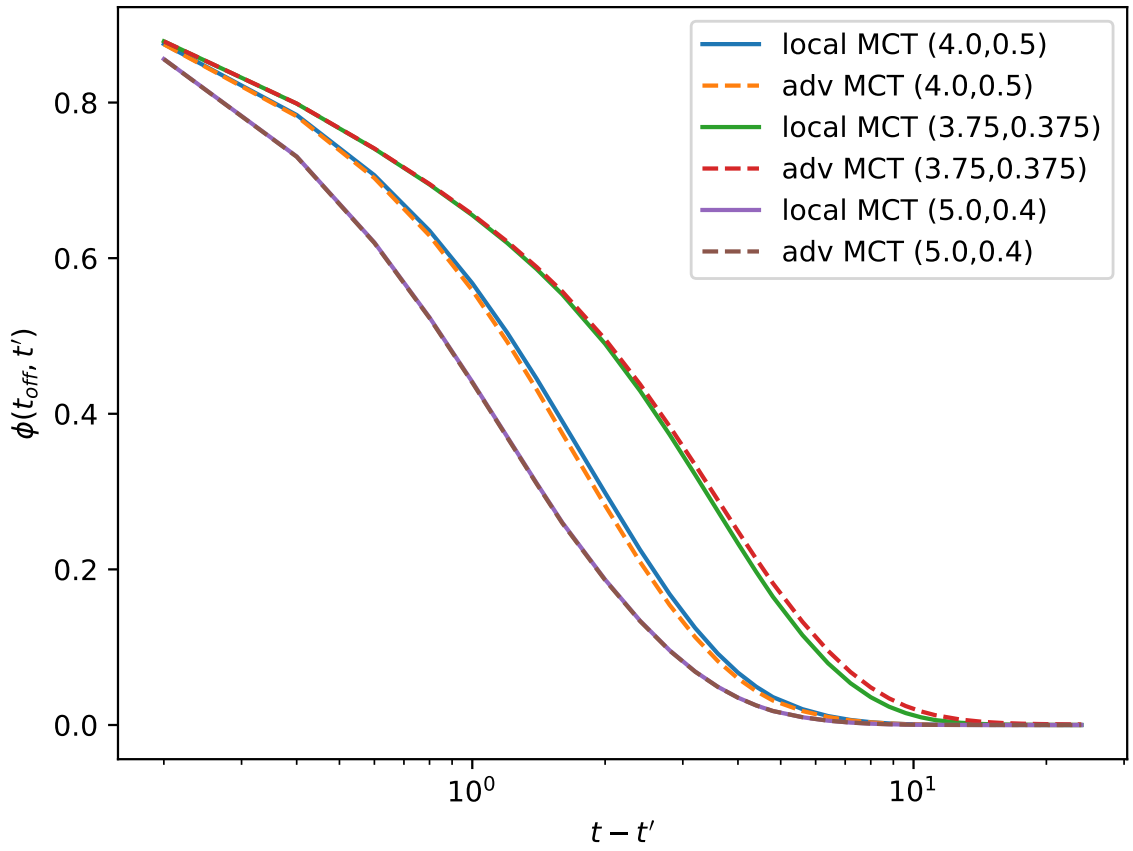

Figure 5.19: Comparison of transient density correlation functions for different positions between the local and the advected MCT-ITT model. All correlation functions evaluated at $t = t_{off}$.

To finalize the discussion on transient density correlation functions in the 4:1 contraction / extension geometry one can look at different heatmaps. Due to limited computational resources these heatmap plot were made with data extracted from simulations on a mesh with lower resolution.
Even though the differences between advected and local MCT-ITT models are bigger (due to the higher pressure gradient and the faster velocities in the narrow channel) the heatmaps look identical for both models.

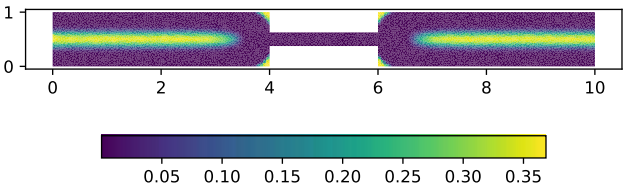

(a) Transient density correlation function $\phi(t_{end}, a = t_{end})$ calculated by the local MCT-ITT model.

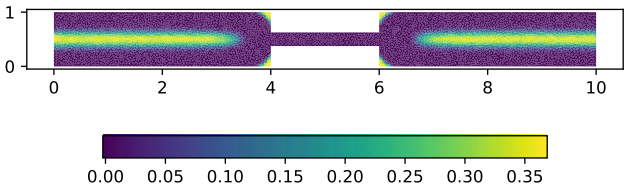

(b) Transient density correlation function $\phi(t_{end}, a = t_{end})$ calculated by the advected MCT-ITT model.

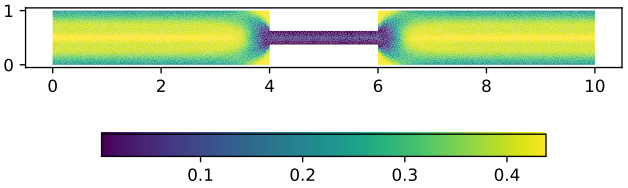

(c) Transient density correlation function $\phi(t_{end}, a = 24.0)$ calculated by the local MCT-ITT model.

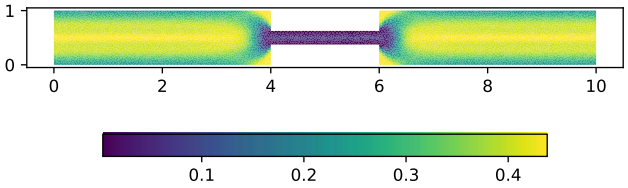

(d) Transient density correlation function $\phi(t_{end}, a = 24.0)$ calculated by the advected MCT-ITT model.

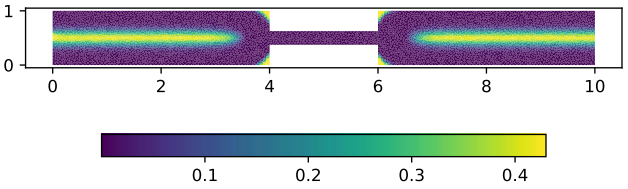

(a) Transient density correlation function $\phi(t_{off}, a = 24.0)$ calculated by the local MCT-ITT model.

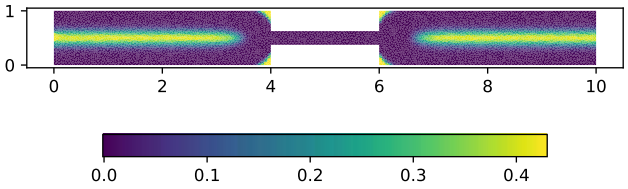

(b) Transient density correlation function $\phi(t_{off}, a = 24.0)$ calculated by the advected MCT-ITT model.

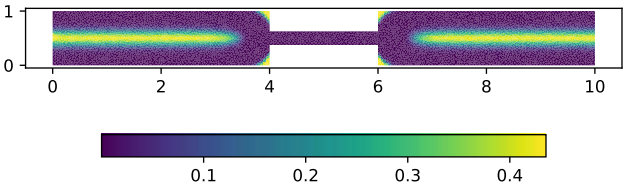

(a) Transient density correlation function $\phi(t = 24.0, a = 24.0)$ (note that $t = 24 < t_{off}$) calculated by the local MCT-ITT model.

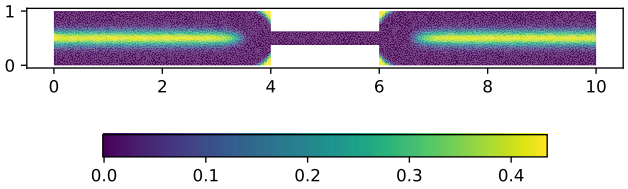

(b) Transient density correlation function $\phi(t = 24.0, a = 20.0)$ (note that $t = 24 < t_{off}$) calculated by the advected MCT-ITT model.

5.4.3 Residual Stresses

Finally we show the resulting residual stresses of the advected MCT-ITT model. Note that due to the high similarity of the correlators the residual stresses look identical to those shown in the previous chapter. First one observes the same sign flip of the shear stress (compare to the colors in Figure 5.16) in the narrow channel while the sign in the wide area remains unchanged.
In the first normal stress difference N_1 we also see a familiar pattern, however there is slightly more finite size error (due to the periodic boundary conditions in x) than in the local MCT-ITT model as simulated in the last chapter.

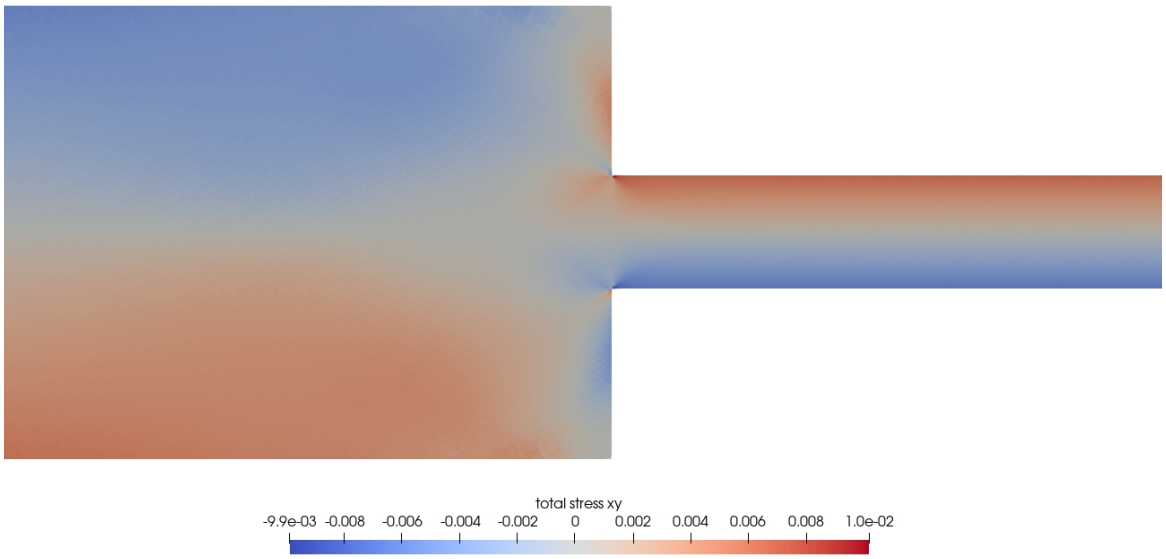

Figure 5.23: Residual shear stress σ_{xy} obtained from the advected MCT-ITT model driven by a pressure drop of $\Delta p = 10.0$ per periodic length of $L = 10$.

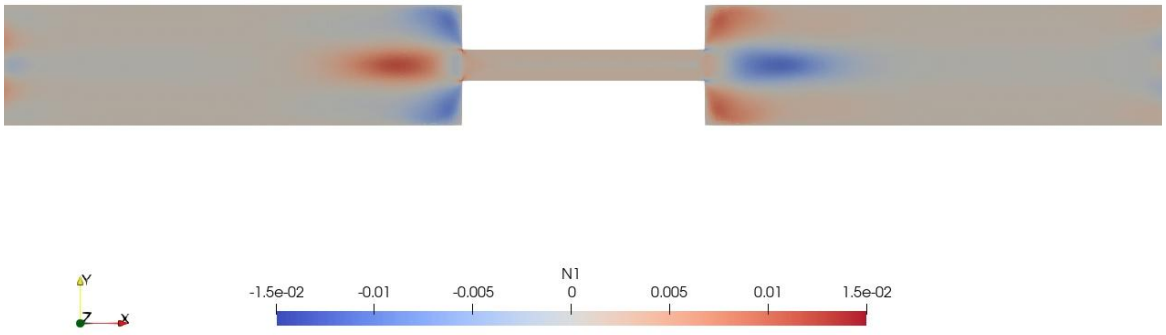

Figure 5.24: Residual first normal stress difference N_1 obtained from the advected MCT-ITT model driven by a pressure drop of $\Delta p = 10.0$ per periodic length of $L = 10$.

Comparison to the local MCT-ITT model

As expected one can say that the pressure drop is still not big enough and maybe also the geometry is not ideal to observe big differences between the local and the advected MCT-ITT model. Therefore an extensive comparison between both model is not done, however there are some differences highlighted in the following graphics.
To ensure a good comparability the same triangulation and numerical parameters (as described in 5.2.3) are used for both models.

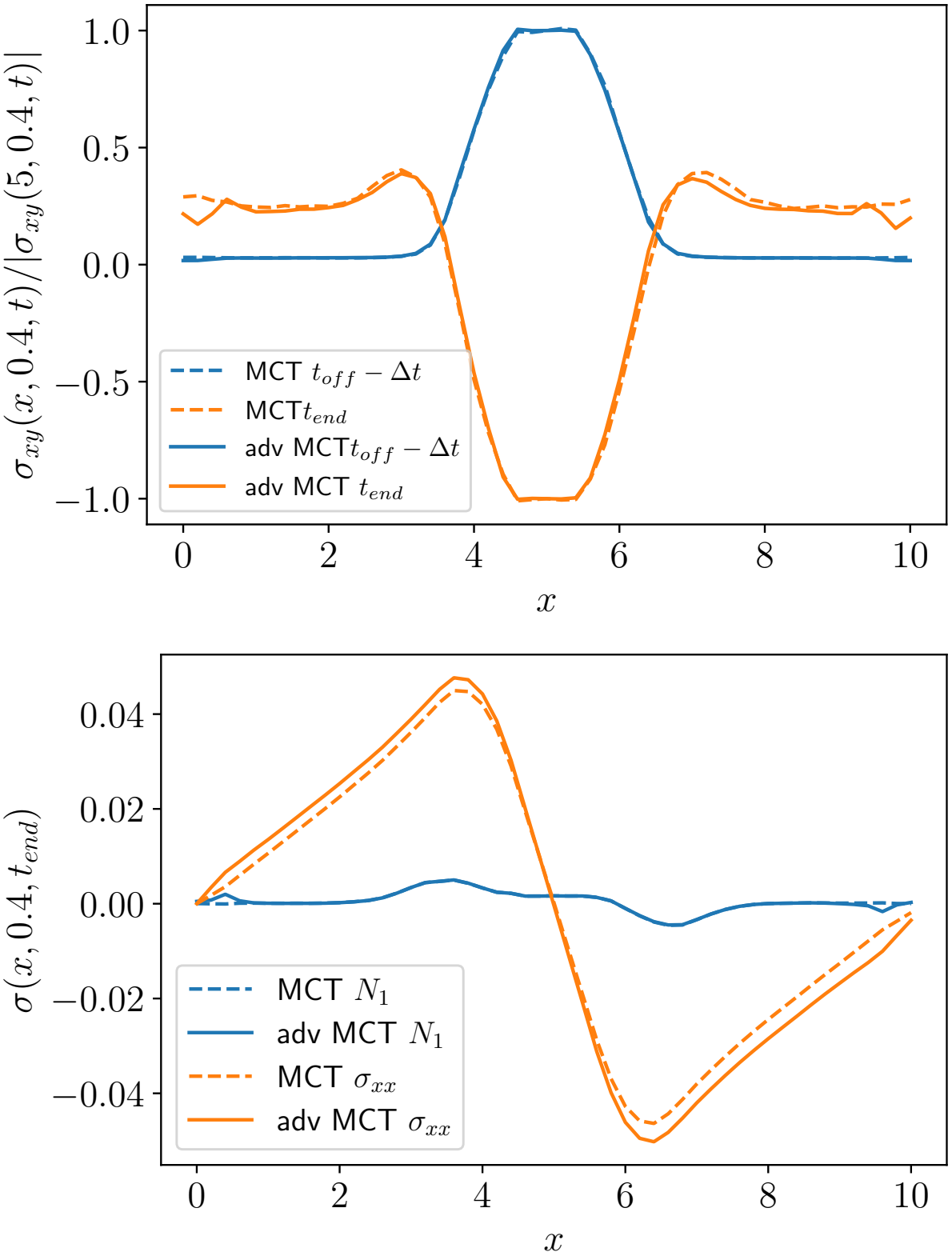

Figure 5.25: Transient density correlation function for different positions and times t calculated by the local MCT model on the left hand side and by the advected MCT-ITT model on the right hand side.

One can – again – see that that both models produce nearly identical results, only at the periodic x boundaries the advected MCT-ITT model seems to be a bit more sensitive to finite size effects. These differences at the periodic x boundaries cannot be induced by the additional advection term $(\vec{\nabla} \cdot \vec{v})$ since $x = 0$ and $x = 10$ are in the middle of plain channel elements where the advection term vanishes. Apart from finite size effects the difference between both models is negligible supporting the findings of the previous chapter (since it is a priory not clear which version to use, but fortunately it does not make a difference in results) that statistical mechanics based (schematic) MCT models are much more powerful than the typical empirical based models widely used because they show quantitatively similar residual stresses like found in experiments [1].

Chapter 6

Summary and Outlook

6.1 Summary

In this thesis the foundations of the Mode-Coupling theory of the glass transition (MCT), mostly in its schematic version, were introduced both from a conceptual, but especially from a numerical point of view. Numerical algorithms for both the standard one-time schematic MCT (sMCT) and the two-time MCT for colloidal systems under time-dependent shear [6] in its schematic version [8] were presented. These algorithms ensure correct predictions of long time limits, given by the bifurcation equation. The need for fast computations of integrals over the second time argument – the reference time t' – arising from a "first-principles" constitutive equation, leads to a new algorithm that steps linear in the time t but (quasi-) logarithmic in the reference time t'.

After understanding the fundamentals of sMCT the Navier-Stokes equations were revisited and reduced to the special case of incompressible time-dependent Stokes flow, in which one assumes advective inertial forces to be negligible compared to viscous forces, which is fairly reasonable when dealing with viscoelastoplastic glass-forming fluids.
To close the time-dependent Stokes problem a variety of known differential and integral constitutive equations were presented, all based on the Maxwell model [40] presented by Maxwell himself in 1853. The Maxwell model of viscoelasticity is derived from the mechanical analog of serial connection of an elastic spring and a viscous damper and leads to a simple ordinary differential equation (ODE) for the stress. Oldroyd later modified this simple ODE model to a tensorial one, by introducing his convected / Oldroyd derivatives. If one makes shear-thinning (viscosity decreases when a strain-rate is applied to the fluid) variations of this model one can derive further differential and even integral models.
However as already shown in [1], and highlighted at the end of the second chapter in this thesis, all the heuristic Maxwell-like model do lack a qualitatively correct prediction of residual stresses after the cessation of flow. Residual stresses are stresses that remain in the material / fluid after the flow has come to rest (because of the dissipation of energy, after a pressure gradient is turned off for example). Experiments on colloidal suspensions have shown that a good model need to make three key-predictions on the residual stress σ^{res}:

(1) partial relaxation of σ^{res} from the steady state stress σ^{ss},

(2) $\sigma = \sigma^{res} \neq 0$ for $t \to \infty$,

(3) the residual stress σ^{res} depends on the deformation history.

It turns out (again [1]) that only the schematic MCT-ITT model developed in [8] is able to predict qualitatively correct residual stresses that are in good agreement with experiments. Therefore it is worth to implement fully two dimensional flow simulations – instead of the quasi one dimensional

numerical predictions in [1] – of this model, despite the extensive computational cost and memory demand of the model.

To be able to simulate the flow in a variety of non-trivial geometries we used the finite element method (FEM) as the main simulation technique. As already mentioned FEM is much more versatile when it comes to the geometry in which the flow should be simulated, especially compared to existing lattice Boltzmann (LB) simulation [44]. Furthermore by choosing proper elements one can assure some import physical laws such as mass or momentum conservation while still maintaining reasonable computational cost (at least in solving the Stokes problem).

We successfully developed an implicit LBB-stable [15] implicit FEM code basis – implemented with the help of the FEniCS environment [32, 38] inside the python programming language – able to perform numerical flow simulations of the MCT-ITT model in various benchmark geometries such as the pressure driven flow inside a rectangular channel or the 4:1 contraction / extension flow. Since the macroscopic Stokes problem and the microscopic MCT-ITT formalism are coupled via the Finger tensor $\underline{\underline{B}}$ we used the Marchuk-Yanenko operator splitting method [39] to decouple the set of equations. A geometry that we were especially interested in is the pressure driven flow past a spherical obstacle inside a rectangular channel, since this geometry is not x-invariant like the standard channel flow. Because of the previously described x-invariance breaking of the spherical obstacle, partial x-derivatives ∂_x no longer vanish (at least not around the obstacle) allowing the self-equilibrated residual shear (xy-component of the stress tensor) stresses. To understand the importance of ∂_x not vanishing, revisit the stationary Stokes problem without any pressure gradient or external force:

$$-\vec{\nabla} \cdot \underline{\underline{\sigma}}^{res} = 0.$$

Thus the x-component of the Stokes leads to $\partial_y \sigma_{xy}^{res} = -\partial_x \sigma_{xx}^{res}$ and if ∂_x would vanish the Residual shear stress σ_{xy}^{res} must be a constant in y, due to symmetry (shear stress must vanish in the middle of the channel) this constant must be zero. This means that we succesfully demonstrated that the MCT-ITT model predicts geometry-dependent residual shear stresses that seem to couple the microscopic (MCT) and macroscopic (fluid mechanics) scales [51].
The 4:1 contraction / extension flow simulations lead to similar residual shear stresses since also the x-invariance is broken at the contraction / extension. Furthermore transient history-dependent effects (during cessation) are discussed. We showed that the historical deformations induce different local viscosity resulting in a transient vortex formation in the contraction edges.

Despite the huge success of the MCT-ITT model in predicting geometry-dependent residual shear stresses in glass-forming fluids the model does lack rheological correctness. From continuum mechanics it is known that the correct rate of change for a scalar quantity (such as the transient density correlation function ϕ) in the (laboraty fixed) Euler frame is given by the advected (also called material) derivative $\frac{D}{Dt} = \partial_t + \vec{v} \cdot \vec{\nabla}$.
Even though there is no microscopical derivation for the advected derivative (yet) we included the advection terms into the MCT-ITT formalism. Unfortunatly this (especially the advection term in the memory integral) massively increases the computational effort. First one now needs to store the historical velocity fields. Second the MCT equation is no longer local (which is kind of desired) resulting in a much more complex functional Newton scheme, instead of the simple one dimensional one in the local MCT.
It turned out that in our simulations, in which the velocities $|\vec{v}|$ are small, the advection term does not change the rheological effects of the MCT-ITT model. Most importantly we found the same residual shear stresses after a cessation of flow past a spherical obstacle as in the local MCT-ITT version. However, in simulations with bigger velocities $|\vec{v}|$ and therefore "bigger" $\vec{v} \cdot \vec{\nabla}$ and especially

in two-component systems the advection will have a influence on the decay of the transient density correlation function ϕ and therefore on the stresses.

6.2 Outlook

The standard local schematic MCT-ITT as proposed in [8] does lack the correct rate of change for scalar quantities which is the advected / material derivative $\frac{D}{Dt} \coloneqq \partial_t + [\vec{v} \cdot \vec{\nabla}]$. In the fifth chapter of this thesis a simply exchange to the – from a fluid mechanics point of view correct – advected derivative was proposed and successfully implemented in our existing local FEM-MCT code basis of the FEniCS environment. However, this exchange was only microscopically motivated. In future work one should try to find a correct microscopical derivation of (schematic) MCT-ITT equation which do contain advected derivatives. Furthermore it is not even clear that our proposed way ($\partial_t \leftrightarrow \frac{D}{Dt}$) would be the result of such a more in depth study of the derivation of MCT-ITT constitutive equations.
An appropriate starting point for a more detailed study of the MCT-ITT constitutive equation would be to go all the way back to the stochastic differential equations for Brownian particles (before the overdamped limit) and formulate the equations carefully with co- and contravariant tensors. In the excursion on the Oldroyd B / upper convected derivative the connections between upper or lower indices and the upper or lower (Oldroyd B or A) convected derivative was shown. Only with a fully tensorial derivation of MCT-ITT constitutive equations one can ensure that it is microscopically correct to only use the upper convected derivative as a rotation invariant deformation measure.
Of course more high pressure simulations in non-trivial geometries should be done to further study the effect of the advectional extension to the MCT-ITT model. Ideally one should compare simulation results to experiments.

Another macroscopically motivated idea, inspired by so called "fluidity models", would be to further exchange the material derivative by diffusion operators ($\frac{D}{Dt} \leftrightarrow \frac{D}{Dt} - D_0\Delta$) to build in further spatial non-locality between the generalized shear moduli $G(t, t')$ given by MCT-like integro-differential equations. Obvious downsides would be that one would need higher order stress elements because of the second derivatives in the $-\Delta$ operator, which would increase the memory demand of the simulations even further and would also increase the computational cost since the assembled matrices would increase in size. However such code would provide a link to the "fluidity" and typical "elasto-plastic" models that are commonly discussed in the context of rheology of glassforming fluids on a more mesoscopic level than MCT.

Furthermore recent work by F. Vogel and M. Fuchs [57] suggests to replace the Zwanzig-Mori projection-operator formalism by a more refined irreducible dynamics. The new approach leads to a more careful treatment of $\vec{q}$-vectors which also include transverse contributions - besides the longitudinal $\vec{q} \cdot \vec{k}$ contributions - resulting in a different memory kernel for the stress tensor. This recovers the expression for the stress autocorrelation including the elastic terms in solid states as found for Newtonian and Langevin systems, in case that those are evaluated in the overdamped limit.

Bibliography

[1] M. Ballauff, J. M. Brader, S. U. Egelhaaf, M. Fuchs, J. Horbach, N. Koumakis, M. Krüger, M. Laurati, K. J. Mutch, G. Petekidis, M. Siebenbürger, Th. Voigtmann, and J. Zausch. Residual stresses in glasses. *Phys. Rev. Lett.*, 110:215701, 2013.

[2] Ludovic Berthier and Giulio Biroli. Theoretical perspective on the glass transition and amorphous materials. *Rev. Mod. Phys.*, 83:587–645, Jun 2011.

[3] D V Boger. Viscoelastic flows through contractions. *Annual Review of Fluid Mechanics*, 19(1):157–182, 1987.

[4] P. Bottiglieri, F. De Sio, G. Fasanaro, G. Mojoli, M. Impembo, and D. Castaldo. Rheological characterization of ketchup. *Journal of Food Quality*, 14(6):497–512, 1991.

[5] J. M. Brader, M. E. Cates, and M. Fuchs. First-principles constitutive equation for suspension rheology. *Phys. Rev. Lett.*, 101:138301, Sep 2008.

[6] J. M. Brader, Th. Voigtmann, M. E. Cates, and M. Fuchs. Dense colloidal suspensions under time-dependent shear. *Phys. Rev. Lett.*, 98:058301, Jan 2007.

[7] Joseph M. Brader, Mike E. Cates, and Matthias Fuchs. First-principles constitutive equation for suspension rheology. *Physical Review E*, 86(2), 2012.

[8] Joseph M. Brader, Thomas Voigtmann, Matthias Fuchs, Ronald G. Larson, and Michael E. Cates. Glass rheology: From mode-coupling theory to a dynamical yield criterion. *Proceedings of the National Academy of Sciences*, 106(36):15186–15191, 2009.

[9] Dietrich Braess. *Finite Elemente Theorie, schnelle Löser und Anwendungen in der Elastizitätstheorie*. Springer-Lehrbuch Masterclass. Springer Berlin Heidelberg, Berlin, Heidelberg, 5. aufl. 2013 edition, 2013.

[10] Susanne C. Brenner. *The mathematical theory of finite element methods*. Texts in applied mathematics. Springer, New York u.a., 2. ed. edition, 2002.

[11] Douglas J. Jr. Marini L.D. Brezzi, F. Two families of mixed finite elements for second order elliptic problems. *Numerische Mathematik*, 47:217–236, 1985.

[12] John C. Butcher. *Numerical Methods for Ordinary Differential Equations*. John Wiley and Sons, 2016.

[13] H. Cardenas. Continuum mechanics studies on glass-forming liquids, phd thesis. *Heinrich-Heine Univesity of Dusseldorf*, 2018.

[14] P G G Debenedetti. Supercooled liquids and the glass transition. *Nature.*, 410(6825), 2001.

[15] J. Donea and A. Huerta. *Finite Element Methods for Flow Problems*. 2003.

[16] Lawrence C. Evans. *Partial differential equations*. American Mathematical Society, 2010.

[17] Matthias Fuchs and Michael E. Cates. Theory of nonlinear rheology and yielding of dense colloidal suspensions. *Phys. Rev. Lett.*, 89:248304, Nov 2002.

[18] Matthias Fuchs and Michael E. Cates. Schematic models for dynamic yielding of sheared colloidal glasses. *Faraday Discuss.*, 123:267–286, 2003.

[19] Matthias Fuchs and Michael E. Cates. Schematic models for dynamic yielding of sheared colloidal glasses. *Faraday Discussions*, 123:267–286, 2003.

[20] Paola Gallo and Mauro Rovere. *Physics of Liquid Matter*. Springer International Publishing, 2021.

[21] Roland Glowinski and Tsorng-Whay Pan. *Numerical Simulation of Incompressible Viscous Flow*. De Gruyter, Berlin, Boston, 2022.

[22] W. Gotze and L. Sjogren. General properties of certain non-linear integro-differential equations. *Journal of Mathematical Analysis and Applications*, 195(1):230–250, 1995.

[23] W. Götze. Some aspects of phase transitions described by the self consistent current relaxation theory. *Zeitschrift für Physik B Condensed Matter*, 56(2):139–154, 1984.

[24] Wolfgang Götze. *Complex dynamics of glass-forming liquids a mode-coupling theory*. International series of monographs on physics. Oxford Univ. Press, Oxford, 2009.

[25] Pouria Hajikarimi and Fereidoon Moghadas Nejad. Chapter 3 - mechanical models of viscoelasticity. In Pouria Hajikarimi and Fereidoon Moghadas Nejad, editors, *Applications of Viscoelasticity*, pages 27–61. Elsevier, 2021.

[26] Soroush Hooshyar and Natalie Germann. Shear banding in 4:1 planar contraction. *Polymers*, 11:417, 03 2019.

[27] Martien Hulsen, E.A.J.F. Peters, and B.H.A.A. Brule. A new approach to the deformation fields method for solving complex flow using integral constitutive equations. *Journal of Non-Newtonian Fluid Mechanics*, 98:201–221, 03 2001.

[28] Liesbeth M. C. Janssen. Mode-coupling theory of the glass transition: A primer. *Frontiers in Physics*, 6, Oct 2018.

[29] Daniel D Joseph and Roger L Fosdick. The free surface on a liquid between cylinders rotating at different speeds part i. *Archive for Rational Mechanics and Analysis*, 49:321–380, 1973.

[30] Jürgen Jost. *Riemannian geometry and geometric analysis*. Universitext. Springer, Cham, Switzerland, seventh edition edition, 2017.

[31] L. D. Landau and E. M. Lifshitz. *Fluid Mechanics, Second Edition: Volume 6 (Course of Theoretical Physics)*. Course of theoretical physics / by L. D. Landau and E. M. Lifshitz, Vol. 6. Butterworth-Heinemann, second edition edition, 1987.

[32] Hans Petter Langtangen and Anders Logg. *Solving PDEs in Python - The FEniCs Tutorial Volume I*. Springer, 2017.

[33] M.G. Larson and F. Bengzon. *The Finite Element Method: Theory, Implementation, and Applications*. Texts in Computational Science and Engineering. Springer Berlin Heidelberg, 2013.

[34] Fredrik Larsson, Pedro Díez, and Antonio Huerta. A flux-free a posteriori error estimator for the incompressible stokes problem using a mixed fe formulation. *Computer Methods in Applied Mechanics and Engineering*, 199(37):2383–2402, 2010.

[35] L.G. Leal, M.M. Denn, and R. Keunings. Lake arrowhead workshop special issue papers—introduction. *Journal of Non-Newtonian Fluid Mechanics*, 29:1–8, 1988.

[36] A. Liluashvili. Mode coupling theory of active brownian hard disks, phd thesis. *Heinrich-Heine Univesity of Dusseldorf*, 2017.

[37] Alexander Liluashvili, Jonathan Ónody, and Thomas Voigtmann. Mode-coupling theory for active brownian particles. *Phys. Rev. E*, 96:062608, Dec 2017.

[38] Anders Logg, Kent-Andre Mardal, Garth N. Wells, et al. *Automated Solution of Differential Equations by the Finite Element Method*. Springer, 2012.

[39] G.I. Marchuk. Splitting and alternating direction methods. volume 1 of *Handbook of Numerical Analysis*, pages 197–462. Elsevier, 1990.

[40] James Clerk Maxwell. On the equilibrium of elastic solids. *J. Trans. Roy. Soc. Edinb.*, 20:87–120, 1853.

[41] Alexandre Nicolas and Matthias Fuchs. Shear-thinning in dense colloidal suspensions and its effect on elastic instabilities: From the microscopic equations of motion to an approximation of the macroscopic rheology. *Journal of Non-Newtonian Fluid Mechanics*, 228:64–78, 2016.

[42] J. G. Oldroyd. On the formulation of rheological equations of state. *Proceedings of the Royal Society A: Mathematical, Physical and Engineering Sciences*, 200:523–541, 1950.

[43] S. Papenkort and Th. Voigtmann. Channel flow of a tensorial shear-thinning maxwell model : Lattice boltzmann simulations. *Journal of Chemical Physics*, 140(16), 2014. Article Number: 164507.

[44] S. Papenkort and Th. Voigtmann. Multi-scale lattice boltzmann and mode-coupling theory calculations of the flow of a glass-forming liquid. *Journal of Chemical Physics*, 143:204502, 2015. Article Number: 204502.

[45] Wolfgang Paul and Jörg Baschnagel. *Stochastic processes from physics to finance*. Springer, Heidelberg New York Dordrecht London, second edition edition, 2013.

[46] W H Reed and T R Hill. Triangular mesh methods for the neutron transport equation. *Tech. Report LA-UR-73–479*.

[47] David R Reichman and Patrick Charbonneau. Mode-coupling theory. *Journal of Statistical Mechanics: Theory and Experiment*, 2005(05):P05013, May 2005.

[48] Michael Renardy and Becca Thomases. A mathematician's perspective on the oldroyd b model: Progress and future challenges. *Journal of Non-Newtonian Fluid Mechanics*, 293:104573, 2021.

[49] M. Siebenbürger, M. Ballauff, and Th. Voigtmann. Creep in colloidal glasses. *Phys. Rev. Lett.*, 108:255701, Jun 2012.

[50] Bjørn Eske Sørensen. A revised michel-lévy interference colour chart based on first-principles calculations. *Eur. J. Mineral.*, 25:5–10, 2013.

[51] Sebastian Steinhäuser, Timm Treskatis, Stefan Turek, and Thomas Voigtmann. Residual stresses couple microscopic and macroscopic scales. *arXiv preprint arXiv:2307.12764*, 2023.

[52] J. Stoer and R Bulirsch. *Introduction to numerical analysis*. Texts in applied mathematics. Springer, 2002.

[53] F. Tone and D. Wirosoetisno. On the long-time stability of the implicit euler scheme for the two-dimensional navier–stokes equations. *SIAM Journal on Numerical Analysis*, 44(1):29–40, 2006.

[54] F.G. Tricomi. *Integral Equations*. (Pure and applied mathematics, v. 5). Dover Publications, 1985.

[55] Yankeelov Tunc, Rodin. Implementing coupled models in fenics: Viscoelastic flows, poroelasticity, and tumor growth. *not published yet*, 2021.

[56] David C. Ullrich. *https://math.stackexchange.com/questions/2795383/the-tauberian-final-value-theorem/2795640#2795640*, 2018.

[57] Florian Vogel and Matthias Fuchs. Stress correlation function and linear response of brownian particles. *The European Physical Journal E : Soft Matter and Biological Physics*, 43, 2020. Article Number: 70.

[58] Th. Voigtmann. *Lecture Notes on Stochastic Processes*. Heinrich-Heine University, Dusseldorf, SS 2019.

[59] Th. Voigtmann. *Lecture Notes on Classical Field Theory*. Heinrich-Heine University, Dusseldorf, WS 2019/20.

[60] F. Weysser, A. M. Puertas, M. Fuchs, and Th. Voigtmann. Structural relaxation of polydisperse hard spheres: Comparison of the mode-coupling theory to a langevin dynamics simulation. *Phys. Rev. E*, 82:011504, Jul 2010.

[61] Robert Zwanzig. *Nonequilibrium statistical mechanics*. Oxford Univ. Press, Oxford u.a., 2001.